The Relationship Between Microstructure and Stable Pitting Initiation in Aerospace Aluminium Alloy 2024-T3

A thesis submitted in fulfillment of the requirements for the degree of Doctor of Philosophy

Adam Paul Boag

B. App Science (Applied Physics) / B. Eng. (Communications) Hons

School of Applied Science (Applied Physics)
Science, Engineering and Technology Portfolio
RMIT University

December 2008

Declaration

I certify that except where due acknowledgement has been made, the work is that of the author alone; the work has not been submitted previously, in whole or in part, to qualify for any other academic award; the content of the thesis is the result of work which has been carried out since the official commencement date of the approved research program; any editorial work, paid or unpaid, carried out by a third party is acknowledged.

Adam Paul Boag

22 December, 2008

To my Nana and Pa
Whose love I will always cherish

Acknowledgments

Firstly I would like to acknowledge my supervisors Dougal McCulloch, Tony Hughes and David Jamieson for their guidance and support through out my candidature. In particular I would like to acknowledge Dougal for all his assistance and for teaching me many of the techniques as well as Tony for his knowledge and countless hours he has dedicated towards this project.

I would also like to thank the following people for their contributions to this work.

- Lenore Pedrina (DSTO), for your expertise and guidance in corrosion and in particular electrochemical measurements.
- Phil Francis (RMIT), for all your help with the EM suite and in keeping all the equipment operational.
- Bruce Robinson (RMIT), for all your help in the workshop, you made many of the things inside this thesis possible.
- Chris Ryan and David Belton (CSIRO), for all your help with the NMP, GeoPIXE and ImageJ.
- Roland Szymanski, (University of Melbourne), for your assistance with the CSIRO beamline / pelletron facility.
- Colin Macrae, Nick Wilson and Matt Glenn (CSIRO), for all your assistance with the microprobe study.

I would like to thank the many people in Applied Physics at RMIT University, for creating such an enjoyable workplace environment

I would also like to give special thanks to Flame Burgmann, who always provided a helping hand and kept me on track through out my time at RMIT.

My mother and step father deserve particular acknowledgement for their encouragement and support throughout my many years as a ‘professional student’. Thankyou for providing me with a harmonious atmosphere in which to live and study. In addition,

thanks to my sister Emma and brother Nathan who have always showed enthusiasm and encouragement.

My Nana and Pa, for a lifetime of support and for helping to shape me into the person I am today.

Lastly I'd like to thank my wife Tamara and son James, firstly for putting up with me during this time and for without their love and understanding I could not have come this far.

Table of Contents

List of Figures

Chapter 2:

Chapter 3:

Chapter 4:

Chapter 5:

Chapter 6:

Chapter 7:

Chapter 9:

List of Tables

Publications and Conference Proceedings

Publications:

A P Boag, D.G. McCulloch, D.N Jamieson, S.M. Hearne, A.E. Hughes and C.G Ryan, Combines Nuclear Microprobe and TEM Study of Corrosion Pit Nucleation by Intermetallics in Aerospace Aluminium Alloys, NIMb **231**, 457-462 (2005)

T.G. Harvey, A.E. Hughes, S.G. Hardin, T. Nikpour, S.K. Toh, A P Boag, D.G. McCulloch and M. Horne, Non-Chromate Deoxidation of AA2024-T3: Sodium Bromate – Nitric Acid (20-60º), App. Surf. Sci. **254,** 2352-3575 (2008)

A P Boag, A.E. Hughes, D.G. McCulloch, M Glenn and T Muste, Corrosion of AA2024-T3 Part I: Localised Corrosion, To be submitted to Corr Sci.

A P Boag, A.E. Hughes, D.G. McCulloch, M Glenn, T Muster and C G Ryan, Corrosion of AA2024-T3 Part II: Co-Operative Corrosion, To be submitted to Corr Sci.

A P Boag, A.E. Hughes, D.G. McCulloch, C Macrae, N Wilson and M Glenn, Characterisation of Aluminium Alloy 2024-T3 by Electron Microprobe, To be submitted to Corr Sci.

Conference Proceedings:

A P Boag, D.G. McCulloch, D.N Jamieson, A.E. Hughes, L.M. Pedrina and C.G Ryan, Analysis of Pitting Corrosion in Aerospace Aluminium Alloy AA2024-T3, presented at Australian Microbeam Analysis Society (2005)

A P Boag, D.G. McCulloch, D.N Jamieson, S.M. Hearne, A.E. Hughes, C.G Ryan and B. Rout, Analysis of Intermetallic Phases in Aerospace Aluminium Alloy Using a Nuclear

Microprobe and Phase Correlation Mapping, presented Australian Institute of Physics (2005)

A P Boag, D.G. McCulloch, D.N Jamieson, A.E. Hughes, L.M. Pedrina and C.G Ryan, Analysis of Pitting Corrosion in Aerospace Alloy AA2024-T3, presented at Microscopy & Microanalysis (2005)

A.E. Hughes, A.P. Boag, L.M. Pedrina, L. Juffs, D.G. McCulloch, J. DuPlessis, P. Paterson, I. Snook and B. O'Malley, Statistical Approach to Determine Spatial and Elemental Correlations of Corrosion Sites on Al-Alloys, presented at Aluminium Surface Science & Technology (2006)

Abstract

Aluminium alloys are essential to a variety of industry sectors, particularly transport, where they are used in the production of cars and aeroplanes. However, aluminium alloys are susceptible to degradation through corrosion which can compromise the integrity of components manufactured from this material. Therefore research into the means by which these alloys degrade is important. This thesis aims to understand how one of the more potentially damaging types of corrosion, known as pitting corrosion, occurs in the important aluminium alloy 2024-T3 (AA2024-T3).

In order to study this phenomenon, this thesis first characterises the alloy microstructure in detail, particularly the type and distribution of intermetallic particles since these play an important role in corrosion processes. The microstructure was studied using an electron microprobe analysis of a 5 mm x 5 mm area of AA2024-T3 and some 80,000 particles were characterised. This investigation was one of the most comprehensive studies to date of any aluminium alloy. Of the particles studied, it was found that the major types included the S and θ phases and a number of compositions based around AlCuFeMn and AlCuFeMnSi. Depletion zones were an integral feature of the alloy microstructure. Pair correlation functions were used to determine the degree of clustering and it was found that there was both inter particle as well as intra particle clustering. Inter particle clustering was observed at length scales well beyond 50 μm.

A detailed study of corrosion on AA2024-T3 was undertaken by examining the surface after corrosion over a time period spanning 2.5 minutes to 120 minutes. From this investigation, a hierarchy of the localised corrosion was observed as it was very apparent that particles of particular elemental compositions were more susceptible to attack much sooner than other compositions. Larger corrosion attack sites on the surface, which were called co-operative corrosion, were attributed to intermetallic clustering affects and changes in chemical composition such as Cu-enrichment. These results were used to develop a detailed model of the initiation of stable pitting corrosion in AA2024-T3,

which will lead to a better understanding on how to prevent pitting attack on commercially important aluminium alloys.

AA2024-T3 is rarely used in the polished state, for real world applications is it generally finished by mechanical or chemical processing. In the final part of this thesis, the influence of clusters on metal finishing was examined using a standard aluminium chemical deoxidiser. It was found that the etch rate of this deoxidiser increased dramatically with the increase in temperature. Under certain processing conditions only the intermetallic particles are etched out and these retain the history of the spatial distribution of the clustering of the intermetallic particles. This leaves a cluster of ‘holes‘ which could trap metal finishing solution and lead to severe subsurface attack.

Chapter 1 - Introduction

1.0 Background

Aluminium alloys for commercial applications contain numerous intermetallic (IM) particles comprising one or more of the following major elements: Al, Mg, Zn, Fe, Si, Cu, Mn and Li [1]. These particles typically take on many shapes and have diameters up to 50 μm on a rolled surface [2]. Particle densities ranging from 3 x 10^5 to 1 x 10^6 /cm^2 for polished surfaces have been measured [2,3], these only include constituent and large impurity particles. Exposed surfaces of these alloys require protection against environmental corrosion, which is usually accomplished by means of a conversion coating using Cr compounds or anodising followed by the application of a paint system which may include a chromate inhibited primer and topcoat. The breakdown of these coatings result in the onset of corrosion in the aluminium alloy which is a significant problem given the wide application of aluminium alloys in infrastructure and transport (particularly aerospace).

Pitting corrosion in aluminium alloys is particularly important since pitting can lead to other forms of corrosion such as exfoliation corrosion, which under cyclic loading can be the initiation point for fatigue cracks which undermine structural integrity [4]. Pitting corrosion is localised and it has been demonstrated that particles play an important role in the sequence of events that leads to pit formation [3,5]. The focus of this thesis is to investigate how composition and location of IM particles relates to the establishment of pitting in AA2024-T3, an important Al alloy commonly used in the aircraft industry. This study was undertaken as there is still no definitive model of stable pit initiation on aluminium alloys. The aim is to understand the mechanisms behind corrosion initiation and propagation leading to the onset of stable pitting. Due to the size of these pits, analysis was undertaken using a wide variety of analytical techniques to best understand the processes involved in stable pit formation. It is believed that understanding the conditions that lead to pitting will lead to more advanced techniques for prevention and assist in computational modelling of corrosion allowing a better *a priori* understanding

and practical solutions such as the reduction in maintenance costs through structural health monitoring software [6].

1.1 Research Objectives

The research objective of this thesis is to gain a detailed understanding of stable pitting corrosion in AA2024-T3. In order to achieve this, the study has been broken up into the following sub sections;

Characterisation of the alloy microstructure: Particular attention has been paid to the characterisation of the AA2024-T3 IM particle statistics in which a study of the composition and distribution of over 80,000 particles is presented.

Pitting corrosion on polished AA2024-T3: This study builds on the previous section by investigating how the alloys properties including, particle distribution and size, elemental composition and the anodic/cathodic reactions between particles of differing elemental composition was explored. This work was undertaken to provide an understanding into the basic phenomena of pitting corrosion in this alloy.

Finally a study investigating pre treatment techniques used to protect against corrosion in this alloy is presented. This section provides a preliminary investigation into the effect of non chromate de-oxidisers as part of chemical pre-treatment prior to conversion coatings.

1.2 Research Scope

This thesis is focused on characterisation of both virgin and corroded AA2024-T3 to investigate both statistically and experimentally factors which lead to pitting corrosion in this material.

Chapter 2 presents the literature review of work pertinent to this research. This involves the basic understanding of the alloy including both its history and characteristics. Pitting corrosion will be discussed in detail with a focus on metastable and stable pitting phenomena as well as factors known to accelerate and retard the formation of pits in the alloy's surface such as inhibitors and alloying additions.

Chapter 3 concentrates on the experimental aspects of the project. A detailed description of the analytical techniques used is given. As well, a discussion explaining why each technique was used for this investigation as well as experimental and operating conditions.

Chapter 4 gives a detailed analysis using an electron microprobe of the IM particles in AA2024-T3. Image analysis of high resolution (step size of 0.4 μm) broad area (5mm x 5mm) maps provided details of the lateral distribution of particles with evidence of clustering.

Chapter 5 describes the application of novel analysis techniques such as particle induced X-ray emission spectroscopy (PIXE) and associated image analysis to the study of pitting corrosion both on virgin and corroded AA2024-T3 samples. Part of this chapter is devoted to the examination of some examples of IM compounds found in AA2024-T3.

Chapter 6 presents results obtained for the study of the corrosion steps of AA2024-T3 as a function of time. The work in this chapter identifies different stages in the corrosion process that leads to stable pit formation. Conclusions are drawn from both an experimental and statistical standpoint.

Chapter 7 investigates a metal finishing deoxidation process in detail using SEM, TEM and energy filtered TEM (EFTEM). It examines how the surface is modified and identifies regions where only IM particles are removed leaving etch pits which have the same special relationship as the original IM particles.

Chapter 8 draws an overall conclusion for this work. Furthermore, a section discussing possible future work is presented.

1.3 Bibliography

1 J. E. Hatch, *Aluminium: Properties and Physical Metalurgy*, Metals Park, OH, (1984).

2 L. Juffs, Investigation of Conversion Coating Deposition on Microscopic and Macroscopic Intermetallic Phases of Aluminium Alloy, RMIT University, (2002).

3 G. S. Chen, M. Gao, and R. P. Wei, Corrosion **52,** 8 (1996).

4 J. R. Davis, *Corrosion of Aluminium Alloys*, ASM International, (1999).

5 R. G. Buchheit, R. P. Grant, P. F. Hlava, B. McKenzie, and G. L. Zender, J. Electrochem Soc. **144,** 2621 (1997).

6 A. E. Hughes, B. R. W. Hinton, S. A. Furman, I. S. Cole, D. Paterson, A. Stonham, G. McAdam, D. Dixon, S. J. Harris, A. Trueman, M. Hebbron, C. Bowden, P. C. Morgan, and M. Ranson, Corr. Revs **20,** 275 (2007).

Chapter 2 - Review of Corrosion Phenomena

2.0 Introduction

This chapter reviews AA2024-T3 and the current understanding of the pitting corrosion phenomena and current prevention methods used. It includes the following sections.

1. The alloy, in which an outline into the alloy's history and applications is reviewed.

2. Corrosion in metals, in which characteristics of corrosion are discussed where the major focus of this section is the development of localised corrosion on AA2024-T3.

2.1 The Alloy

Aluminium alloys have long been used in the transport industry, especially aerospace, to retain both structural integrity as well as dramatically decrease weight. Since the first flight of the Wright brothers in 1903 where an alloy block engine was used to power their aircraft, the use of aluminium has continually grown in order to reduce weight and has been the primary means by which aviation advancements have been made [1,2].

AA2024-T3 was developed by Alcoa in 1931 and belongs to the 2XXX series of Alloys (Al–Cu–Mg). It was the first of this type to have a yield strength approaching 490 MPa [3] and generally replaced its predecessor AA2017-T4 (Duralumin) as the predominant 2XXX series alloy used in the aerospace industry. Its desirable properties include high strength and fatigue performance [3] and is used in aerospace applications like aircraft fuselage, wing skins and engine areas. The main alloying elements are Cu (3.8–4.9%) and Mg (1.2–1.8%), however it also contains Si (0.5%), Fe (0.5%), Mn (0.3–0.9%), Cr (0.1%), Zn (0.25%) and Ti (0.15%). Today this alloy is still the most common aluminium alloy prevalent in most airfleets in both the commercial and military aerospace industries.

2.1.1 Microstructure

There are two broad classifications for wrought aluminium alloys; non-heat treatable and heat treatable [4]. Non-heat treatable alloys, which obtain most of their strength through solid solution hardening and strain hardening, contain major additions of Cr, Fe, Mg, Mn, Si and Zn, whilst only minor additions of copper are permitted (*i.e.* 0.12 – 0.15 wt% in can stock alloys AA3003, AA3104 and AA1100, and 1 wt% in AA8280 and AA8081). Heat treatable aluminium alloys may have levels of Cu up to 6.3 wt% [4]. Ultimately, these alloying elements are present in either solid solution in the matrix, IM particles, or both. Cu, together with Mg, Zn and Si are appreciably soluble at high temperature and considerably less soluble at low temperature. This results in the precipitation of various phases during solidification of the alloy [4]. The AA2*xxx* series, containing copper and magnesium, are high strength aluminium alloys and are therefore often used in applications which require such strength*, one example being* aircraft manufacture.

AA2024-T3 is a precipitate hardened alloy, its micro structure which give it its high strength is determined by the ternary Al-Cu-Mg phase diagram. In Al-Cu-Mg ternary systems that fall in the α + S phase region, the precipitation of Al-Cu-Mg particles occurs in the following sequence; Cu in solid solution with aluminium (α-Al), first precipitates out as clusters of solute elements before Guinier-Preston (GP) zones form as fine rods in the $<001>_{\alpha}$ directions. Much later in the precipitation sequence, or more usually, where cold work is applied, S-phase precipitates form as laths within the microstructure on $\{012\}_{\alpha}$ planes in $<001>_{\alpha}$ directions [1].

Specifically, these fine precipitates often start as clustering of alloying components called GP zones that grow into a range of precipitates with increasing temperature and time. Initially, these precipitates are coherent with the aluminium lattice, which is desirable, but continued ageing will take the precipitates through degrees of coherency until the interfaction bold is broken by coherency strains, then they become incoherent with the lattice [4]. For example in the binary Al-Cu alloy θ-phase forms (Al_2Cu), the stages GP → θ” → θ’ → θ. and similar precipitation series is seen for the S-phase (Al_2CuMg).

Another type of IM particle that forms in heat treatable alloys are the dispersoids. These form by solid state reaction during preheating of the ingot; they represent an important part of the alloy microstructure since they control grain growth. They are formed through precipitation with either chromium, manganese, titanium or zirconium and form dispersoids particles such as $Al_{12}CrMg_2$, $Al_{20}Cu_2Mn_3$, $Al_{12}Mn_3Si$, Al_3Ti and Al_3Zr. These particles are usually a few nanometers up to 200 nm in size [5]. $Al_{20}Cu_2Mn_3$ is the dominant dispersoid in AA2024-T3.

A third type of particles are the constituent particles, most of which are formed during solidification of the initial ingot. For Cu-containing alloys copper is present in solid solution in the matrix (α-Al). AA2024-T3 also has copper incorporated into a range of IM phases called constituent particles. For simplicity we refer to these constituent particles as IM particles. The microstructure of these alloys is complex and depends on thermal and ageing treatments. Common constituent particles and the alloys they appear in are Al_7Cu_2Fe, $Al_{12}(Fe,Mn)_3Si$, Al_2CuMg, Al_2Cu and $Al_6(Cu,Fe)$ [5].

AA2024-T3 is one of the most widely studied of the AA2*xxx* series alloys for corrosion and metal finishing applications, although AA2014-T3 is becoming more prominent in aircraft manufacture, and therefore a subject of research, [5,6]. For AA2024-T3 rolled sheet, total constituent particle number densities have been reported from 300,000 /cm^2 [7] to 530,000 /cm^2 [8,9] for polished surfaces (both prepared using SiC followed by diamond polishing) and as high as 11,700,000 /cm^2 for the rolled surface [8,9]. However, for rolled and polished surfaces, the surface area occupied by IM particles was similar, suggesting that rolling leads to a significant breakup of IM particles. This is also reflected in the average particle size which was much smaller for the rolled surface than the polished surfaces. Particle size distributions for the IM particles in AA2024-T3 have been reported by Jakab *et al*. [10] and [11,9] for polished surfaces, with slightly different distributions revealed, but with similar volume fractions of IM particles (Table 2-1).

Source	Average Particle Size (μm)	% Surface Area
Polished		
Hughes *et al*. (2006), Juffs (2003)	6.6	2.89
Jakab *et al*. (2005)	3.1	2.18
Rolled		
Hughes *et al*. (2006), Juffs (2003)	2.0	2.82

Table 2-1: IM particle distributions in AA2024-T3.

It is not clear whether the difference in the particle number density between 300,000 and 530,000 /cm^2 represents a significant variation. Certainly there will be batch variation and probable processing effects; further the particle population densities will depend on the resolution of the techniques used for the counting statistics. Another possibility for the differences in the published figures is the processing history of the alloy. Specifically, for sheet alloy, the gauge (or thickness) reflects the number of rolling passes that the alloy undergoes. Clearly, at each pass the potential exists for further breakup of IM particles and changes in the IM size, spatial distributions and grain refinement. The sampling size for statistical determination is one of the areas explored in this thesis.

Examination of cross sections of AA2024-T3 revealed that the distribution of IM particle density across the sheet can change significantly, as depicted in Figure 2-1 [8]. The variation in particle density is accompanied by an increase in particle size towards the centre of the sheet; this is reflected in the larger particle size on the polished surfaces (toward the sheet centre) versus the rolled surface. The characteristics of IM particle distributions is an area which warrants further investigation since second phase particles are often sites of corrosion initiation and there is have been little research into the understanding of clustering of these particles [12][13] [39].

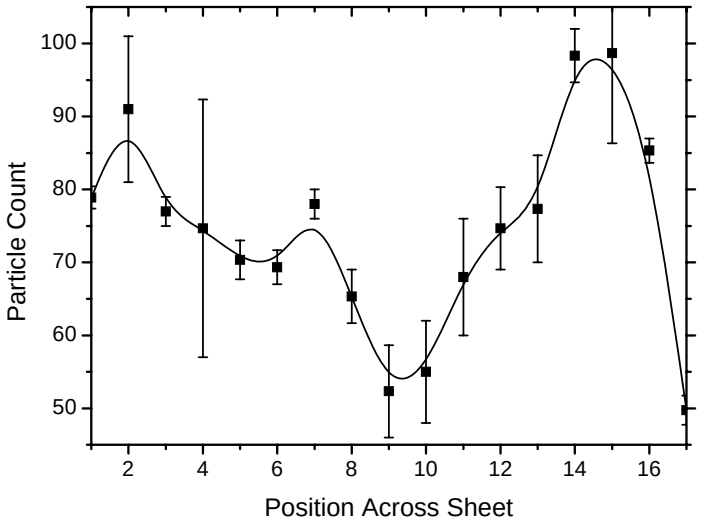

Figure 2-1: IM Particle Count taken on frames across a section of AA2024-T3 with a thickness of 1.2 mm. Sample was mounted in bakelite and polished down to 1 µm [8].

Focusing on the larger IM particles, Buchheit *et al*. [14] reported that roughly 60% of the constituent particles of particle diameter exceeding 0.2 µm were Al_2CuMg (S-phase). The remaining 40% of IMs comprised a range of Al-Cu-Fe-Mn containing phases. The composition of Al-Cu-Fe-Mn phases has been suggested to take various forms. Gao *et al*.[15] suggested compositions based upon $(Al,Cu)_x(Fe,Mn)_ySi$ such as modified forms of Al_8Fe_2Si or $Al_{10}Fe_2Si$ type IMs, although in low silicon–containing AA2*xxx* series alloys, these compositions are different. For example, Buchheit *et al*. [14] reported that of the remaining 40% of IM particles, the most notable included Al_7CuFe_2, Al_6MnFe_2, $(Al,Cu)_6Mn$, and a number of undetermined compositions in the class $Al_6(Cu,Fe,Mn)$ where the Cu:Fe:Mn ratios were approximately 2:1:1. The Al-Cu-Fe-Mn particles consistently exhibited cross-sectional diameters in the range 10 to 50 µm, possessed a high hardness, and were generally irregular in shape according to Liao and Wei [16]. Further, Scholes *et al*. [17] reported that this class of IM particles underwent fracture during milling, whereas the S-phase particles remained largely intact.

There is emerging interest in the spatial relationship of IM particles in surfaces. In an extensive study of clustering, Juffs [8] examined several methods of determining

clustering of IM particles in aluminium alloys. One of the most sensitive methods was the pair correlation function in which the average number of nearest neighbours is determined as a function of distance from the average particle. Juffs [8] observed clustering in AA2024-T3 for both polished and rolled surfaces; indeed the number of nearest neighbours was more than double that expected on a polished surface with a random distribution of IM particles, and a little under twice as many for the rolled surface. On the other hand Jakab *et al*. [10] found no significant clustering in AA2024-T3. The statistical sampling between the two studies may explain the differences. In the former study, Juffs [8] counted several thousand particles, whereas, Jakab *et al*. [10] did not indicate the number of particles counted, although it appeared to be less than one hundred. As will be further detailed in the later in this chapter in the section on corrosion, clustering may prove to be an important issue for pit initiation and is a promising area for further research.

At the submicron scale of the alloy microstructure, there is an even distribution of $Al_{20}Cu_2Mn_3$ dispersoids. Guillaumin and Mankowski [18] have reported that the coarse S-phase IM particles are surrounded by a dispersoid free zone. However, Buchheit *et al*. [14] suggested that only those particles that precipitate after secondary solution heat treatment will have a precipitate free zone surrounding them. At the finest scales there are lenticular particles around 100 nm in length which comprise the Al_2CuMg hardening precipitates. More generally in AA2*xxx* alloys, the hardening precipitates of θ-phase (Al_2Cu) and S-phase (Al_2CuMg), depend on the copper to magnesium ratio [4].

A SEM micrograph depicting a cluster of IM particles in AA2024-T3 is shown in Figure 2-2. In this figure the more angular IM particles (indicated by B) are generally associated with Fe, Mn, Cu, Al and Si containing particles whereas the rounder particles (indicated by A) are commonly associated with the S-phase [19].

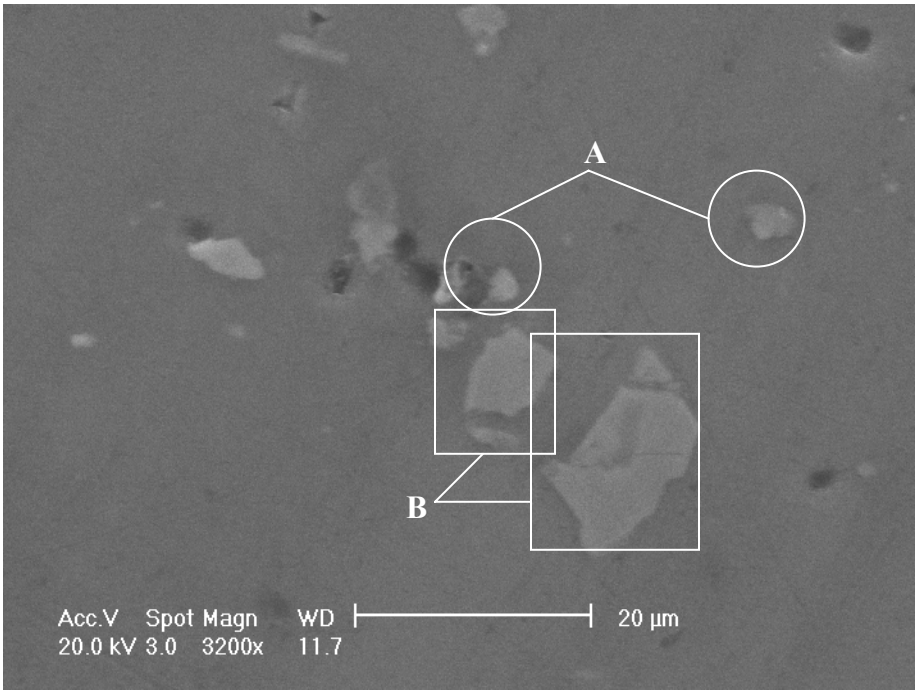

Figure 2-2: SEM micrograph of IM particles on a AA2024-T3 surface. Circled particles (A) indicate selected S-phase particles. Squared particles (B) indicate Fe, Mn, Cu, Al and Si containing particles

The surface condition is obviously important for the initiation of corrosion reactions. Both aluminium and aluminium alloys have a naturally occurring protective oxide layer and although very resilient, this passive film does break down, generally at points where non uniformities occur on the surface such as boundaries between IM particles and the matrix. This is one reason why IM particles are reported to be common sites for pit nucleation in aluminium alloys [1,14,15] Further detail on the role of this passive film and the breakdown can be found in section 2.4 Mechanism of Pitting Corrosion.

2.2 Introduction to Corrosion Processes

Corrosion in metals is the principal means by which metal degradation occurs. It is due to chemical surface reactions with harsh components of the environment, particularly with chloride which deposits and is often present as NaCl or $MgCl_2$. Corrosion is a major problem associated with almost all metals, as only the very noble, such as gold or

platinum, are immune to corrosion under normal environmental conditions. A very common type of corrosion is the rusting of iron. This occurs as a result of iron surface atoms reacting with oxygen and water, both found in the surrounding moist atmosphere, and is known as uniform corrosion. As metals have a high electric conductivity, their corrosion is generally of an electrochemical nature. These types of corrosion include; uniform, pitting, crevice, intergranular and filiform to name just a few.

2.3 Pitting Corrosion

Pitting corrosion is a common type of corrosion in metals, especially for those materials which form passive protective films on their surfaces, such as aluminium alloys, stainless steels, titanium alloys, etc. Pitting corrosion is a localised form of corrosion and is generally associated with the localised breakdown of the protective film on the surface of a metal resulting in an accelerated dissolution of the underlying metal [20]. Chloride is well known for causing breakdown of the passive film on the surface, and its presence is often attributed to this type of corrosion. Unlike general corrosion where the surface is corroded evenly, pitting corrosion is unpredictable, since it is hard to detect as it occurs locally on small areas of the metal surface. Pitting corrosion can be extremely dangerous as it can lead to significantly reduced structural integrity as pits can provide sites for crack initiation, reduced mechanical strength, or penetrate container walls allowing leakage of contained gas or liquid.

2.4 Mechanism of Pitting Corrosion

Pitting is commonly attributed to the breakdown of the protective passive film which covers a metal or alloy. The pitting resistance of a passive film is thought to depend on the electrochemical stability of the film and the ability for it to repassivate the surface [21]. An alloy's resistance to pitting attack is typically measured by the pitting potential, E_p, which defines a passive film's electrochemical stability and the protection potential, E_{pp}, which represents the ability of a film to repassivate. For potentials more cathodic than E_{pp} a metal's surface is passivated, hence a better pitting corrosion resistance is

associated with a more anodic E_{pp}. Pit nucleation can only occur when the potential is above E_p and can continue to grow when the potential is between E_p and E_{pp}. Due to a metal's surface being heterogeneous in nature, especially for alloys containing IM particles, a passive film is not completely homogeneous and as a result local imperfections are found. It is these locations where a passive film is most likely to break down and provide a potential pit nucleation site.

Pitting occurs due to a stimulated anodic – cathodic reaction resulting from an increased anodic reaction caused by activating anions as well as an increased cathodic reaction due to the presence of oxidising agents. In order for a pit to occur in a metal, a minimum pitting potential must be attained, this potential representing the localised potential required to drive the pitting process. A pit is initiated by the adsorption of activating anions, typically chloride ions, at locations where breakdown of the passive film has occurred. By attaining the pitting potential, the electric field strength at thin sections of the passive film is high enough that chloride ions can penetrate the film causing a local dissolution of the passive film. Once a pit has formed it will continue to grow with a power law dependence on time [44] as the pit creates conditions which promote its continued growth.

Figure 2-3 illustrates the mechanism behind pit formation and its autocatalytic self stimulating nature. Once pitting attack occurs, chloride ions migrate into the pit by the corrosion current generated by the pit cell.

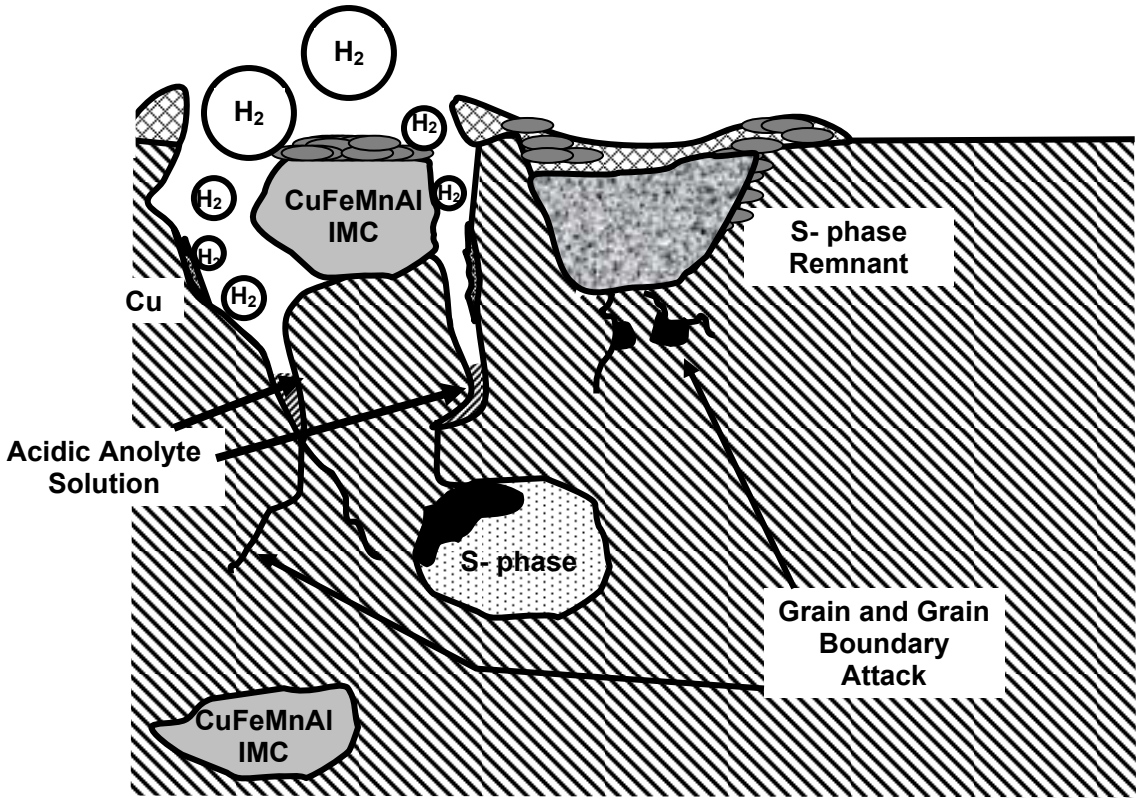

Figure 2-3: Electrochemical mechanism of pit growth within aluminium

2.5 Stable and Metastable Pits

In recent years there has been a trend towards a statistical understanding of pit initiation using electrochemical and microstructural approaches. The electrochemical approach describes pitting in terms of nucleation events, metastable pitting and stable pitting, both in ferrous based metals [22,23] and aluminium [24-27]. The focus of this approach is the "identification of electrochemical factors that promote the transition from metastable to stable pit growth" [24]. The use of this terminology comes from potentiostatic measurement of currents made at potentials between the open circuit potential (OCP) and the breakdown potential [25-27]. For aluminium and ferrous metals, characteristics of these measurements include current transients and increases in total current which have been described as nucleation, metastable and stable pitting events. For ferrous metals these events have been described as follows: *Nucleation* events are spontaneous corrosion and passivation events which typically have a lifetime of a few seconds. *Metastable* pitting appears to initiate in the same fashion but maintains a corrosion current over tens

of seconds possibly through a ruptured oxide coating. Repassivation occurs when this oxide is fully ruptured and the diffusion path is not long enough to maintain a concentration gradient at the head of the pit. It is thought that for these events, corrosion occurs beneath the surface oxide to the point where there is hydrogen production which bursts the oxide and dissipates the anolyte solution into the general solution causing repassivation. *Stable* pitting again initiates in a similar fashion to the other type of pitting events, but has a higher initial current density. It is suggested that when the oxide cap over the pit fully ruptures then the pit is deep enough to maintain a concentration gradient and an acidic anolyte solution is established at the pit head. These type of current transients have been observed for both pure Al [24] and AA2024-T3 [25-27].

Thus in this electrochemical approach characteristics of the current transients such as peak current and total charge passed are used to determine a quantity called the pit stability product. As early as 1976, Gavele [28] proposed the quantity $i.r_{pit}$ (pit stability product) where i is the pit current density and r is the pit radius [10,22,24], in modelling the chemistry within pits and the establishment of chemical conditions for the propagation of a stable pit. He estimated that $i.r_{pit}$ should be $\sim 10^{-2}$ A/cm. For pure aluminium, Pride et al. [24] proposed that the boundary between metastable and stable pitting occurred when the rise in the pit current was steep enough to maintain a $i.r_{pit} > 10^{-2}$ A/cm. Pride et al. [24] found that the number of metastable pits in aluminium increase with increased potential until it reached the pitting potential (Figure 2-4).

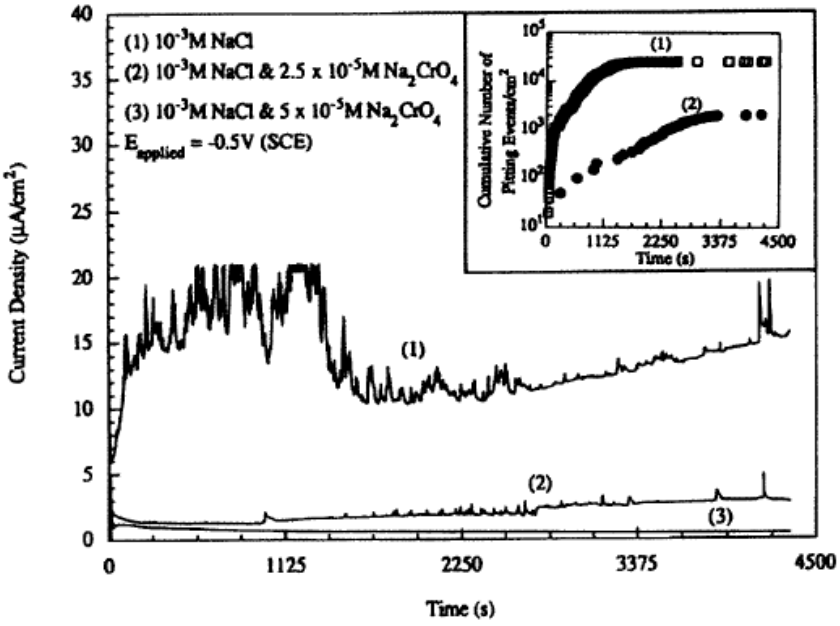

Figure 2-4: Time series showing effect of potential on anodic current spikes associated with metastable pitting [24]

The first limitation of the purely electrochemical approach for an alloy like AA2024-T3 is that it provides no microstructural information on the metastable pit initiation site. While there have been numerous studies of localized corrosion in the form of trenching and S-phase dissolution on commercial alloys such as AA2024-T3, the recent work of Ilevbare *et al.* [29] attempts to make a connection between the microstructure and the types of pitting events behind the current transients. They concluded that metastable pitting occurred at or adjacent to IM particles in the surface. The metastable pitting resulted in local dissolution at both cathodic and anodic IM particles which eventually stopped. Even in the case of S-phase particles, corrosion only resulted in etchout of the particle since the $i.r_{pit}$ was generally below that required to etchout the adjacent matrix.

Two distinct models of localised corrosion associated with pitting corrosion in Al alloys have been observed [14]. The first type is 'dissolution of the IM', where the particle itself dissolves into solution, leaving a pit where the particle was present. The second mode of pitting corrosion is 'trenching', this occurs where the matrix surrounding the IM particle is dissolved. It is assumed that the matrix in the immediate vicinity of the particle is

anodic [18]. These two models are illustrated in **Error! Reference source not found.** and imaged in the SEM micrograph of **Error! Reference source not found.** where both types of pitting attack can clearly be observed.

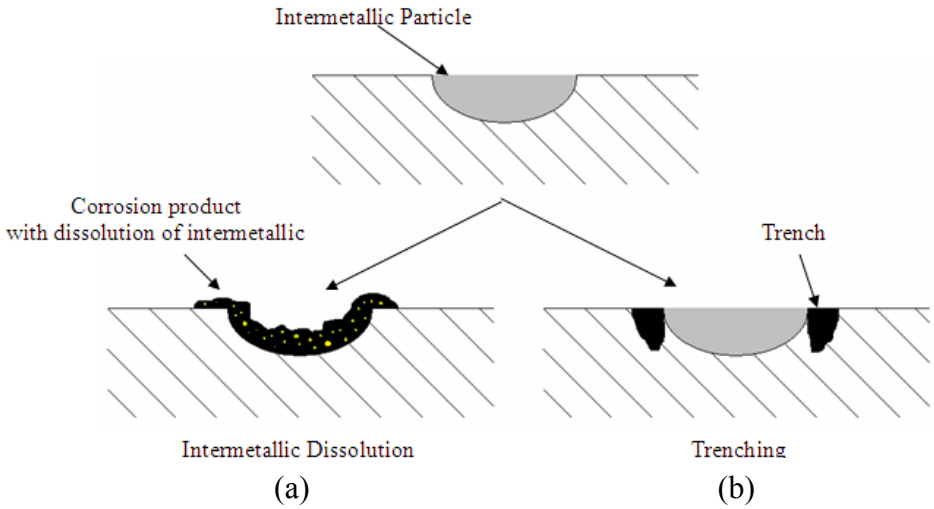

Figure 2-5: Two methods of pitting corrosion, (a) IM dissolution, (b) trenching

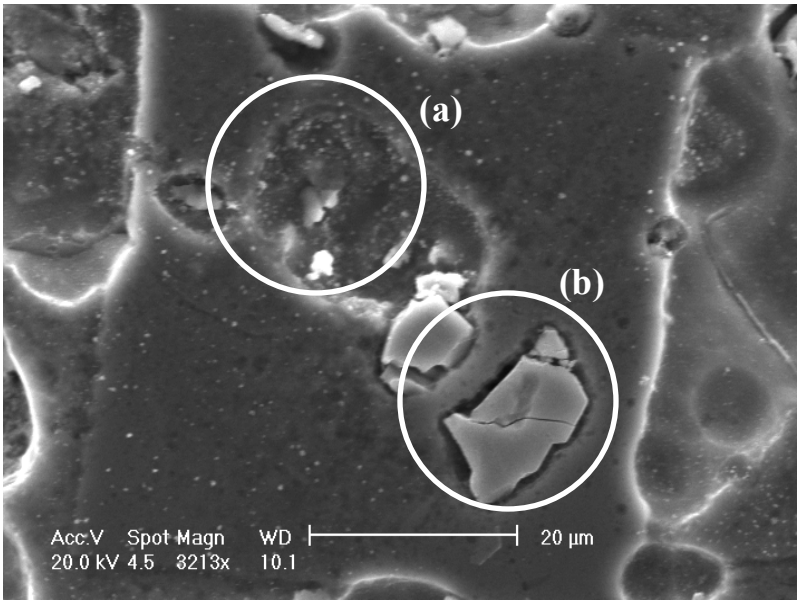

Figure 2-6: SEM micrograph of a corroded surface depicting both (a) IM dissolution modes of pitting corrosion and (b) trenching

The second drawback of the purely electrochemical approach also revolves around the relationship between the microstructure and the observation of a stable pitting current. There is an assumption that because the metastable and stable pitting events "look" the same electrochemically, *i.e.*, a sharp rise in current precedes both events, the population of stable pitting events is simply on the extreme end of the population statistics of metastable pitting events. This view appears to be confirmed for steels since the metastable and stable pit nucleation frequencies appear to have a similar behaviour [30]. This approach has also been applied to pure aluminium by Pride *et al*. [24], as well as by Hughes [32] for AA2024-T3 for modelling for structural health management in airframes [25,26,31,32]. However, Sasaki *et al.* [33] found that while the current transients observed during the early stages of pitting on pure aluminium might be due to metastable pitting, at longer times they are due to activation and passivation events in pits and even between pits.

Thus there is a growing interest in characterizing and understanding the types of sites that lead to stable pitting. In this context clustering of IM particles has emerged as an area of

importance in understanding pit stabilisation however, only a small number of papers allude to clustering as part of the stable pitting process [34-36, 29, 37-39]. Clustering may occur at several different length scales and perhaps even times scales and in a separate report, Boag *et al* [45, 46] also explored the influence that much larger clusters (a few hundred particles) have on stable pit initiation through the establishment of occluded cells that have an internal chemistry significantly different to the background solution [40]. The central premise of previous reports on the role of clustering in stable pit initiation is that clusters drive the electrochemical dissolution of the surrounding matrix with the interaction between particles having no formal role. In this context Wei and co-workers [37, 38] have reported clustering on AA2024-T3 and AA7075-T6 as have Juffs and co-workers [8, 9]. Ilevbare et al. [29] also suggested that large clusters of particles were necessary to establish conditions where S-phase etchout could continue on to stable pitting. These studies conclude that clustering influences stable pit initiation through excessive trenching which leads to particle fallout and other attack. In the work quoted above, the clustered IM particles attack the matrix, however, as suggested by Chen et al. [36], coupling between IM particles might also lead to stable pitting.

One of the aims of this thesis is to examine coupling of anodic to cathodic IM particle types. Thus the degree of clustering of IM particles in AA2024-T3 and the characterization of pits developed on polished AA2024-T3 exposed to NaCl solution were examined using microprobe techniques.

2.6 Pit Growth

Due to the extensive use of metals and alloys in industry, the prediction of pit growth is extremely important and thus much work has been done in this area to understand the kinetics of pit growth [41, 42]. Turnbal states that pits grow under a power law with time (t);

$$d = t^n \qquad (1)$$

Where d is the pit depth which is generally considered to be the distance from the surface to the bottom of the etched out region. This is often determined using differential focusing in optical microscopy. Turnball discuses a number of models based on electrochemical data. If the average pitting current is a constant and no new pits develop on the surface within a given period then n=0.33. If however, the current is proportional to time (ie. the anode is increasing) and there are no new pits developed within the timeframe, then n=0.66. In this later situation the pit may eventually become cathodically limited if the total area of the sample is fixed.

2.7 Current Methods for Prevention of Pitting Corrosion

Corrosion in aluminium alloys has and continues to be a problem in the aerospace industry. The conventional technique used in prolonging the service lifetime of the alloys involves using chromate based conversion coatings to protect against corrosion or anodising [43, 44]. This effectively improves not only the corrosion resistance of the alloys, but also better paint adhesion to the alloy surface. The issues around IM composition and distribution are also important or metal finishing as these treatments have to deal with a heterogeneous surface.

Both coating processes involve a series of chemical treatment steps, including degreasing, alkaline cleaning followed by acid deoxidation. Degreasing removes organic contaminants, such as oils and greases. The next step is treatment in a mildly etching alkaline solution that dissolves surface oxides or corrosion products but leaves a surface film rich in $Mg(OH)_2$ (or other basic oxides depending on the alloy), which must be removed by further acid treatment [43, 44]. As a final step the aluminium surface is deoxidised by immersion in an acidic solution which removes the smut (loosely bound IM material and basic oxide film) left on the surface after alkaline treatment.

A side study of this thesis was the examination of the influence of deoxidation on the surface chemistry and morphology for AA2024-T3 in a commercially available

deoxidiser, containing HNO_3 and $NaBrO_3$, which is used for surface pre treatment prior to conversion coating and painting. This study is presented in chapter 7.

2.8 Bibliography

1 T. H. Muster, A. E. Hughes, and G. E. Thompson, Frontiers in Corr. Sci. (2007).
2 I. S. Wang, in *Corrosion Research Trends*, Cernobbio, Lake Como, Italy, 35 - 106, (2006), .
3 J. R. Davis, *Corrosion of Aluminium Alloys*, ASM International, (1999).
4 J. E. Hatch, *Aluminium: Properties and Physical Metalurgy,* Metals Park, OH, (1984).
5 E. A. Starke and J. T. Staley, Progress in Aerospace Sciences **32,** 131-172 (1996).
6 D. J. E. Smith, K. R. Baldwin, M. A. H. Hewins, and M. C. Gibson, Barcelona, Spain, The Institute of Material, 1652 - 1663, (1993)
7 G. S. Chen, M. Gao, and R. P. Wei, Corrosion, **52,** 8, (1996).
8 L. Juffs, Investigation of Conversion Coating Deposition on Microscopic and Macroscopic Intermetallic Phases of Aluminium Alloy, RMIT University, (2002).
9 A. E. Hughes, A. P. Boag, L. M. Pedrina, L. Juffs, D. G. McCulloch, J. P. Du Plessis, P.J.K., I. K. Snook, and B. O'Malley, ATB Metallurige, 551-556, (2006)..
10 M. A. Jakab, D. A. Little, and J. R. Scully, J. Electrochem. Soc. **152,** 311-320 (2005).
11 M. J. Vasquez, G. P. Halada, C. R. Clayton, and J. P. Longtin, Surf. Coat. Technol **33,** 607, (2002).
12 N.R. Cawley D.G.Harlow, Journal of material science, **31** 5127-5134,(1996).
13 Y. Mao, A.M. Gokhale, Computational Material Science **37** 543-556, (2006).
14 R. G. Buchheit, R. P. Grant, P. F. Hlava, B. McKenzie, and G. L. Zender, J. Electrochem Soc. **144,** 2621, (1997).
15 M. Gao, C. R. Feng, and R. P. Wei, Metall. Mater. Trans. A**,** 1145-1151 (1998).
16 C. M. Liao and R. P. Wei, Electrochim. Acta**,** 881-888, (1999).
17 F. H. Scholes, S. A. Furman, A. E. Hughes, and T. A. Markley, Corr. Sci. **48,** 1812 - 1826, (2006).
18 V. Guillaumin and G. Mankowski, Corr. Sci.**,** 421, (1999).
19 Z. Szklarska-Smialowska, Corr. Sci. **41,** 1743-1767, (1999).
20 M. Metzger, J. Zahavi, N. D. Tomashov, and E. N. Mirolubov, Corrosion of Metals and Alloys**,** 48 (1966).
21 G. T. Burstein, P. C. Pistorius, and S. P. Mattin, Corr. Sci. **35,** 57 (1993).
22 ASM Handbook Vol 13A, Corrosion: Fundamentals, Testing and Protection, ASM International, (2003).
23 P. C. Pistorius and G. T. Burstein, Corr. Sci. **36,** 525 (1994).
24 S. T. Pride, J. R. Scull, and J. L. Hudson, J. Electrochem Soc. **141,** 3028 (1994).
25 A. R. Trueman, Corr. Sci. **47,** 2240 - 2256, (2005).
26 A. E. Hughes, A. R. Trueman, S. A. Furman, and R. J. Taylor, Corr. Sci.
27 J. Wloka and S. Virtanen, Surf. Int. Anal. **40,** 1219 - 1225, (2008).

[28] J. R. Galvele, J. Electrochem Soc. **123,** 464, (1976).
[29] G. O. Llevabare, O. Schneider, R. G. Kelly, and J. R. Scully, J. Electrochem. Soc. **151,** B453, (2004).
[30] D. E. Williams, J. Stewart, and P. H. Blackwell, Corr. Sci. **36,** 1213, (1994).
[31] A. E. Hughes, B. R. W. Hinton, S. A. Furman, I. S. Cole, D. Paterson, A. Stonham, G. McAdam, D. Dixon, S. J. Harris, A. Tureman, M. Hebbron, C. Bowden, P. C. Morgan, and M. Ranson, Corr. Revs **20,** 275, (2007).
[32] A. E. Hughes and S. A. Furman, ATB Metallurgie **45,** 340 - 346, (2006).
[33] K. Sasaki, P. W. Levy, and H. S. Isaacs, Electrochem.& Sol. State Letts. **5,** B25 - B27, (2002).
[34] J. O. Park, C. H. Paik, Y. H. Huang, and R. C. Alkire, J. Electrochem Soc. **146,** 517, (1999).
[35] J. O. Park, C. H. Paik, and R. C. Alkire, *Critical Factors in Localised Corrosion II*, The Electrochem Soc., (1996).
[36] G. S. Chen, M. Gao, and R. P. Wei, Corrosion **52,** 8, (1996).
[37] C. M. Liou, J. M. Olive, M. Gao, and R. P. Wei, Corr. Revs **54,** 451, (1998).
[38] O. Schneider, G. O. Llevbare, J. R. Scully, and R. G. Kelly, J. Electrochem. Soc. **151,** B465, (2004).
[39] D. G. Harlow, M. Z. Wang, and R. P. Wei, Metall. Mat. Trans A **37A,** 3367 - 3373, (2006).
[40] T. H. Muster, M. A. Glenn, and A. E. Hughes, Corr Sci.
[41] A. Turnball, Br. Corr. J. **28,** 297 (1993).
[42] G. S. Frenkel, J. Electrochem. Soc. **145,** 2186.0 (1998).
[43] S. Wernick, R. Pinner, and P. G. Sheasby, *The Surface Treatment and Finishing of Aluminium and Its Alloys*, 5th ed., Finishing Publications Ltd, (1987).
[44] R. G. King, *Surface Treatment and Finishing of Aluminium*, Pergamon Press, (1988).
[45] A. P. Boag, M. A. Glenn, D. G. McCulloch, T. H. Muster, and A. E. Hughes, To Be Submitted to Corr. Sci. (2009).
[46] A. P. Boag, M. A. Glenn, D. G. McCulloch, T. H. Muster, C. Ryan, and A. E. Hughes, To Be Submitted to Corr. Sci. (2009).

Chapter 3 - Experimental Techniques

3.0 Introduction

The focus of this chapter is to cover the experimental aspects of this thesis. This will include the specimen preparation, characterisation and analysis tools employed for this study.

Several analytical techniques have been utilised for this study. Electron Microprobe, Proton Induced X-ray Emission Spectroscopy (PIXE) and Energy Dispersive X-ray Analysis (EDX) were used to investigate elemental concentration and provided data for IM particle statistics. Imaging of specimens was performed by Scanning Electron Microscopy (SEM) and Transmission Electron Microscopy (TEM) with further elemental analysis conducted utilising Electron Filtered Transmission Electron Microscopy (EFTEM).

3.1 Specimens Characterisation Techniques

3.1.1 Scanning Electron Microscopy (SEM) & Environmental SEM (ESEM)

A SEM operates by rastering a focused beam of electrons across the surface of a specimen. The electrons interact with the surface in a variety of ways and different processes occur. The primary technique involved with imaging in a SEM is detecting secondary electrons (SE) which are emitted by atoms ionized by the incident beam. Another method used for imaging the surface is using backscattered electrons (BE). These are the primary electrons which are recoiled and loose only a small portion of their energies. Two other major processes occur as a result of atom ionization, the emission of characteristic X-rays and Auger electrons. Both of these processes can be detected and used to obtain elemental composition of a specimen.

SEM was chosen due to its fast and efficient imaging capability which enabled rapid imagery of the alloy's surface and IM particle characteristics such as size, shape and distribution. A FEI Quanta 200 Environmental SEM (ESEM) with a W filament was used for both imaging with SE and BE. Throughout this investigation, a working distance of 10 mm and an accelerating voltage of 30 kV was used.

An Environmental Scanning Electron Microscope (ESEM) operates with the same basic principals of an SEM except it can image and analyse materials which are either semi conductive (using a low vacuum mode) or non conductive materials (using 'ESEM' or 'wet' mode) without having to apply a conductive coating [1]. To achieve this, water vapor is introduced into the specimen chamber through a dedicated vacuum pump that can accurately control the chamber pressure. The primary electron beam is very energetic, and it penetrates the water vapor with little apparent scatter, scanning across the surface of the sample. Secondary electrons are released from the surface of the sample, as they are in normal SEM, but they encounter water vapor molecules once they exit the surface. The water vapor molecules, when they are struck by the secondary electrons, produce secondary electrons themselves, which in turn produce secondary electrons from adjacent water vapor molecules. Thus the water vapor functions as a cascade amplifier, amplifying the original secondary electron signal from the sample which is detected by the secondary electron detector (SED).

An ESEM can operate with minimal sample charging due to the strong positive bias on the SED which drives the water vapor molecules, which are positively charged, toward the sample. The sample has a net negative charge from interaction with the primary electron beam and the positive ions that are driven towards it by the water vapor effectively neutralize that charge and permit imaging.

3.1.2 Energy Dispersive X-Ray Emission Spectroscopy (EDX)

Electron interaction with a specimen in a SEM results in multiple processes. As described in the previous section 3.1.1, SE and BE are ideal for imaging. The two other processes that occur are the emission of characteristic X-rays and Auger electrons which result from the ionization of an atoms inner shell. Using an X-ray detector (generally a Lithium drifted Silicon, Si(Li) detector), these characteristic X-rays can be collected and used to provide the chemical information of a sample.

A collected X-ray spectrum contains two main components, a characterisation component which is used to identify chemical composition and a background component. The characterisation component consists of a series of peaks representative of the elements and relative amount of each element in the sample. Weight concentrations can also be calculated by analysing the individual counts in each peak and used to quantify detected elements.

The background component of the X-ray spectrum is generated from bremsstrahlung X-rays. This process occurs when an energetic electron decelerates in the Coulumbic field of a specimen's atoms. This causes a loss in energy which in turn is converted into a photon of electromagnetic energy. This is known as bremsstrahlung radiation ("braking radiation"). Bremsstrahlung X-rays form a continuous spectrum from zero to that of the beam energy as the energy loss can take on any value from a fraction of an electron volt to the total energy carried by the incident electrons. Although characterised by a continuous and non specific distribution of radiation, it becomes more intense and shifts towards higher frequencies when the energy of the incident electrons is increased. Figure 3-1 shows curves from the 1918 data of Ulrey [2], who bombarded W targets with electrons of four different energies.

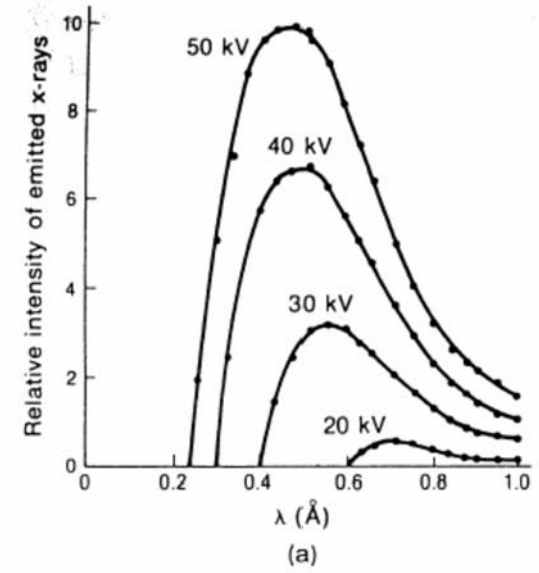

Figure 3-1: Bremstrahlung intensity as a function of incident electron voltage [42]

EDX is a powerful tool for rapid qualitative chemical analysis of major elements in a specimen. It has elemental detection limits ranging from B to U, but is limited in its detection of trace elements as it has a lower detection limit of around 0.1 wt %.

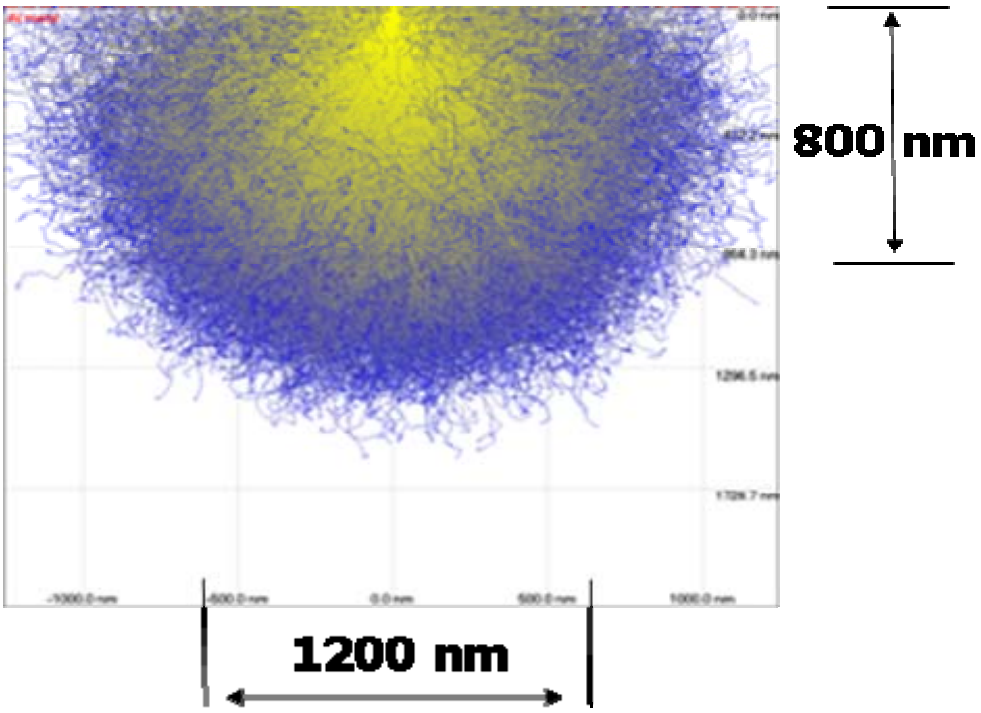

Figure 3-2: Monte Carlo Simulation at 12keV of Interaction Volume of EDX

Elemental mapping is another useful tool associated with EDX. Here the electron beam is rastered across a sample and counts of selected elements are represented for each pixel on individual elemental maps. Although a very good analysis tool, obtaining good results is very time consuming and thus beam drift does play a part, especially at high magnifications.

EDX was also performed on a FEI Quanta 200 ESEM with a W filament. Elemental mapping was collected in 'live' mode with a dead time of 30%. In 'live' mode individual elemental maps are collected and superimposed to generate the final map. Although it does not have the sensitivity of PIXE (see section 3.1.6) for trace elemental analysis, EDX mapping was also employed as it allows for rapid identification of the elemental composition of IM particles.

3.1.3 Electron Probe Microanalyser (EPMA)

The electron probe microanalyser (EPMA) is an important tool that can be used to solve a wide range of problems. Like the SEM, it is a microbeam instrument, but uses a combination of high-resolution wavelength dispersive (WD) and low resolution energy dispersive (ED) spectrometers to detect X-rays. The use of WD spectrometers provides greater analytical precision, superior peak resolution and lower detection limits, down to a few ppm. In simpler terms, an EPMA is essentially a hybrid instrument combining the capabilities of both the SEM and an X-ray fluorescence (XRF) spectrometer, with the added features of finespot focusing (in this instance around 0.4 μm) and precision-automated sample positioning. Modern EPMAs are equipped with mapping facilities enabling mapping of element distributions at various scales. In this application, there is the opportunity to obtain not only the absolute elemental concentration, but also the spatial distribution of elemental concentrations.

As an alternative to the above approach an EPMA-based mapping method has been developed. The method requires an electron microprobe analyser (JEOL 8900R Superprobe) equipped with 1 ED and 5 WD spectrometers to collect a series of single-element distribution maps that are then processed using the software package 'Chimage' [3]. The mapping procedure differs from traditional automated X-ray based image analysis techniques in that no detailed *a priori* knowledge of the mineral phases is required. The mapping procedure works in reverse, that is, given only a bulk chemical analysis of an unknown sample, the mapping technique can be used to discriminate and identify the distribution of most of the phases present.

To differentiate phases, elemental data is displayed as elemental maps, scatter plots or ternary diagrams [4]. The elemental data is produced by correcting the raw counts for count time, beam current and referencing to a count rate collected on standards of known composition. This results in elemental data being expressed as K-ratios. If absorption of X-ray lines is significant within a phase, then all the data can be post processed through a Bence–Albee matrix correction algorithm [5]. This is especially important when light elements are being mapped. With the data in K-ratio form, cluster centroids correspond to

individual chemical phases. Data points within each cluster are manually selected and the phase represented by the cluster is given a name or chemical phase composition and saved before displaying the complete set of data as a phase-patched map.

For systems with complex mineralogy, an automated cluster recognition technique has also been developed to define phases [6]. This minimises operator bias and aids in interpretation and characterisation.

3.1.4 Transmission Electron Microscopy (TEM)

A TEM operates by passing a beam of electrons through a thin section of a specimen. Transmitted electrons containing information on the internal structure of the sample is then projected onto a viewing screen or CCD camera. A comprehensive description of the functions of a TEM can be found in Williams and Carter [7].

TEM was carried out on samples because of its high spatial resolution. Analysis was performed on a JOEL 2010 TEM fitted with a Gatan Imaging Filter (GIF) 2000. A LaB_6 filament and an accelerating voltage of 200 keV was used for all analysis with this microscope. Images were taken with a 1M pixel CCD camera located in the GIF.

Cross sections of the samples were prepared for TEM using Ultramicrotomy. This technique involves cutting ~100nm sections of the aluminium sample using a diamond knife mounted in an ultramicrotome. Sections were then removed from the boat of the diamond knife with a single hair fibre probe and placed into a copper oyster TEM grid for analysis.

3.1.5 Energy Filtered Transmission Electron Microscopy (EFTEM)

EFTEM is an elemental mapping technique which can be used to generate elemental maps within TEM samples. EFTEM mapping utilises Electron Energy Loss Spectroscopy (EELS) edges to produce an elemental map by placing an energy filter around the energy

of a corresponding EELS edge of the desired element. Each pixel in the image represents the intensity of the EELS edge

EELS is used for elemental characterisation and has detection sensitivity down to ppm [8]. This process works by measuring the energies of scattered electrons after they have interacted with the specimen. As the energy of the incident electrons is known, the energy loss can be calculated and segregated by kinetic energy using an electron spectrometer. This process produces an electron energy loss spectrum depicting scattered intensity as a function of the decrease in kinetic energy of the incident electron. An EELS spectrum contains characteristic edges which can be related to individual atoms as well as plasmon peaks and a zero-loss peak. Characteristic edges, or 'core-loss' edges represent the energy loss of the inelastically scattered electron from the inner shell. Electron energies that are not significantly effected by their interaction with the specimen are displayed as part of the zero-loss peak, these can be treated as unscattered electrons. Plasmon peaks are found in the region 5-50 eV and represent inelastic scattering from the outer-shell electrons. A more in depth description of EELS can be found in Edgerton [8].

EFTEM mapping was performed using the standard GIF three window subtraction method (two for the background and the other for the characteristic edge) as shown in Figure 3-. The resultant count intensity for every pixel was then plotted out as an elemental map.

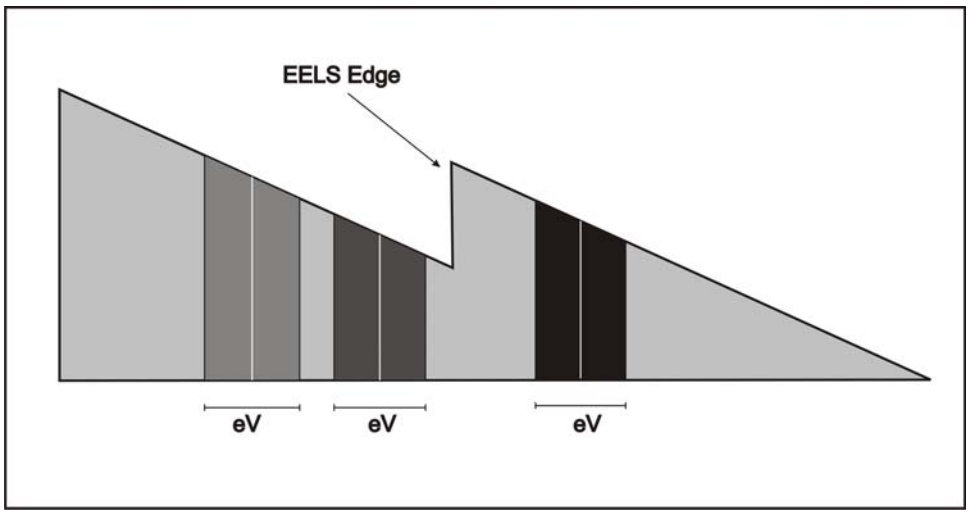

Figure 3-3: Diagram illustrating individual window selection for the 3 window method used for EFTEM mapping

Analysis of the elemental maps was conducted using Gatan Inc. DigitalMicrograph 3.4 [9]. This technique was utilised as it assisted in detection of localised corrosion products and composition of IM particles around sectioned pit sites.

3.1.6 Particle Induced X-Ray Emission (PIXE)

PIXE is a technique used to determine the elemental composition of samples. This technique involves the use of an ion beam to generate characteristic X-rays from a sample and then measuring the number and energies of these X-rays. Either protons or helium ions are normally used as the source particles. For this work only proton ions were used and thus Proton Induced X-ray Emission will be intended when the term PIXE is used. PIXE analysis uses proton ions generally of the order of a few MeV to bombard a surface resulting in ionisation of the inner-shell electrons which then emit characteristic X-rays. These can be analysed to gain a qualitative elemental analysis of the specimen. The process can also be used to produce quantitative results by analysing X-ray yields (X-rays per particle) to get elemental concentrations.

Proton interaction with atoms in the sample can lead to ionisation of inner atomic-shell electrons. Outer atomic-shell electrons subsequently fill these vacancies leading to the

emission of characteristic X-rays for each element, allowing unique identification of elements in a sample. This is illustrated in Figure 3-. Bremsstrahlung X-ray emission is much lower for PIXE than for EDX (see section 3.1.2) as the deceleration of the incident proton as it interacts with the sample is smooth and predictable. Combining this and the fact that the ions experience very little scattering leads to low continuous background.

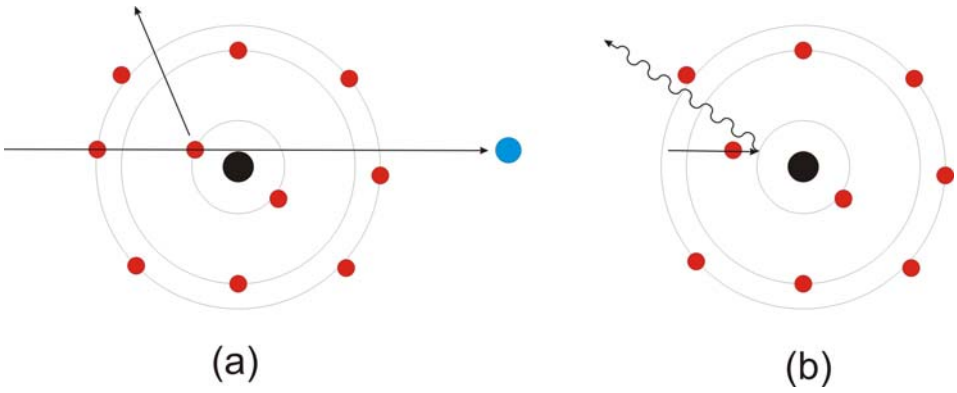

Figure 3-4: Diagram of ionization process. Blue: incident proton, Red: atomic electrons, Black: atomic nuclei. (a) Incident proton ionizes inner shell electron and (b) characteristic x-ray is produced when an outer shell electron fills the inner shell vacancy

Two types of X-rays are released from a specimen; characteristic X-rays that depend on composition and bremsstrahlung X-rays which are generated from interactions with the proton beam. For analysis, it is the characteristic X-rays that are of primary importance although the presence of the bremsstrahlung X-rays require that we have good statistics in the acquired data so that the measured bremsstrahlung X-rays are only present as background noise and elemental information can be extracted.

PIXE is a fully quantitative, multi-elemental analysis technique, which has the capability of determining elemental concentrations down to ppb. The number of counts in each elemental line of a PIXE spectrum is a measure of the concentration of that corresponding element and by measuring the current and knowing the X-ray cross

sections and detector parameters absolute values for elemental concentrations can be calculated. PIXE has a wide elemental detection range extending from Li to U.

Elemental mapping is possible by focusing the ion beam with apertures and a system of magnetic quadrupoles. This results in a beam size of the order of microns which can be rastered across a sample in a similar fashion to that of an electron microprobe. In this method a complete PIXE spectrum is collected at each pixel, which can be used to analyse elemental concentrations of small regions of interest. The main advantage of elemental mapping with this technique over electron microprobes is that the detection limits are of the order of a 100 times greater [10]. This is due primarily to the large background caused by electrons in electron microprobe techniques. High resolution is also a key feature of this technique with beam diameters ranging between 1-2 μm depending on beam current.

The probability with which a single proton will induce an atom to emit an X-ray is low and thus strong beam currents typically of the order of picoamps or above are required. The trade off here is that although strong beam currents are required and an increase in the current results in an increase in the number of X-rays emitted, if the beam current is too high the risk of specimen damage increases.

PIXE was used for this analysis because the research required high sensitivity to investigate trace elements in corrosion induced pit sites. Although other techniques were found to be very efficient in obtaining elemental information to identify IM particles, detection of Cl in or at pit sites required the extra sensitivity that PIXE offered.

Analysis was performed on the CSIRO PIXE beamline at the University of Melbourne, which is illustrated in Figure 3-. A 3 MeV proton beam was used as the illumination source, with a combination filter containing 80 μm Be and 24 μm Kapton to suppress the bulk Al signal and gain better statistics from the trace elements in the matrix. Beam currents around 300 picoamps were used.

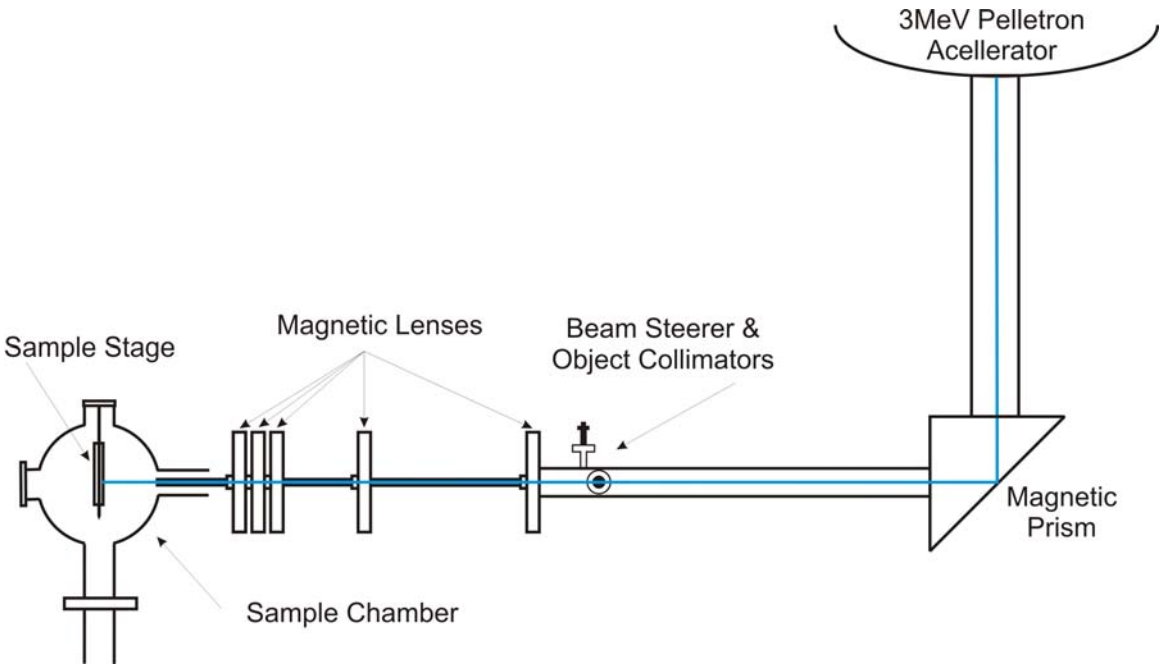

Figure 3-5: Diagram of CSIRO PIXE beamline setup

Data collection was performed using the University of Melbourne's Nuclear Microprobe's proprietary software 'MPSys' utilising the 'x-step' function. Standard x-y rastering of the beam allows for an image area no larger than that of the beam tube, approximately 100 μm^2. X-step permits a wider scan region by scanning only in the y-direction and moving the sample stage in the x-direction, thus removing the limitations of the standard scanning method. Collected PIXE spectra were analysed using GeoPIXE [11]. This software allows for quick and efficient elemental analysis and generation of elemental maps. A comprehensive guide to using the software package can be found in the 'GeoPIXE User Guide' [12].

3.2 Bibliography

[1] Danilatos, G.D. Foundations of Environmental Scanning Electron Microscopy: Advances in Electronics and Electron Physics, Academic Press, **71** 109-250, (1988)

[2] C. T. Ulrey, Phys. Rev. **11,** 401 (1918).

[3] I. R. Harrowfield, C. M. MacRae, and C. M. Wilson, Microbeam Analysis Society, New York, 547 - 548, (2003)

[4] M. I. Pownceby, C. M. MacRae, and N. C. Wilson, Min. Eng. **20,** 444-451, (2007).

[5] A. E. Bence and A. L. Albee, J. Geo. **76,** 382-403, (1968).

[6] N. C. Wilson and C. M. MacRae, Microsc. Microanal. **11,** 434CD, (2005).

[7] D. B. Williams and C. B. Carter, *Transmission Electron Microscopy*, Plenum, (1996).

[8] R. F. Egerton, *Electron Energy Loss Spectroscopy in the Electron Microscope*, 2nd ed., Plenum Press, (1996).

[9] Gatan, *DigitalMicrograph 3.4* (1999).

[10] S. A. E. Johansson, J. L. Campbell, and K. G. Malmqvist, *Particle-Induced X-Ray Emission Spectrometry (PIXE)*, Wiley, (1995).

[11] C. G. Ryan, GeoPIXE, http://nmp.csiro.au/Geopixe.html, CSIRO (2001).

[12] C. G. Ryan and D. R. Cousens, *GeoPIXE II - Quantitative PIXE Trace Element Imaging and Analysis,* CSIRO, (2002).

Chapter 4 - Statistical Analysis of Particle Composition and Distribution in AA2024-T3

4.0 Introduction

Corrosion phenomena on aluminium alloys are related to the microstructure of the alloy as well as the corrosion conditions such as environment and chemistry [1-3]. The underlying microstructure for AA2024-T3, as described in Chapter 2, Section 2.2.1, is complex, comprising the aluminium matrix, a range of IM particles as listed in Table 4-1 and depletion zones along grain boundaries as well as around some particle types. The objective of this chapter is to examine the IM particle composition and distribution with a view to understanding how these two aspects of IM particles influence the establishment of stable pits.

With respect to the IM particles, as was described in Chapter 2, Section 2.2.1, there is some uncertainty about the compositions of some phases [4,5]. Even metallurgical literature [6-9] is not clear about constituent particle composition and structure in AA2024-T3 due to the ability of alloying elements to substitute for one another. The first uncertainty is principally due to two factors: sampling size and technique resolution. Most studies where the compositions have been determined have dealt with sample sizes in the tens of particles range. With such small sample sizes it has been difficult to tie down the compositions of different groups of particles. In addition to sampling size, these studies are now some years old and there have been advances in characterisation technology that have led to automation of instruments meaning that it is possible to collect data at high resolution over a relatively large scale with greater spatial resolution and sensitivity than was previously possible.

Typically, aluminium alloys comprise phases of heterogenous composition. The current approach to characterisation in AA2024-T3 typically involves EDS in an SEM and the division of particles into anodic (based on the presence of Mg and Cu in the particle) and cathodic particles [4,5]. More recently Ilevbare *et al* [10] have identified that S-phase and

θ-phase coexist in particles. The challenges imposed by variable phase compositions requires sensitive BE and X-ray signals to supply elemental composition data for individual particles.

Developments in instrumentation have been accompanied by developments in the capacity of storage media which has increased significantly the ability to collect larger and larger data sets including full spectra at each pixel. Taking advantage of these developments, this chapter presents the results of a study of polished AA2024-T3 where the elemental composition and spatial distribution of IM particles has been determined for a 5 mm x 5 mm square at a resolution of 0.4 μm using an electron microprobe facility, see Chapter 3, Section 3.1.3.

4.1 Electron Probe Image Analysis

From the combined microprobe mapping analysis produced using Chimage [11], individual phases were selected from Figure 4-1 using the colour picking tool in "Adobe Photoshop" [12] and separate images containing each individual phase were created. "ImageJ" [13] was used to convert the images to 8bit images and then using its inbuilt macro language, code was written to measure the number and size details of particles and log the co-ordinates of each particles centroid position, in either the whole image or of individual tiles either 2x2, 4x4, 8x8 or 16x16 across. This code can be found in Appendix A. The inbuilt macro language was also utilised to create code to calculate the Pair Correlation Function (*g(r)*), which was used to gain a statistical insight into nearest neighbour distributions. The code for *g(r)* can be found in Appendix B

4.2 Pair Correlation Function (g(r))

The pair correlation function (*g(r)*) is related to the probability of finding the centre of a particle at a given distance from the centre of another particle. For short distances this information is related to how close the particles are packed together or the clustering of the particles. The pair correlation function is normalized by the mean particle density,

this means that for particles that are large distances from one another the $g(r) \rightarrow 1$. To determine $g(r)$ for the total field of a particular X-ray map it is necessary to measure interparticle distances beyond the boundary of individual maps. This is done by reproducing the maps at each of the four side boundaries as well as at each of the corners.

4.3 Results

4.3.1 IM Compositions

Once the data was collected the IM particles compositions were determined using K-ratio cluster analysis on large fields of over 80,000 particles.

The output of the mapping process produces an image where every pixel has an associated set of data including WD intensities and ED spectra. The analysis begins with an unsupervised clustering that is the refined manually based on the number of pixels per phase, edge effects and other features that may provide artefacts. The K-ratio analysis forms clusters out of pixels with similar composition. The K-ratio analysis was performed using the Chimage software [11] described above in Chapter 3.

The clustering process identified nine different phases within the alloy including the matrix. These phases are listed in Table 4-1 along with some other statistics related to them. The total particle count is approximately 80,000 which converts to approximately 320,000 particles/cm^2 in agreement with previous results of 300,000 [5] and 500,000/cm^2 for the polished surface of AA2024-T3 [14,15]. The area of the IM particles expressed as a percentage of the total area is 2.83%, which is again typical of values recorded for IM particles in AA2024-T3 [40,16]. This particular result gives some confidence that the large field recorded here is representative, since the particle areas are generally reported for a much smaller sample.

The phases with composition, Al_2CuMg, Al_7Cu_3Fe and Al_2Cu are consistent with phases previously observed in AA2024-T3. $Al_{20}(Cu,Mn,Fe)_5Si$ phase has a composition

consistent with Al_8Fe_2Si and $Al_{73}(Cu,Mn,Fe)_{24}Si$ is consistent with $Al_3(Cu,Mn,Fe)$ or $(Al,Cu)_6(FeMn)$, however the Cu content is too high for the reported solubility for Cu [17] in this phase, thus we are suggesting $Al_3(Cu,Mn,Fe)$.

As can be seen from Table 4-1, there are a number of phases that contain Mg, Al, and Cu as the main constituents. If it assumed that these particles are anodic with respect to the matrix, as indicated the OCP of Mg containing particles [18], then these particles only constitute approximately 40% of the total with the remaining 60% of the IM particles being cathodic. This is the opposite to earlier reports that put the S-phase at 60% of the total [4]. However, these earlier studies showed no evidence of being able to distinguish S-phase from θ-phase co-precipitated within individual particles [4]. This study shows that the vast majority of S-phase particles include both phases, hence the inclusion of the θ-phase in the particle counts results in the majority of cathodic particles in the alloy. Table 4-1, also includes the label of each phase which will be used throughout this chapter.

Phase Label	Measured Stoichiometry	Particle Count	Area (% of total)	Particle Density (number/cm^2)	Mean Particle Diameter (μm)
$Al_{20}(Cu,Mn,Fe)_5Si$	$Al_{77}Cu_5Mn_5Fe_{10}Si_4$	5513	0.742	22052	5.19
Al_2CuMg	$Al_{61}Cu_{20}Mg_{15}Co_1$	5603	0.381	22412	4.52
Al_7Cu_3Fe	$Al_{70}Cu_{18}Mn_1Fe_6$	5519	0.089	22076	1.84
$Al_{90}(Cu,Mn,Fe)_8(Mg,Si)_2$	$Al_{90}Cu_3Mg_1Mn_2Fe_3\ Si_1$	35074	0.252	140296	1.46
$Al_{20}Cu_3Mg$	$Al_{81}Cu_{12}Mg_4Zn_1$	20464	0.983	81856	5.38
$Al_{73}(Cu,Mn,Fe)_{24}Si$	$Al_{73}Cu_{11}Mn_4Fe_{10}Si_1$	4432	0.062	17728	1.97
$Al_{12}Cu_3Mg$	$Al_{61}Cu_{14}Mg_5Co_2$	967	0.018	3868	2.26
Al_2Cu	$Al_{70}Cu_{27}Co_1Zn_1$	4392	0.298	17568	4.60
Total		**81964**	**2.83%**	**320,000**	**N/A**

Table 4-1: Measured stoichiometry and statistics for various phases identified using the K-ratio cluster analysis, Phase labels used throughout chapter also included

The distribution of these phases is presented in Figure 4-1. The top left is the total map over the 5 mm x 5 mm area. The bottom right expands a section of the top map in the bottom left hand corner as indicated. The colour code for the identification of the phases is indicated on the bottom left hand side of the figure. The enlargement shows that there is a large range of particle sizes and that many particles are multiphase including shell phases (those forming a shell around particles, which we believe to be a transition zone, which is a unique zone containing Fe which the phases either side do not have and Mn at higher levels than either side.), particles comprising two adjacent phases and particles with regions of different composition. The presence of shell phases of different composition around the edge of S-phase precipitates have previously been observed by Campestrini et al. [19] but a composition based on a large area analysis has not been reported.

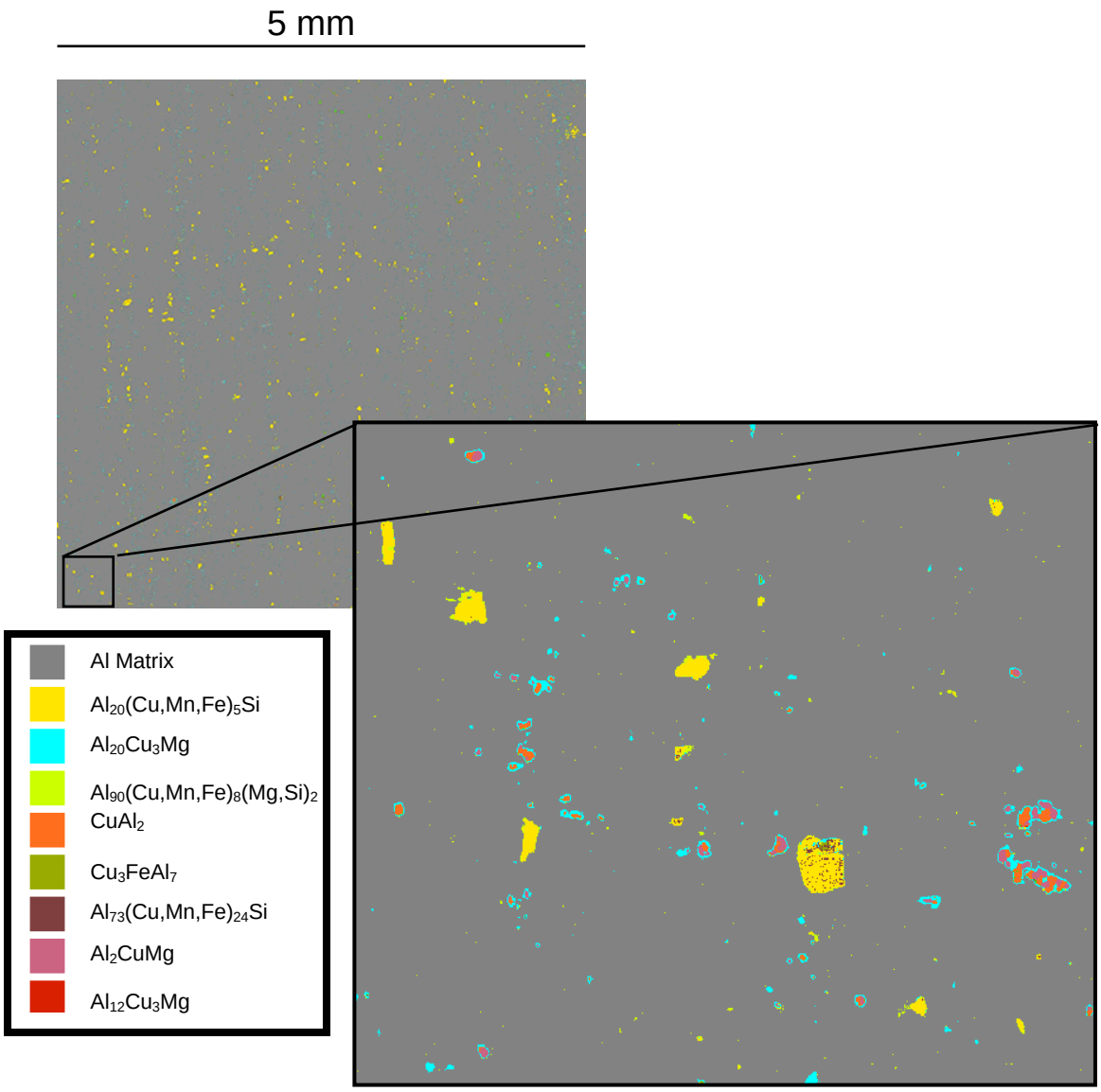

Figure 4-1: Top full image covering 5 mm x 5 mm of the polished surface of AA2024-T3, bottom enlargement of the region on the bottom left showing detail in map image.

Figure 4-2 shows the extent to which Al_2CuMg (S-phase) and Al_2Cu (θ phase) co-precipitate as observed in recent studies [10,20]. There are however, other studies that suggest no other phases apart from S-phase are present in these particles at these types of sites [5,21]. Indeed, the exception would be to find single phase particles in this category. The cyan phase is an Al-enriched phase containing Mg and Cu. While it might be suggested that this phase is an artefact of the measurement processes such as an edge effect, there are too many pixels in the shell for it to be an edge effect. The yellow

particles are of the type that contains Al, Fe, Mn, Cu and Si whereas the brown particles are similar but without Si. These two groups are mixed in many of the IM particles of this type along with another variant also containing Al, Mn, Fe and Cu.

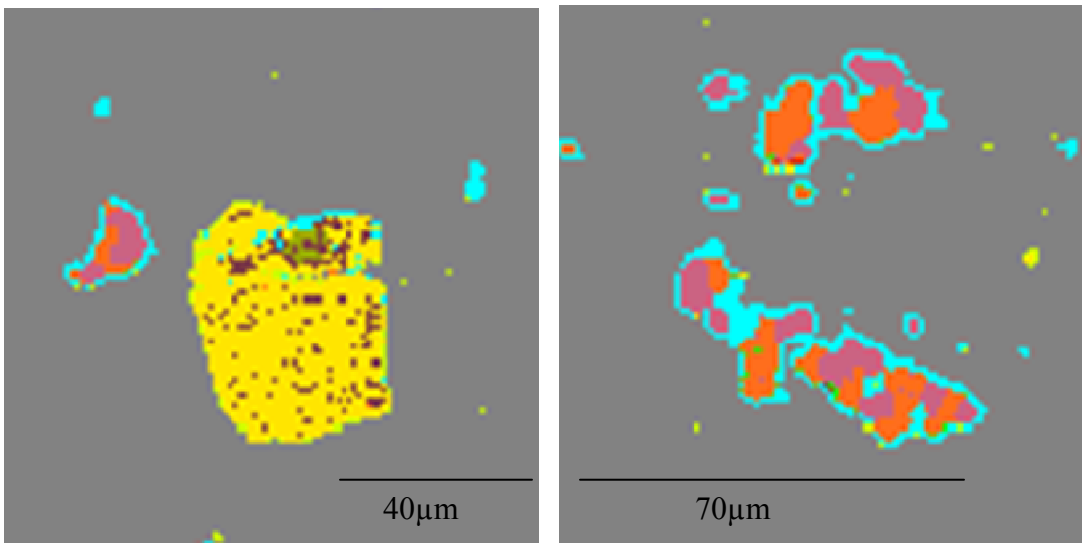

Figure 4-2: Examples of the different morphologies in the surface. Left: small areas of sub-phase containing Al, Cu, Fe and Mn (brown) in a larger particle which has Si in addition to the other elements. Right: multiphase particles of Al_2CuMg (mauve), Al_2Cu (orange), and shells (cyan)

Particle size distributions for each of the phases are reported in Figure 4-3 to Figure 4-10. At the low end of the particle size distributions each pixel has an unambiguous composition but because the resolution of the analysis is around 1200 nm it is for particles greater than this size that the distribution is meaningful. $Al_{90}(Cu,Mn,Fe)_8(Mg,Si)_2$, $Al_{20}(Cu,Mn,Fe)_5Si$, Al_7Cu_3Fe, $Al_{73}(Cu,Mn,Fe)_{24}Si$, and $Al_{12}Cu_3Mg$ all have distributions where the majority of the particles are well below 2 µm. Some of these particles included in phases such as $Al_{73}(Cu,Mn,Fe)_{24}Si$, where isolated domains appear inside $Al_{20}(Cu,Mn,Fe)_5Si$. There were very few $Al_{12}Cu_3Mg$ particles which were also isolated.

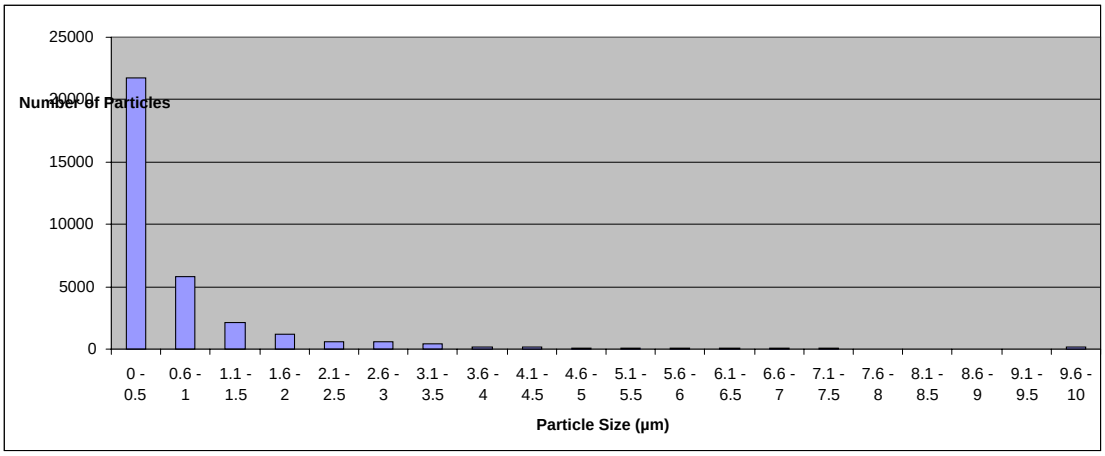

Figure 4-3: Particle size distribution of $Al_{90}(Cu,Mn,Fe)_8(Mg,Si)_2$

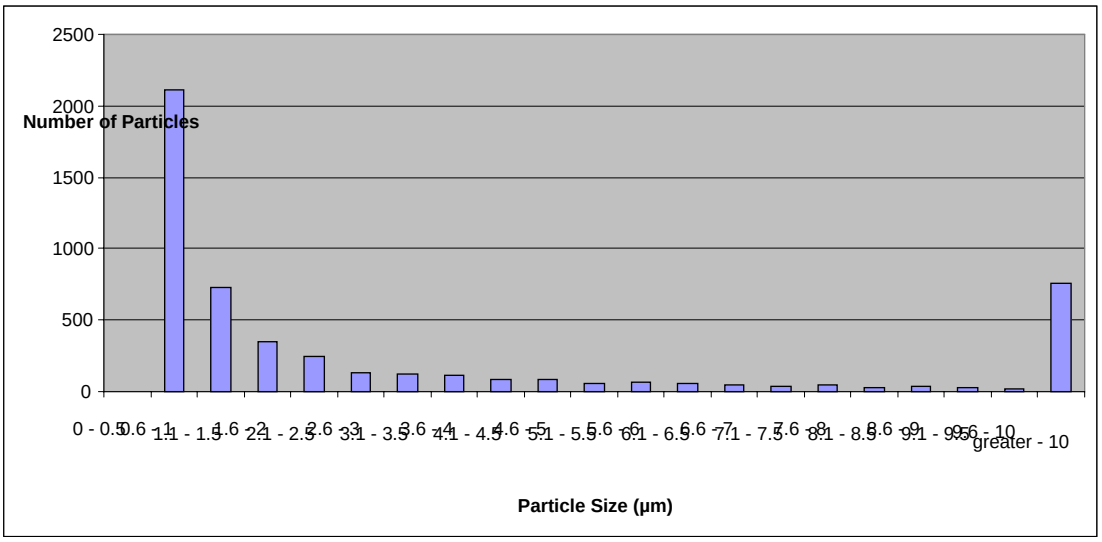

Figure 4-4: Particle size distribution of $Al_{20}(Cu,Mn,Fe)_5Si$.

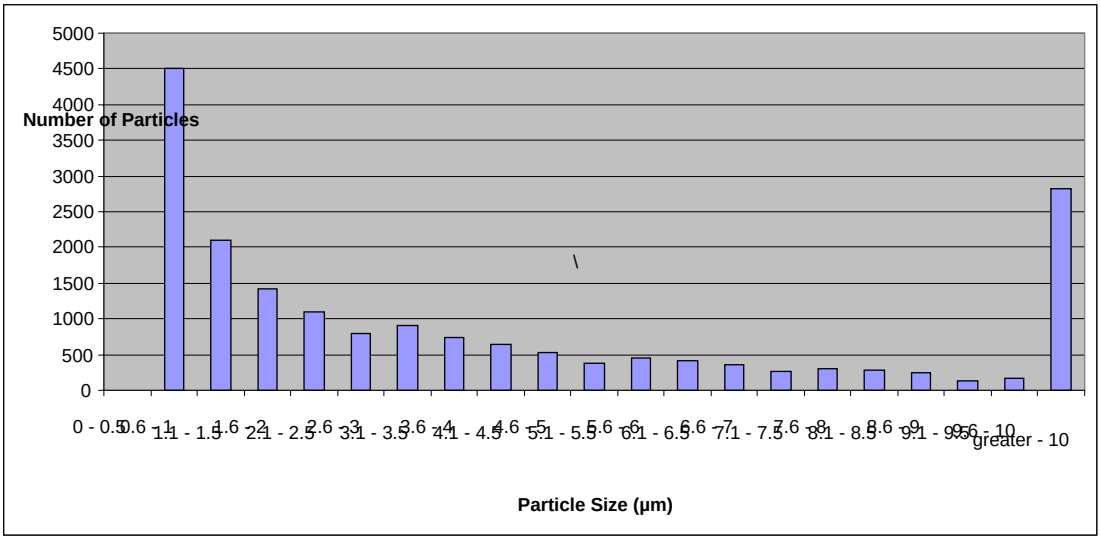

Figure 4-5: Particle size distribution of $Al_{20}Cu_3Mg$.

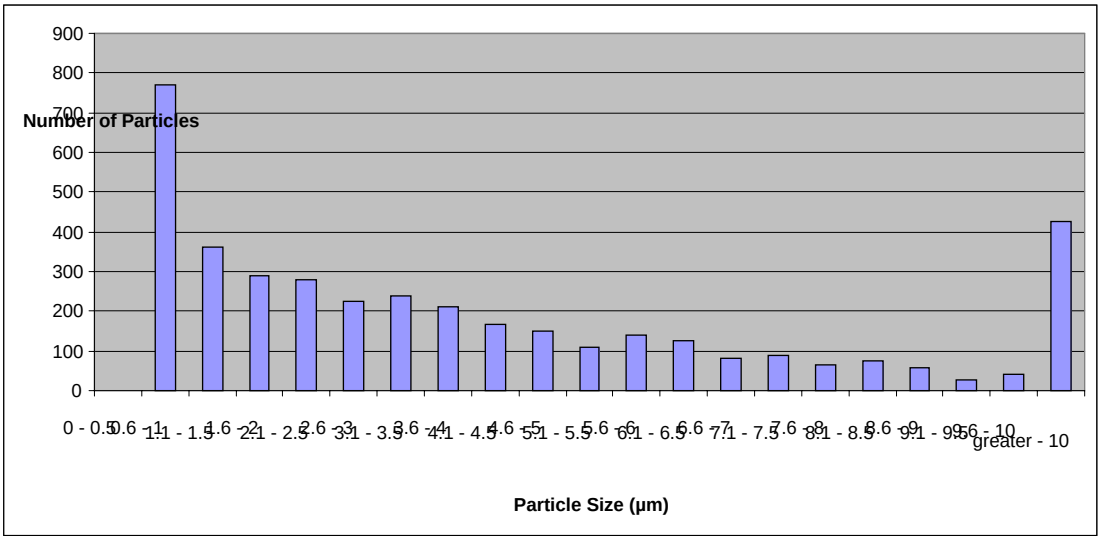

Figure 4-6: Particle size distribution of Al_2Cu

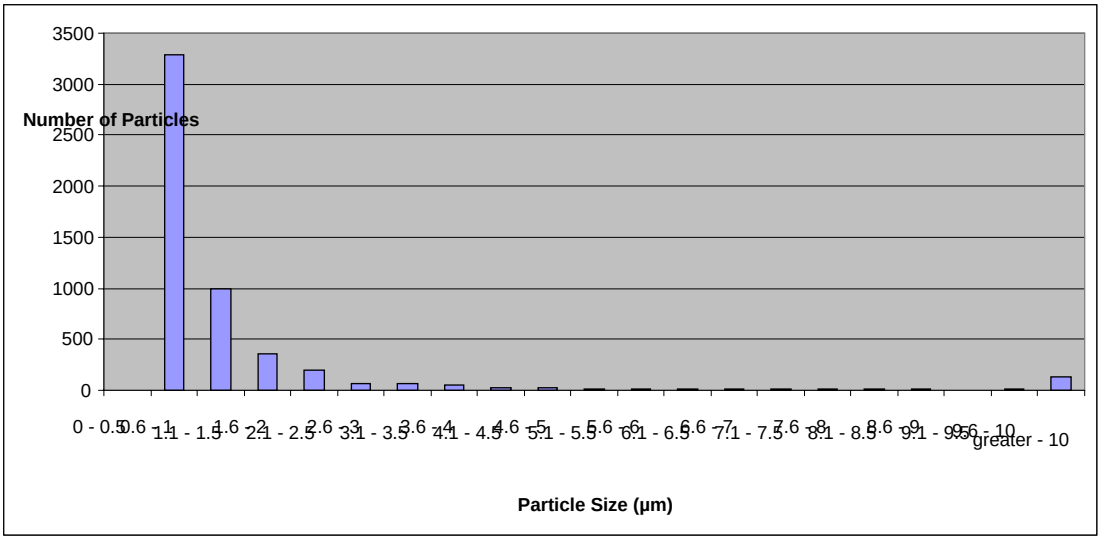

Figure 4-7: Particle size distribution of Al_7Cu_3Fe

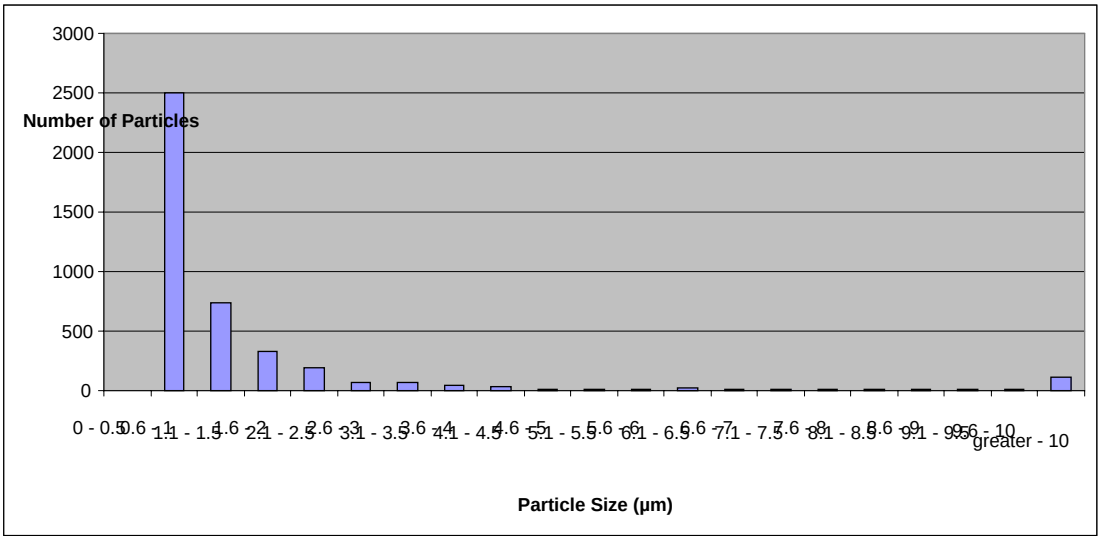

Figure 4-8: Particle size distribution of $Al_{73}(Cu,Mn,Fe)_{24}Si$.

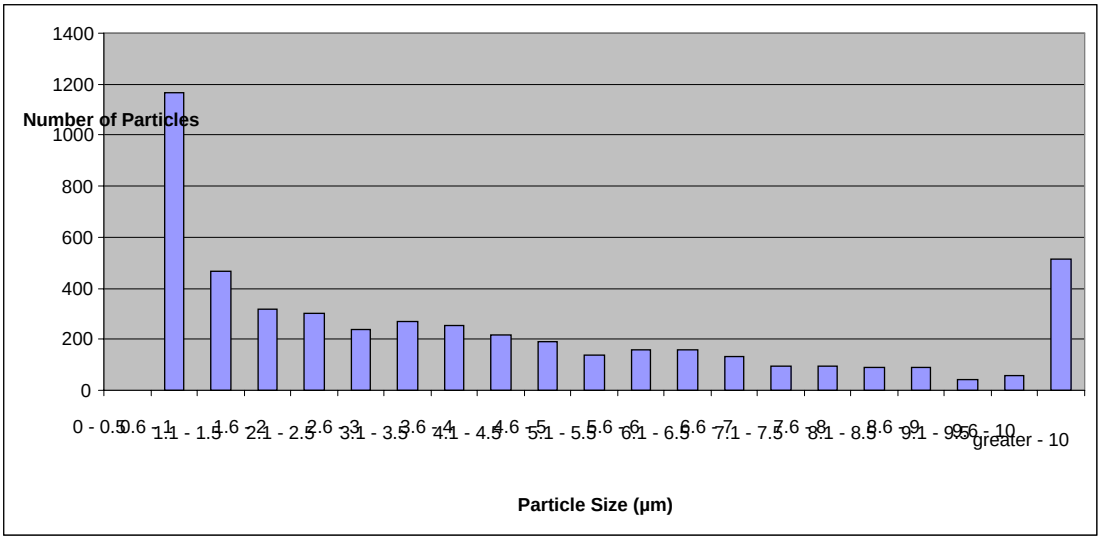

Figure 4-9: Particle size distribution of Al_2CuMg

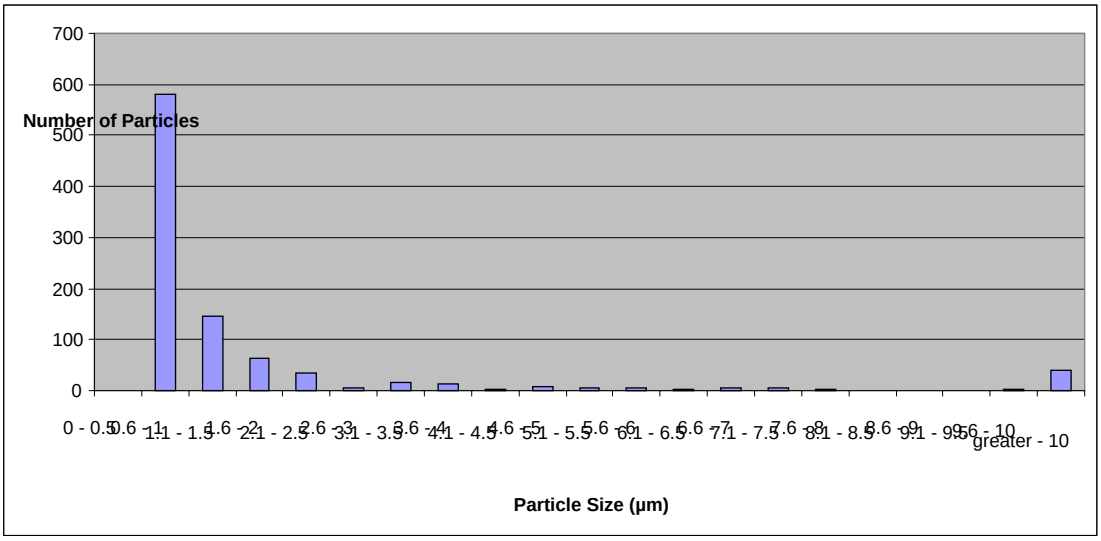

Figure 4-10: Particle size distribution of $Al_{12}Cu_3Mg$.

On the other hand the particles distributions for Al_2CuMg, Al_2Cu and $Al_{20}Cu_3Mg$ (transition zone) have broader distributions with a greater population of particles with sizes up to 10 µm. The size distributions are similar as would be expected given the spatial relationships shown in Figure 4-1.

The distributions that have a larger number of larger sized particles include Al_2CuMg, $Al_{20}Cu_3Mg$, Al_2Cu, $Al_{20}(Cu,Mn,Fe)_5Si$ with lesser contributions from Al_7Cu_3Fe,

$Al_{73}(Cu,Mn,Fe)_{24}Si$ and $Al_{12}Cu_3Mg$. These particles are contribute the largest cathodic area and hence will have the biggest cathodic density.

4.4 Particle Statistics

Maps of the individual phases were generated from the composite image (described above) and a range of statistical measurements were made for each phase. Figure 4-3 to Figure 4-10 shows the particle size distributions for all of the individual phases. Pair correlation functions were also calculated for all the phases and are plotted along with examples of the distribution of each phase in Figure 4-11 to Figure 4-17.

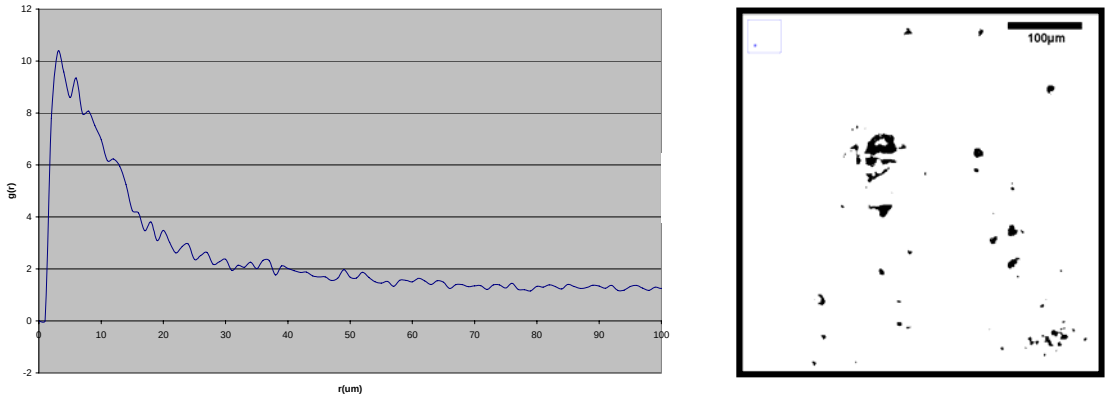

Figure 4-11: Pair Correlation *g(r)* of Al_2Cu.

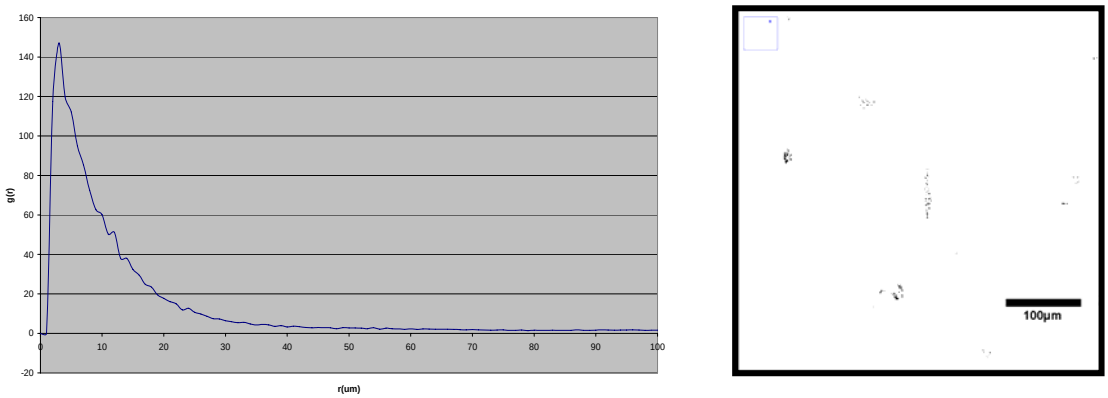

Figure 4-12: Pair Correlation *g(r)* of $Al_{73}(Cu,Mn,Fe)_{24}Si$.

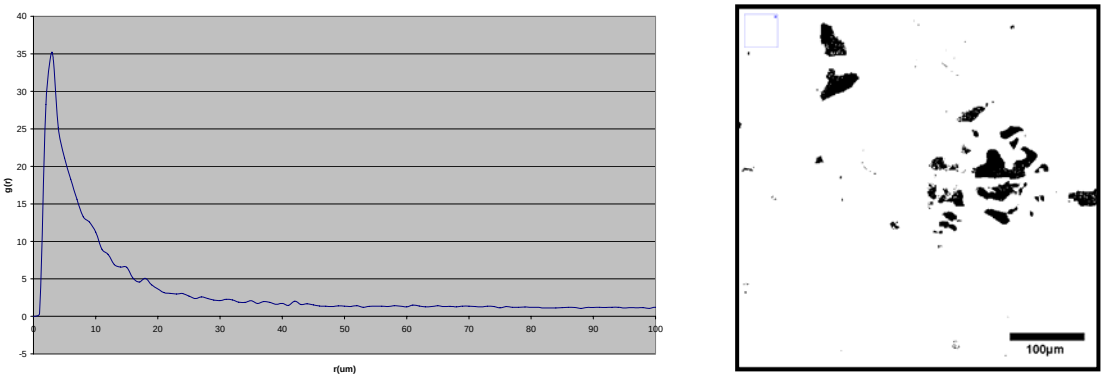

Figure 4-13: Pair Correlation *g(r)* of $Al_{20}(Cu,Mn,Fe)_5Si$.

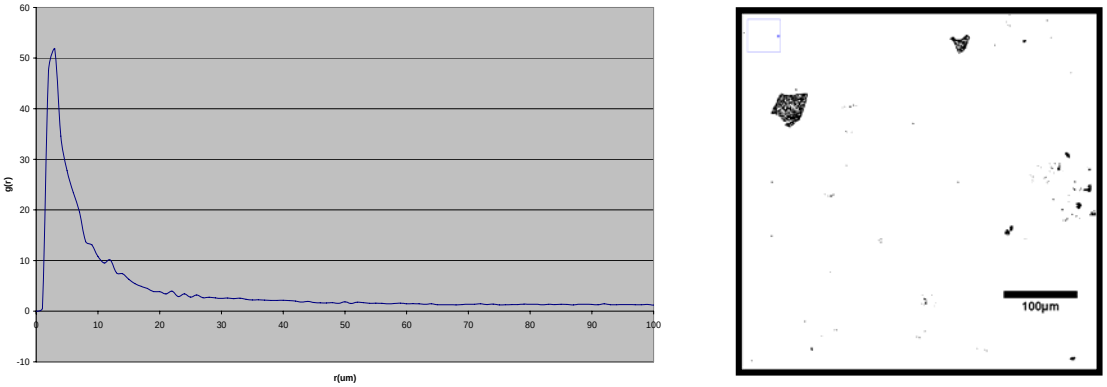

Figure 4-14: Pair Correlation *g(r)* of Al_7Cu_3Fe.

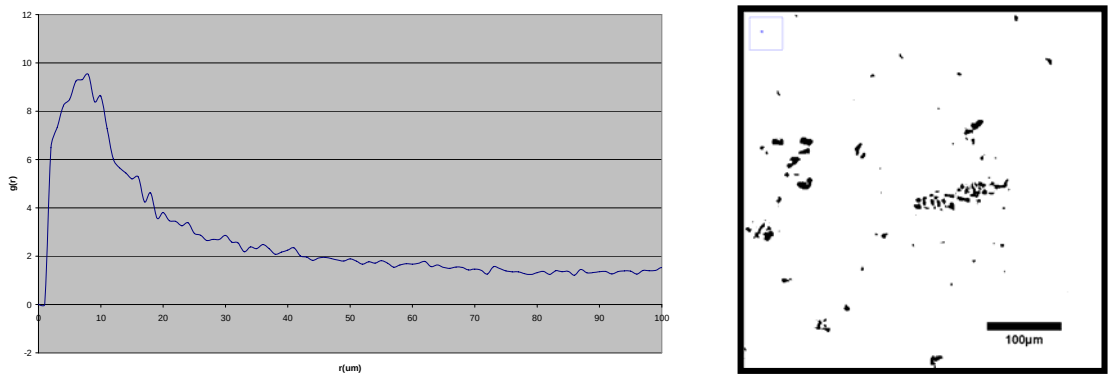

Figure 4-15: Pair Correlation *g(r)* of Al_2CuMg

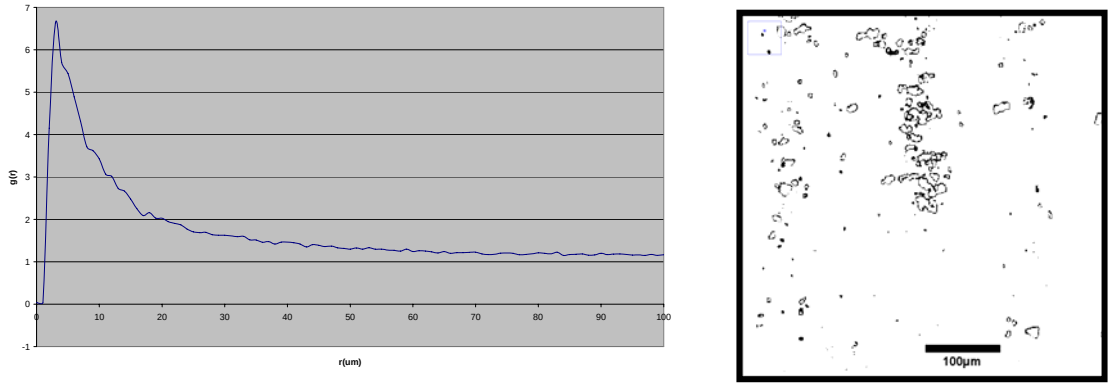

Figure 4-16: Pair Correlation *g(r)* of $Al_{20}Cu_3Mg$.

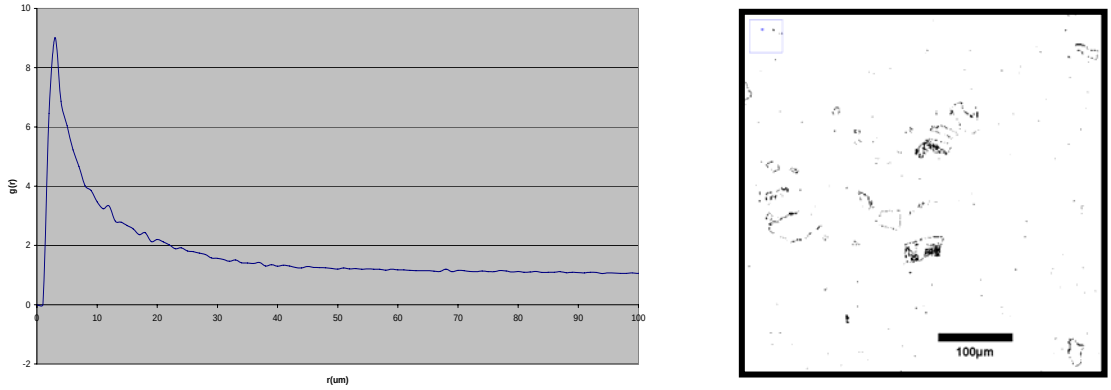

Figure 4-17: Pair Correlation *g(r)* of $Al_{90}(Cu,Mn,Fe)_8(Mg,Si)_2$.

In all of the *g(r)* plots there is evidence of a large number of nearest neighbours around 5 μm. These neighbours arise mostly from multiphase particles as described in the previous section and are shown in Figure 4-2 as well as the shell phase.

Figure 4-18 shows two particles magnified from the $Al_{20}(Cu,Mn,Fe)_5Si$ image. On the right hand side of the insert is a series of black pixels representing the incorporation of $Al_{20}(Cu,Mn,Fe)_5Si$ into a second phase (not shown). The red lines indicate the pair correlation between 1-10 μm of one phase domain with similar phase domains within the same particle for a multi phase particle.

Figure 4-19 shows a cluster of particles from the $Al_{20}(Cu,Mn,Fe)_5Si$ map with pair correlations for a single particle with the surrounding IMs between 20-50 μm in red.

The shell phase presents its own problems from the perspective of particle counting. It was often continuous and the software generally placed the centre of the particle at the geometric centre of the shell, however, wherever it was discontinuous it was counted separately. This resulted in one type of clustering including the S-phase/θ-phase/shell which is particularly important since there are adjacent particles of opposite electrochemical activities in the cluster. Significant correlation in the *g(r)* for S and θ-phase also extends out to the 15 to 20 μm region. In Figure 4-2 it was evident that the S-phase/θ-phase particles themselves occurred in groups and not necessarily as isolated pairs of phases. Clustering out to 20 μm is therefore likely to be due to these configurations of the S-phase/θ-phase particles.

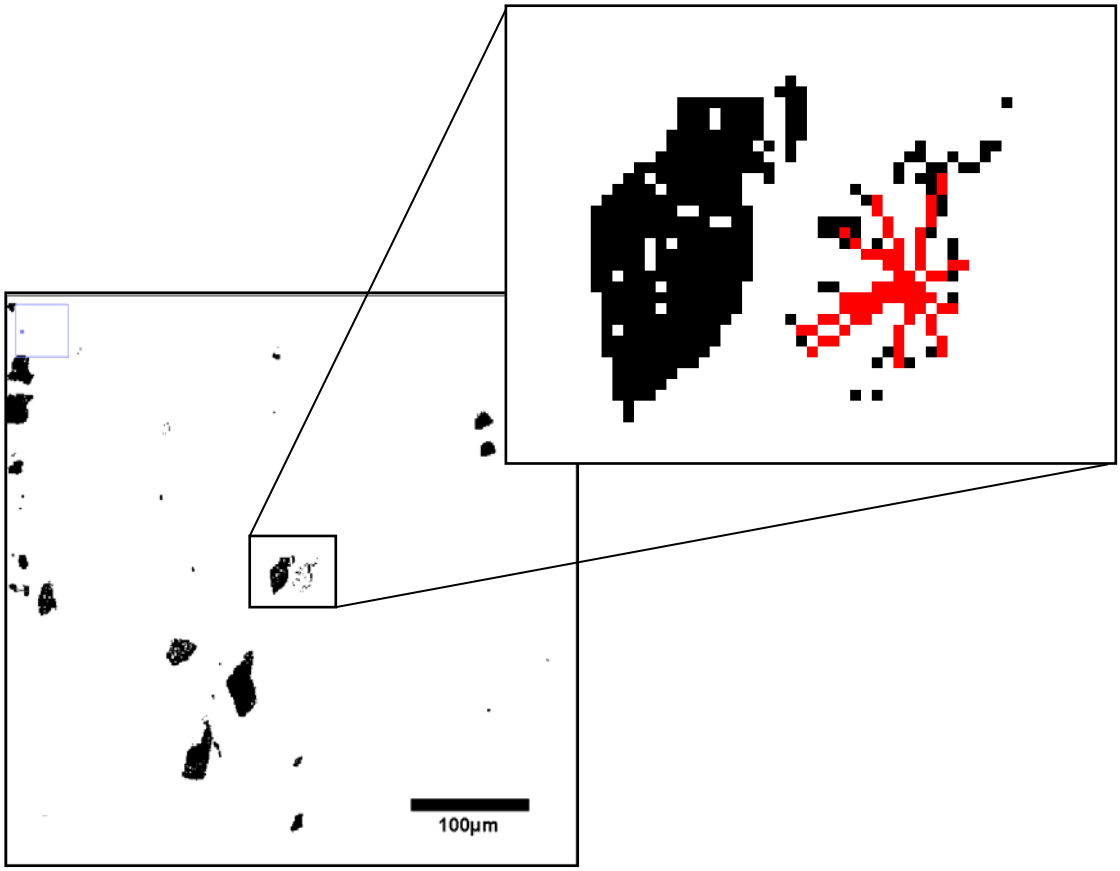

Figure 4-18: A magnified section of $Al_{20}(Cu,Mn,Fe)_5Si$ indicating particles with a separation distance between 1-10 µm (intra-particle) from a single particle origin

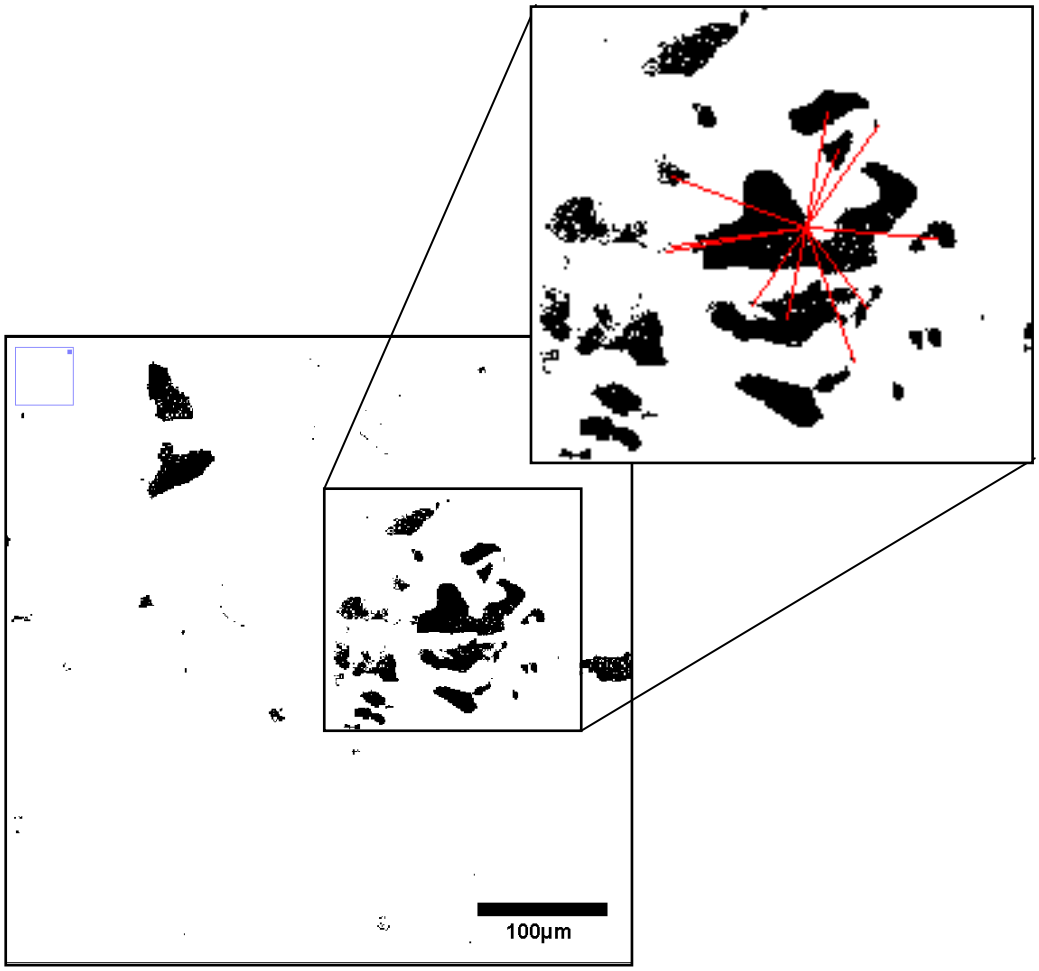

Figure 4-19: A magnified section of $Al_{20}(Cu,Mn,Fe)_5Si$ indicating particles with a separation distance between 20-50 µm (inter-particle) from a single particle origin

Aside from the clustering within the 0–10 µm range, the pair correlation functions show evidence of clustering over longer distances up to 80 µm since *g(r)* is still above 1 (representing a random distribution). This reflects clustering of the same type of particles as can be seen by inspection of the map in Figure 4-1.

The origin of the different types of clustering can be explained through a mixture of primary and secondary precipitation processes as well as mechanical processing of the alloy. The Al, Cu, Mn, Si and Fe containing IM particles are formed during ingot preparation. In AA2024-T3 the alloying addition of Mg and Cu are added to form precipitates that markedly improve the mechanical properties primarily through the

formation of S' laths (very fine particles which are coherent with the matrix) [22]. Mn also improves the mechanical properties through the formation of the dispersoid phase $Al_{20}Cu_3Mn_2$. $MnAl_6$ also forms which dissolves Fe in the melt, purifying the alloy matrix [23]. The Mn containing phases have a similar potential to the aluminium so this reduces the propensity for corrosion in the alloy [23]. Large IM phases that form tend to sink to the bottom of the melt, purifying the remaining Al. Fe-aluminides and Si have deleterious properties for corrosion [23]. Thus, precipitation in the melt will be dictated by the local concentration of solute atoms and the phase assemblage changes according to the availability of solute atoms. S-phase precipitation can also occur during this stage [4]. Thus the origin of the strong correlation in *g(r)* at short distances probably relates to the primary precipitation process. The shell zone around the S-phase/θ-phase clusters may arise during cooling of the ingot or as a secondary precipitation process which occurs during solutionising and ageing at elevated temperature (which is not the case for the T3 condition since it is aged at room temperature). Again, this contributes to the magnitude of *g(r)* at short distances. Mechanical working of the alloy such as rolling and milling, is more likely to produce clusters at the larger distances. For example, Scholes et al [24] found that the Cu-Fe-Mn-Al IM particles fractured during milling whereas the S-phase/θ-phase clusters remained intact. This was attributed to the brittleness of the former particles. Clustering of particles during rolling is well known through the formation of lines of fractured particles along the rolling direction called stringers. In summary, clustering in *g(r)* probably reflects a range of processes related to the alloy's manufacturing history.

The pair correlation functions between S-phase (Al_2CuMg) and other IM particles in the alloy are shown in Figure 4-20 to Figure 4-25. These correlation functions measure the likelihood of finding particles of the designated type near a S-phase particle. The normalisation factor for the *g(r)* in this instance is the particle density for the S-phase map, so as $r \rightarrow \infty$, *g(r)* will not approach 1.

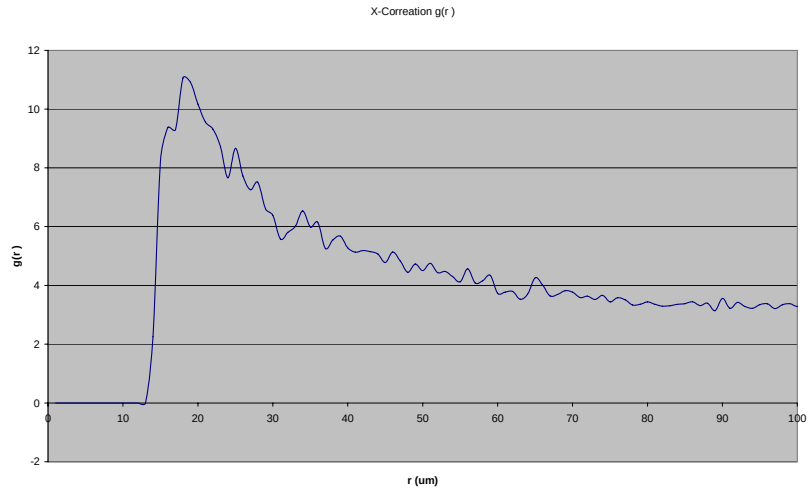

Figure 4-20: Cross correlation *g(r)* between Al_2CuMg and Al_2Cu.

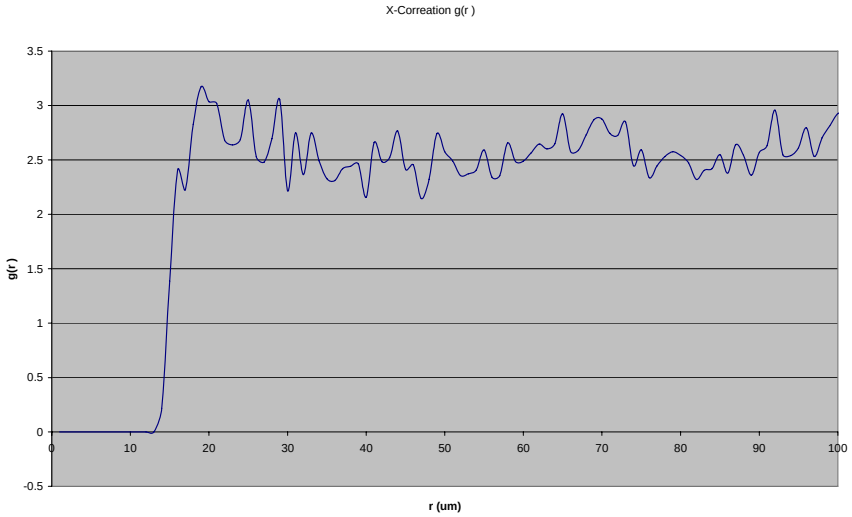

Figure 4-21: Cross correlation *g(r)* between Al_2CuMg and $Al_{73}(Cu,Mn,Fe)_{24}Si$.

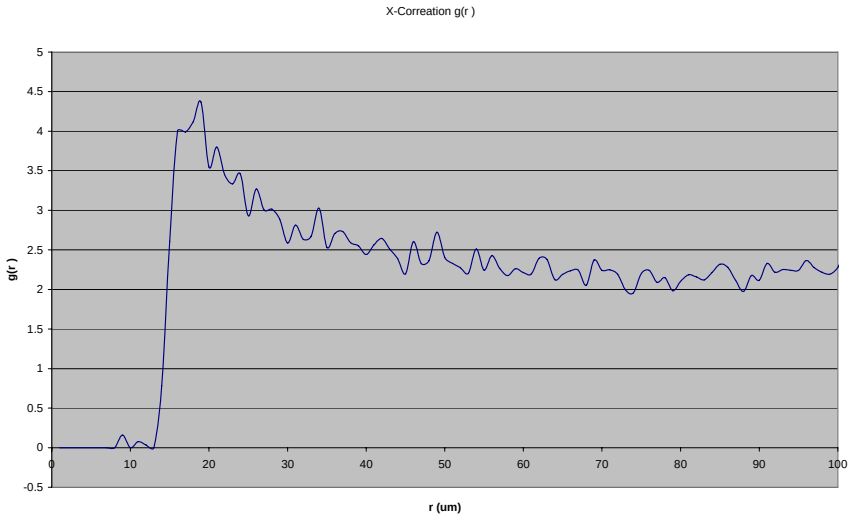

Figure 4-22: Cross correlation *g(r)* between Al_2CuMg and $Al_{20}(Cu,Mn,Fe)_5Si$.

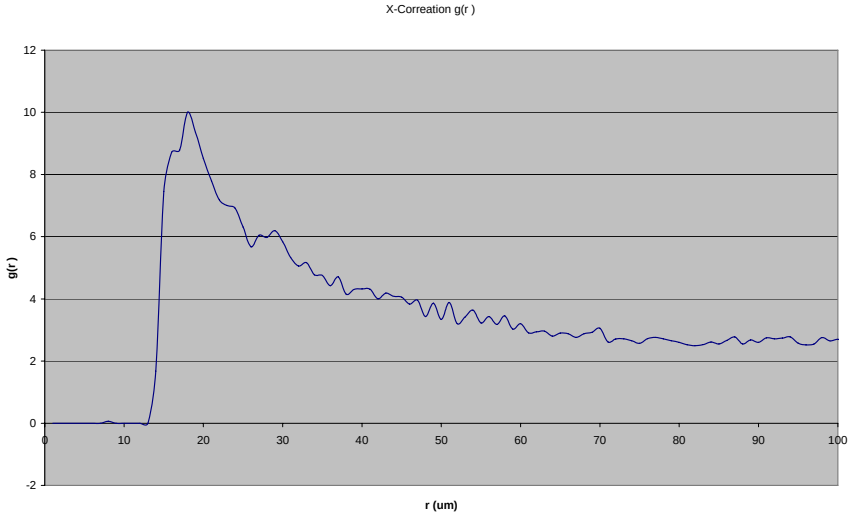

Figure 4-23: Cross correlation *g(r)* between Al_2CuMg and Al_7Cu_3Fe.

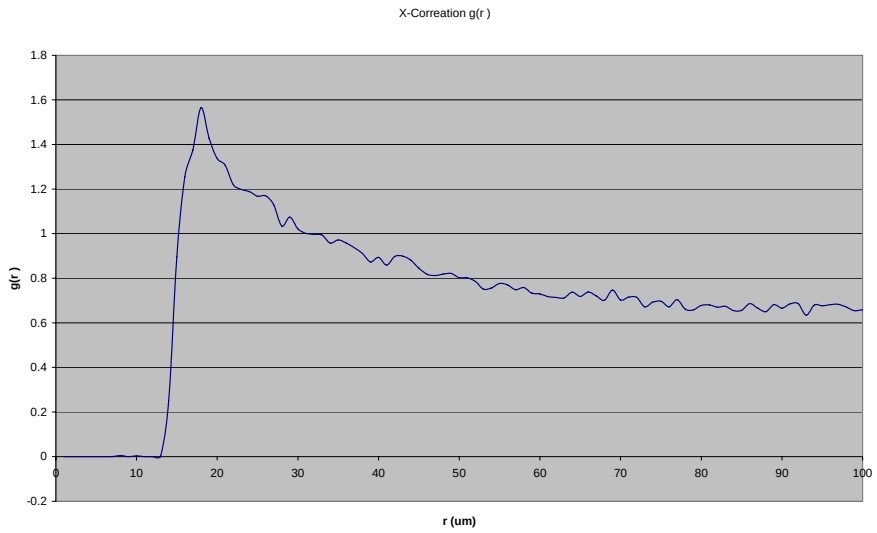

Figure 4-24: Cross correlation *g(r)* between Al_2CuMg and $Al_{20}Cu_3Mg$.

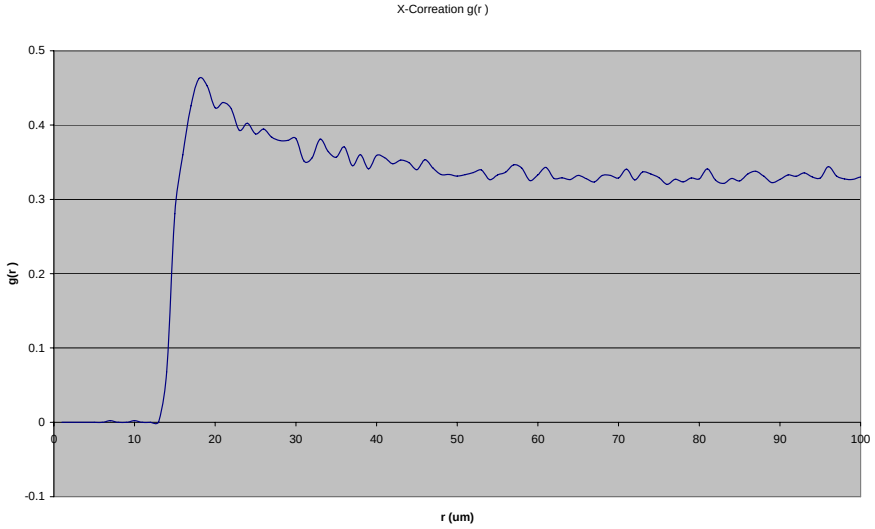

Figure 4-25: Cross correlation *g(r)* between Al_2CuMg and $Al_{90}(Cu,Mn,Fe)_8(Mg,Si)_2$.

The correlation functions can be divided into those showing strong clustering (Al_2Cu, $Al_{20}(Cu,Mn,Fe)_5Si$, Al_7Cu_3Fe, $Al_{20}Cu_3Mg$,) and those where weak clustering was observed ($Al_{90}(Cu,Mn,Fe)_8(Mg,Si)_2$, $Cu_7Fe_4Mn_2$). Where clustering was observed around S-phase particles, there appeared to be a peak at around 20 μm with evidence of

clustering extending out to 50 μm and beyond. The S-phase/θ-phase couples were discussed above along with the shell phase ($Al_{20}Cu_3Mg$).

4.5 Regional Variability

Electrochemistry is often performed on a range of electrode sizes ranging from several square centimetres to microelectrodes. While it is recognised that there is variability in parameters such as the particle density from one region to another, there are no studies that explore this in any detail. There are some studies, however, that look at the influence of electrode area on corrosion phenomena.

Given this gap in information it was decided to breakdown the image in Figure 4-1 into a number of smaller regions and examine the variation in particles density from region to region. Thus the maps were divided into firstly 4, then 16, then 64 and finally 256 regions and particle counts were made for each region. These figures were then scaled up to the total area of the map. The particle count for the total area (81,964) was then subtracted from the scaled up value giving a dataset containing the deviation in number from the total for the full map (81964). These results were then tranched into groups of 5000 and the number of regions that fell in these tranches were counted with the data plotted in Figure 4-26.

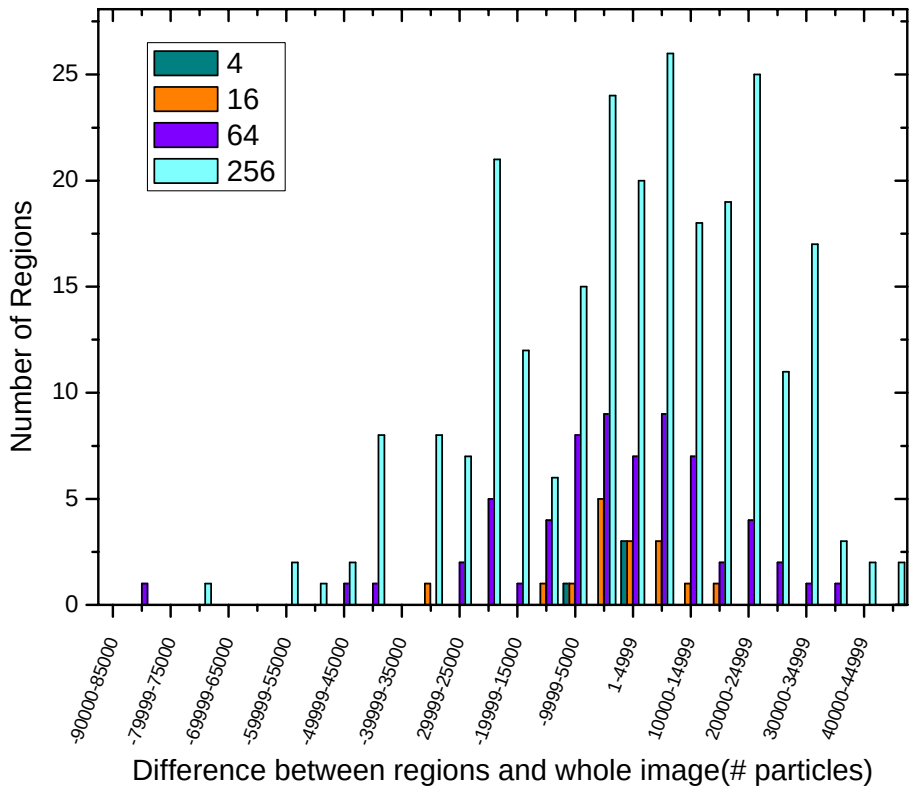

Figure 4-26: The maps of Figure 4-1 were divided in 4, then 16, 64 and lastly 256 separate regions. Particle counts were taken for each region and adjusted to the area of the total map.

When the surface was divided into 4 individual regions (deep green), they had similar particle densities to the original (most were within 5000 counts of the 81,964). However, when the surface was divided into 16 regions (orange) then the variation from 81,964 increased to values ranging from + 20,000 to -35,000. The distribution of regions broadened even further with smaller regions. The spread was greatest on the negative side of the distribution indicating that there were regions with very few particles. These results confirmed that clustering existed on the surface, since if the particles were evenly distributed then smaller regions would have particle densities much closer to the total for the map in Figure 4-1. Indeed the increase in spread can be used to indicate the scale at which clustering becomes important. For example the distributions start to broaden significantly between 16 and 64 suggesting that some clustering may occur on a scale between 80 and 300 μm. This agrees well with the pair correlation functions that show clustering still occurs at 80 μm and beyond.

The variation in the number of particles from region to region suggests that the active electrode area is probably also changing from region to region. To measure this, the ratio of the anode to cathode areas was calculated for the whole image as well as for each of the regions when the image was subdivided. The value for the total image was then subtracted from each of the regions with the data plotted in Figure 4-27. The particle phases that were included as part of the anodic IM phases were all the Mg containing phases. Particles without Mg were counted as cathodic, although some of these may be very close to the open circuit potential of AA2024-T3 [25,26]. The matrix was not included in either category. As with the particle numbers, the ratio of anode to cathode area broadens significantly as the region size is reduced. The distribution broadens significantly towards large negative numbers indicating that the smaller regions have a large anode to cathode area. This data again suggests that there is clustering, but in this instance suggests that the clustering is associated with the cathodic particles and the anodic particles are much more evenly spread through the alloy.

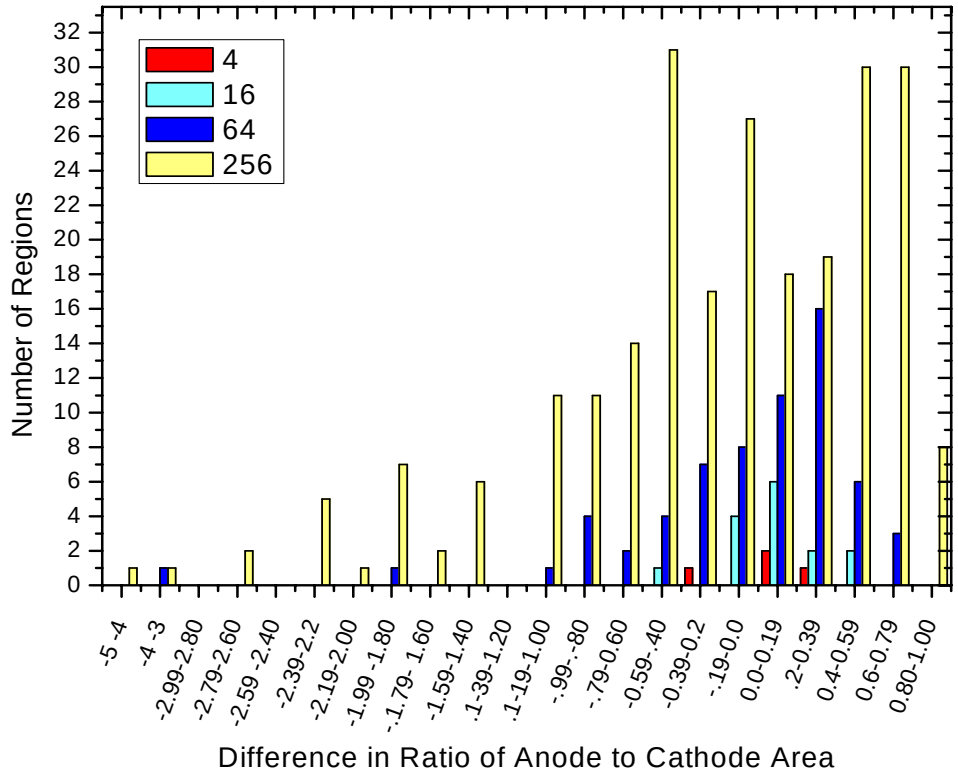

Figure 4-27: Difference between the anode to cathode area for individual regions compared to the total image.

4.6 Summary

From this statistical analysis of AA2024-T3, the microprobe analysis showed the extent to which Al_2CuMg (S-phase) and Al_2Cu (θ phase) co-precipitate in individual particles, which confirmed recent studies [10]. It also showed that there were a number of other phases that contain Mg, Al, and Cu as the main constituents. If it is assumed that all these particles are anodic with respect to the matrix and that the remaining particles are cathodic, then 60% of the total particles are cathodic. This in contrast to what was found by Buchheit *et al* [4].

By calculating the pair correlation *g(r)* for each phase, a large number of nearest neighbours around 5 μm were found. These neighbours arise mostly from multiphase particles as well as the shell phase. Significant correlation in the *g(r)* for S and θ-phase was also observed in the 15 to 20 μm region. Here it was evident that the S-phase/θ-phase particles themselves occurred in groups and not necessarily as isolated pairs of phases. Clustering out to 20 μm is therefore likely, due to these configurations of the S-phase/θ-phase particles.

From the regional variability study it was shown that when the area is divided into 4 parts, the particle densities don't differ much from the original, but as we divide the total area into smaller and smaller regions, then there are variations from the average of the total map. Thus proving that clustering is evident on the surface, as particle densities would have remained similar to the total image, independant of size. The increase in spread can be used to indicate the scale at which clustering becomes important. As distributions start to broaden significantly between 16 and 64, this suggests that some clustering may occur on a scale between 80 and 300 μm, which agrees with pair correlation functions that show clustering still occurs at 80 μm and beyond. The distribution broadens significantly towards large negative numbers indicating that the smaller regions have a large anode to cathode area. This data again suggests that there is clustering, but in this instance suggests that the clustering is associated with the cathodic particles and the anodic particles are much more evenly spread through the alloy.

4.7 Bibliography

1 I. S. Cole, D. Lau, and D. A. Paterson, Corr. Eng. Sci. Tech. **39,** 209-218 (2004).

2 A. E. Hughes, B. R. W. Hinton, S. A. Furman, I. S. Cole, D. Paterson, A. Stonham, G. McAdam, D. Dixon, S. J. Harris, A. Tureman, M. Hebbron, C. Bowden, P. C. Morgan, and M. Ranson, Corr. Revs **20,** 275 (2007).

3 T. H. Muster, A. E. Hughes, and G. E. Thompson, *Copper Distributions in Al-Alloys in Corrosion research Trends* (Nova Publishers, 2007).

4 R. G. Buchheit, R. P. Grant, P. F. Hlava, B. McKenzie, and G. L. Zender, J. Electrochem Soc. **144,** 2621 (1997).

5 G. S. Chen, M. Gao, and R. P. Wei, Corrosion **52,** 8 (1996).

[6] M. Warmuzek, ASM handbook Volume 9 Metalurgy and Microstructures, ASM International, 712 (2004)

[7] J. E. Hatch, *Aluminium: Properties and Physical Metalurgy,* Metals Park, OH, (1984).

[8] G.T. Hahn A.R. Rosenfield, Metal. Trans A, **6A,** 653, (1975)

[9] M. Gao, C. R. Feng, and R. P. Wei, Metal. Mater. Trans. A**,** 1145-1151, (1998).

[10] G. O. Ilevabare, O. Schneider, R. G. Kelly, and J. R. Scully, J. Electrochem. Soc. **151,** B453, (2004).

[11] I. R. Harrowfield, C. M. MacRae, and C. M. Wilson, Microbeam Analysis Society, New York, 547 - 548, (2003)

[12] Adobe Systems Inc, (2005).

[13] W. Rasband, NIH, 2007).

[14] A. E. Hughes, A. P. Boag, L. M. Pedrina, L. Juffs, D. G. McCulloch, J. P. Du Plessis, P.J.K., I. K. Snook, and B. O'Malley, ATB Metallurige, 551-556, (2006)

[15] L. Juffs, Investigation of Conversion Coating Deposition on Microscopic and Macroscopic Intermetallic Phases of Aluminium Alloy, RMIT University, (2002)..

[16] M. I. Pownceby, C. M. MacRae, and N. C. Wilson, Min. Eng. **20,** 444-451 (2007).

[17] L.F. Mondolfo, Aluminium Alloys Structure and Properties, The Whitefriars Press London, 505, (1976).

[18] R.G. Buchheit, J. Electrochem. Soc. **142**, 3994-3996, (1995)

[19] P. Campestrini, E. P. M. Van Westing, H. W. Van Rooijen, and J. H. W. De Wit, Corr. Sci. **42,** 1853 - 1861, (2000).

[20] C. M. Liao, J. M. Olive, M. Gao, and R. P. Wei, Corrosion **54,** 451-458, (1998).

[21] L. Lacroix, L. Ressier, C. Blanc, and G. Mankowski, J. Electrochem. Soc. **155,** C8-C15, (2008).

[22] J. E. Hatch, *Aluminium: Properties and Physical Metalurgy,* Metals Park, OH, (1984).

[23] I. J. Polymear, *Light Alloys: Metallurgy of the Light Metals*, 2nd Edition,. Metallurgy and Materials Science Series, (1989).

[24] F. H. Scholes, S. A. Furman, A. E. Hughes, and T. A. Markley, Corr. Sci. **48,** 1812 - 1826 (2006).

[25] R. G. Buchheit, J. Electrochem Soc. **142,** 3994- 3996 (1995).

[26] I. Polymear, *Light Alloys: Metallurgy of the Light Metals*, 2nd Edition,. Metallurgy and Materials Science Series, 34 (1989).

Chapter 5 - Development of Characterisation Techniques for Investigating Pitting Corrosion

5.0 Introduction

As seen in Chapter 4, the IM particle distribution in an aluminium alloy shows some evidence of clustering and are aligned in the rolling direction. There has been considerable effort in developing methods for identifying and locating different phases of these particles. It is important to identify clustering of the IM particles in alloys in order to understand the corrosion mechanisms as there is believed to be an association between these particles and the onset of pitting and other types of corrosion. Chapter 4 showed clustering occurs in AA2024-T3 at different levels, however this chapter introduces techniques commonly used for this IM particle analysis as well as some novel approaches which were developed for this thesis. In particular, this chapter presents an investigation into the use of phase correlation mapping produced using PIXE analysis to identify different IM phases at high spatial resolution. One aim of this study was to determine whether coupling of particular IM particles has a high correlation with pit nucleation. In addition we explore whether this analysis method can be used to show dealloying of S-phase particles following corrosion.

5.1 Background

IM phases have different chemical composition to the matrix, and in the case of aluminium alloys, consist of combinations of Al, Fe, Mn, Mg, Si, and Cu. The composition of the IM particles determines their electrochemical nature. A particle may be either cathodic or anodic to the alloy [1] and if the environmental conditions are right, these can lead to the creation of microscopic galvanic cells across the alloy's surface.

Microscopic second phase IM particles are difficult to analyse individually, particularly when their elemental compositions are similar. The use of EDX, SEM, as well as surface sensitive techniques like Auger Electron Spectroscopy (AES), have been applied to this problem [1,2,3]. Techniques such as XPS, which gives useful chemical state information,

has been used to study surface coatings on alloys but does not normally have the spatial resolution to look at individual IMs [3,4]. Electron Backscattered Diffraction (EBSD) and Transmission Electron Microscopy (TEM) can are two techniques that offer high resolution and crystal structure [4-7]. Using a combination of these techniques, the geometry and elemental composition can normally be determined. However, for this thesis a rapid identification process was required in order to investigate the association of different IMs with the onset of pitting corrosion in aluminium alloys. PIXE elemental mapping was employed because of its extremely high sensitivity to trace elements and its ability to collect the data rapidly.

5.2 Specimen Preparation

AA2024-T3 sheet, 1.6 mm in thickness from lot number 229621, Kaiser Aluminium Corporation was cut into panels (254 x 76 mm or 127 x 76 mm), with the long axis of the panel cut parallel to the rolling direction of the alloy sheet. Analysis by ICP showed that the following alloying elements were present at or above 400 ppm; Cu 5.3%, Mg 1.6%, Mn 0.6%, Fe 0.2%, Si 0.06% and Ti 0.04%. This batch of AA2024-T3 was used for samples investigated in this thesis.

Polished substrates were prepared by pressing out 10 mm diameter discs of this sheet, then grinding using SiC paper to P1200. Final polishing using 0.25 μm diamond paste was performed on these samples using rotary polishing techniques.

5.3 SEM Study of Pitting Corrosion

5.3.1 Introduction

This section introduced SEM and EDX mapping as a powerful characterisation technique which can be used to study pitting events on a corroded aluminium alloy surface. A time lapse experiment was developed to help better understand the nature of pitting corrosion in this alloy. Results of this section were the initial inspiration behind a vast majority of work conducted post this set of experiments.

5.3.2 Specimen Preparation and Experimental

Electron microprobe investigations using the SEM were conducted at RMIT Microscopy and Microanalysis Facility (RMMF) on a Philips XL30. Imaging was performed with a Lab_6 filament, an electron beam voltage of 20 kV and a spot size ranging between 4 and 4.5. EDX and imaging was performed at a working distance of 10 mm and a spot size of 5, all other parameters were constant with that of imaging.

The sample analysed for this chapter was firstly imaged and the EDX was performed. The sample was then removed from the microscope and a droplet of 0.5M NaCl was placed on top for one hour. The sample was then rinsed with DI water to remove the corrosion product and placed back in microscope and re positioned so as to re image the same area of analysis. This process was repeated in one hour increments up to five hours imaging and obtaining EDX maps between each cycle.

5.3.3 Results and Discussion

The SEM micrograph (Figure 5-1) shows a region of the alloy's surface with different IMs ranging in size from 1 – 20 μm prior to the start of the experiment. Corresponding elemental EDX maps for this region are also displayed. From the EDX maps it is shown that the larger particles in the bottom right of the micrograph are Fe-Mn rich and from the Cu map there are many regions with Cu rich particles. Unfortunately due to the resolution of the EDX maps the precise locations of these Cu rich particles cannot be identified as they are a mixture of S-phase and θ-phase. Although a good indication of these particles is shown by the deficiencies in the Al signal of Al elemental EDX map.

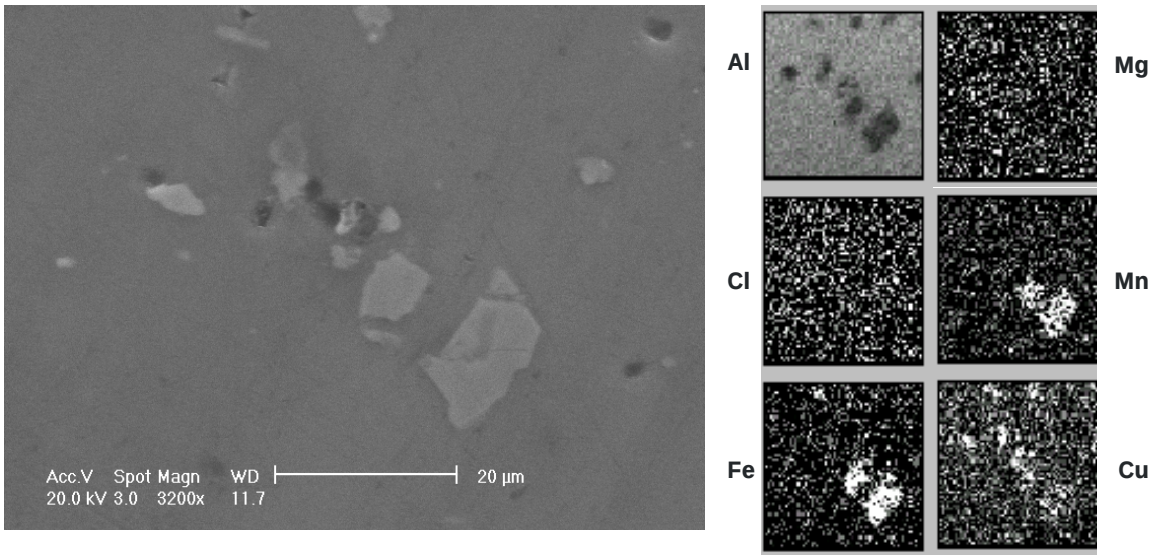

Figure 5-1: Polished AA2024-T3 sample and corresponding EDX elemental maps

Upon initial inspection of the sample after one hour of exposure to the NaCl solution, 3 major points were instantly obvious and can be seen in Figure 5-2. Firstly a trench started to appear around the large Fe-Mn particle (indicated by A), consistent with the trenching method of pitting which was described in Chapter 2. Secondly a large void appeared in the centre region which was the area that appeared to contain Cu rich particles (indicated by B). These results are consistent with the IM dissolution method for pitting corrosion also discussed in Chapter 2. Finally, a large square region across the sample formed as a result of carbon stitching from the electron beam, this was caused due to the lengthy duration of the beam exposure during EDX mapping. It was also observed in the regions surrounding the carbon stitching that the surface degradation was much more severe, see Figure 5-3. This indicated that the carbon stitching of the electron beam may have provided increased protection from attack from the NaCl solution.

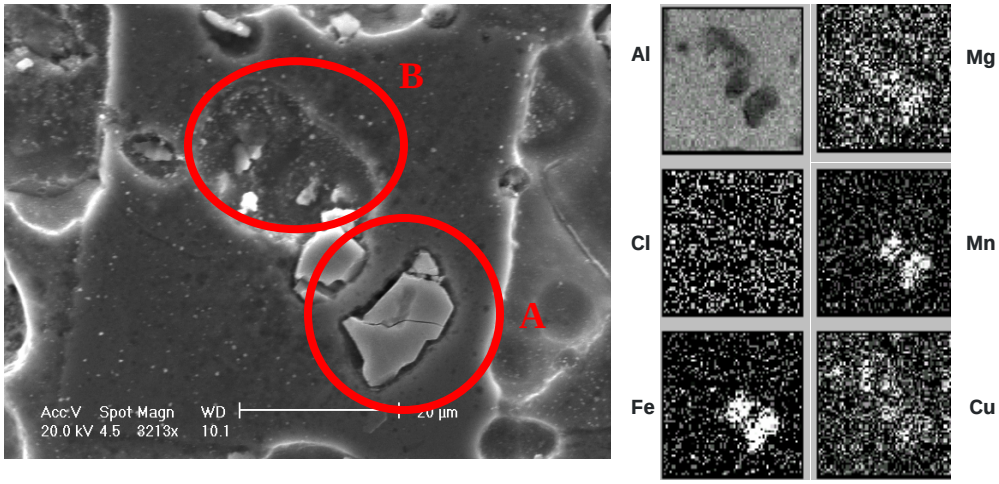

Figure 5-2: AA2024-T3 sample corroded with 0.5M NaCl solution for 1 hour and corresponding EDX elemental maps

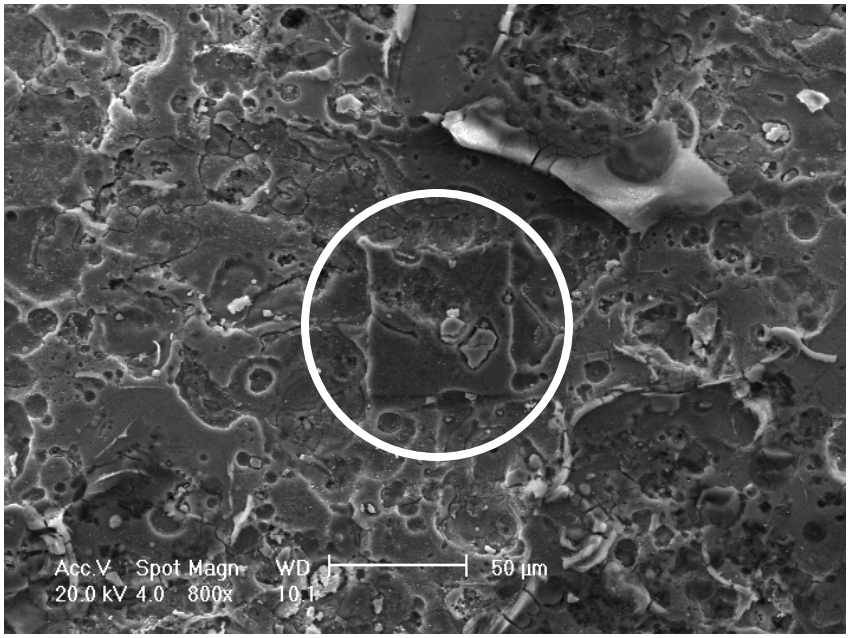

Figure 5-3: SEM micrograph of corroded surface around exposed analysis area, indicated by the circle

After the second hour of exposure a slightly wider trench was observed around the large Fe-Mn particle, as can be seen in Figure 5-4. It was also observed from the EDX maps in Figure 5-4 that there was Cu enrichment in the vicinity of this particle. A much greater

amount of damage to the surface caused by the second hour of exposure to the NaCl solution was also observed.

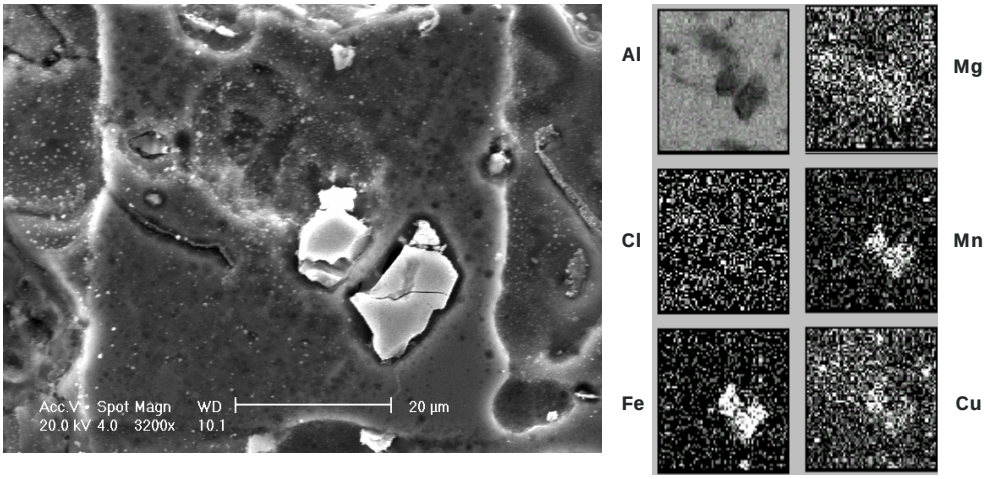

Figure 5-4: AA2024-T3 sample corroded with 0.5M NaCl solution for 2 hours and corresponding EDX elemental maps

Exposure to solution and EDX mapping continued in 1 hour increments until 5 hours. Imaging and EDX elemental maps at each increment revealed an increase in the width of the trench around the large Fe-Mn particle and further dissolution of the Cu particles. After 5 hours of exposure both the trenching and dissolution methods of pitting were very clear, with no visual evidence of the Cu particles which were evident in the initial polished image. The micrograph and corresponding EDX elemental maps of the surface after 5 hours are shown in Figure 5-5.

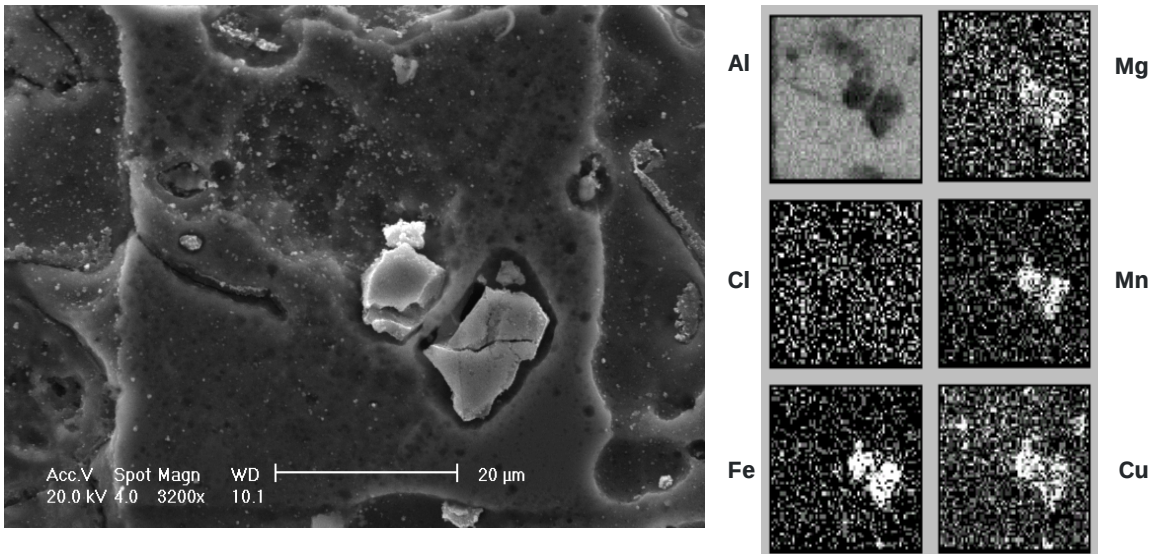

Figure 5-5: AA2024-T3 sample corroded with 0.5M NaCl solution for 5 hours and corresponding EDX elemental maps

By comparing the Cu EDX elemental maps of the alloy's polished surface with that of the surface after 5 hours of exposure, see Figure 5-6, the migration of Cu to the region where the large Fe-Mn particle is located is further evident. This appears to be a result of cathodic reduction of Cu onto the FeMn particle, supporting the dissolution of IM particle method of pitting.

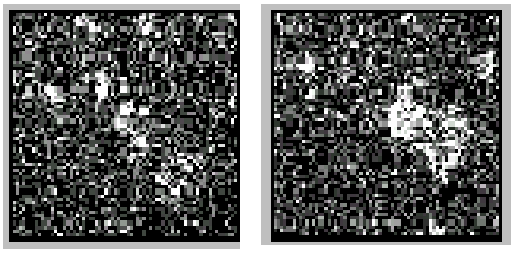

(a) (b)

Figure 5-6: Comparison of Cu EDX elemental map for the (a) polished sample and (b) after 5 hours exposed to 0.5M NaCl solution

5.3.4 Summary

This study clearly shows that a number of phenomena occur during the early stages of corrosion. These include trenching and dissolution of S-phase particles, as observed in a number of studies [2,9-16] as well as Cu enrichment of cathodic IM particles. The challenge in the following sections is to find techniques for measuring the degree of change of these processes.

5.4 Phase Correlation Mapping using PIXE

5.4.1 Introduction

In this section PIXE and phase correlation mapping was used to identify both individual phase information and the locations of individual IM particles and identify their presence with pit nucleation sites. This work initially identifies a means of standardising the phase correlation information by using model IM standard samples and then applies this understanding to a corroded sample.

Through PIXE imaging and elemental mapping alone, IM phases are not always clearly identifiable, especially when there are multiple phases containing the same or similar elements. For this reason phase correlation mapping was employed to determine the different IM phases present in AA2024-T3.

Phase correlation mapping (PCM) is a process where the phase information at each pixel of entire elemental images is mapped onto a single element vs single element concentration diagram. Individual phases are often highlighted by groups of similar concentration around the bulk.

5.4.2 Specimen Preparation and Experimental

Four standard alloys were positioned in a checkerboard arrangement for analysis. The IM phases were of four chemical types, $CuAl_2$, $CuMgAl_2$, Cu_2FeAl_7 and $FeAl_3$ as shown in

Figure 5-7, which represent the major classes of IMs in AA2024-T3. Care in preparation was required in order to obtain a homogeneous, single-phase alloy and an accurate measure of components was made. Melting was carried out in an argon vacuum arc furnace. Repeated melting and arc tip mixing was carried out keeping the slug near the melting temperature. Rods of the IMs were cast to 5 mm diameter in-situ. Samples were prepared at CSIRO by Darryl Jones.

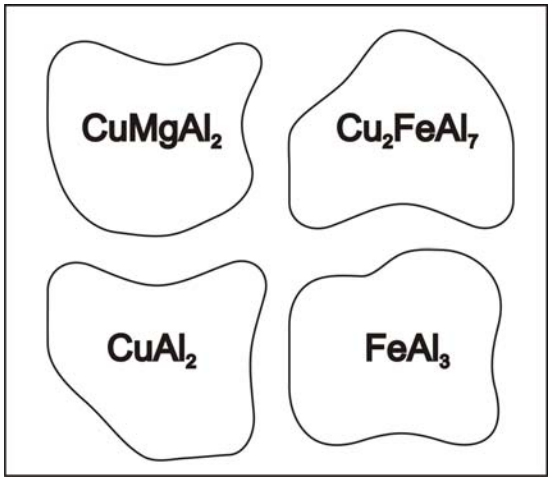

Figure 5-7: Diagram of IM standards sample

Both the polished samples and the standards sample were mounted on an aluminium mounting stub with carbon tape for PIXE analysis.

The experimental data collected for the phase correlation mapping analysis was conducted using PIXE on the 'MP2' beamline at the University of Melbourne's Micro Analytical Research Centre (MARC). A 3 MeV proton beam was selected with a Ge X-ray detector located 165 mm from the sample on a 45º angle. An 80 μm Be filter was placed in front of the detector window to a attenuate the large Al peak for better identification of trace elements.

5.4.3 *Results and Discussion*

To test the ability of PCM to distinguish different phases, the test sample shown in Figure 5-7 was designed to include four macroscopic IM compounds positioned in a checkerboard arrangement for PIXE analysis (Figure 5-7) and the resulting PIXE imaged maps of this sample are shown in Figure 5-8. The chosen alloys represent the major classes of IMs in AA2024-T3: $CuAl_2$, $CuMgAl_2$, Cu_2FeAl_7 and $FeAl_3$, labelled 1-4 in the order listed.

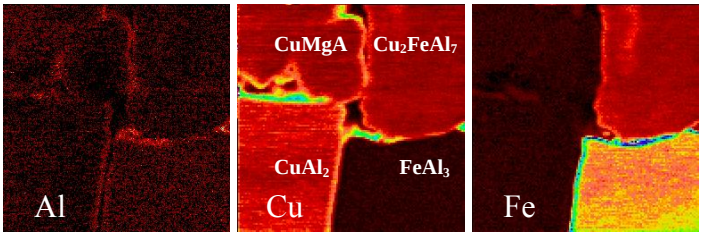

Figure 5-8: PIXE elemental maps for Al, Cu and Fe. Region 1-$CuMgAl_2$, 2-Cu_2FeAl_7, 3-$CuAl_2$ and 4 - $FeAl_3$. (Green highlight around particles is an edge effect).

$CuAl_2$ is typically found in binary Al-Cu alloys or 2XXX series alloys with a low Mg content [70]. As seen in Chapter 4, AA 2024-T3 sheets may contain both $CuAl_2$ and $CuMgAl_2$ IM particles. Alloying elements mixed with Fe-impurity lead to a complex multiphase structure, this includes the cathodic Cu_2FeAl_7 IM phase [1], while $FeAl_3$ is a common constituent in alloys AA 5005 and AA 7075 [17]. $CuAl_2$, Cu_2FeAl_7 and $FeAl_3$ are all known to be cathodic to the aluminium matrix [18].

Although the samples are visible in the elemental maps, it is difficult to distinguish the exact elemental compositions from these maps alone. For this reason, phase correlation diagrams were generated by selecting two aluminium elemental systems, and plotting the individual pixel intensities of the aluminium against the intensity of the element. The systems chosen were Al-Cu and Al-Fe shown in Figure 5-9 (a) and (b) respectively. As expected there were three clear phases present in the case of Al-Cu, arrows 1-3, while two phases were evident in the case of the Al-Fe, arrows 4-5.

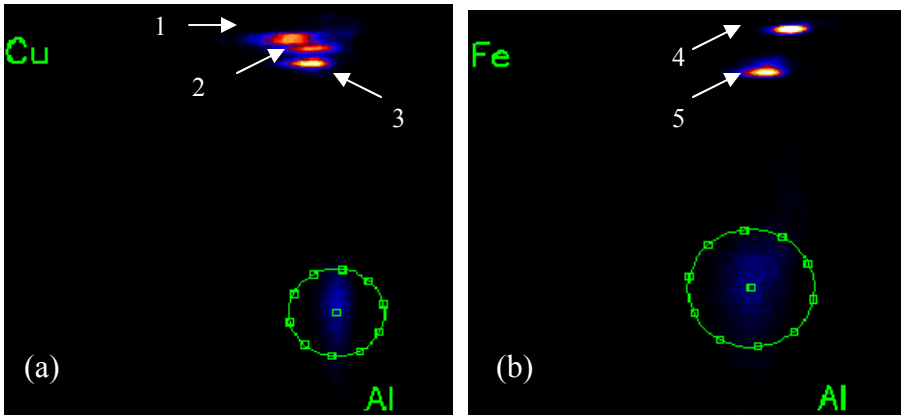

Figure 5-9: Phase correlation diagrams of the Al-elemental systems (a) Al-Cu and (b) Al-Fe. Arrows 1-3 highlight the Al-Cu phases $CuAl_2$, $CuMgAl_2$ and $CuFeAl_7$, respectively. Arrows 4-5 represent the Al-Fe phases $FeAl_3$ and $CuFeAl_7$. The circled regions indicate noise.

The origin of the phase signals of the Al elemental systems were then physically correlated with the surface maps. Figure 5-10 shows these surface maps for Al elemental systems. The first two systems $CuAl_2$ and $CuMgAl_2$ were directly identified using the Cu-Al PCM. The third system observed was the Cu_2FeAl_7. As aluminium is bonded to both Cu and Fe in this system and in the case of the $FeAl_3$, the Fe-Al PCM was also used in order to distinguish between these two phases. On each map the Al elemental system observed is highlighted in green. Map 1 in Figure 5-10 shows the location of $CuAl_2$ on the surface; map 2 shows $CuMgAl_2$; map 3 Cu_2FeAl_7 and map 4 $FeAl_3$.

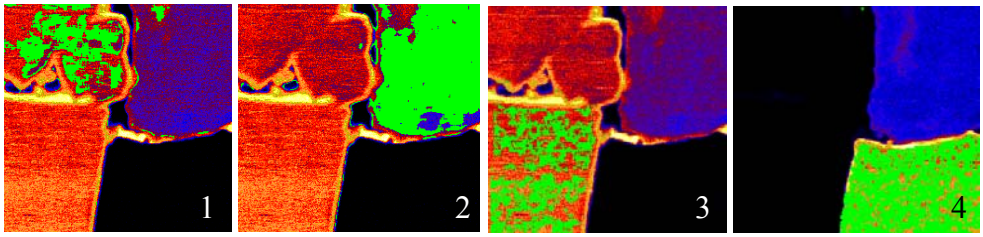

Figure 5-10: Origin of the phase signals of the four elemental systems; map 1 shows the location of $CuAl_2$; map 2 shows $CuMgAl_2$; map 3 Cu_2FeAl_7 and map 4 $FeAl_3$.

5.4.4 Phase Correlation Mapping – AA2024-T3 Sample

This identification technique was then applied to AA2024-T3 polished and samples exposed to the NaCl solution. The region of polished AA2024-T3 shown in Figure 5-11, clearly shows a vast number of IM particles of different elemental composition. It is also seen that there are a much greater number of Cu rich particles, this confirming statistics consistent with previous studies by Buchheit et al. [1] and Chapter 4. The PCM method in conjunction with model compounds provides an easy way to distinguish IM particles in AA2024-T3.

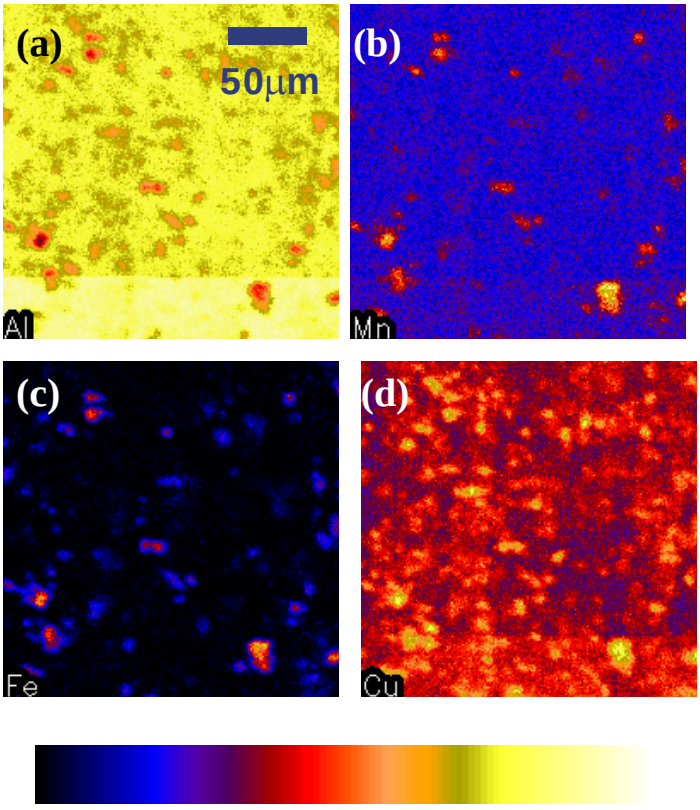

Figure 5-11: Elemental maps of a region of a polished AA2024-T3 sample containing (a) Al (b) Mn (c) Fe and (c) Cu Map

The analysis area of the corroded sample was chosen to include two pits formed during exposure. Figure 5-12 shows Al, Cl, Cu, Fe and Mn PIXE elemental maps obtained for AA2024-T3 exposed to 0.1M NaCl. The arrows indicate the location of each pitting event and are labelled 1 and 2 in Figure 5-12(a) and are depicted by the blue and black

regions in Figure 5-12(a). A strong Cl signal was detected on the right of event 1, see Figure 5-12(b).

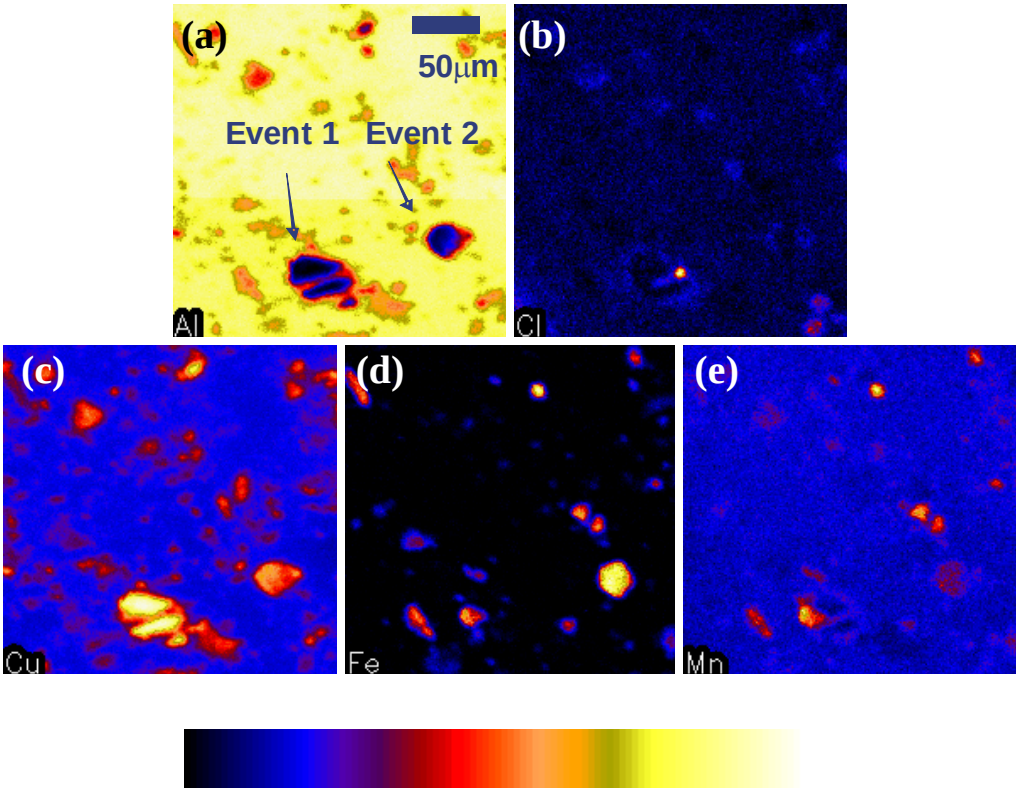

Figure 5-12: Elemental maps of a region of a corroded AA2024-T3 sample containing (a) Al (b) Cl (c) Cu (d) Fe and (e) Mn map

From the maps alone it would be believed that there is a Cu-Fe-Mn and an S-phase particle surrounding both pitting events, although this cannot be confirmed from the maps alone so PCM was adopted to verify these results.

To investigate changes in the IMs phase maps the corroded AA2024-T3 sample was compared with phase maps of a polished AA2024-T3 reference sample. Areas on the phase correlation maps for the polished surface were highlighted and their relationship to areas on the elemental maps showed bright regions representing Cu in solid solution with the alloy. The presence of two main types of IMs is evident in the Al-Cu phase correlation map shown in **Error! Reference source not found.**(a). The upper zone

(arrow 1), has a higher Cu concentration, representing S-phase particles, the lower zone (arrow 2) represents Cu-Fe-Mn-Al particles.

By analysing the phase diagram for the corroding sample two major differences were observed. The first is that the S-phase zone extends to around ten times the Cu levels (with decreasing Al levels) of the polished surface. The second difference is that the S-phase zone has split, (**Error! Reference source not found.**(b) arrow 1). Both these changes are due to Cu-enrichment resulting from dealloying of the S-phase particles that lose Al ($Al \rightarrow Al^{3+} + 3e^-$) and Mg ($Mg \rightarrow Mg^{2+} + 2e^-$) producing a Cu residue [1,15]. There is also some evidence of Cu enrichment of the Cu-Mn-Fe-Al IMs indicated by the lengthening of the second phase shown in **Error! Reference source not found.**(b) arrow 2. This could be due to the deposition of Cu from solution, since they are strong cathodes ($Cu^{2+} + 2e^- \rightarrow Cu$) observed by Wei et al. [19].

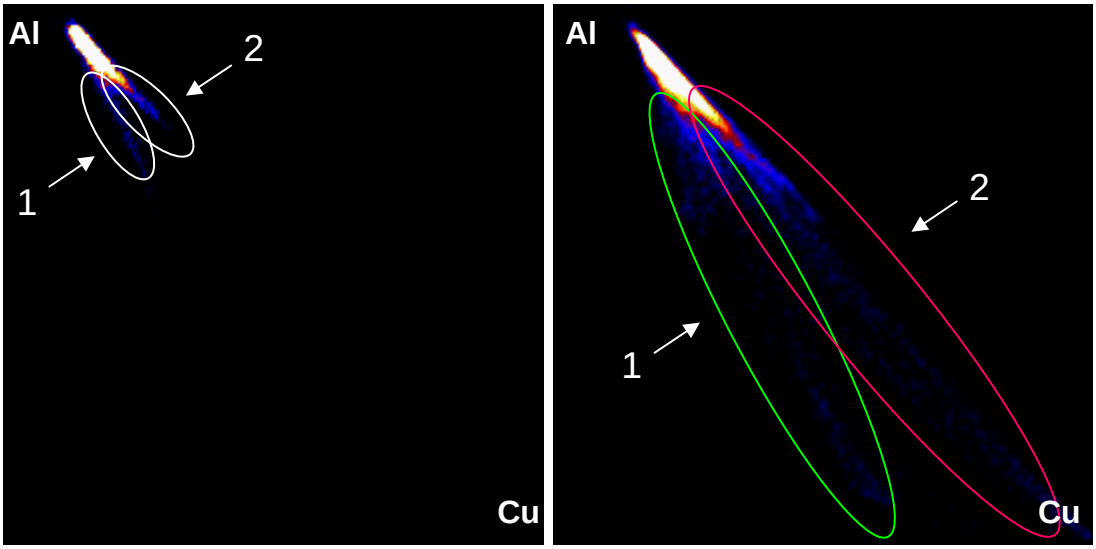

Figure 5-13: Al-Cu phase correlation diagram for the (a) lished and (b) AA2024-T3 sample exposed to the NaCl solution. Arrow 1 represents S-phase **particles and arrow 2 represents Cu-Fe-Mn-Al particles.**

The physical locations from where the S-phase and Cu-Mn-Fe-Al zone information seen in **Error! Reference source not found.**(b) were mapped back to the elemental maps and their locations are shown in Figure 5-14(b). The purple regions represent the S-phase

enrichment, the green regions represent the Cu-Mn-Fe-Al IMs and the black area is the matrix. By comparing the locations of the pit sites in Figure 5-14(a) and the locations of the two different phase particles in Figure 5-14(b), it is clearly shown that the S-phase particle were located around both these pits sites and the Cu-Fe-Mn-Al was located within the pit site. The coupling of these two types of IM particles at a site of pit formation was evident in a number of maps taken of the corroded surface and is further evidence to show that this pair of particles is associated with the establishment of pits.

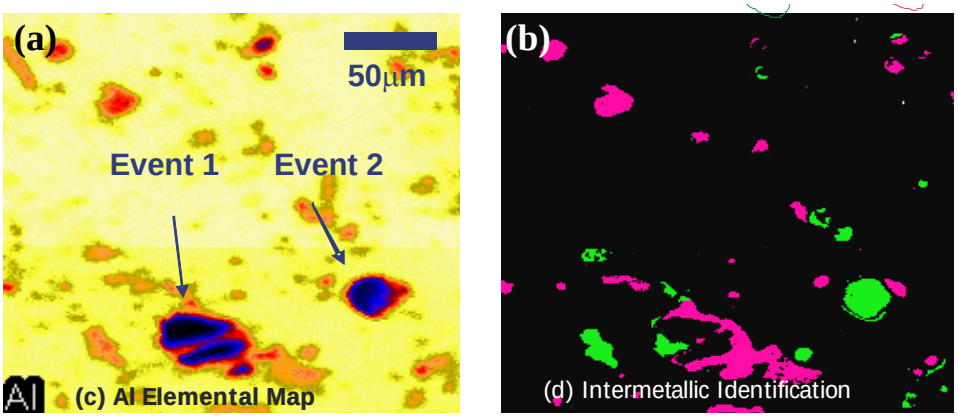

Figure 5-14: IM identification, (a) shows the Al elemental map with the 2 corrosion events indicated and (b) shows regions which correlate to the two phases, the purple represents S-phase**, green represents Cu-Fe-Mn-Al. The black area is the matrix.**

A Cu rich region is shown as a higher intensity region to the right hand side of pit 2 in Figure 5-12(c) (repeated in Figure 5-15) and a purple region in Figure 5-14(b). This may also be an S-phase particle.

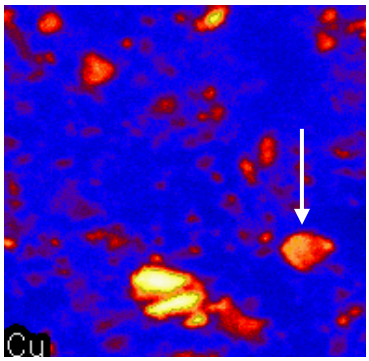

Figure 5-15: Cu PIXE elemental map highlighting Cu rich region to the right of the pit site 2

Pride et al. [20] showed that stable pit formation only occurs when the current density to pit radius is greater than 2 mA/cm^2. High current densities could be established when the cathodic Cu-Fe-Mn-Al particles drive the dissolution of the anodic S-phase particles. While such dissolution would lead to Cu-enrichment, it would also lead to a cavity in the surface where acidic conditions could be established and pitting could ensue.

5.5 Summary

The SEM study of pitting corrosion revealed both types of pitting corrosion: trenching and dissolution. After long exposure times, the presence of Cu enrichment was evident on cathodic IM particles. In addition electron beam carbon stitching appeared to provide an increase in corrosion resistance on the surface.

It was shown that Nuclear Microprobe analysis combined with phase correlation mapping can be used to investigate rapidly the association between IM particles and the site for corrosion pits in aluminium alloys. Paired S-phase and Cu-Fe-Mn-Al type IM particles were found to be associated with pit sites in AA2024-T3 samples exposed to the NaCl solution.

5.6 Bibliography

[1] R. G. Buchheit, R. P. Grant, P. F. Hlava, B. McKenzie, and G. L. Zender, J. Electrochem Soc. **144,** 2621, (1997).

[2] G. S. Chen, M. Gao, and R. P. Wei, Corrosion **52,** 8 (1996).

[3] A. E. Hughes, R. J. Taylor, and B. R. W. Hinton, Surface and Interface Analysis **25,** 223-234, (1997).

[4] R.G. Buchheit, L.P. Montes, M.A. Martiniez, J.michael and P.F. Hlava. J. Elec Soc. **146** p4424-4428, (1999)

[5] [N. Birbilis, M. K. Cavanaugh, L. Kovarik and R. G. Buchheit, Electrochem Com. **10,** 32-37, (2008)

[6] M. Gao, C. R. Feng, and R. P. Wei, Metal. Mater. Trans. A**,** 1145-1151, (1998)

[7] N. Birbilis, M. K. Cavanaugh, and R. G. Buchheit, Corr. Sci. **48,** 4202, (2006).

[8] J. A. Treverton and N. C. Davies, Metals Technology, **10**, 480, (1977).

[9] O. Schneider, G. O. Llevbare, J. R. Scully, and R. G. Kelly, J. Electrochem. Soc. **151,** B465, (2004).

[10] A. Kolics, A. S. Besing, and A. Wieckowski, J. Electrochem. Soc. **148,** B322,(2001).

[11] V. Guillaumin and G. Mankowski, Corr. Sci.**,** 421, (1999).

[12] N. Dimitrov, J. A. Mann, and K. Sieradzki, J. Electrochem Soc. **146,** 98, (1999).

[13] G. O. Ilevabare, O. Schneider, R. G. Kelly, and J. R. Scully, J. Electrochem. Soc. **151,** B453, (2004).

[14] M. Metzger, J. Zahavi, N. D. Tomashov, and E. N. Mirolubov, Corrosion of Metals and Alloys**,** 48, (1966).

[15] C. M. Liou, J. M. Olive, M. Gao and R. P. Wei, Corr. Revs **54,** 451, (1998).

[16] K. Kowal, J. Deluccia, J. Y. Josefowicz, C. Laird, and G. C. Farrington, J. Electroceh. Soc. **143,** 2471, (1996).

[17] I. J. Polmear, Scripta Metallurgica **23,** 1213 - 1217, (1989).

[18] R.G. Buchheit J Electrochem Soc, **142** 3994-3996, (1995)

[19] R. P. Wei, C. M. Liao, and M. Gao, Metallurgical and Materials Transactions a-Physical Metallurgy and Materials Science **29,** 1153-1160, (1998).

[20] S. T. Pride, J. R. Scull, and J. L. Hudson, J. Electrochem Soc. **141,** 3028, (1994).

Chapter 6 - Statistical Analysis of Particle Composition and Distribution in AA2024-T3

6.0 Introduction

Localised corrosion attack on aluminium alloys in Cl media has been the focus of many recent studies in the literature [1-30]. Whereas corrosion of pure Al relates more to the properties of Al itself, in Al alloys, corrosion relates to the distribution and composition of a large range of IM particles with compositions that depend on the alloy additions and processing conditions [8,9]. These particles are generally the initiation sites for corrosion in commercial alloys since flaws in the oxide surrounding these IM particles and the galvanic coupling between the IM particles and the surrounding matrix promote localized corrosion [8,10-31].

The very nature of IM particles such as their distributions, compositions and electrochemical characteristics means that a statistical approach to understanding the initiation and propagation of pitting is necessary as seen in Chapter 4. Thus in recent years there has been a trend towards a statistical approach to corrosion phenomena. Electrochemical approaches include the measurement of current transients to study metastable and stable pitting events as well as Scanning Kelvin Probe Atomic Force Microscopy (SKPAFM) to measure the potential of large numbers of S-phase particles. The measurement of current transients has led to a description of pitting phenomena in Al alloys in terms of nucleation events, metastable pitting and stable pitting [31-34] and draws on research of ferrous based metals [35,36]. This event-based description of pitting has emerged from the potentiostatic behavior of currents made at potentials between the open circuit potential (OCP) and the breakdown potential [31-33] and aims to identify factors that lead to the transition from metastable to stable pit growth [31]. Nucleation events are spontaneous corrosion and passivation events, and have a lifetime of a few seconds. Metastable pitting events maintain a corrosion current over tens of seconds possibly through a ruptured oxide coating, before decaying. Stable pitting initiates in a

similar fashion to metastable pitting, but has a higher initial current density. In ferrous metals, for both metastable and stable pitting events, it is suggested that when the oxide cap over the pit fully ruptures as in the case of stable pits, the pit is deep enough to maintain a concentration gradient and an acidic anolyte solution is established at the pit head. In the case of metastable pits the anolyte solution is dispersed into the general solution and the pitting event repassivates. These type of current transients have been observed for both pure Al [31], AA7075-T6 and AA2024-T3 [32-34].

As Sasaki *et al.* [37] have demonstrated, however, while the early stages of pitting in commercial Al alloys may be described in the above terms, the latter stages may be complicated by activation and passivation processes in active pits as well as "cross" talk between pits. So one limitation of the purely electrochemical approach for an alloy like AA2024-T3 is that it provides no direct microstructural information on the metastable or stable pit initiation site. Part of the problem is that normal corrosion occurs under OCP conditions and is driven by the balance of cathode and anode sites on the surface, where as electrochemical measurements drive the potential so that this balance is changed. This makes it difficult to connect the results of stable pitting under OCP conditions to the potentiostatic measurements. Some recent studies have recognized this shortfall and have attempted to connect the electrochemical measurements with microstructural changes. For example, Ilevbare *et al.* [20] concluded that metastable pitting occurred at or adjacent to intermetallic particles on the surface. The metastable pitting resulted in local dissolution phenomena at depleted zones around cathodic IP particles and S-phase particles which eventually ceased.

It is also implicit in the purely electrochemical approach that because the metastable and stable pitting events "look" the same electrochemically, *i.e.*, a sharp rise in current precedes both events, the population of stable pitting events is simply on the extreme end of the population statistics of metastable pitting events. This approach has also been applied to pure Al [31], and to AA2024-T3 for modeling for structural health management in airframes [32,33,38,39]. However, there is no clear connection between the stable pits generated at OCP conditions and potentiostatic measurements has been

established, indeed, the work of Ilvebare et al [20], suggests that a different mechanism exists for stable pit initiation in AA2024-T3 since the localized corrosion of depletion zones and S-phase dissolution generally activate and then passivate without demonstrating any further activity. In their case clustering is invoked for the onset of stable pitting.

Clustering of IM particles is an emerging area of importance in understanding pit stabilisation [12,13,18,20,24,40,41]. Clustering may be important at several different length scales and perhaps even times scales as reported. Previously it was reported that coupling of IM particles types of different electrochemical activity may result in stable pit initiation. It was also noted that Cl attack sites in AA2024-T3 appeared to have a higher number of IM particles in the immediate vicinity (within a 50 μm region) than the average particle number. The current work presents a more elaborate study of the early evolution of corrosion events as a function of time on AA2024-T3. In this context Wei and co-workers [24,40] have reported clustering on AA2024-T3 and AA7075-T6 as have Juffs and coworkers [42,43]. Ilevbare et al. [20] also suggested that large clusters of particles were necessary to establish conditions where S-phase etchout could continue on to stable pitting. These studies conclude that clustering influences stable pit initiation through excessive trenching which leads to particle fallout and other attack.

One aim of this chapter is to examine how corrosion develops on AA2024-T3 during the early stages of exposure to Cl containing solution. The corrosion has been followed using SEM in conjunction with EDX analysis, as well as PIXE and focuses on isolated IM particles. The degree of clustering of IM particles and the influence of clusters on the establishment of stable pits in AA2024-T3 is the second objective of this chapter.

6.1 Experimental

6.1.1 Specimen Preparation

6.1.1.1 Rod Samples

Alloy rod samples were prepared for analysis with PIXE, SEM and EDX, as seen in Figure 6-1. Al 2024-T3 sheet was cut into 2mm^2 rods and then encased in epoxy.

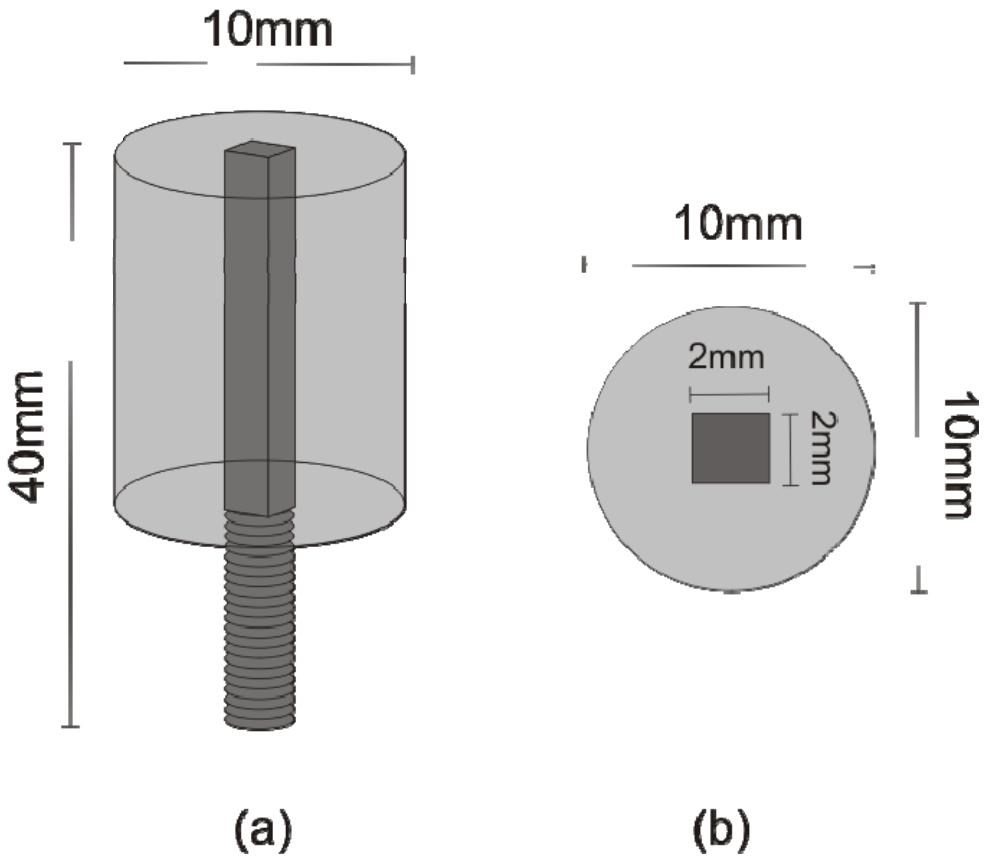

Figure 6-1: Diagram of rod type samples from (a) side view, and (b) top down view

Polishing was performed on the specimens before corrosion to create a uniform surface to analyse. Samples were ground using SiC paper to P1200. Final polishing was performed

on a Struers Rotopol-21 as a 2 step process, firstly with 2 μm diamond paste and a DP-Mol polishing pad then with 1μm diamond paste with a DP-Nap polishing pad.

6.1.2 Corrosion Initiation

Polished specimens of AA2024-T3 were immersed for times including 2.5, 5, 7.5, 10, 15, 30 and 120 minutes in 0.1M NaCl prepared from analytical grade chemicals at ambient temperature (21°C). After immersion the samples were removed, rinsed in deionised water and allowed to dry in laboratory air. The development of corrosion was monitored using SEM with EDX and PIXE. Both techniques revealed the IM particle distributions as well as attack sites as distinguished by Cl buildup.

6.1.3 Nuclear Microprobe Analysis

The specimens were analysed using the CSIRO Beamline at the University of Melbourne (see Section 3.1.6).

The spatial elemental maps from the characteristic X-ray signals were used to form a phase correlation map as a two dimensional histogram of the number of occurrences of the ratio of the yield of element A to the yield of element B, at each corresponding pixel of the elemental maps of A and B. The histogram is two dimensional because the number of occurrences is plotted as a function of the yield of A (on the horizontal axis) and the yield of B (on the vertical axis). The resulting two dimensional histogram, displayed as an intensity map, reveals high intensity peaks corresponding to different phases originally present in the spatial maps. Further details of this technique are described elsewhere [45].

6.1.4 SEM & EDX Analysis

SEM was performed on a FEI Quanta 400 field emission, ESEM under high vacuum conditions. The coated samples were mounted on standard 25 mm SEM stubs using electrically-conducting, double-sided, adhesive, carbon tape. SE and BE imaging were

performed using beam energies of 20 kV and probe currents of approximately 140 to 145 pA. EDX mapping was performed using a beam energy of 20 kV and a probe current of approximately 100 pA, resulting in count rates of approximately 10000 cps.

6.2 Results

6.2.1 Localised Corrosion

After 2.5 minutes immersion there was extensive localized corrosion evident on the surface of the AA2024-T3 (Figure 6-2(a) and (b)). Without exception this attack was confined to S-phase particles, which had begun the process of dealloying (Figure 6-2(b) and (d)). It is worth noting here that the presence of corrosion product makes it difficult to distinguish S-phase and θ-phase, hence both these particle types will be described as S-phase. There was no evidence of attack around any of the other IM particles. Cl was detected at all these sites using EDX, but was not detected elsewhere on the surface indicating that the initial sites of attack were the S-phase particles. At the shortest exposure time (2.5m) the corrosion product from the dealloying S-phase particles formed domes of Cl containing oxide above the S-phase particles (Figure 6-2 and Figure 6-3(a) and (b)). These domes are best seen in the BE images in Figure 6-2 and Figure 6-3. As the immersion time increased the nature of the product changed as can be seen in Figure 6-3. By 5 minutes immersion, the domes of oxide product had largely disappeared over many of the S-phase particles and by 15 minutes trenching had appeared around the particles. Additionally, no Cl was detected in the particles which had changed to the appearance in Figure 6-3(c) and (d). This change was accompanied by Cu-enrichment of the particles, presumably due to dealloying. These changes presumably accompany the switching of the S-phase from an anodic attack site to a cathodic site. Schneider et al. [24] suggested that the pH can reach as high as 9.5 over cathodic IM particles. If the remnant S-phase particles behave in the same manner, then this pH is likely to result in the dissolution of any hydrated Al oxide product that may form above the S-phase particle during anodic dissolution when the free Al ions migrate from the acidic

environment at the dissolution sites into the general solution above the remnants. The switching process probably expels the Cl due to the generation of a large amount of OH^- which will dissipate into the surrounding, taking the Cl with it. The localized attack around isolated IM particles, including the S-phase remnants, did not develop into any more extensive attack and so will not be discussed further here.

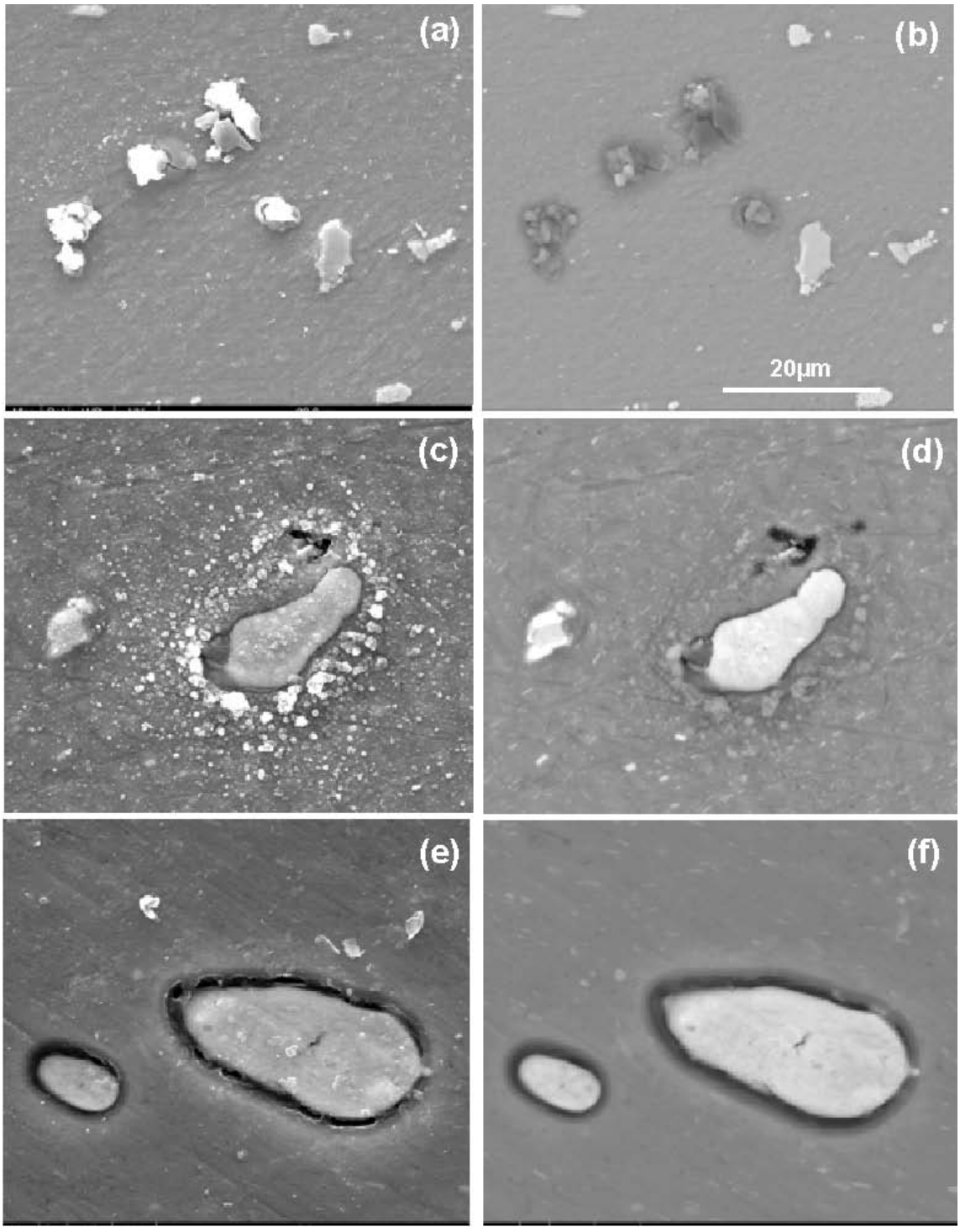

Figure 6-2: SEM micrograph of secondary ((a), (c) and (e)) and backscattered ((b), (d) and (f)) electron images selected S-phase particles after (a) and (b) 2.5, (c) and (d), 5 and (e) and (f) 15 minutes exposure to 0.1M NaCl at ambient conditions.

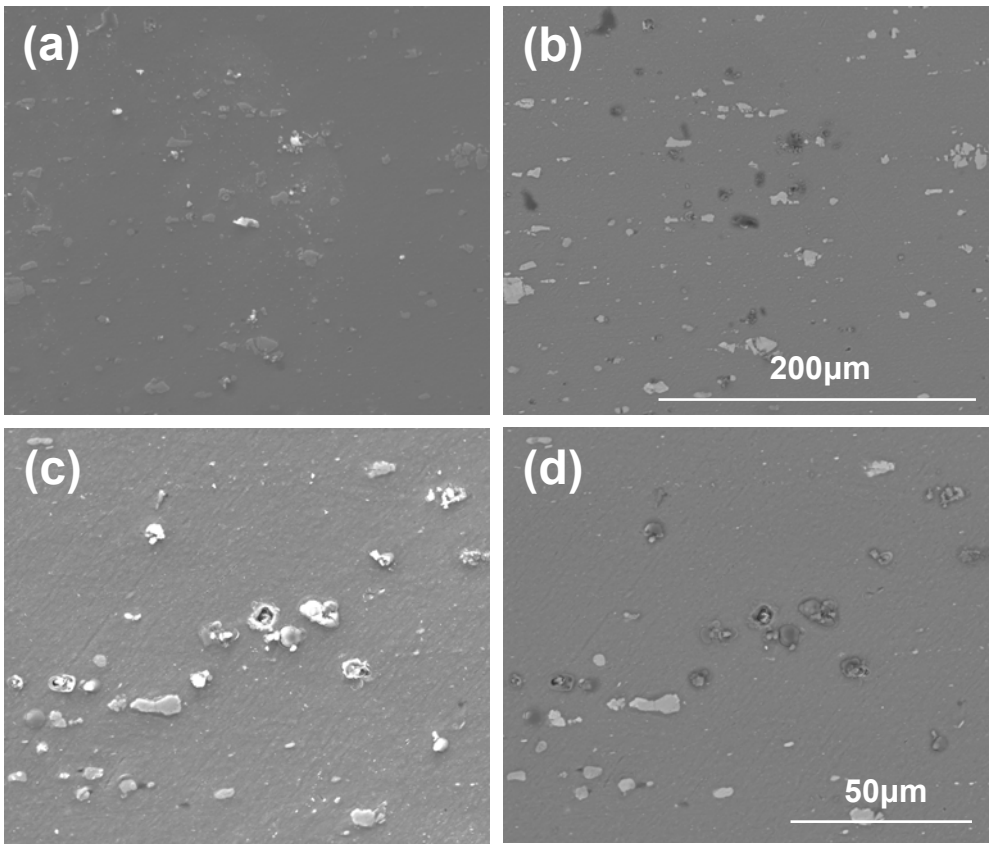

Figure 6-3: Secondary electron ((a) and (c)) and backscattered electron ((b) and (d)) electron images of two different regions of the surface of AA2024-T3 after 2.5 minutes exposure to 0.1M NaCl solution at ambient conditions.

The cathodic particles *i.e.*, those containing Al, Cu, Mn, Fe and Si showed a different progression of corrosion. The progress of corrosion related to the cathodic particles was tracked by examining individual IM particles. Some 80 particles were analysed based on whether Si was present or not. This process did not provide the detailed classification in Chapter 4 where particles containing these elements were divided into several groups. So for the purposes of following corrosion here, a simpler categorization is used following Gao *et al*. [15] who suggested compositions based upon $(Al,Cu)_x(Fe,Mn)_ySi$ such as modified forms of Al_8Fe_2Si or $Al_{10}Fe_2Si$ type IMs and for those without Si following Buchheit *et al*. [46] who defined a range of composition including Al_7CuFe_2, Al_6MnFe_2, $(Al,Cu)_6Mn$, and a number of undetermined compositions in the class $Al_6(Cu,Fe,Mn)$. In summary, the IM particles were divided into two broad groups.

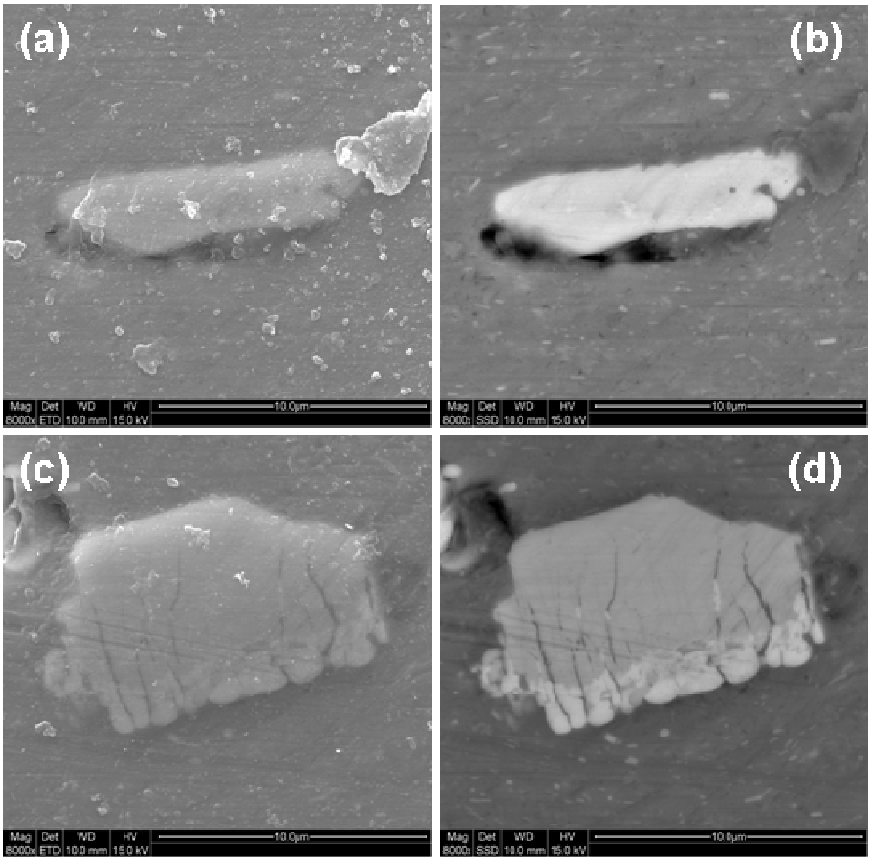

Figure 6-4: Secondary (left) and backscattered (right) electron images of IM particles after 15 minutes exposure to 0.1M NaCl. (a) and (b) Cu-Fe-Mn-Al IM particles and (c) and (d) Si-Cu-Fe-Mn-Al IM particles.

At the early stages of corrosion (described above), the S-phase particles show no evidence of trenching for either class of cathodic IM particle. After 15 minutes, there was evidence of etching starting around the Al-Cu-Fe-Mn type IM particles but those with Si showed no trenching as displayed in Figure 6-4. By 30 minutes immersion the trenching process appeared complete around the Al-Cu-Fe-Mn type IM particles which had progressed to full trenching (Figure 6-5). However, there was little evidence of trenching beginning around the Al-Cu-Fe-Mn-Si type IM particles (Figure 6-5).

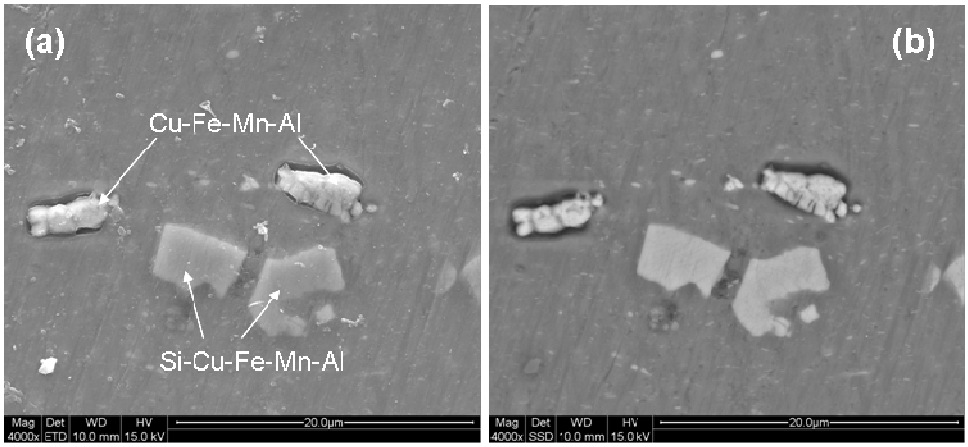

Figure 6-5: SEM micrographs of (a) Secondary and backscattered electron images of IM particles after 30 minutes exposure to 0.1M NaCl.

By 120 minutes exposure to 0.1M NaCl solution, both types of particles exhibited trenching around their peripheries as evident in Figure 6-6. Indeed there were no particles without some form of trenching around their peripheries.

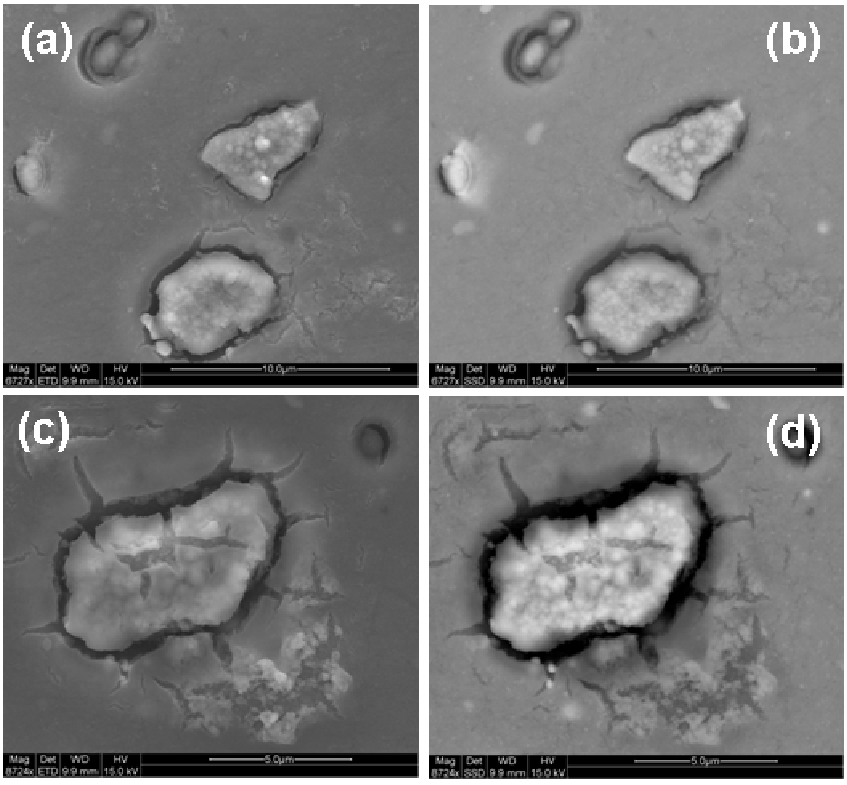

Figure 6-6: Secondary (left) and backscattered (right) electron images of IM particles after 120 minutes exposure to 0.1M NaCl. (a) and (b) Cu-Fe-Mn-Al IM particles and (c) and (d) Si-Cu-Fe-Mn-Al IM particles.

Figure 6-7 shows a summary of the differences in composition between the Si rich and the Si-poor IM particles after 30 and 120 minutes. After 30 minutes, the Si levels were around 4 at% in the Si-rich particles (left, labeled "Si") but only 0.6 at% in the particles which exhibited trenching. The Cu/Fe ratio in the Si-rich particles was low (2nd from left) compared to those with lower Si (far left). The Si levels appeared to change at 120 minutes, reflecting an overall change in surface composition possibly due to oxide development or the dissolution of Si. The Cu/Fe ratios remained fairly consistent for the two different immersion times.

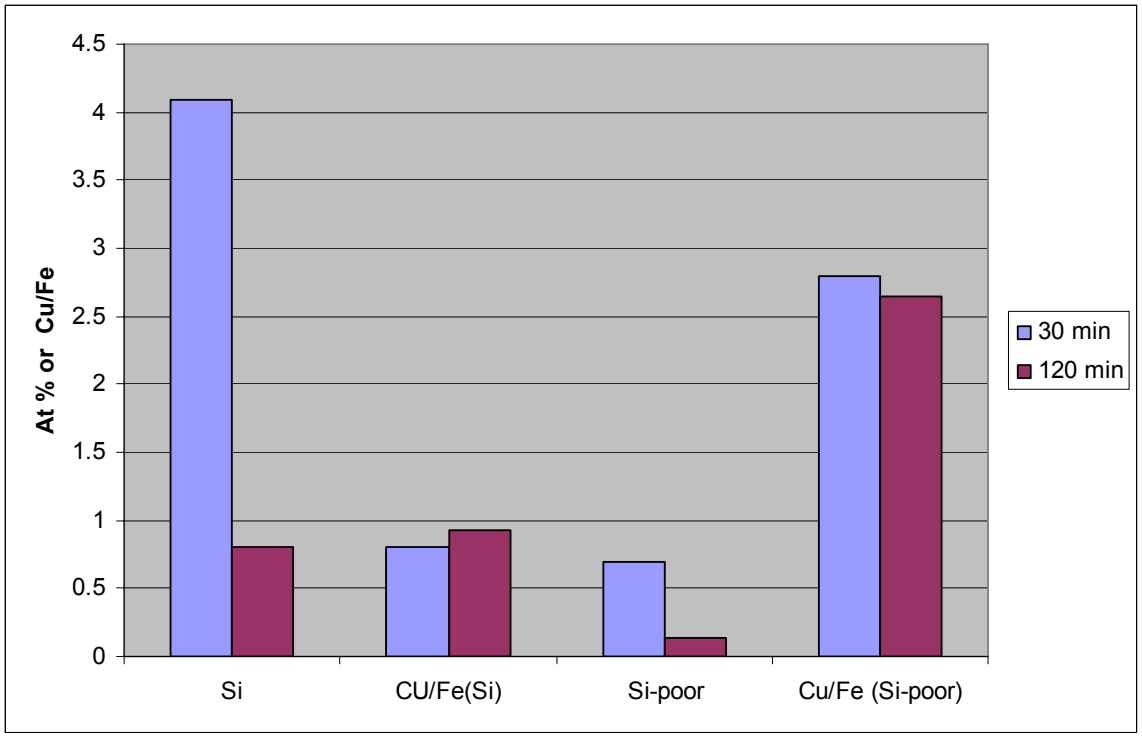

Figure 6-7: At% of Si in the "Si-rich" particles (left) and the Cu/Fe ratios for these particles (centre left) as well as the at% Si for the Si-poor particles (centre right) and the Cu/Fe ratio for these particles (far right).

The matrix had a continuous nodular oxide layer present on the surface (Figure 6-8(a)). This appearance did not change significantly for longer exposure times as seen in Figure 6-8, suggesting that is was largely unaffected by attack elsewhere on the surface.

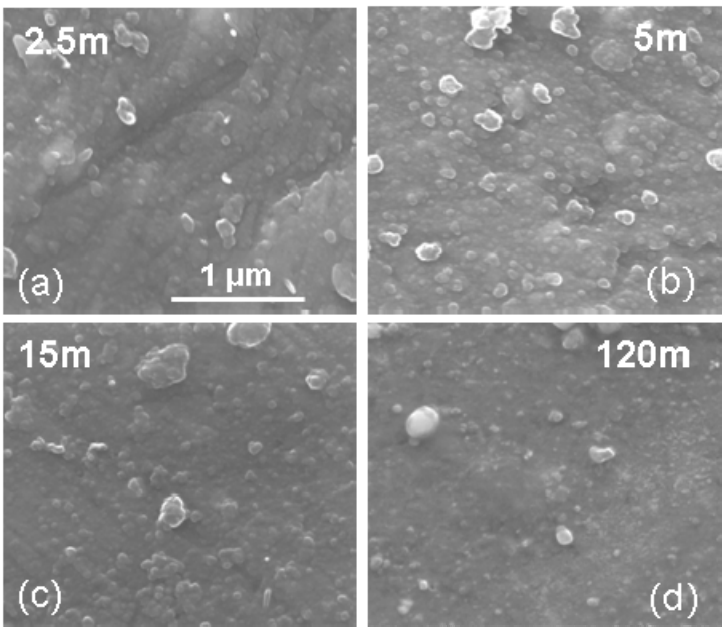

Figure 6-8: Oxide covering the matrix for different immersion times.

A third type of attack that was observed on the surface resulted in isolated rings of corrosion product as seen in Figure 6-9. The central features of this type of attack were IM particles such as dealloyed S-phase or CuFeMnAl-type IM particles. For both immersion times presented in Figure 6-9, the particle is a dealloyed S-phase particle. This data suggests that the features are associated with a very active cathodic process on the surface.

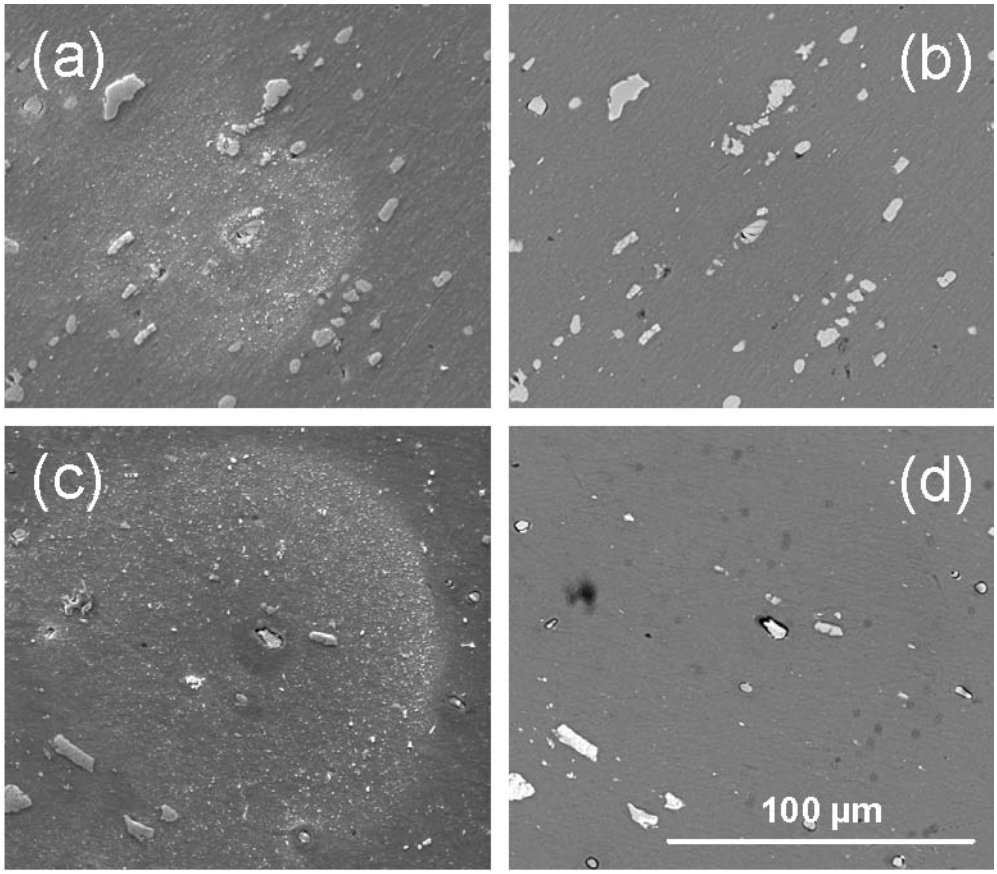

Figure 6-9: Secondary electron ((a) and (c)) and backscattered electron ((b) and (d)) electron images of circular corrosion product features on the surface of AA2024-T3 after (a) and (b) 7.5 and (c) and (d) 15 minutes exposure to 0.1M NaCl solution at ambient conditions

6.2.1.1 Localised Corrosion Summary

In summary, the localised corrosion around isolated IM particles in AA2024-T3 showed a succession of stages (hierarchy) which appeared to be related to the activity of the IM particles according to what is known about their electrochemical potentials [47], is depicted in Figure 6-6-10. Initially the S-phase particles corrode very quickly by dealloying and then trenching; this process is completed after 5 minutes. The later process resulted in a change of appearance possibly related to switching from anodic

dissolution to cathodic activity resulting in the apparent expulsion of the corrosion product formed during anodic dissolution. This may be related to a locally high pH associated with cathodic particles which is enough to dissolve the surface oxides [12,24].

For the cathodic particles, local trenching was observed in the Al-Cu-Fe-Mn type IM particles by 15 minutes. The appearance of trenching appears to follow the completion of S-phase dissolution and trenching. As this process moves towards completion, the Al-Cu-Fe-Mn type IM particles containing Si start to exhibit trenching and this process reaches completion by 120 minutes. These have been labelled as $(Al,Cu)_x(Fe,Mn)_ySi$ in Figure 6-6-10.

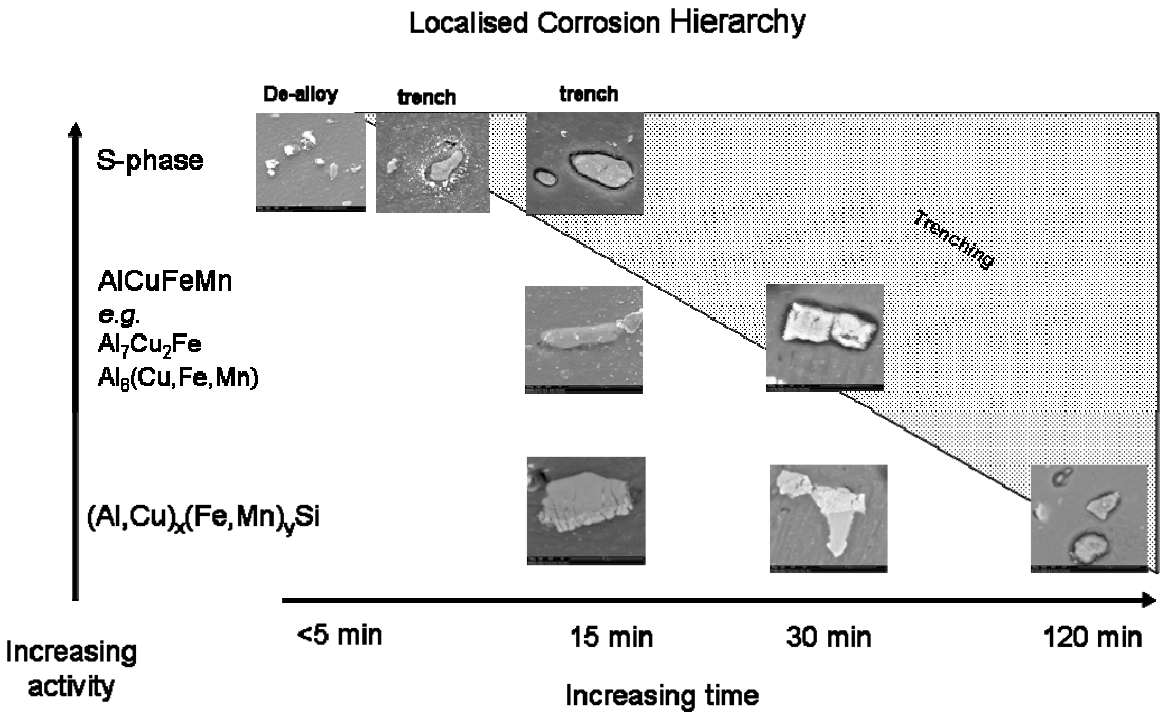

Figure 6-6-10: Hierarchy of localised corrosion attack.

Ilevbare et al [20] and Schneider et al [24] suggested that trenching and S-phase dissolution are the basis of metastable pitting events in AA2024-T3. However, Sasaki et

al. [37] suggested that while trenching may explain some of the metastable pitting processes, transient activation within established pits, interaction between pits and also transients in the corrosion current during pitting of AA2024-T3. The results presented here support Sasaki et al. [37], suggesting that early in the corrosion process, transient events such as trenching occur mostly in the first 30 minutes and at a lower levels up to 2 hours, but are largely completed by this time. Current transients observed after this time are more likely related to events in established pits.

6.2.2 Co-Operative Corrosion

6.2.2.1 General Observations

In addition to the localized corrosion around isolated IM particles in the surface such as S-phase and CuFeMnAl type IM particles discussed in the previous section, there is a second type of attack that appeared to result from a broader interaction of IM particles with either themselves, the wider matrix or both. This type of attack led to more severe corrosion events and is referred to in this section as co-operative corrosion. While clustering of IM particles may be responsible for some of these attacks, it was not clear if clustering was responsible for all these attacks, hence the term co-operative corrosion is used to avoid the implication that all attacks are related to clustering.

6.2.2.2 Co-Operative Corrosion

As alluded to above, there are features on the surface that develop into large sites of attack and consequently involve a larger number of particles than localized corrosion like trenching.

The first of these types of sites are large rings of corrosion products as depicted in Figure 6-11. These appeared to develop early in the corrosion process and were observed as early as 5 minutes after immersion where faints rings of corrosion product in the vicinity of 100 to 200 μm were observed. The size of these features did not appear to change much during the first 30 minutes of corrosion. However, the amount of corrosion product

comprising the external ring suggested that more corrosion product was deposited with increasing time.

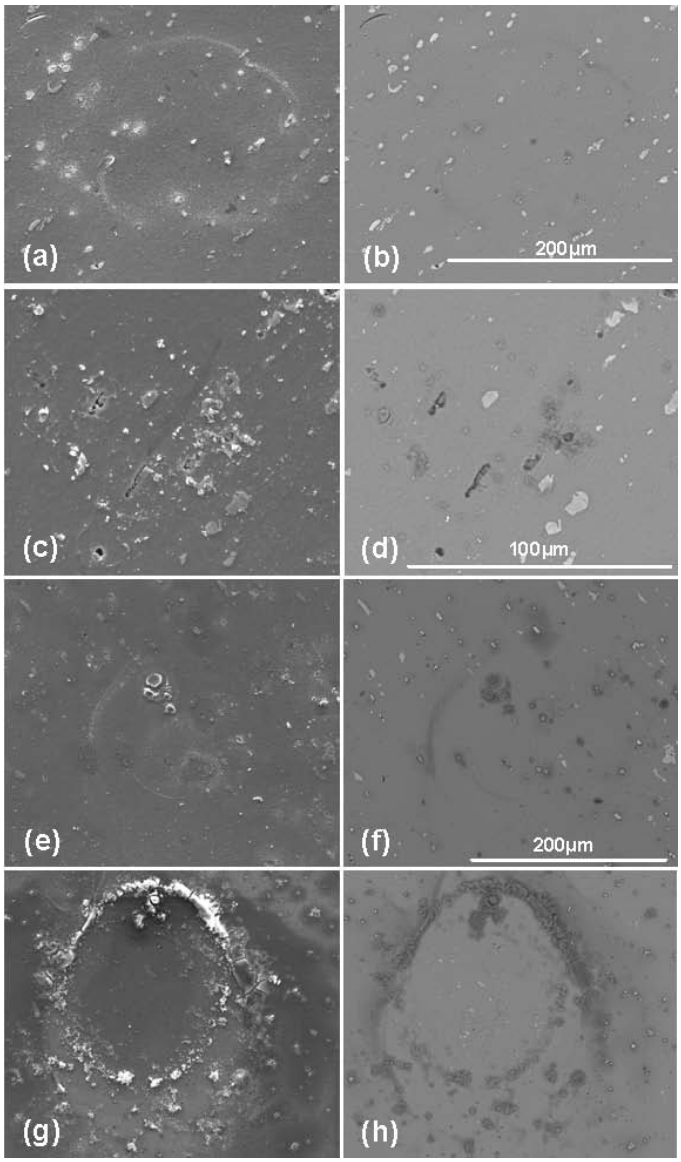

Figure 6-11: Secondary ((a), (c), (e) and (g)) and backscattered ((b), (d), (f) and (h)) electron images selected after (a) and (b) 5, (c) and (d), 7.5, (e) and (f) 30 and (g) and (h) 120 minutes exposure to 0.1M NaCl at ambient.

There were other features within the ring of corrosion product such as the small "halos" of corrosion product similar to those observed for the S-phase as reported in Figure 6-2(c) and (d). As can be seen in Figure 6-12, domes of corrosion product developed within the

corrosion product ring. These domes of corrosion product were almost exclusively the only sites that contained Cl ions. In SEM these domes appeared cracked but the remaining intact pieces shared an interlocking shape across crack interfaces, suggesting that they are formed by dehydration gels. At earlier stages in the corrosion process (Figure 6-12 (a) to (d)) these areas were identified (within the corrosion product ring) as dark areas in BE imaging. Their formation during the early stages of corrosion, such as Figure 6-12(a) to (d), suggests that they are associated with the presence of IM Particles. In the examples depicted in Figure 6-12, the particle where the dome formed is a dealloyed S-phase as it shows a very high Cu-rich signal. At the latter stages of corrosion, particles were not evident at these sites, but they may have been obscured by the large volume of corrosion product (Figure 6-12(e) to (h)).

The patterns in Figure 6-12(a) and (b) around the central developing dome of corrosion product, suggest a dynamic situation involving flow of solution since the precipitation patterns at the particles surrounding the central dome are asymmetric. The morphology of the corrosion domes with their smooth appearance is quite different to the particulate structure of the fine precipitates deposited elsewhere on the surface and in the rings of corrosion product. This is particularly evident in the latter stages of corrosion such as depicted in Figure 6-12(e) to (h). The difference in the nature of the precipitates also indicates a mixing of solution with different compositions and probably varying pH.

The CuFeMnAl IM particles appeared largely unattacked both inside and outside these regions apart from trenching observed around some particles. An overview of the distribution of elements within the corrosion rings is provided by taking the field surrounding the dome of corrosion product depicted in Figure 6-12(e), and generating a four color map from X-ray maps of the region as seen in Figure 6-13. The red represents oxide, pink is Cl and oxide, and green represents the particles that contain Cu and Fe. The particles that contain only Cu or Cu and Mg are represented by the red particles. Islands of corrosion product surround the S-phase or their remnants, whereas the IM particles that were initially cathodic appear largely unattacked. The ring of corrosion product is clearly visible as is the pink dome of corrosion product where there is a strong Cl signal.

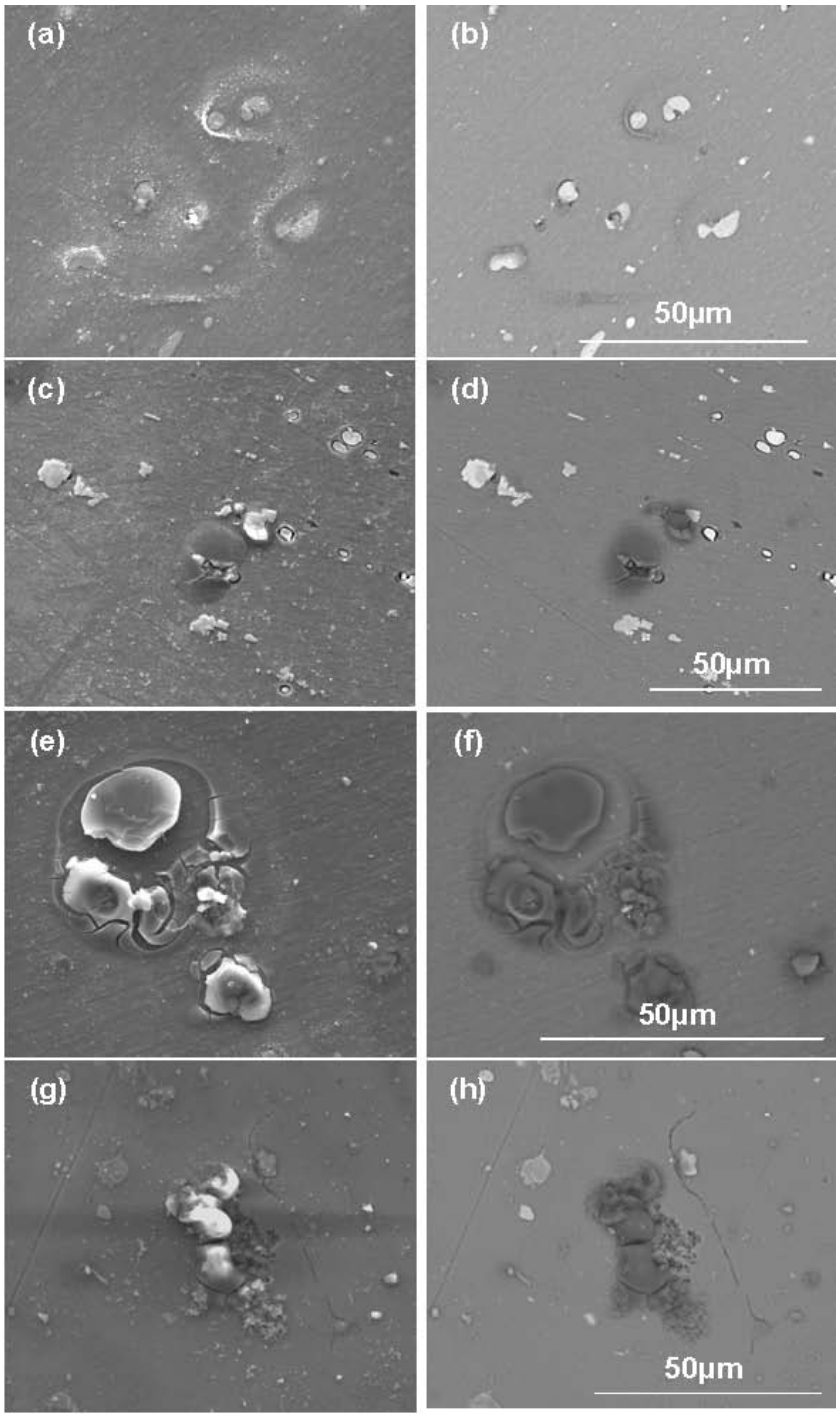

Figure 6-12: Secondary ((a), (c), (e) and (g)) and backscattered ((b), (d), (f) and (h)) electron images of domes of corrosion product (a) and (b) 7.5, (c) and (d), 15, (e) and (f) 30 and (g) and (h) 120 minutes exposure to 0.1M NaCl at ambient conditions.

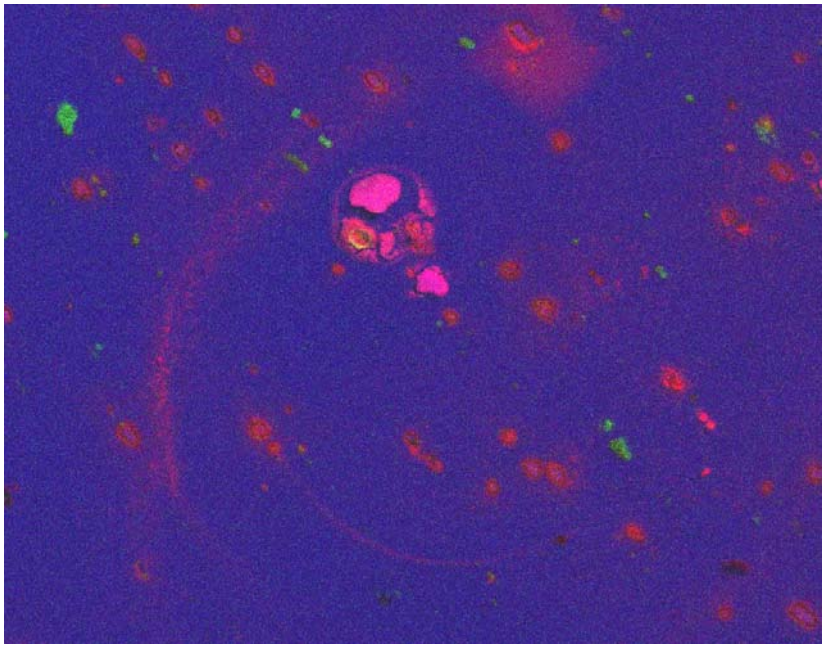

Figure 6-13: Colour map based on X-ray maps for the ring of corrosion product with dome depicted in Figure 6-12 (e) and (f). The red indicates oxide while pink indicates a mixture of oxide and chloride. Cu is present in all the particles with red and green represent particles with both Cu and Fe. Sample was exposed for 30 minutes.

After 120 minutes, grain boundary etching was observed within the rings of corrosion product as can be seen in Figure 6-14(g) and (h). Evidence of grain boundary attack, however, was present early during the immersion process. For the example in Figure 6-14(a) and (b), it was evident that grain boundary etching was developing from the S-phase particle at the left of the image after 15 minutes of immersion. This region was near a dome of oxide. In Figure 6-14(c) and (d) the two domes of oxide were connected by an etch feature similar to grain boundary etching, but with a crystallographic appearance at 30 minutes exposure and by 120 minutes there was extensive grain boundary etching within rings of corrosion product. In a separate study, Hughes et al [42] showed that the grain boundary etching observed here on the surface extended up to 60 μm into the surface. As an example, it can be seen in Figure 6-15 that for one sectioned ring, the attack penetrated up to 40 μm. There was little grain etchout, but dealloying of S-phase particles was evident. The subsurface attack within the rings of corrosion product

(particularly under the domes of oxide) constitute the severest sites of attack on and into the surface.

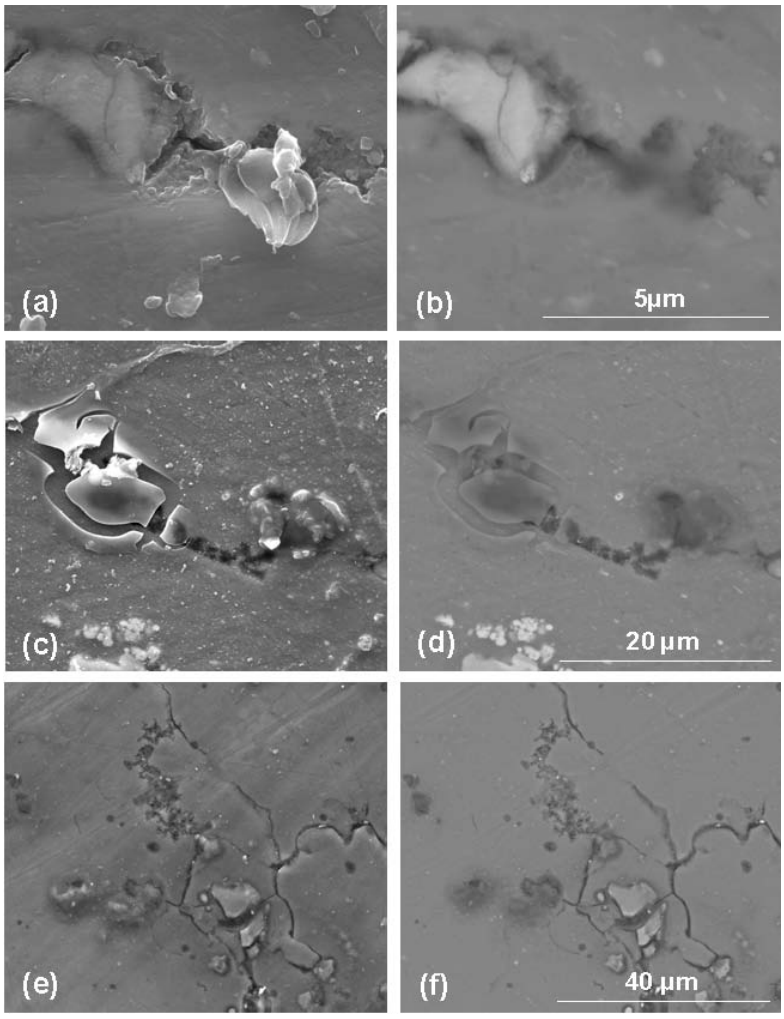

Figure 6-14: Secondary ((a), (c) and (e)) and backscattered ((b), (d) and (f)) electron images of grain boundary etching after (a) and (b) 15, (c) and (d), 30 and (e) and (f) 120 minutes exposure to 0.1M NaCl at ambient conditions.

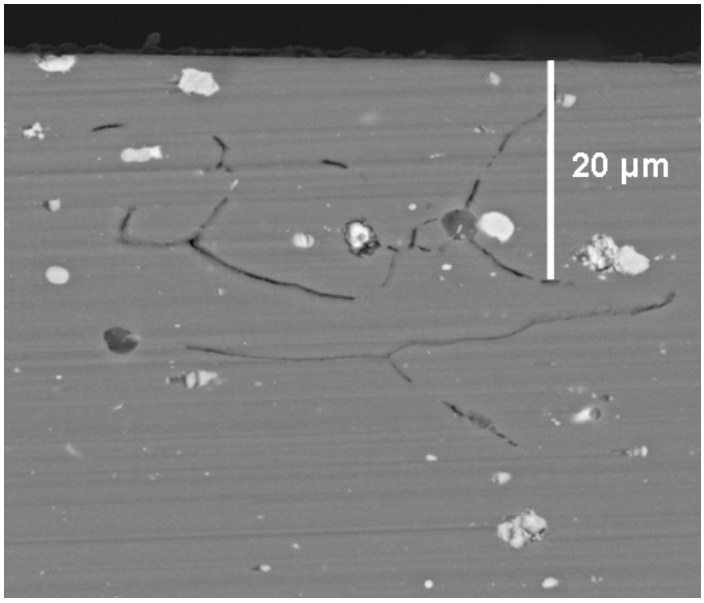

Figure 6-15: Subsurface attack observed by Hughes et al [42] within the ring of corrosion product. The sample was sectioned using dry diamond microtomy.

6.2.3 Nuclear Microprobe

The samples described above for immersion times up to 30 minutes were examined using the nuclear microprobe. X–ray maps were collected prior to and after exposure to 0.1M NaCl solution.

6.2.3.1 General Observations

Elemental images collected for corresponding regions of the virgin and corroded samples using PIXE are presented in Figure 6-17 - Figure 6-23. The maps for the virgin surfaces are presented at the top of each diagram and the corroded specimens in the bottom. For all the specimens there was corrosion at a number of sites, however, Cl was not observed at all these sites.

For all PIXE images, the relative concentration legend shown in Figure 6-16 applies.

Figure 6-16: Relative concentration legend for PIXE results

PCM was then used to identify regions where the Cl attack had occurred. From overlaying regions containing Cl onto the exposed images (light green areas) (Figure 6-17 - Figure 6-23) and comparing the virgin regions, it was possible to identify that in almost all cases where a localised concentration of Cl was found it had adjacent particles containing both S-phase and CuFeMnAl type IM particles.

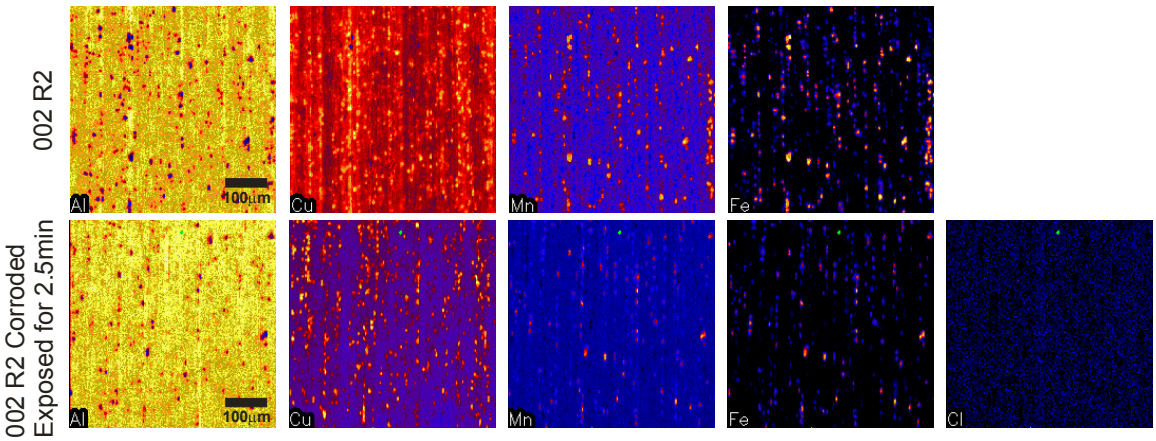

Figure 6-17: Sample 002 region 2, elemental maps of virgin and 2.5min exposed to NaCl solution

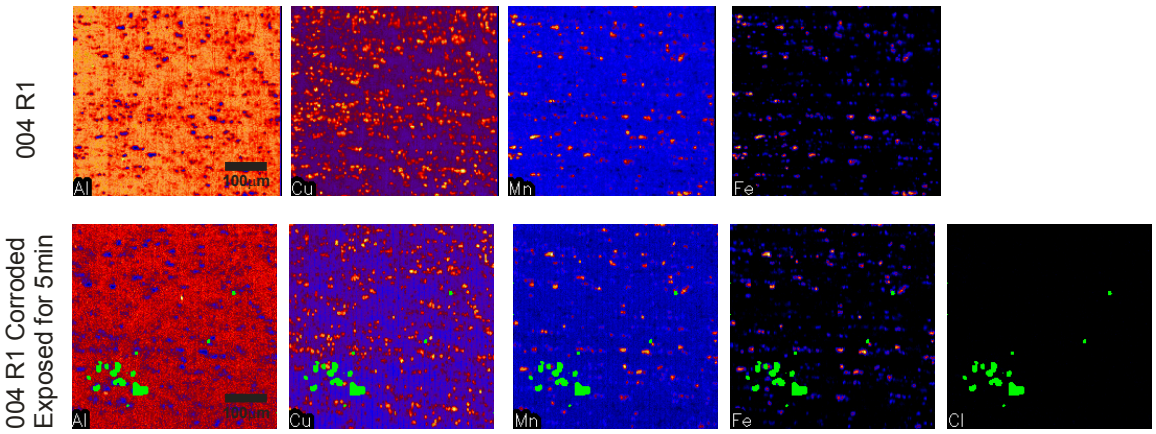

Figure 6-18: Sample 004 region 1, elemental maps of virgin and 5min exposed to NaCl solution

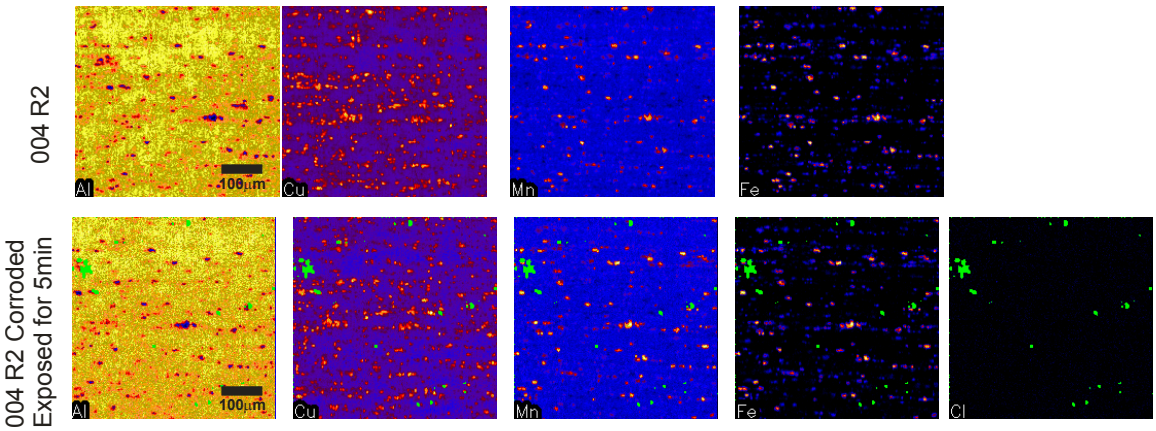

Figure 6-19: Sample 004 region 2, elemental maps of virgin and 5min exposed to NaCl solution

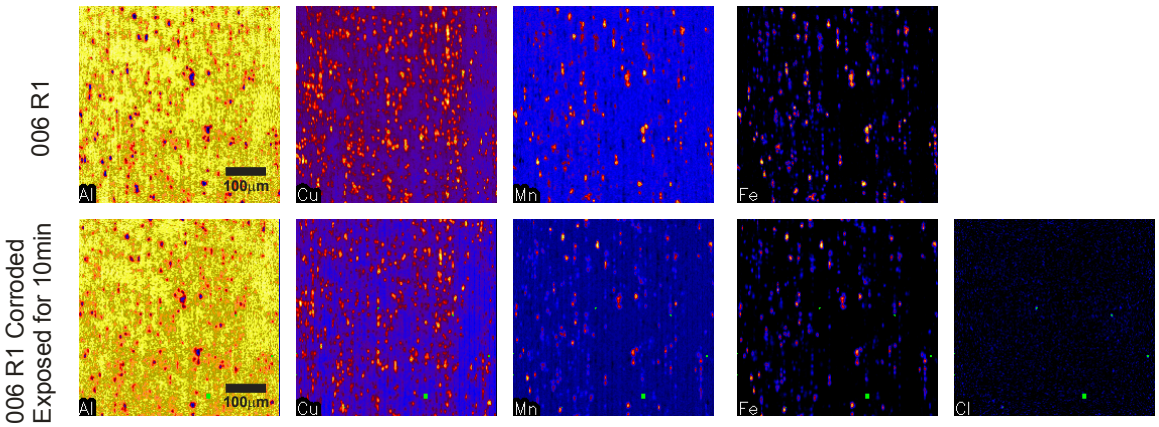

Figure 6-20: Sample 006 region 1, elemental maps of virgin and 10min exposed to NaCl solution

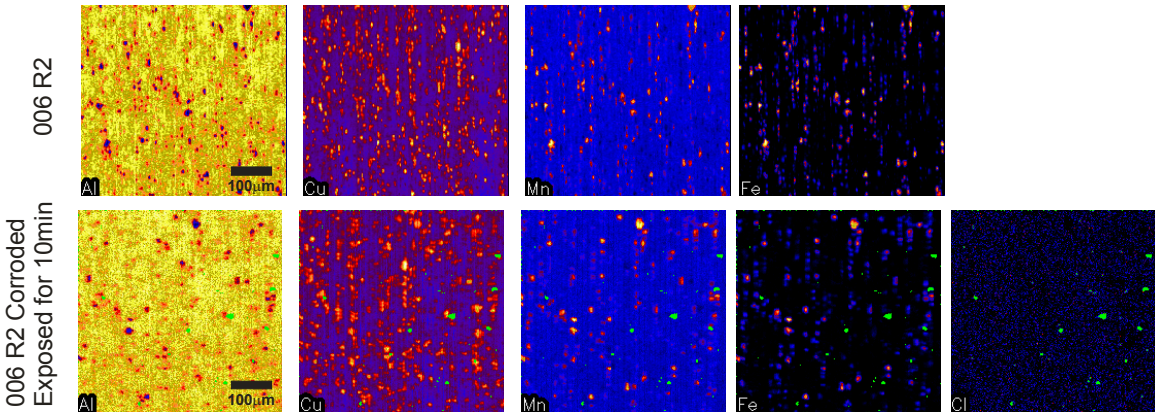

Figure 6-21: Sample 006 region 2, elemental maps of virgin and 10min exposed to NaCl solution

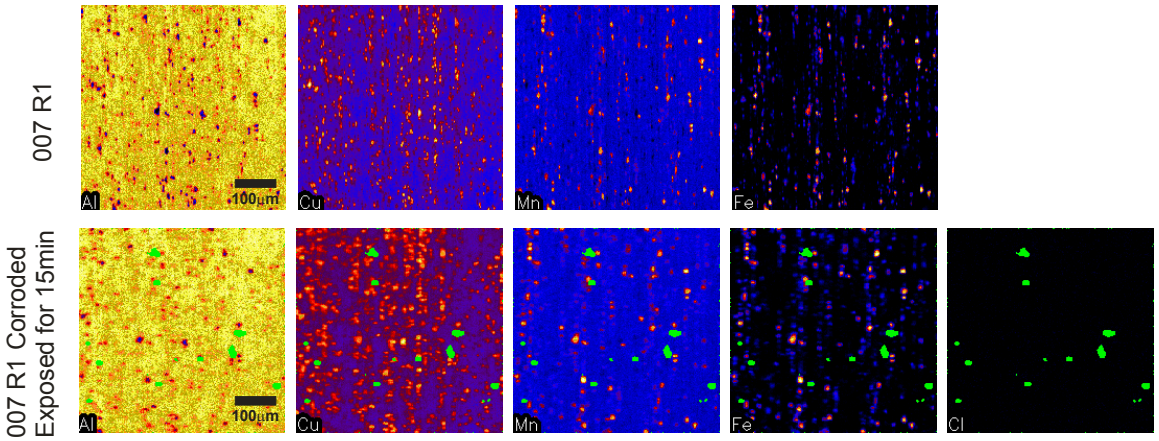

Figure 6-22: Sample 007 region 1, elemental maps of virgin and 15min exposed to NaCl solution

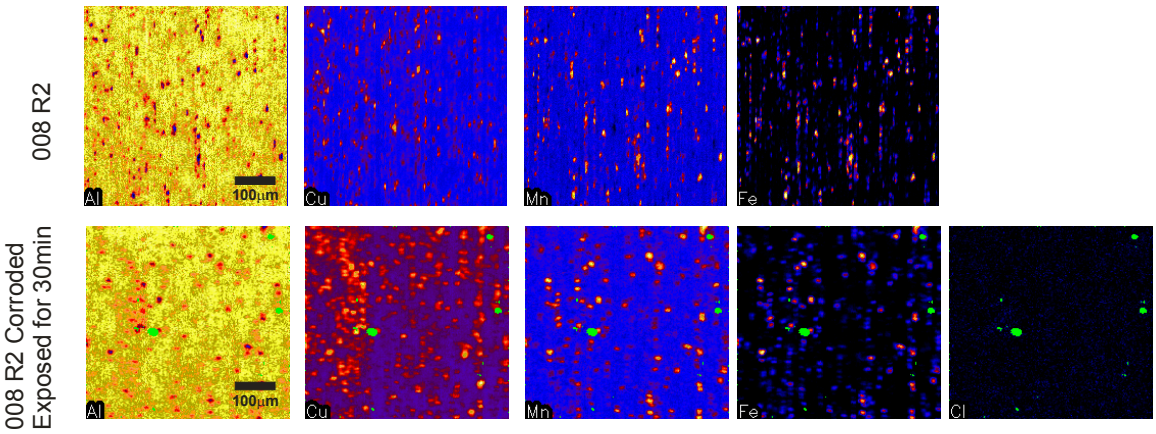

Figure 6-23: Sample 008 region 2, elemental maps of virgin and 30min exposed to NaCl solution

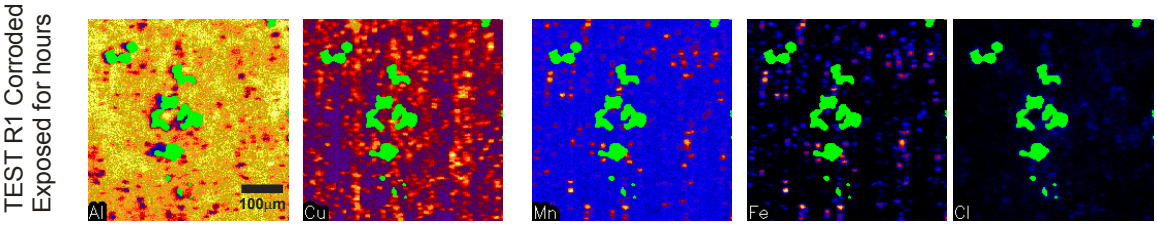

Figure 6-24: Test sample, elemental maps of surface exposed to NaCl solution for multiple hours

To summarise the data, four colour maps were created for each sample (Figure 6-26) by taking the original maps, converting them to greyscale, taking the negative and assigning a single colour to them. The colours are Cl-Red, Cu-blue, Fe-green and Mn-black. These maps were used to identify the Cl attack sites.

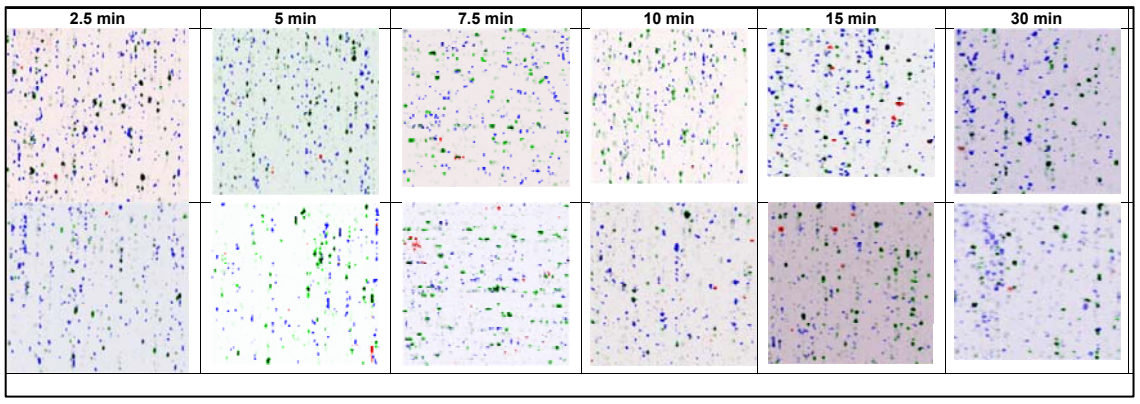

Figure 6-25: The colours are Cl-Red, Cu-blue, Fe-green and Mn-black. The times are given in the diagram. The top row is region 1 and the bottom region 2.

The particle density around the attack sites was then calculated by drawing a 50 µm radius circle around the site and manually counting all the particles within the circle and comparing them with the average particle density calculated for each map. An example of this procedure is shown in Figure 6-26 for the sample after 15 minutes exposure to 0.1M NaCl. The radius of 50 µm was chosen because the *g(r)* presented in Chapter 4 suggests clustering out to this radius. This procedure provides a visual procedure to verify particle counting and clustering.

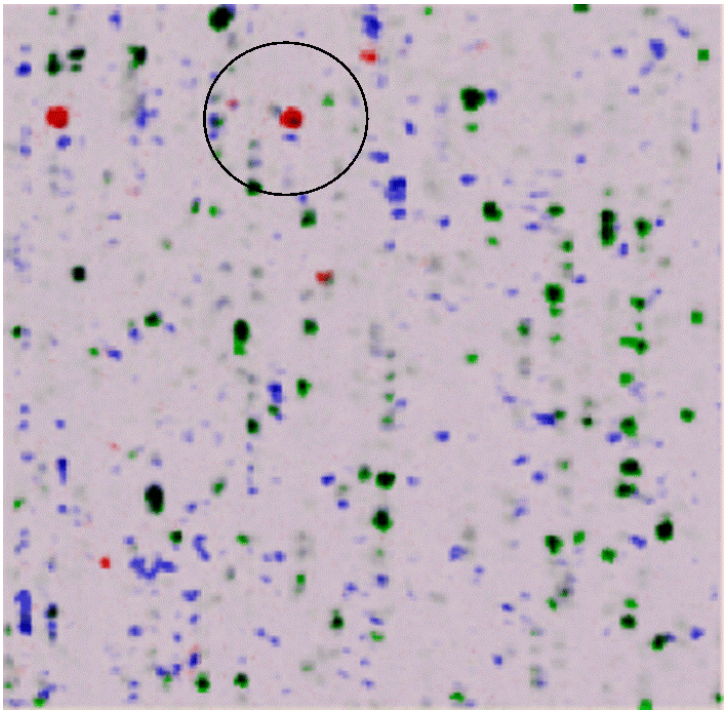

Figure 6-26: Four colour map for R2 of the 15 minute sample. The colours are Cl-Red, Cu-blue, Fe-green and Mn-Green. The black circle indicates a region of 50 µm radius in which particles were counted. All particles were counted.

The results of this procedure for forty chloride-attack sites are plotted in Figure 6-27. For most immersion times there were significantly larger numbers of particles in the attacked sites than the average for the map suggesting that clustering has a role to play at these sites.

Additionally, *g(r)* was calculated for the Cu-containing particles for each map prior to and after corrosion, as well as for the Mn containing particles representing the cathodic

particles. The small number of counts for these images compared to the image analysed in Chapter 4, resulted in noisy *g(r)* which nevertheless showed some clustering out to 50 µm. An example of both types of *g(r)* is shown in Figure 6-28. Figure 6-28(a) shows that there is clustering *i.e., g(r)* is > 1, at scales approaching 40 µm for the Cu-containing particles. Unlike Chapter 4 where individual phases were separated, here the Cu map will include AlCuFeMn particles as well.

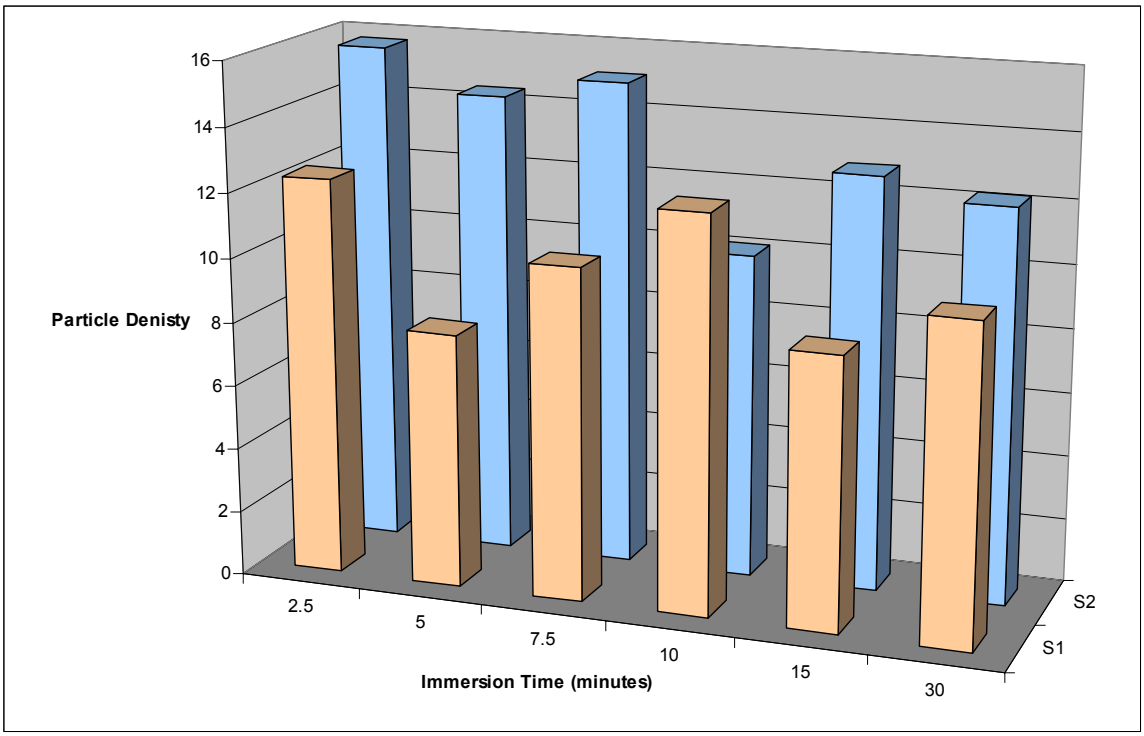

Figure 6-27: Nearest neighbour statistics for all maps averaged as a function of time. Yellow data is the average for the map while blue data is for an area of 50 µm radius around the chloride attacked sites.

Figure 6-28(b) is *g(r)* for the Mn-containing particles. The Mn containing particles represent the cathodic particles containing Al and any of a number of Fe or Si and, of course Cu. The Mn containing particles show evidence of clustering out to 40 µm as well as some suggestion of clustering between 50 and 100 µm. This second peak was only observed in two of the Mn *g(r)*. If this second peak represents real clustering for this region, then the reason it was only observed in two of the regions probably relates to

variability from region to region as noted in Chapter 4. The region size here is 500 μm so the statistical variation most closely matches that of the 8 x 8 (64 divisions) data in Chapter 4 where it was clear that there was significant variation from region to region, particularly with the cathodic particle types. Forty eight individual *g(r)* were calculated in all and are presented in Appendix C.

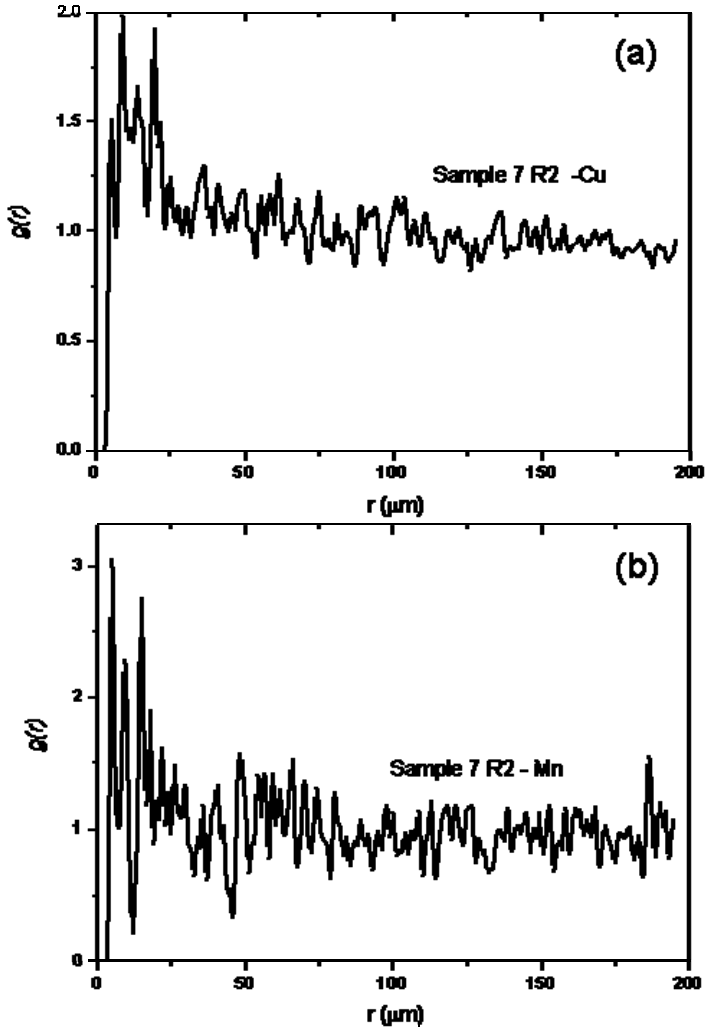

Figure 6-28: *g(r)* for (a) Cu-containing particles in Region 1 of the sample of AA2024-T3 which was eventually exposed to 0.1M NaCl for 15 minutes and (b) cross correlation with Mn containing particles representing cathodic IM particles in the surface.

Finally the effects of clustering were confirmed using *g(r)*. Where attack sites were observed in the PIXE maps through the red Cl colour (see for example the five sites labelled in Figure 6-6-29) then the particle nearest this site was identified and found to be on the surface. Figure 6-6-29 plots the clustering around the attack sites in the sample immersed for 15 minutes in green. The attack sites have neighbours numbering from 27 to 44, with an average of 34.4 which is consistent with the average of the clustered particles that had nearest neighbours between 1 and 50 μm, which was 33.1 ± 5.9. This is above the average number of nearest neighbours associated with clustering on this sample.

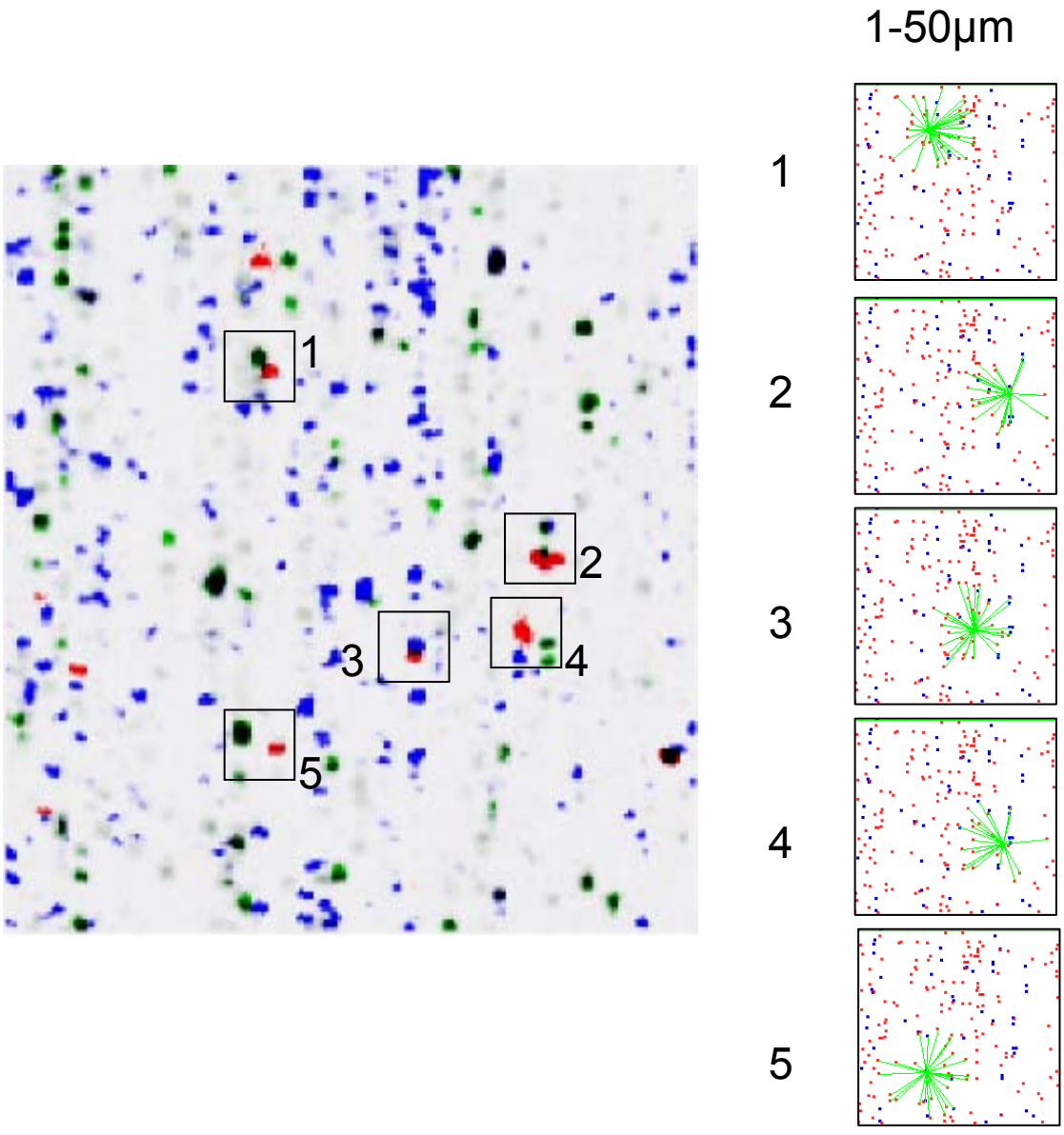

Figure 6-6-29: Left: four colour map identifying numbered (1-5) chloride attack sites and right show the spider diagrams for the clustering in green. Red is Cu-containing particle centroids and blue is the Mn-containing particle centroids.

As seen in previous sections, the nature of the attack site changes considerably from 2.5 minutes where there is localized attack of S-phase particles, to 30 and 120 minutes where co-operative attack appears to dominate. The above procedure for measuring the influence of clustering includes counts of both S-phase (here S-phase includes θ-phase) and the Al-Cu-Mn-Fe type IM particles. In Figure 6-6-30 the fraction of Al-Cu-Mn-Fe

type IM particles is plotted as a function of the total particle number. In the early stages of corrosion the fraction is roughly 40%, similar to the figure that Buchheit measured [46]. (For this part of the study S-phase includes θ-phase and are counted as S-phase and so the value of 40% is appropriate). However as time increased, the fraction of Al-Cu-Mn-Fe type IM particles decreased. We know from the section on localized corrosion that the S-phase particles have completely dealloyed by 5 minutes. This is an important observation, because the dealloyed S-phase remnants are cathodic compared to the matrix as are most of the Al-Cu-Mn-Fe type IM particles. Thus where clustering is involved with the attack sites at times of 15 minutes and greater, it suggests that these are dominated by clustering of cathodic particles.

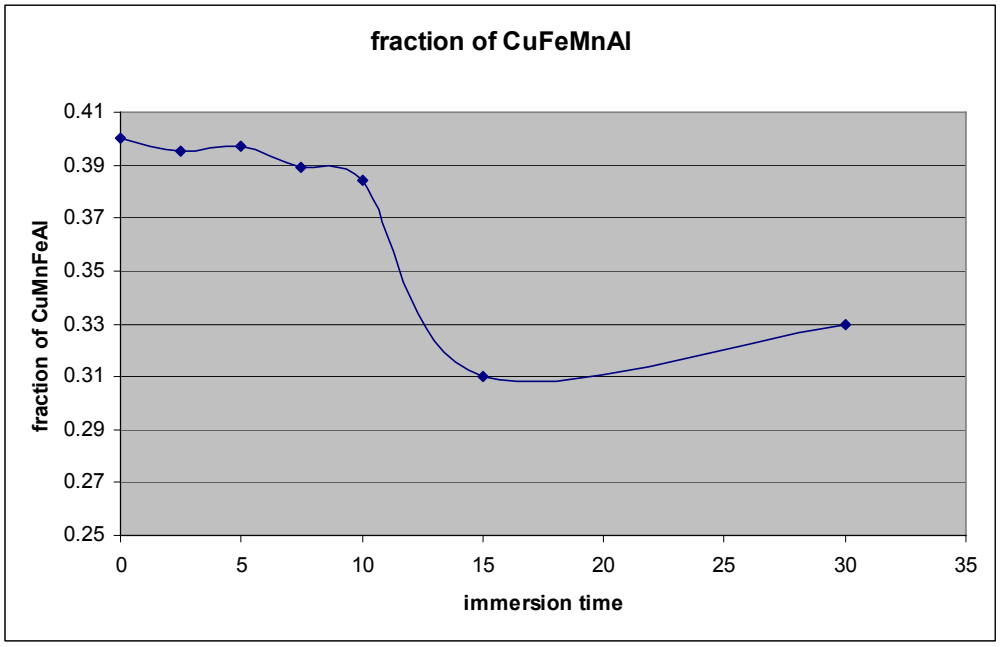

Figure 6-6-30: Ratio of Al-Cu-Mn-Fe type IM particles to the total number of particles, at attack sites where there is clustering.

In Chapter 5 it was shown that PCM could be used to identify whether Cu-enrichment was observed through lengthening of the tail towards the Cu rich end of the Cu axis. Figure 6-31 shows the Al-Cu PCM before and after corrosion. These PCMs do not show as clearly the distinction between the S-phase and other particles as observed in the PCMs in Chapter 5. The reason for this is that the system was optimised in Chapter 5 to

help distinguish the different types of particles and the analysis area was much smaller ~250 μm^2, whereas here the optimisation of the experimental setup was not possible for these experiments as a much larger area ~0.5 mm was investigated. However, tailing to higher Cu levels was still observed in Figure 6-31 and the two particles types could be identified by selecting different regions in this tailing. The important point to note here is that there is no significant difference between the two diagrams indicating that the changes that had occurred on the surface could not be detected using PCM at this early stage of corrosion.

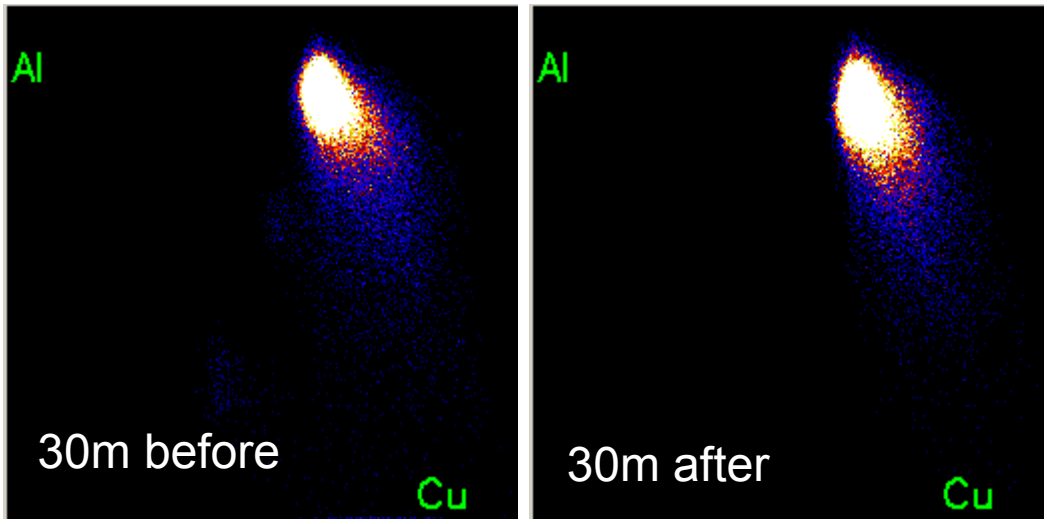

Figure 6-31:Al-Cu PCM for region 1 of the 30 minute sample.

While no changes were observed for the Al-Cu PCM for 30 minutes, changes were observed for the test sample (Figure 6-32). The Al-Cu PCM showed tailing towards lower Al content at a constant Cu content. These changes were different to that observed Chapter 5 for the reasons described above, however the region where this depletion was observed coincided with the generation of oxide corrosion product as observed through the Al-Cl PCM and showed an enrichment of Cu around the attack site.

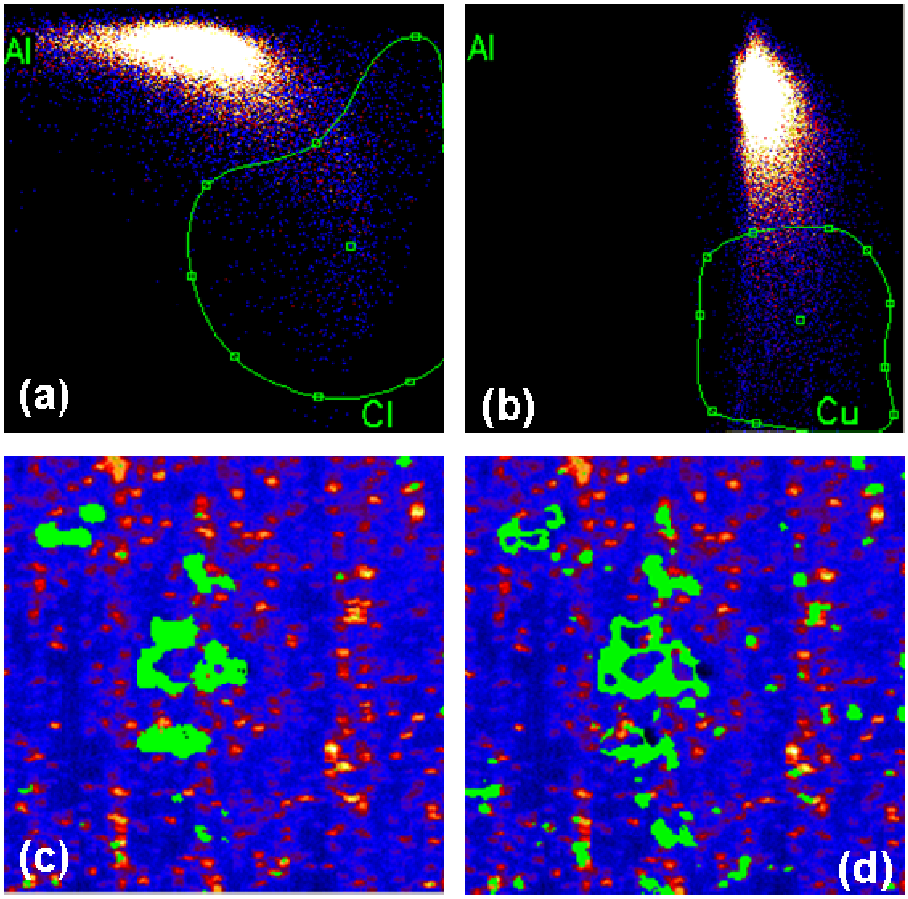

Figure 6-32: (a) Al-Cl PCM of test sample, (b) Al-Cu PCM of test sample, (c) positions of the selected ROI in (a) shown in green on the elemental map, (d) positions of the selected ROI in (b) shown in green on the elemental map.

6.2.3.2 Discussion

The thrust of this chapter was to identify different types of corrosion that occur on the surface with the aim of understanding the establishment of stable pits. The first part of the chapter looked at localised corrosion around different types of IM particles and it was established that there was a hierarchy of activities, all of which led to trenching around isolated particles. In the case of S-phase particles, dealloying precedes trenching. The process of trenching was largely complete after 120 minutes. It was also seen in Chapter 5 that Cu enrichment was eventually observed after 300 minutes exposure to 0.1M NaCl. All this data points towards a gradual enrichment of all the IM particles with Cu. The corrosion around the isolated particles examined in this part of the study did not appear to

develop beyond the trenching stage. While Cl was observed at the S-phase sites during anodic dissolution, it was not observed at these localised corrosion sites at latter stages.

In Chapter 5 it was shown that coupled particles appeared at sites of heavy attack where there was evidence of Cl and pitting. These sites were assumed to be stable pits since it took over 90 minutes for the current to stabilize and the pits were evolving H_2. The PIXE results in Chapter 5 and those shown here provided evidence that there are often Cu-rich particles, which are likely to be S-phase remnants, adjacent to CuFeMnAl particles. Additionally the clustering studies and *g(r)* work showed that corrosion events were associated with clustering of IM particles. Finally, the rings of corrosion product observed in this chapter point to a co-operative corrosion effect involving a number of particles.

In the following discussion two models are proposed to explain the observed results in Chapters 4 to 6. In the first model it is proposed that coupling between IM particles of opposite electrochemical activities may be used to explain the establishment of at least part of the population of stable pits on the surface of AA2024-T3. This model relies on the presence of clusters spread laterally on the surface which contain IM particles of opposite electrochemical activity for *initiation.* The more general application of this model to other alloys will depend on the nature of the IM particles and whether they support anodic and cathodic reactions at the OCP of the alloy matrix. Al-Cu-Li alloys are likely to display similar behaviours. In the second model it is proposed that clusters of particles of similar cathodic electrochemical nature may lead to a local alkaline environment which is confined by a gel-like layer over the cluster formed when the species, which are soluble in the alkaline environment, meet the more neutral pH of the general solution.

With respect to the first model that involves coupling of particles of opposite electrochemical activity, potentiodynamic scans of the IM model compounds have shown that some of these can support large current densities. For example, it is reported by Boag et al. [48] that S-phase particles can support anodic current densities up to 1mA/cm^2 and

Ilevbare et al. [20] have reported an anodic current density as high as 10 mA/cm^2. Unpublished work by Hughes and co-workers have shown that the cathodic, Cu - containing Al_6(Cu.Mn.Fe) IMCs support much lower current densities (Table 6-1) although they can provide cathodic current densities up to 10 mA/cm^2 in the presence of a good oxygen supply [49]. Previous work on S-phase particles in AA2024-T3 showed that, studied in isolation in an Al matrix, they undergo dealloying leaving either a Cu-rich residue with some Cu redispersion around the pit or etchout [24,25,36,40]. The reason why an S-phase IM particle progresses towards a dealloyed sponge or is completely removed is not clear, but may be due to local chemistry, pH, size, convection and mechanical action of the corrosion product or even the generation of H_2 from the pit. For the cathodic IM particle, trenching is commonly observed at the periphery of these particles and has been proposed to be due to the alkaline dissolution of the surrounding matrix as a result of oxygen reduction reactions [15,18,19,23,24,40]. In support of alkaline dissolution pH values as high as 9.5 have been measured around Al_3Fe in AA6061 [12]. Birbulis et al. [19] reported a high cathodic current density (in the vicinity of several hundred $\mu A/cm^2$) which would help to maintain the local alkaline environment. Alternatively, Guillaumin and Mankowski [16] and Schneider *et al.* [24] have suggested that trenching around cathodic IM particles is due to a Cu-depleted zone and anodic attack of this depleted zone. This model of trenching aligns better with some experimental results such as the measured depletion zones around both S-phase particles and CuFeMnAl particles [16]. In either case, where the particles are in isolation from other IM particles, then the "electrode" they draw on to match their reaction rate is the surrounding matrix. However, reaction rates for either anodic dissolution or cathodic reduction on the matrix are much lower [32,33] than on the IM particles so the current density on the IM particles will be rate limited by the available matrix area. The corrosion rate in depleted zones surrounding IM particles will be higher than the bulk alloy and its proximity makes it a likely target for anodic dissolution.

Intermetallic	OCP (0.1M NaCl) mV	i_{corr} at OCP of 2024 A/cm^2	i_{corr} at its own OCP A/cm^2
Al_2CuMg	-830	8×10^{-4} (a)	2.3×10^{-6}
Al_7Cu_2Fe	-640	2.7×10^{-4} (a)	4.8×10^{-7}
$Al_6(Fe,Mn)$	-609	9×10^{-5} (a)	3×10^{-7}
AA2024-T3	-508	2×10^{-6}	2×10^{-6}
Al_2Cu	-484	7×10^{-7} (c)	6×10^{-7}
Al_3Fe	-406	2.5×10^{-6} (c)	7×10^{-7}

Table 6-1: OCP's vs SCE and corrosion currents from various IM compositions reproduced from Boag et al [48].

As stated above, a number of papers have noted that stable pit formation is associated with the presence of clusters of IM particles on the surface [8,12,18,20,40,43,50,51]. Clustering is, in essence, three dimensional, however, the relationship of clustering to stable pit initiation and propagation can probably be divided into surface clustering for pit *initiation* and subsurface clustering for pit *propagation*. It is the intention here to only look at the initiation stage. The initiation of a stable pit as a result of clustering of IM particles might occur in one of two ways:

1. Coupling of active cathodic IM particles to the S-phase leads to rapid electrochemical dealloying of S-phase resulting in a deep enough pit for the diffusion path to be established that supports a concentration gradient from the base of the pit to the surface.
2. The initial anodic dissolution of the S-phase results in very active trenching around the cathodic IM particles leading to matrix etchout around cathodic IM particles and subsurface attack.

With respect to the first method of pit initiation, considerable work has been devoted to the examination of S-phase particles as the source of pit initiation. S-phase and its

surrounding Cu-depleted zone[1] are known to undergo active dissolution at the OCP of AA2024-T3 [16]. Ilevbare et al. [20] showed that much of this etchout however, occurred at very small pit stability products (*i.r* ratios) which are too small to effect the dissolution of the surrounding matrix once the S-phase had been removed (*i.r* in the vicinity of 10^{-3} A/cm).

To achieve the maximum current density for anodic dissolution of S-phase which might lead to electrochemical drillout and pit initation, the S-phase would need either a large available area of matrix to act as the cathode (since the current density for oxygen reduction on the matrix is of the order of 2 $\mu A/cm^2$ [32,33]) or a range of local cathodes that can support much higher current densities. The clustering results presented here indicate that a typical S-phase particle (say 2 to 5 μm) would need to draw on an area of the surface so large that other S-phase particles would be competing due simply to the particle density which was reported here in Chapter 4 as 320,000 and in other studies was reported as 300,000 [18] or 530,000 $/cm^2$ [51] respectively. In the latter study [51], the average particle area on polished AA2024-T3 was 6.66 μm^2 and would require 2640 μm^2 of matrix to fully support its anodic current density. Given, that there is one particle every 333 μm^2 at a particle density of 300,000 then at least eight S-phase particles will be competing for the cathodic area required to sustain the full anodic dissolution current for a single S-phase particle, even without clustering. Coupling of the S-phase to local cathodes, however, increases the available cathodic current. Observations in the literature do not, however, make a strong case for S-phase etchout sites being sites for initiation of stable pits. It is not clear why this is the case. Certainly, many S-phase particles are small and may not develop the critical *i.r* product since the activity of the S-phase particles varies considerably from one particle to the next [29]. The gradual conversion of the anodic S-phase particles to the cathodic Cu sponge may mean that the particles are also self neutralizing, *i.e.* for an active S-phase particle undergoing dealloying, the cathodic reaction in the Cu sponge generates enough OH^- to prevent acidification at the interface where the S-phase is undergoing dissolution, *i.e.*, galvanic corrosion requires a separation

[1] Buchheit notes that only a sub population of the S-phase might have Cu-depleted zone which depends on what stage the S-phase particle is formed during processing. S-phase formed pre-solutionising will not have a depletion zone.

of the electrodes. It has also been reported that during S-phase dissolution, small occluded volumes within the dissolving S-phase particle undergo dissolution-saturation-precipitation-dissolution reaction cycles which slow down the process of dealloying [25]. This process possibly interrupts the anodic part of the half reaction thereby making it difficult for the S-phase to maintain an *i.r* high enough to establish a stable pit.

On the other hand, if the trenching observed around the cathodic IM particles is due to the anodic etchout of depleted zones, replating of the Cu onto coupled CuFeMnAl particles by nearby S-phase particles in the process of dissolution, will result in a more efficient cathode, thus increasing the activity of the cathodic CuFeMnAl particles and drive the local anodic etchout of the adjacent depleted zones. Grain boundaries in AA2024-T3 are more susceptible to attack than the matrix [16] and the subsurface attack may occur down grain boundaries. So the establishment of a stable pit may require the conjunction of three things (i) coupling of S-phase with cathodic IM particles, (ii) replating of Cu and (iii) the presence of the IM particles at the intersection of the grain boundary with the surface.

In summary, the model proposed here is summarised in Figure 6-33. Part I of Figure 6-33 simply shows adjacent CuFeMnAl and S-phase IM particles. In reality several cathodic particles may be in the vicinity of the S-phase particle. As described in the diagram the cathodic current density on the matrix is a few orders of magnitude less than the anodic dissolution current of the S-phase and a large area would be required to match the S-phase current density. However, all the CuFeMnAl IM particles have a higher cathodic current density than the matrix and can support a more rapid dissolution of the S-phase particles. In part II of Figure 6-33 the S-phase particles have undergone dealloying creating (i) a Cu sponge, (ii) Cu particulates in oxide that develops on the S-phase and (iii) Cu ions dissolved in solution which are plated out cathodic IM particles. The creation of a more efficient cathode as well as the conversion of the S-phase to a cathode then results in local trenching that initiates the stable pit. It is suggested that the rate of localized attack on the matrix, particularly at depleted zones is accelerated due to the increased activity of the CuFeMnAl particle with replated Cu and the creation of Cu

sponges. The original composition of the IM particles may become less important as time proceeds and that all particles in the active clusters become Cu-enriched suggesting that clustering of cathodic IM particles may be the key for stable pit formation and the most active sites that can be created are when S-phase and cathodic particles are coupled. This means that the anodic dissolution of the S-phase is simply an avenue to Cu-enrichment within the local cluster and increased activity of the cluster. In Part III the alkaline environment around the CuFeMnAl particle leads to formation of corrosion product, which reduces O transport to the IM particle. Under these conditions, the dissolution of the Al matrix leads to acidification at the base of the trench, resulting in the formation of an acidic anolyte solution.

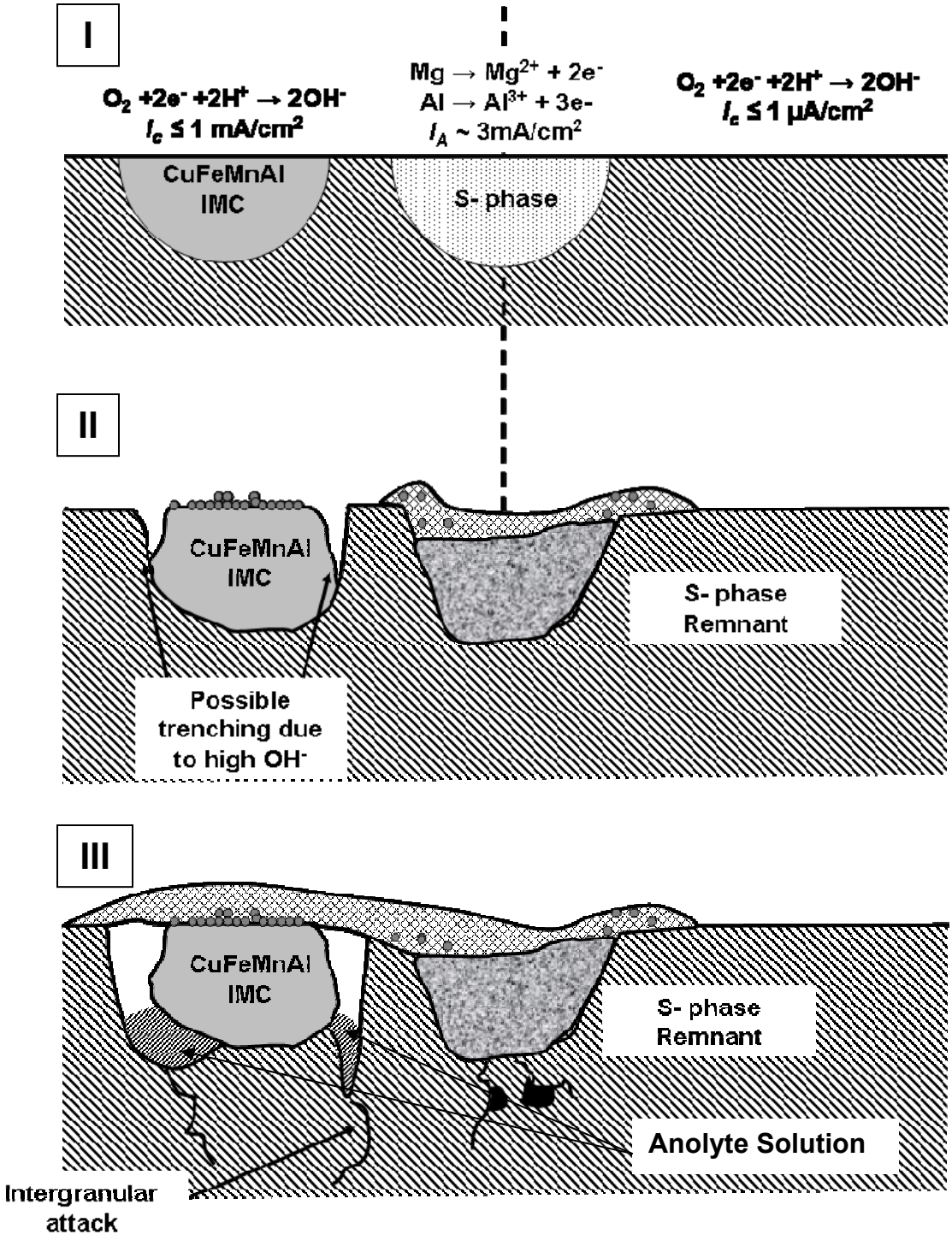

Figure 6-33:Model for coupling of IM particles leading to stable pit initiation. (I) the cathodic current density supported by cathodic IM particles is much greater than the matrix. In (II) this leads to rapid dealloying of the S-phase particle resulting in corrosion product growth incorporating nano particular Cu particles (grey circles) and more cathodic activity around the cathodic particle resulting in trenching. In (III) the coupling leads to intergranular attack which eventually results in stable pit formation.

The second model involves the generation of the rings of corrosion product in which the most severe attack was observed. These sites often contained domes of corrosion product indicating severe localised attack. These sites may well be explained by the model presented above as there is strong evidence that the domes are associated with IM particles. However, there is considerable grain boundary attack within the rings of corrosion product which is apparently not directly related to the domes of corrosion product. This type of attack was not observed outside the rings of corrosion product, suggesting that a different local environment exists within the rings.

One way a different environment could exist within the rings is through the formation of a gel layer over these sites. A gel layer would provide a diffusion barrier which would confine the reacts and products of the corrosion event at the site of activity. It is proposed that the pH of the solution within or under the gel layer is probably alkaline. The reason for this is that the only particles left in the surface are cathodes at the time of first appearance of the rings (15 minutes) and there is strong anodic activity under the domes of anodic corrosion product. As reported above, a pH as high as 9.5 has been predicted at cathodic sites [12]. This pH is high enough to produce the soluble aluminate ion. With an isolated particle the pH falls away to neutral rapidly with distance resulting in precipitation of corrosion product around the periphery of these particles. In the presence of clustering of the cathodic IM particles, particularly if they are enriched with deposited Cu, a large domain of high pH could be generated which only falls away to the bulk solution pH outside the cluster boundary. This boundary would extend into the solution away from the surface, perhaps to a greater height than the isolated particles, but its bigger impact would be its lateral extent over the surface which would be larger than the cluster size. In Chapter 4, clustering for some particle types was observed to extend out to a radius in the vicinity of 100 μm and in this chapter in some instances it was observed to 70 to 80 μm. These sizes are of similar magnitude to the rings of corrosion product which would be expected to be slightly bigger than the cluster size, providing strong evidence that clustering of cathodic IM particles may explain the corrosion rings.

Three stages for this second model are presented in Figure 6-34. The exact cause of the initiation of these sites is not clear, however, it is proposed that for part of the population of these sites, coupled IM particles cause initiation; this is indicated by the red arrow (Figure 6-34(a)). This couple is in a region of clustering where there are 12 neighbours making a total of 14 particles all together. Early in the corrosion process, perhaps as early as within the first 10 minutes of exposure to 0.1M NaCl, the S-phase have undergone dealloying and all particles have experienced trenching (Figure 6-34(b)). The diagram also suggests that Cu-enrichment has occurred but this was not observed until longer times. While the Cu enrichment is not critical to the model it will increase the overall activity of the surface. Cu-enrichment probably occurs earlier than observed in these studies because it would only take a very thin layer to increase the activity, but the detection of Cu-enrichment may only be possible once a thick layer is present. The earliest time that Cu-enrichment was observed was 120 minutes and it was already well established at this point, so Cu-enrichment begins prior to this time. Additionally a dome of corrosion product has developed over the central active site and there is evidence of subsurface grain boundary attack. Thus a strong anode develops at this site. In response to the strong anode there is increasing cathodic activity from the local cluster resulting in gel formation over the cluster. If the pH under the gel is high enough (>pH 9) then an alkaline solution will form within gelation at its boundary with the bulk solution. The alkaline solution then causes further attack on the alloy principally in the form of grain boundary attack.

It is probably worth mentioning that the corrosion product observed using SEM (and also observed with optical microscopy) forms a ring around an attack site, however the model suggest a gel layer over the site. It is assumed here that the gel layer is largely rinsed away after removal from the test solution, leaving only the periphery which is better bound to the substrate.

The other observation worth mentioning here is that when H_2 evolution was observed at these sites, corrosion product was often observed being carried towards the surface of the

solution. This clearly has to migrate through the gel layer and must cause disruption to the gel layer, but the extent of that disruption was not determined here.

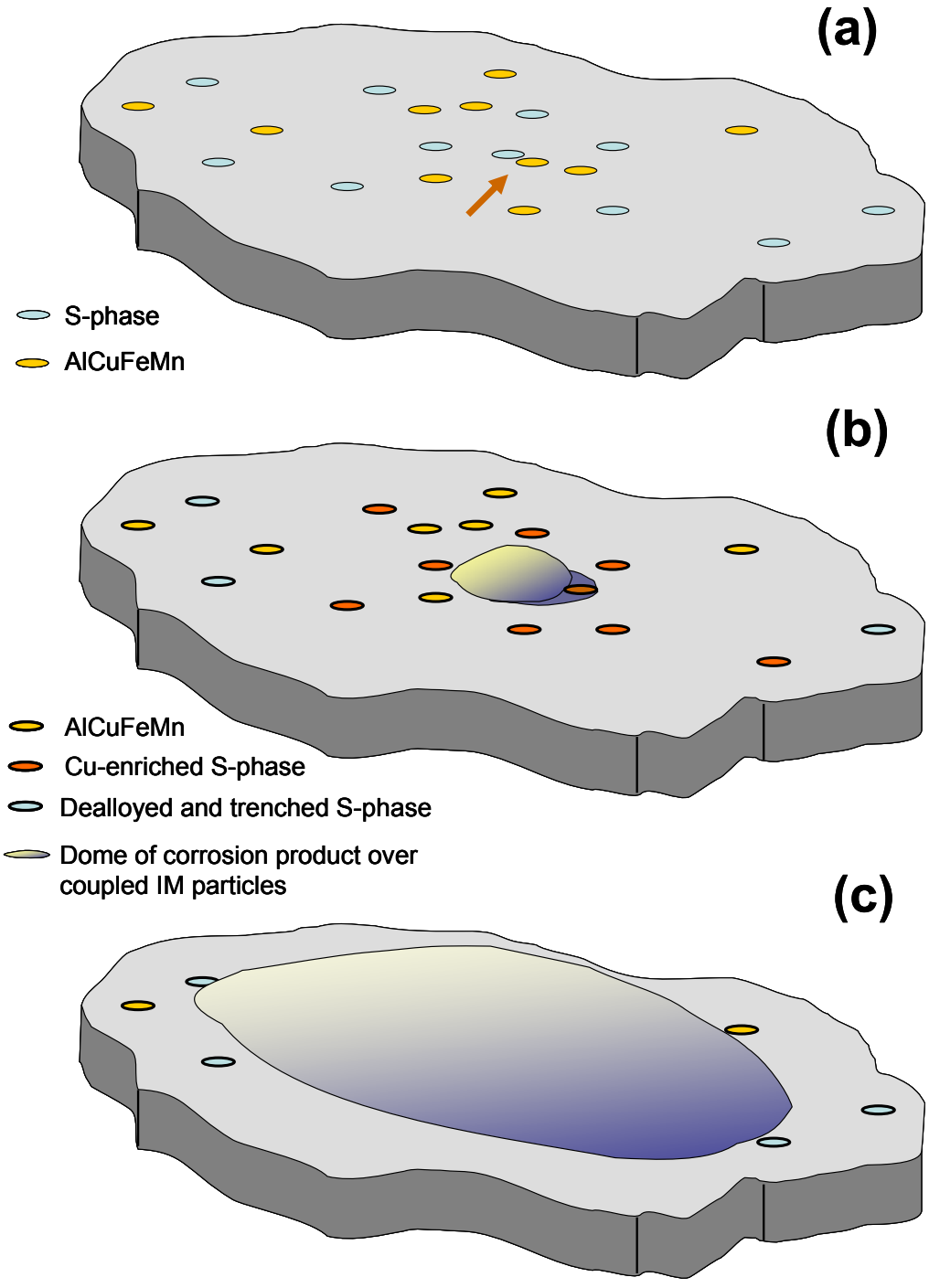

Figure 6-34: Model of co-operative corrosion.

6.3 Summary

Corrosion studies were performed on polished AA2024-T3 immersed in 0.1M NaCl for times ranging from 2.5 minutes up to 120 minutes. The corrosion observed on the surface was divided into two types of attack sites:

(i) localised corrosion – which involved isolated particles
(ii) co-operative corrosion – where clusters of particles contributed to the corrosion event.

Corrosion at the isolated particles involved both S-phase and AlCuFeMn(Si) IM particles. For the S-phase, the particles first underwent dealloying resulting in Cu-enriched remnants. The AlCuFeMn particles display trenching after the S-phase particles have dealloyed an trenched. Lastly the AlCuFeMn(Si) IM particles formed trenches around their periphery. All of these isolated particles played little further role in corrosion after trenching.

The co-operative corrosion events were characterised by domes of corrosion product within a ring of corrosion product. The central domes appeared to be anodicaly active sites since Cl was often observed there, and at least some of them were initiated by the coupling between S-phase and cathodic IM particles within the surface. It was demonstrated that clustering was involved in the establishment of these types of sites and it was proposed that clustering of cathodic particles results in an alkaline environment around the anodically active site that form a gel at its periphery (both in the solution and laterally on the surface). These sites were where the most subsurface attack occurred.

6.4 Bibliography

1 M. Janik-Czachor, G. C. Wood, and G. E. Thompson, Br. Corr. J. **15,** 154, (1980).
2 G. S. Frankel, "Pitting Corrosion of Metals; A summary of critical factors," (2000).
3 Z. Szklarska-Smialowska, Corr. Sci. **41,** 1743-1767, (1999).
4 E. McCafferty, Corr. Sci. **45,** 1421, (2003).
5 R. T. Foley, Corr. Sci. **37,** 481, (1995).

[6] K. Shimazu, K. Kobayashi, P. Skeldon, G. E. Thompson, and G. C. Wood, Corr. Sci. **39,** 701-708, (1997).
[7] N. Sato, Electrochimica Acta **16,** 1683 - 1692, (1971).
[8] T. H. Muster, A. E. Hughes, and G. E. Thompson, *Copper Distributions in Al-Alloys in Corrosion research Trends,* Nova Publishers, (2007).
[9] J. E. Hatch, *Aluminium: Properties and Physical Metalurgy*, Metals Park, OH, (1984).
[10] R. M. Ryders, C. H. Paik, R. Ke, and R. C. Alkire, J. Electrochem. Soc. **141,** 1439, (1994).
[11] K. Nisancioglu, J. Electrochem Soc. **137,** 69, (1990).
[12] J. O. Park, C. H. Paik, Y. H. Huang, and R. C. Alkire, J. Electrochem Soc. **146,** 517, (1999).
[13] J. O. Park, C. H. Paik, and R. C. Alkire, *Critical Factors in Localised Corrosion II*,The Electrochem Soc., (1996).
[14] R. G. Buchheit, J. P. Moran, and G. E. Stoner, Corr. Sci. **46,** 610, (1990).
[15] A. Kolics, A. S. Besing, and A. Wieckowski, J. Electrochem. Soc. **148,** B322, (2001).
[16] V. Guillaumin and G. Mankowski, Corr. Sci.**,** 421, (1999).
[17] N. Dimitrov, J. A. Mann, and K. Sieradzki, J. Electrochem Soc. **146,** 98, (1999).
[18] G. S. Chen, M. Gao, and R. P. Wei, Corrosion **52,** 8, (1996).
[19] N. Birbilis, M. K. Cavanaugh, and R. G. Buchheit, Corr. Sci. **48,** 4202, (2006).
[20] G. O. Ilevabare, O. Schneider, R. G. Kelly, and J. R. Scully, J. Electrochem. Soc. **151,** B453, (2004).
[21] M. Metzger, J. Zahavi, N. D. Tomashov, and E. N. Mirolubov, Corrosion of Metals and Alloys**,** 48, (1966).
[22] C. M. Liao, J. M. Olive, M. Gao, and R. P. Wei, Corrosion **54,** 451-458, (1998).
[23] K. Kowal, J. Deluccia, J. Y. Josefowicz, C. Laird, and G. C. Farrington, J. ElectroChem. Soc. **143,** 2471, (1996).
[24] O. Schneider, G. O. Llevbare, J. R. Scully, and R. G. Kelly, J. Electrochem. Soc. **151,** B465, (2004).
[25] N. Dimitrov, J. A. Mann, M. Vukmirovic, and K. Sieradzki, J. Electrochem. Soc. **147,** 3283 - 3285, (2000).
[26] A. Conde and J. De Damborenea, Corr. Sci. **39,** 295 - 303, (1997).
[27] L. Lacroix, L. Ressier, C. Blanc, and G. Mankowski, J. Electrochem. Soc. **155,** C8-C15, (2008).
[28] A. Davoodi, J. Pan, C. Leygraf, and S. Norgren, J. Electrochem Soc. **155,** C138 - C146, (2008).
[29] L. Lacrroix, L. Ressier, C. Blanc, and G. Mankowski, J. Electrochem Soc. **155,** C131-C137, (2008).
[30] A. Davoodi, J. Pan, C. Leygraf, and S. Norgren, J. Electrochem Soc. **155,** C211 - C218, (2008).
[31] S. T. Pride, J. R. Scull, and J. L. Hudson, J. Electrochem. Soc. **141,** 3028, (1994).
[32] A. R. Trueman, Corr. Sci. **47,** 2240 - 2256, (2005).
[33] A. E. Hughes, A. R. Trueman, S. A. Furman, and R. J. Taylor, To be submited to Corr. Sci.
[34] J. Wloka and S. Virtanen, Surf. Int. Anal. **40,** 1219 - 1225, (2008).

[35] G. T. Burstein, P. C. Pistorius, and S. P. Mattin, Corr. Sci. **35,** 57, (1993).
[36] P. C. Pistorius and G. T. Burstein, Corr. Sci. **36,** 525, (1994).
[37] K. Sasaki, P. W. Levy, and H. S. Isaacs, Electrochem.& Sol. State Letts. **5,** B25 - B27, (2002).
[38] A. E. Hughes, B. R. W. Hinton, S. A. Furman, I. S. Cole, D. Paterson, A. Stonham, G. McAdam, D. Dixon, S. J. Harris, A. Tureman, M. Hebbron, C. Bowden, P. C. Morgan, and M. Ranson, Corr. Revs **20,** 275, (2007).
[39] A. E. Hughes and S. A. Furman, ATB Metallurgie **45,** 340 - 346, (2006).
[40] C. M. Liou, J. M. Olive, M. Gao, and R. P. Wei, Corr. Rev. **54,** 451, (1998).
[41] D. G. Harlow, M. Z. Wang, and R. P. Wei, Metall. Mat. Trans A **37A,** 3367 - 3373 (2006).
[42] T. H. Muster, M. A. Glenn, and A. E. Hughes, Corr. Sci.
[43] L. Juffs, Investigation of Conversion Coating Deposition on Microscopic and Macroscopic Intermetallic Phases of Aluminium Alloy, RMIT University, (2002).
[44] D. N. Jamieson, P. Spizzirri, R. Szymanski, B. Rout, A. Sakellariou, W. Belcher, and R. G. Ryan Nucl. Inst. Micr:. B **190,** 54 - 59, (2002).
[45] B. Rout, D. N. Jamieson, T. Hopf, and C. G. Ryan, Nuclear Instruments & Methods in Physics Research Section B-Beam Interactions with Materials and Atoms **210,** 129-134, (2003).
[46] R. G. Buchheit, R. P. Grant, P. F. Hlava, B. McKenzie, and G. L. Zender, J. Electrochem Soc. **144,** 2621, (1997).
[47] R. G. Bucheit, J Electrochem soc, **12**, 3994-3996, (1995)
[48] A. Boag, R. J. Taylor, T. H. Muster, N. Goodman, D. McCulloch, C. Ryan, A. E. Hughes, B. Rout, and D. Jamieson, Submitted to Corr. Sci.
[49] Y. L. Cheng, Z. Zhang, F. H. Cao, J. F. Li, J. Q. Zhang, J. M. Wang, and C. N. Cao, Corr. Sci. **46,** 1649, (2004).
[50] M. A. Jakab, D. A. Little, and J. R. Scully, J. Electrochem. Soc. **152,** 311-320, (2005).
[51] A. E. Hughes, A. P. Boag, L. M. Pedrina, L. Juffs, D. G. McCulloch, J. P. Du Plessis, P.J.K., I. K. Snook, and B. O'Malley, ATB Metallurige, 551-556, (2006).

Chapter 7 - Surface Pre-Treatment

7.0 Introduction

The work of the previous chapters examined, in detail, the corrosion processes on AA2024-T3. However, AA2024-T3 is very rarely used in the polished state, for real world applications it is generally finished by mechanical processing such as milling and/or processed chemically by anodising or conversion coating before it is finally painted. This is not to say, that what has been learnt from the previous chapters is of no importance in the finishing of AA2024-T3 for real world applications. Specifically the chemical composition of the IM particles is relevant to the chemical pre-treatment as described below and the distribution of particles is relevant because the clustering of IM particles will result in clustered etchout sites when chemical pre-treatment only removes IM particles.

This chapter therefore presents a preliminary investigation into the influence of surface pre-treatments used to both aid in corrosion protection on metals. In particular, it focuses on deoxidisers used as part of chemical pre-treamtent prior to conversion coating through the investigation of a non chromate based deoxidiser, which can be used to replace existing less environmentally friendly deoxidisers.

This work was completed and published [1] as a study of the deoxidation itself, so these results will be presented, but, in addition, the knowledge obtained in previous chapters will also be incorporated to address where clustering might have an influence on the conversion coating process.

7.1 Background

Conversion coatings are used extensively in the metal finishing industry to change the surface properties of metals to both increase corrosion protection and to promote paint adhesion. Figure 7-1 shows a schematic of the substrate metal which has the conversion coating applied and finally has a top coat applied. Several formulations of conversion

coatings rely on the use of Cr(VI) compounds which have been targeted for elimination and the search for potential replacements for chromate conversion coatings has been an active area of research for a number of years [4-7].

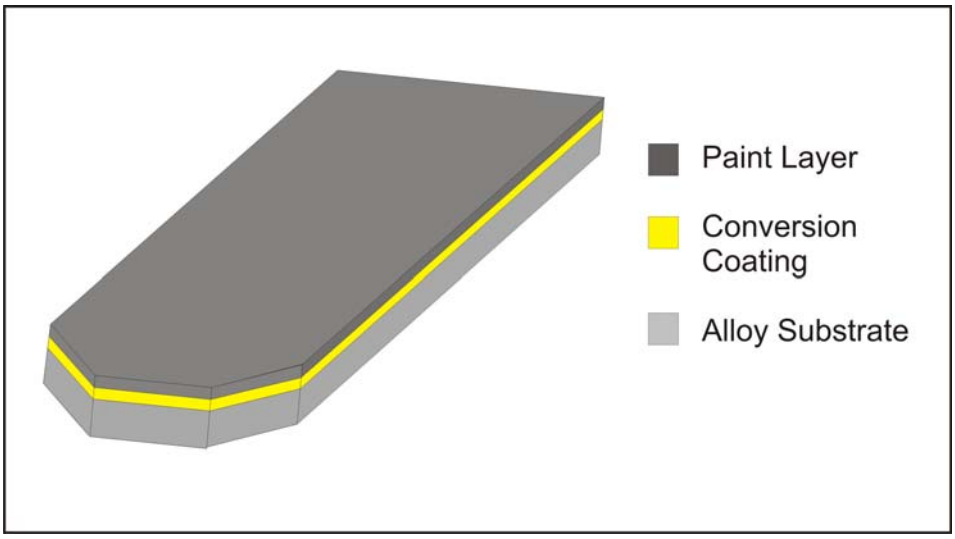

Figure 7-1: Diagram of the conversion coating sample.

Prior to conversion coating, a metal substrate is cleaned in a series of steps (Figure 7-2) which combine alkaline cleaning, acid treatment (deoxidising) and rinsing steps [7]. The objectives of the cleaning process are several fold. The first two cleaning steps remove any grease or grime from the surface, but also modify the surface chemistry by enriching it in basic oxide such as Zn and Mg hydroxyl oxide. The deoxidation step as well as removing these basic oxides, results in IM particles etchout and etching of the Al matrix. Many of these deoxidisers contain chromate along with HNO_3 and HF.

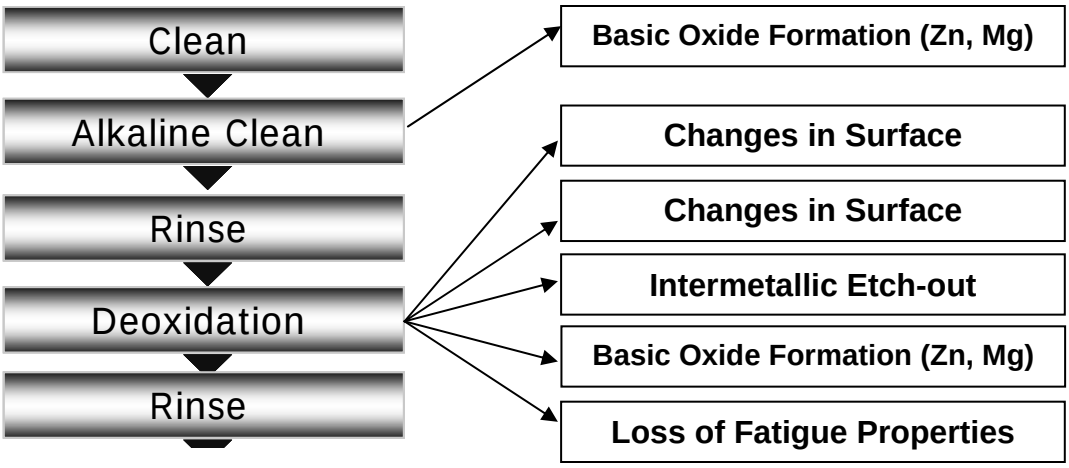

Figure 7-2: Description of the processing stages up to deoxidation.

There has been an ongoing drive to remove chromate from the chemical processing of metals including Al alloys [7]. Considerable attention has focused on chromate conversion coating replacements whilst less attention has been paid to the replacement of chromate deoxidisers. While there are several non-chromate deoxidiser chemistries available, their effect on Al alloys such as AA2024-T3 has not been particularly well documented [2,3]. The subject of this study is a deoxidiser based on sodium bromate (NaBrO3) and nitric acid (HNO3). This deoxidiser is free of both Cr and F which makes it more acceptable environmentally [2]. In this section, the effects of bromate-nitric acid deoxidation on AA2024-T3 was examined at three different temperatures (20°, 40° and 60°C) and immersion times (1, 5 and 10 minutes) using TEM and EFTEM.

For AA2024-T3 it has been reported that these deoxidisers remove around 1 μm of the surface during treatment, this includes the surface oxide and the majority of surface IM particles, leaving the surface with a Cr-rich oxide [9,10]. As only one micron is removed, the probability of new IMs being exposed is low and any that are exposed are heavily etched or completely removed.

7.1.1 Specimen Preparation and Experimental

Samples were produced from AA2024-T3 sheet which was cut into panels 127 x 76 mm. The alkaline cleaner (Gibson Process 204B), supplied by Ecolab was used at a concentration of 45 g/L (in de-ionised (DI) water) and operated at 60° C. The $NaBrO_3$

component of the deoxidiser (Sanchem 1000) was supplied by Sanchem. It was used at a concentration of 30 g/L in 100 g/L 70 %w/w nitric acid, and operated at 20-60°C.

The deoxidation of the AA2024-T3 panels was performed on an automated 60 L processing line. The cleaning and deoxidation tanks were agitated.

Following Figure 7-2, each sample was processed as follows:

1. Solvent cleaned using a lanolin-free tissue (Kimwipe 4103) soaked in acetone (AR Grade, BDH)
2. Alkaline cleaned (five minutes)
3. Immersed in a flowing rinse tank containing DI water (2 minutes)
4. Deoxidised (for 1, 5 or 10 minutes at 20°C, 40°C or 60°C)
5. Immersed in a flowing rinse tank containing DI water (2 minutes)

The samples were then blown dry under a compressed stream of dry nitrogen before characterisation.

Samples were then shaped and cross-sectional TEM (X-TEM) specimens were prepared and analysed as described in Sections 3.3.4 and 3.3.5.

SEM was performed on a Leica Thermal Field Emission SEM (360FE SEM) on uncoated specimens mounted using conducting, double-sided adhesive, carbon tape. Specimens were imaged at an accelerating voltage of 15 kV, probe current of 400 – 700 pA, working distance of 11 or 22 mm and no rotation of the specimens.

7.1.2 Results

To understand the effects of the deoxidiser on the alloy it is important to characterise the surface prior to treatment. Figure 7-3 shows composite three colour EFTEM maps (a) Mg-Al-O and (b) Cu-Al-O obtained from the TEM cross section of the as-received

AA2024-T3. From these maps it can be seen that the surface oxide is a mixed oxide with separate regions of Mg oxide incorporated into an Al oxide. The thickness of the oxide was measured to range between 80-140 nm and was determined through integrated linescans.

Some Cu enrichment were also observed in the oxide as islands lying parallel to the surface. In Figure 7-3(b), two $Al_{20}Cu_3Mn_2$ rod-like dispersoid particles around 200 nm in length can be seen at the surface just beneath the oxide. A Cu/Cu-oxide particle around 100 nm can also been seen at the metal/surface oxide interface. These particles were often observed within the oxide or at the metal surface oxide interface. As the size of the Cu/Cu-oxide particles was always significantly less than the dispersoid phase, it suggests that they probably result from the oxidation of Al_2CuMg hardening precipitates rather than the dispersoid phase.

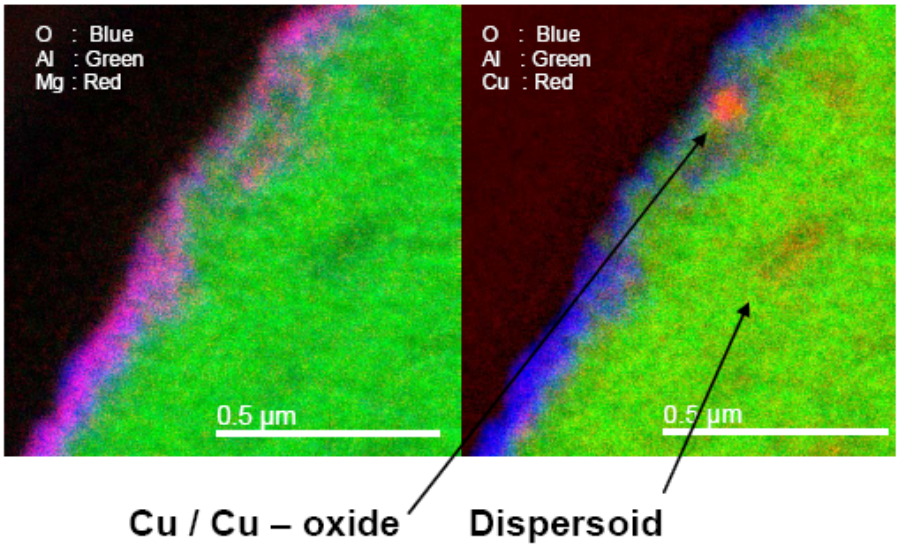

Figure 7-3: TEM of the as received AA2024-T3 showing (a) Mg-Al-O and (b) Cu-Al-O composite maps of a section of the surface oxide.

The next step was to characterise the surface after it was alkaline cleaned. From Figure 7-4, it can be seen that the alkaline cleaning appears to thin the surface oxide to 50-80 nm, which is consistent with that of mild etching.

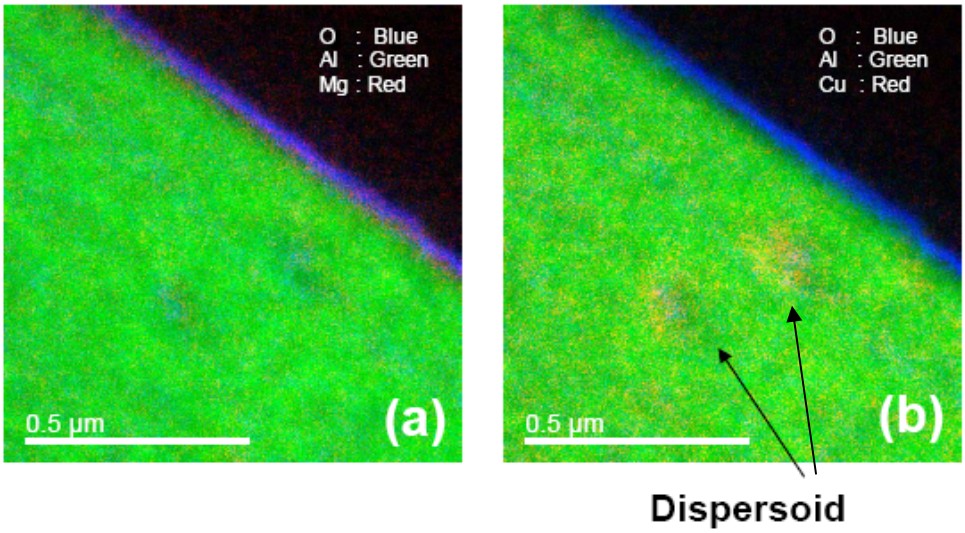

Figure 7-4: TEM of the alkaline cleaned AA2024-T3 showing (a) Mg-Al-O and (b) Cu-Al-O composite maps of a section of the surface oxide.

Treatment of 2024-T3 at 20ºC in the BrO_3^-/HNO_3 deoxidiser only led to very mild local, etching of the alloy matrix surface (Figure 7-5(a)-(c)) but XPS indicated some attack of the surface oxide in the form of Mg and F removal [2]. Increasing the treatment temperature led to significant etching at 40ºC particularly for 10 minutes immersion (Figure 7-5(d)-(f)) and for all processing times at 60ºC (Figure 7-5(g)-(i)). The heavy etching at 60ºC was accompanied by complete removal of the oxide left after alkaline cleaning, as evidenced by the decrease in the Si level [2].

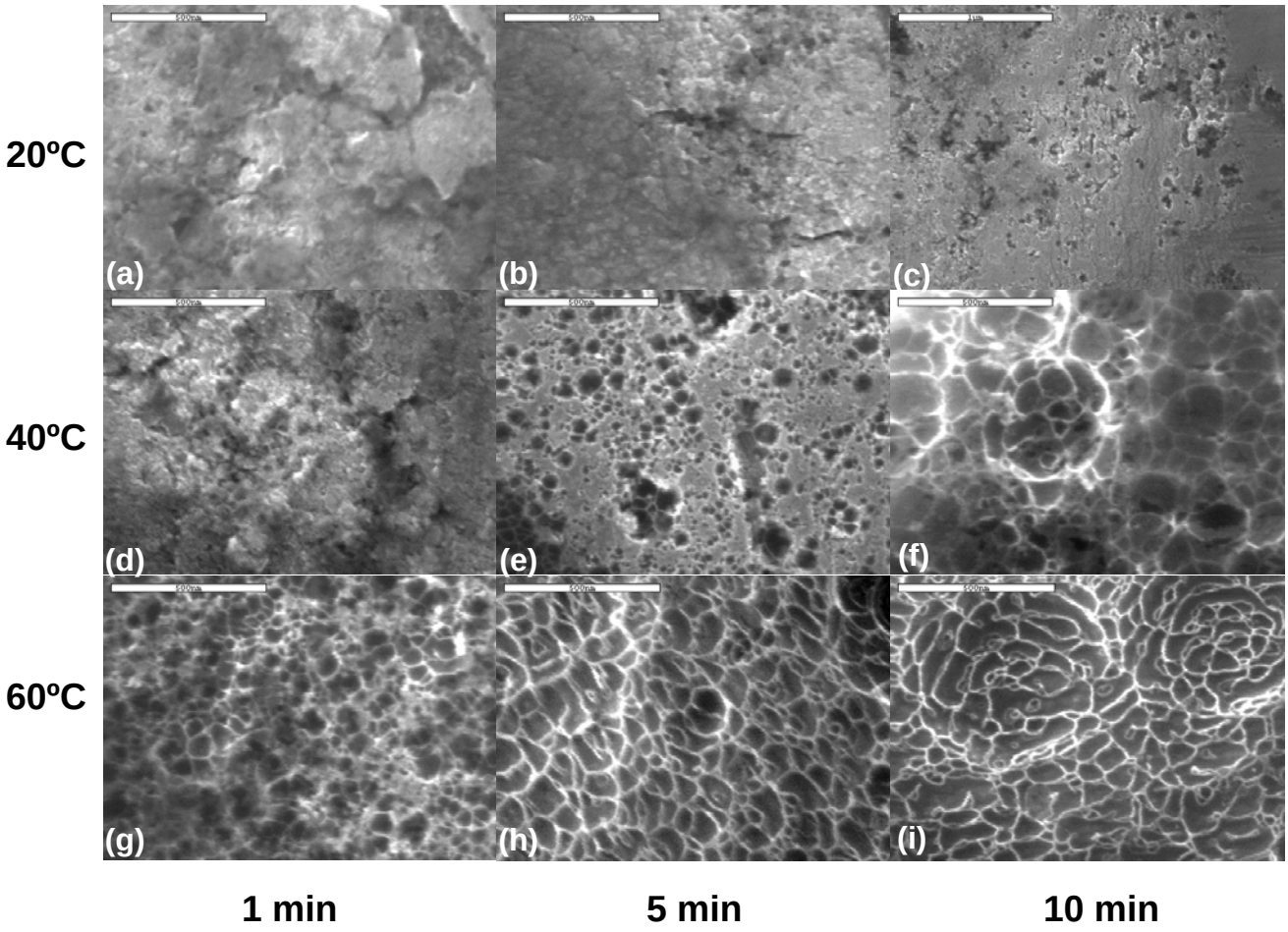

Figure 7-5: 2024-T3 after deoxidation for various times and temperatures in BrO_3 / HNO_3 based deoxidiser. (Scale marker for (c) = 1 µm, for all other images = 500 nm).

At much higher temperatures (60ºC, 5-10 mins) the etching observed with the BrO_3^- /HNO_3 deoxidiser was similar to that observed with Cr-based deoxidisers [28]. The presence of HNO_3 led to the complete removal of all IM particles, even at the lower process temperatures (Figure 7-6). At the lower processing temperatures, however, the etchout pits appeared to contain a considerable amount of material which EDS analysis suggested was Al oxides. It was only at 60ºC that the etchout pits were clean and accompanied by etching of the surrounding matrix. At higher processing temperatures, where the surface oxide had been removed, the Cu levels on the alloy matrix were generally lower than for the Cr-based deoxidiser. The more efficient removal of Cu in this deoxidiser was probably due to the presence of an additional oxidant in the form of

bromate. Previous studies on the addition of H_2O_2 or $K_2S_2O_4$ to a $Ce^{4+}/HNO_3/HF$ deoxidiser revealed better Cu removal with the additional oxidant [29].

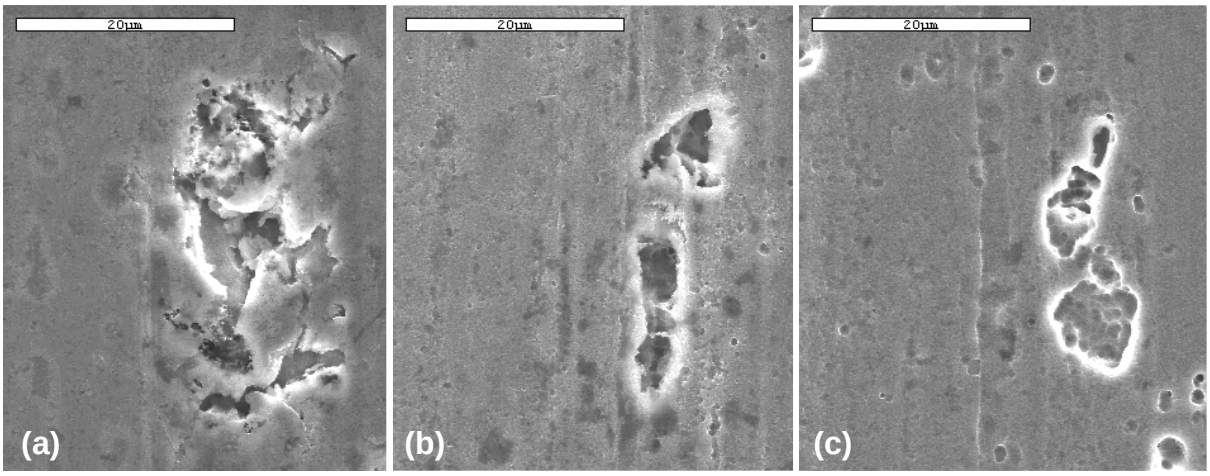

Figure 7-6: 2024-T3 after deoxidation in BrO_3^- / HNO_3^- - based deoxidiser at (a) 20°C (b) 40°C, and (c) 60°C. (Scale markers = 20 µm)

7.1.3 Deoxidation at 20°C

TEM was used to characterize the changes to the surface oxide were observed using SEM. Composite Cu-Al-O EFTEM elemental maps were collected from ultramicrotomed X-TEM sections of the surface for 1, 5 and 10 minute exposures, see Figure 7-7. In Figure 7-7 (20°C, 1 minute), Cu-oxide particles can be seen incorporated into the surface oxide. Similar particles of Cu-oxide can be seen after 5 minutes of deoxidation, but these particles were much less prevalent after 10 minutes. These particles were also observed in the as-rolled condition in Figure 7-3. These particles are thought to be associated with an oxidised form of the hardening precipitates. There is some evidence, however, that they may also be associated with the rolling processes, since deposition of Mn particles from solid solution has been observed in 3000 series alloys [12,13]. Since AA2024-T3 contains some 0.5 at% Cu in solid solution [14], the presence of these particles could be a result of precipitation of Cu during rolling.

Composite EELS maps of the oxide covering the surface in the as-received condition (Figure 7-3), after alkaline cleaning (Figure 7-4) and during deoxidation at 1 and 5 minutes in the Al-Mg-O composite elemental maps (Figure 7-7) revealed that the oxide covering the surface was partitioned into separate Al- or Mg-oxide rich regions.

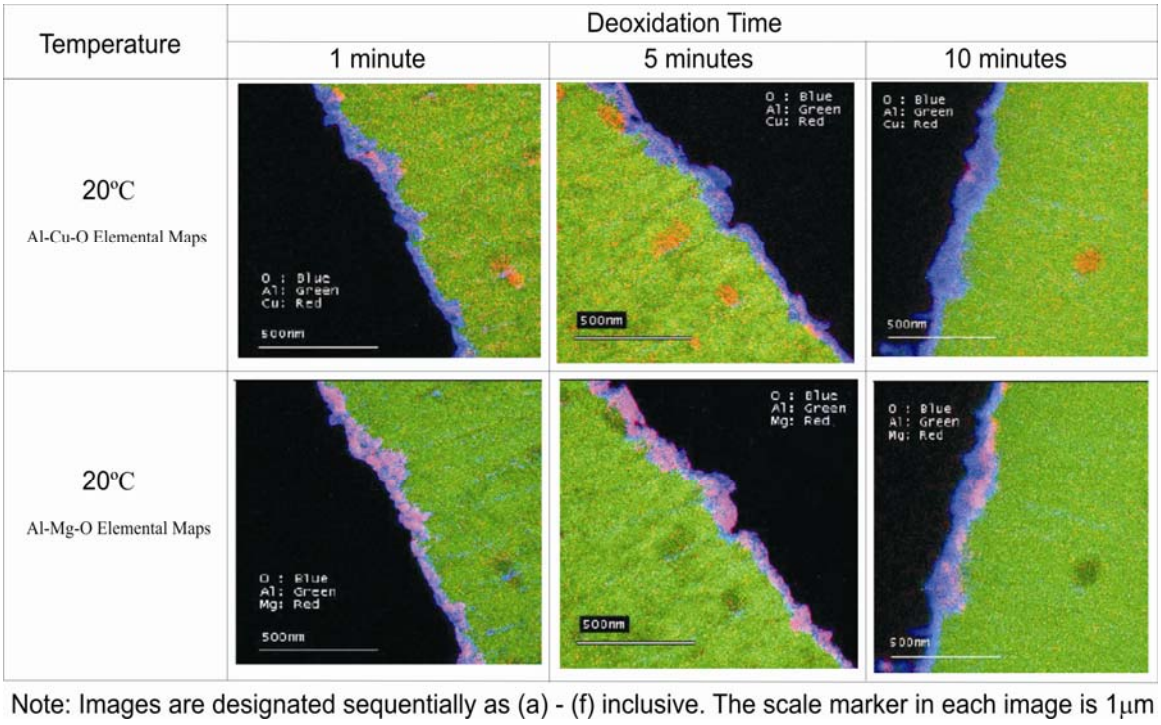

Figure 7-7: EFTEM composite Al-Cu-O and Al-Mg-O elemental maps of sections of the surface of AA2024-T3 immersion in a HNO_3/BrO_3 deoxidiser for 1, 5 and 10 minutes at 20°C.

Si was also observed at the surface with EFTEM elemental maps suggesting that the Si was confined to a thin layer on the external surface, and the absence of this layer in some sections meant that it was not continuous (e.g. Figure 7-8 (a) and (b)). By contrast, high etch rate deoxidisers resulted in the removal of most or all of the Al and Si oxide [15].

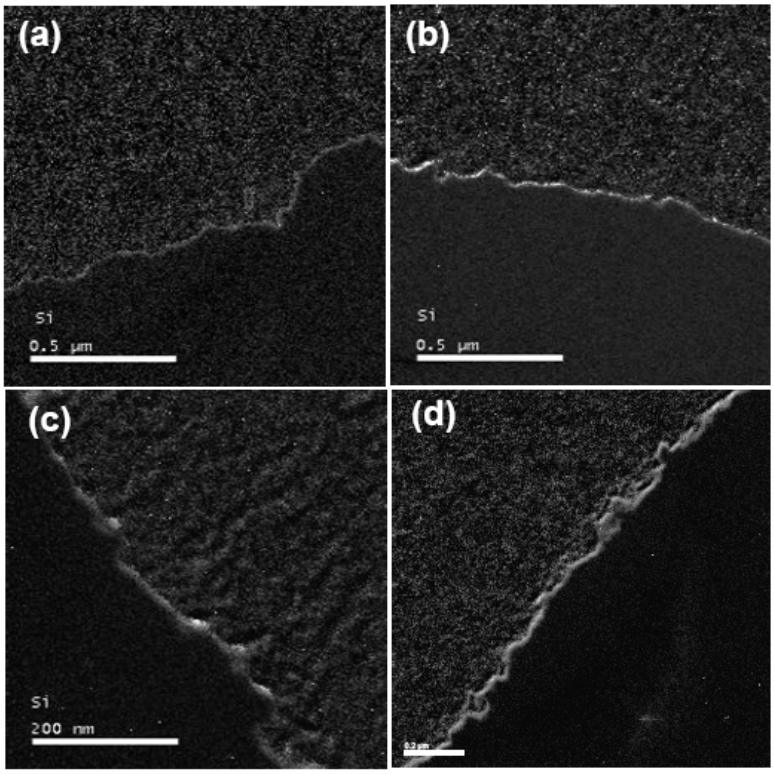

Figure 7-8: EELS maps of the Si distribution on the surface at (a) 20°C, and 1 minute, (b) 20°C, and 5 minute, (c) 40°C and 1 minute and (d) 40°C and 5 minute.

In summary, EFTEM results for the deoxidation at 20°C indicated that the Mg removal was associated with the formation of etch structures on the surface. In spite of the relative mildness of the deoxidation, these panels end up with the lowest surface Cu levels of all the conditions tested. This was probably due to the removal of Cu from the surface IMs without the aggressive removal of surface oxide that would expose new sub-surface Cu-containing material.

7.1.4 Deoxidation at 40°C

The small heavy atomic number particulates (100 to 200 nm) identified in EFTEM composite maps in Figure 7-3 as Cu-oxide were still incorporated into the surface oxide after 1 minute treatment at 40°C, Figure 7-9, much as they were at 20°C. This indicated that the short etch time was not adequate to remove the existing surface oxide. The Cu

oxide distribution within the oxide in the EFTEM maps also changed. The large Cu particulates observed at 20°C and also observed after 1 minute at 40°C were absent after the 5 minute treatment, Figure 7-9. However Cu was still present in the oxide, but was distributed as a finer dispersion of oxide close to the metal /surface oxide interface rather than as isolated particles. The presence of Cu in the surface oxide is unlikely to be due to dissolution from IM particles and subsequent re-deposition of Cu since the build-up occurs at the metal/surface oxide interface. It is likely, instead, to be due to the accumulation of Cu from solid solution or dissolution of hardening precipitates. This type of accumulation has been observed during processes which involve the dissolution of the matrix such as etching [9,15-20], conversion coating [19,20-24] and anodizing [25,26].

Al-Mg-O EFTEM maps in Figure 7-9 show significantly less Mg in the oxide over the matrix. Regions of Mg oxide just under 100 nm were still evident in some EFTEM maps of the surface oxide, but their absence in other sections indicated that some areas of the surface had undergone attack whereas others had not. Even given the extensive changes to the surface as a result of etching, the Si was confined to the external surface in the EFTEM elemental maps of 1 and 5 minutes deoxidation (Figure 7-8(c) and (d)).

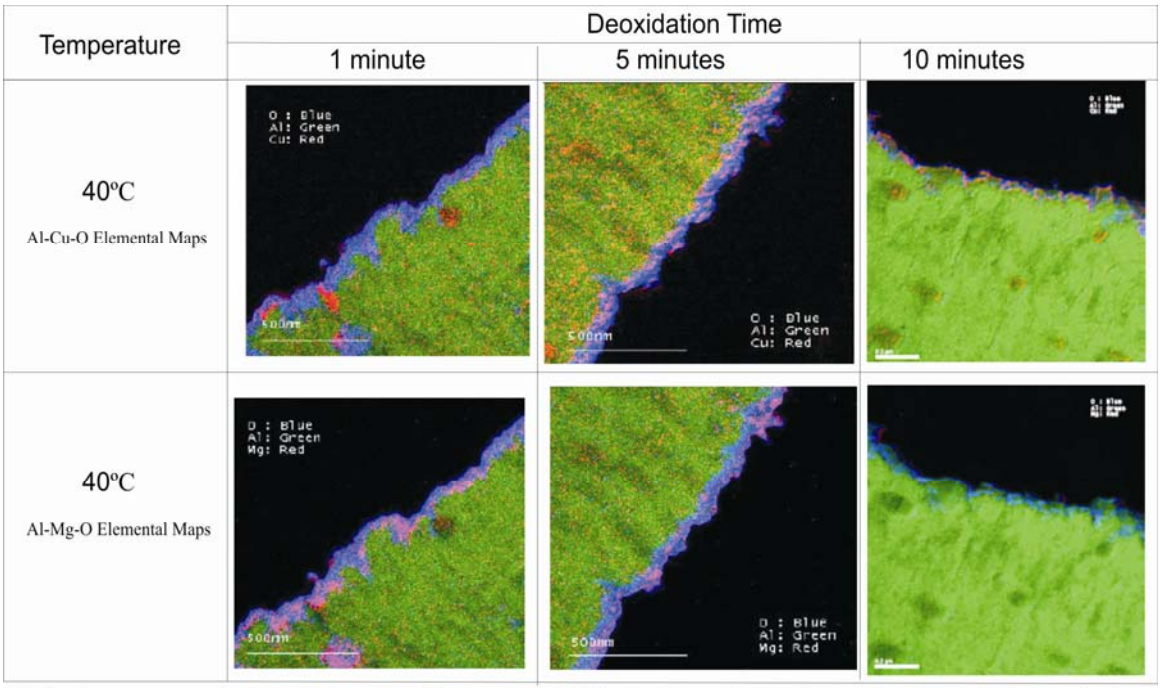

Figure 7-9: EFTEM composite Al-Cu-O and Al-Mg-O elemental maps of sections of the surface of AA2024-T3 immersion in a HNO_3/BrO_3 deoxidiser for 1, 5 and 10 minutes at 40°C.

In summary, as with 20°C, the EFTEM results of the deoxidation at 40°C indicated that the Mg removal was associated with the selective removal of a Mg-oxide phase from the surface oxide and the etch pattern of the surface supports this finding. While the shorter times were associated with attack of the original oxide on the surface, after 10 minutes immersion, it appeared that the underlying metal was in the process of attack and the surface oxide resulted from a mixture of oxidation and dissolution reactions. Hence the distribution of Cu within the surface changed from isolated Cu-oxides to an enrichment at the metal/surface oxide interface.

7.1.5 Deoxidation at 60°C

Effects of the deoxidization at 60ºC were similar to those of the deoxidization at 40ºC, only more pronounced. From EFTEM mapping in Figure 7-10, it was observed that for longer immersion times it was rare to observe any Mg in the surface oxide. Si was still

observed on the external surface of the oxide in some sections of the EFTEM elemental maps (not shown).

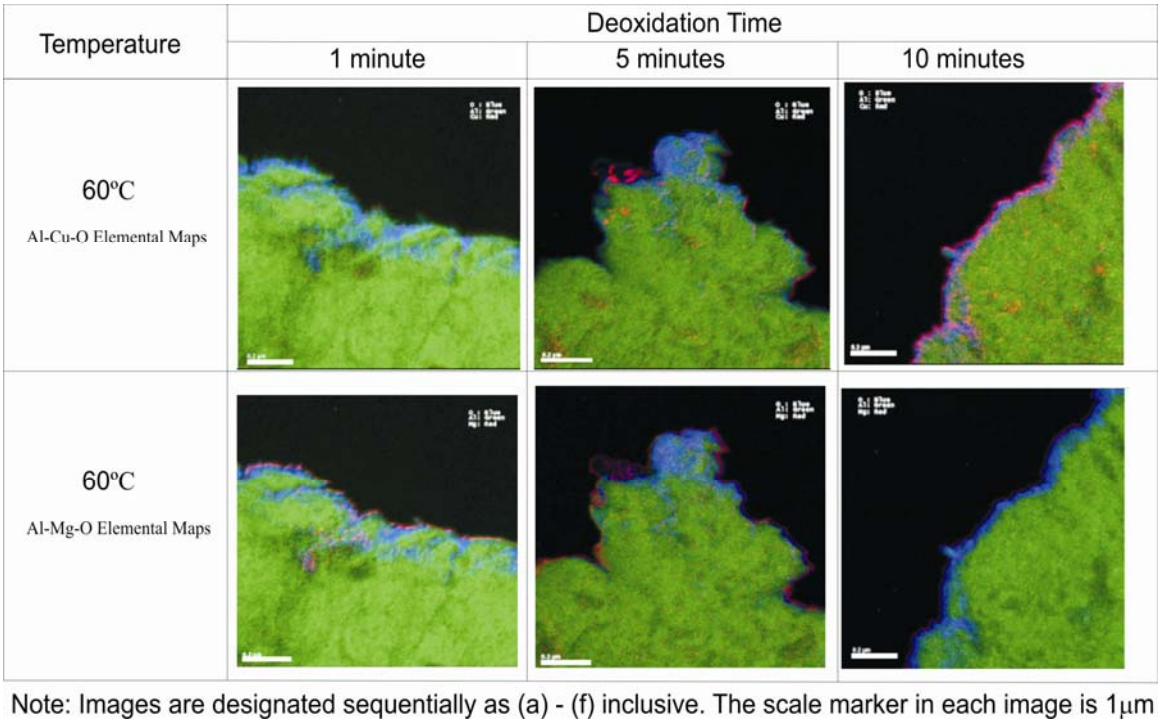

Figure 7-10: EFTEM composite Al-Cu-O and Al-Mg-O elemental maps of sections of the surface of AA2024-T3 immersion in a HNO_3/BrO_3 deoxidiser for 1, 5 and 10 minutes at 60°C.

7.1.6 Discussion

The use of the HNO_3/BrO_3 combination as a deoxidiser has been the subject of papers by Bibber [2], which stressed both the relatively low etch-rate of this combination compared with other deoxidisers (particularly those containing chromate) and the absence of either chromate or fluoride in the solution.

The oxide thicknesses as determined by EFTEM analysis of ultramicrotomed sections of samples are presented in Figure 7-11 and show decreasing trends moving to limiting values with immersion time. The oxide remaining on the surface is thickest when AA2024-T3 is processed at 20°C and thinnest at 10 minutes or greater at 40°C and 60°C.

At longer times and higher temperatures, a limiting oxide thickness of around 20 nm appears to be reached. At shorter times and lower temperatures the oxide thickness examined using EFTEM analysis is probably similar to that of the original oxide remaining on the surface, whereas at longer times and higher temperatures (*e.g.,* for 10 minutes at 60°C, approximately 1 μm would be removed) the significant etch rate would indicate that the oxide on the surface develops as a result of etching of the matrix and reaction with rinse water; it has been observed that oxide re-growth will occur during water rinsing [27].

From the perspective of clustering in IM particles, deoxidation at lower temperatures and shorter times results in complete IM particle etchout. This results in a series of "holes" in the surface which reflect the IM particle distribution. Thus if there is clustering on the surface then the residual "holes" will also be clustered. It was proposed that part of the function of cluster in corrosion was to change the chemistry at the clustered site. This function is not possible with the "holes". However, these 'holes" can trap acidic solution and lead to subsurface attack. This concept needs more exploration but is probably important from a processing viewpoint and suggests that generalised etching is a better proposition for surface finishing.

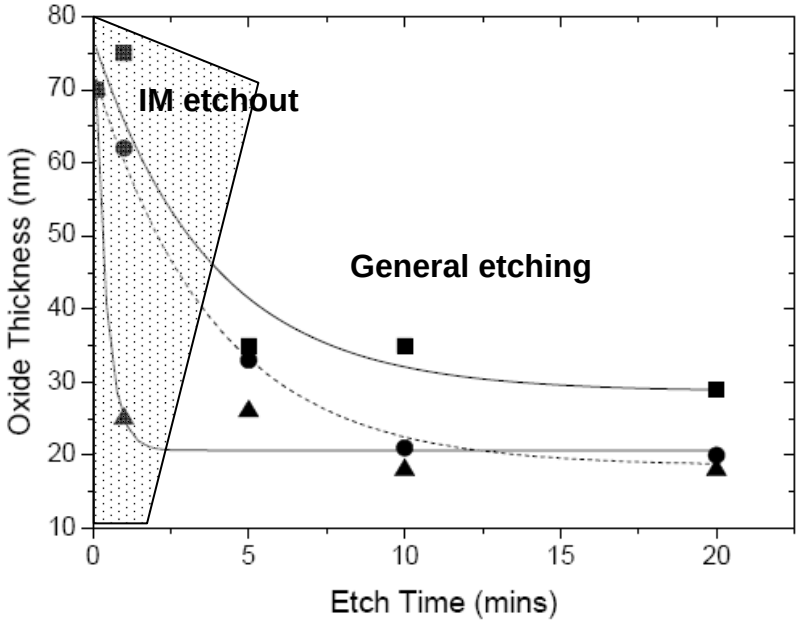

Figure 7-11: Oxide thicknesses determined through O EELS maps of ultramicrotomed section of the coating left after treatment in a HNO_3/BrO_3 deoxidiser. ■ = 20°C, ● = 40°C and ▲= 60°C. The shaded area indicates the times that IM Etchout was observed, where the non shaded region indicates the times that general etching of the surface was observed

7.2 Summary

The HNO_3/BrO_3 deoxidiser efficiently removes large IM particles from the surface for the longer processing times at all temperatures. For shorter immersion times at 20-40°C, there was only mild attack of the oxide covering the matrix resulting in localised removal of Mg-oxide from the surface oxide. Attack of the underlying metal and removal of the original surface oxide only began after 10 minutes of immersion at 40°C, and was complete after 5 minutes or longer at 60°C. Therefore, at temperatures below 40°C, bromate – nitric acid essentially acts as a low etch-rate deoxidiser. The widespread attack at 60°C and removal of IMs resulted in extensive scalloping of the alloy surface characteristic of fluoride-containing non-chromate deoxidisers observed previously [3,15,28] and is only observed with this deoxidiser at higher temperatures, or longer times at lower temperatures (e.g. 10 minutes at 40°C).

7.3 Bibliography

[1] T. G. Harvey, A. E. Hughes, S. G. Hardin, T. Nikpour, S. K. Toh, A. P. Boag, D. G. McCulloch, and M. Horne, Applied Surface Science **254,** 3562-3575 (2008).

[2] J. W. Bibber, Prod. Finish. **43,** 459 (1997).

[3] A. E. Hughes, K. J. H. Nelson, and P. R. Miller, Mater. Sci. Technol. **15,** 1124 (1999).

[4] A. Nylund, Alum. Trans. **2,** 121 (2000).

[5] S. M. Cohen, Corrosion **51,** 71 (1995).

[6] H. Terryn, ATB Metall. **38,** 41 (1998).

[7] R. G. Buchheit and A. E. Hughes, *Corrosion: Fundamentals, Testing and Protection* (American Society for Materials, Ohio, 2003).

[8] R. G. King, *Surface Treatment and Finishing of Aluminium* (Pergamon Press, Oxford, 1988).

[9] C. E. Moffitt, D. M. Wieliczka, and H. K. Yasuda, Surf. Coat. Technol **137,** 188 (2001).

[10] A. E. Hughes, S. G. Hardin, T. G. Harvey, T. Nikpour, B. R. W. Hinton, A. Galassi, G. McAdam, A. Stonham, S. J. Harris, C. C. Figgures, S. Church, D. Dixon, C. Bowden, P. C. Morgan, S. K. Toh, D. G. McCulloch, and J. DuPlessis, ATB Metall. **43,** 459 (2003).

[11] R. F. Egerton, *Electron Energy Loss Spectroscopy in the Electron Microscope*, 2nd ed. (Plenum Press, New York, 1996).

[12] H. Leth-Olsen, J. H. Nordlien, and K. Nisancioglu, Corrosion Science **40,** 2051-2063 (1998).

[13] A. Afseth, J. H. Nordlien, G. M. Scamans, and K. Nisancioglu, Corrosion Science **43,** 2093-2109 (2001).

[14] L. F. Mondolfo, *Aluminium Alloys: Structure and Properties* (Butterworth and Co., London, 1976).

[15] A. E. Hughes, T. G. Harvey, T. Nikpour, T. H. Muster, and S. G. Hardin, Surf. Coat. Technol **36,** 15 (2004).

[16] A. V. Pocius, *Materials and Processes - Coating Innovations* (Society for the Advancement of Material and Process Engineering, Anaheim CA, USA, 1983).

[17] F. J. Monteiro, M. A. R. Barbosa, D. H., and D. R. Gabe, Surf. Coat. Technol **17,** 519 (1991).

[18] N. Dimitrov, J. A. Mann, and K. Sieradzki, J. Electrochem Soc. **146,** 98 (1999).

[19] D. Y. Jung, I. Dumler, and M. Metzger, J. Electrochem Soc. **132,** 2308 (1985).

[20] P. Campestrini, H. Terryn, A. Hovestad, and J. H. W. De Wit, Surf. Coat. Technol **176,** 365 (2004).

[21] M. J. Vasquez, G. P. Halada, C. R. Clayton, and J. P. Longtin, Surf. Coat. Technol **33,** 607 (2002).

[22] A. E. Hughes, R. J. Taylor, and B. R. W. Hinton, Surface and Interface Analysis **25,** 223-234 (1997).

[23] X. Sun, R. Li, K. C. Wong, A. R. Mitchell, and T. Foster, Journal of Materials Science **36,** 3215 (2001).

[24] M. J. Vasquez, K. Kearns, G. P. Halada, and C. R. Clayton, Surf. Coat. Technol **33,** 796 (2002).
[25] H. Habazaki, K. Shimizu, M. A. Paez, P. Skeldon, G. E. Thompson, G. C. Wood, and X. Zhou, Surf. Coat. Technol **23,** 892 (1995).
[26] H. Habazaki, K. Shimizu, P. Skeldon, G. E. Thompson, G. C. Wood, and X. Zhou, Corrosion Science **39,** 731 (1997).
[27] W. J. Russell and E. A. Garnis, in *SAMPE Quaterly,* 5 (1976).
[28] K. J. H. Nelson, A. E. Hughes, R. J. Taylor, B. R. W. Hinton, L. Wilson, and M. Henderson, Mater. Sci. Technol. **17,** 1211 (2001).
[29] A. E. Hughes, K. J. H. Nelson, and P. R. Miller, Mater. Sci. Technol. **15,** 1124 (1999).

Chapter 8 - Conclusions

8.0 Introduction

The objective of this thesis was to understand the contributions to the establishment of stable pitting corrosion in AA2024-T3. The methodology was to first understand the compositional microstructure of the alloy, then to develop techniques which enable the investigation of stable pitting and then to investigate the processes that lead to larger corrosion features on the alloy's surface.

8.1 Characterisation of AA2024-T3

A detailed Electron Microprobe study of the IM particles within the alloy was undertaken involving more than 80,000 particles. This study identified eight individual phase compositions and revealed their locations. In many instances, these phases contributed to individual particles and in other instances existed as isolated phases. Depletion zones were also observed. From this analysis a statistical survey showed the extent to which Al_2CuMg (S-phase) and Al_2Cu (θ phase) co-precipitate. It also showed that there were a number of phases that contain Mg, Al, and Cu as the main constituents. As we could distinguish S-phase from θ-phase co-precipitated within individual particles. It was also found that, approximately 40% of the total IM particles were anodic, with the remaining 60% of the IM particles being cathodic. Of the cathodic particles it was also observed that these could be divided into two general categories; AlCuFeMn and AlCuFeMnSi.

By calculating the *g(r)* for each phase, a large number of nearest neighbours around (5 μm) were found. These neighbours arose mostly from multiphase particles as well as the depletion zones. Significant correlation in the *g(r)* for S-phase and θ-phase was also observed in the 15 to 20 μm region. Here it was evident that the S-phase/θ-phase particles themselves occurred in groups and not necessarily as isolated pairs of phases. Clustering

out to 20 μm is therefore likely due to these configurations of the S-phase/θ-phase particles.

The regional variability was also studied and it was shown that when the area was divided into 4 parts the particles densities didn't differ much from the original, but as the total area was divided into smaller and smaller pieces, large variations resulted. This proved that clustering was present on the surface, otherwise particle densities would have remained similar to the total image independent of size. The increase in spread could be used to indicate the scale at which clustering became important. As distributions started to broaden significantly between 16 and 64 suggesting that some clustering may have occurred on a scale between 80 and 300 μm, this agreed with pair correlation functions that showed clustering still occurred at 80 μm and beyond. The distribution broadened significantly towards large negative numbers indicating that the smaller regions had a large anode to cathode area. This data again suggested that there is clustering, but in this instance suggested that the clustering was associated with the cathodic particles and the anodic particles were much more evenly spread through the alloy.

8.2 Development of Techniques to investigate Pitting Corrosion in AA2024-T3

Different approaches for studying stable pitting initiation were investigated including SEM and PIXE analysis. The SEM study of pitting corrosion revealed both types of pitting corrosion: trenching and dissolution. In addition electron beam carbon stitching appeared to provide an increase in corrosion resistance on the surface. The study of isolated corrosion on the surface did not provide a good path forward to understanding stable pitting from a statistical point of view, on the other hand examining corrosion as a function of time revealed trends which required further study.

The PIXE analysis combined with phase correlation mapping was shown as a novel approach for investigating the association between IM particles and the site for corrosion

pits in large areas, providing an avenue for more statistical analysis of the IM particle distributions. Paired S-phase and Cu-Fe-Mn-Al type IM particles were found to be associated with pit sites in AA2024-T3 samples exposed to NaCl solution.

8.3 Detailed investigation of pitting corrosion in AA2024-T3

The development of corrosion as a function of time on AA2024-T3 was investigated using detailed PIXE and SEM analysis. The corrosion observed on the surface was divided into two types of attack sites:

(i) localised corrosion – which involved isolated particles
(ii) co-operative corrosion – where clusters of particles contributed to the corrosion event.

It was found that corrosion at the isolated particles involved both S-phase and AlCuFeMn(Si) IM particles. The S-phase the particles first underwent dealloying resulting in Cu-enriched remnants. These particles along with the AlCuFeMn(Si) IM particles gradually formed trenches around their periphery, but played little further role in corrosion.

The co-operative corrosion events were characterised by domes of corrosion product within a ring of corrosion product. The central domes appeared to be anodicaly active sites since Cl was often observed there, and at least some of them were initiated by the coupling between S-phase and cathodic IM particles within the surface. It was demonstrated that clustering was involved in the establishment of these types of sites and it was proposed that clustering of cathodic particles resulted in an alkaline environment around the anodically active site that formed a gel at its periphery (both in the solution and laterally on the surface). These sites were where the most subsurface attacks occurred. This is of strong importance as stable pitting attack can lead to sub surface attack and undermine the mechanical integrity of structures made with AA2024-T3. Stable pit initiation appeared to progress through grain boundary attack followed by grain

etchout. Based on electrochemistry, this model differs from models based on metastable to stable pit transition and suggests that stable pit sites do not evolve from meta stable pit sites, but are a separate phenomenon. The identification of different stages in the establishment of stable pits leads to better methods of prevention and even remediation.

8.4 Surface Pre Treatment

A detailed study of the action of non chromate deoxidisers for AA2024-T3 was undertaken. It was found that the influence of the deoxidiser was more apparent with increase in temperature and as time increases. At low temperatures only the IM particles were removed. At intermediate times and temperatures the surface oxide was modified through selective dissolution of Mg phases and at long times the surface under went general dissolution. Clustering of IM particles was studied and it was found that they also influenced the performance of metal finishing processes. It was identified that for certain processing conditions, only the IM particles were etched out. The etch pits retained the clustering configuration of the original IM particle and if they trap processing solutions may lead to severe attack.

8.5 Future Work

From the findings of this thesis, numerous ideas and suggestions have arisen. Possibilities for future work and direction are given below:

- Extending this study to other Al alloys in order to understand the microstructure and to confirm if the processes that form stable pitting are the same.

- Correlating observed pitting events on the alloy's surface with electrochemical measurements.

- Further investigation into the influence of IM clustering on metal finishing surfaces.

Chapter 9 - Appendix

9.0 Appendix A: Particle Counting Code

```
var p=0;
var q=0;
var n=1;
var x1=0;
var x2=0;
var y1=0;
var y2=0;
var height=0;
var i=0;



height=getHeight();

title = getTitle();
//convertTo8Bit();
setAutoThreshold();
saveSettings();



//***************************************
//        1x1 elctrode
//***************************************

            x1=0;
            y1=0;
            x2=height;
            y2=height;


rename("1x1 Cell 1 of 1");
newtitle=getTitle;

makeRectangle(x1, y1, x2, y2 );

run("Set Measurements...", "centroid redirect=None decimal=2");

run("Analyze Particles...", "minimum=1 maximum=999999999 bins=100 show=Nothing display clear
summarize");       // show results without image          // show results without image

//run("Analyze Particles...", "minimum=1 maximum=999999999 bins=100 show=Outlines display clear");
            // show results with image
```

```
//run("Analyze Particles...", "minimum=1 maximum=9999 bins=100 show=Outlines clear");          //don't
show results

p=nResults;



q="Q"+n+" - ";


directory="/Documents and Settings/Adam/Desktop/Split Images/Split Results/1x1/";

path=directory+q+title+" - "+p+" particles.xls";

selectWindow("Results");
saveAs("Measurements",path );

selectWindow(newtitle);
rename(title);
selectWindow(title);


restoreSettings();


//****************************************
//        2x2 elctrode
//****************************************



for (n=1; n<5; n++)          {

i=0;

if (n==1) {

            x1=0;
            y1=0;
            x2=height/2;
            y2=height/2;

            rename("2x2 Cell 1 of 4");
            newtitle=getTitle;

            };


if (n==2) {

            x1=height/2;
            y1=0;
            x2=height;
            y2=height/2;
```

```
		rename("2x2 Cell 2 of 4");
		newtitle=getTitle;

		};

if (n==3) {

		x1=0;
		y1=height/2;
		x2=height/2;
		y2=height;

		rename("2x2 Cell 3 of 4");
		newtitle=getTitle;

		};

if (n==4) {

		x1=height/2;
		y1=height/2;
		x2=height;
		y2=height;

		rename("2x2 Cell 4 of 4");
		newtitle=getTitle;

		};
makeRectangle(x1, y1, x2, y2 );



run("Set Measurements...", "centroid redirect=None decimal=2");

run("Analyze Particles...", "minimum=1 maximum=999999999 bins=100 show=Nothing display clear
summarize");	// show results without image		// show results without image


//run("Analyze Particles...", "minimum=1 maximum=999999999 bins=100 show=Outlines display clear");
		// show results with image

//run("Analyze Particles...", "minimum=1 maximum=9999 bins=100 show=Outlines clear");		//don't
show results

p=nResults;



q="Q"+n+" - ";


directory="/Documents and Settings/Adam/Desktop/Split Images/Split Results/2x2/";

path=directory+q+title+" - "+p+" particles.xls";
```

```
selectWindow("Results");
saveAs("Measurements",path );

selectWindow(newtitle);
rename(title);
selectWindow(title);


restoreSettings();

                                }



//***************************************
//        4x4 elctrode
//***************************************

i=0;

for (n=1; n<17; n++)        {


if (n==1) {

            x1=0;
            y1=0;
            x2=height/4;
            y2=height/4;

            rename("4x4 Cell 1 of 16");
            newtitle=getTitle;

            };


if (n==2) {

            x1=height/4;
            y1=0;
            x2=height/4;
            y2=height/4;

            rename("4x4 Cell 2 of 16");
            newtitle=getTitle;

            };

if (n==3) {

            x1=height/2;
            y1=0;
            x2=height/4;
            y2=height/4;
```

```
        rename("4x4 Cell 3 of 16");
        newtitle=getTitle;

        };

if (n==4) {

        x1=(3*height)/4;
        y1=0;
        x2=height/4;
        y2=height/4;

        rename("4x4 Cell 4 of 16");
        newtitle=getTitle;

        };

if (n==5) {

        x1=0;
        y1=height/4;
        x2=height/4;
        y2=height/4;

        rename("4x4 Cell 5 of 16");
        newtitle=getTitle;

        };


if (n==6) {

        x1=height/4;
        y1=height/4;
        x2=height/4;
        y2=height/4;

        rename("4x4 Cell 6 of 16");
        newtitle=getTitle;

        };

if (n==7) {

        x1=height/2;
        y1=height/4;
        x2=height/4;
        y2=height/4;

        rename("4x4 Cell 7 of 16");
        newtitle=getTitle;

        };

if (n==8) {
```

```
        x1=(3*height)/4;
        y1=height/4;
        x2=height/4;
        y2=height/4;

        rename("4x4 Cell 8 of 16");
        newtitle=getTitle;

        };


if (n==9) {

        x1=0;
        y1=height/2;
        x2=height/4;
        y2=height/4;

        rename("4x4 Cell 9 of 16");
        newtitle=getTitle;

        };


if (n==10) {

        x1=height/4;
        y1=height/2;
        x2=height/4;
        y2=height/4;

        rename("4x4 Cell 10 of 16");
        newtitle=getTitle;

        };

if (n==11) {

        x1=height/2;
        y1=height/2;
        x2=height/4;
        y2=height/4;

        rename("4x4 Cell 11 of 16");
        newtitle=getTitle;

        };

if (n==12) {

        x1=(3*height)/4;
        y1=height/2;
        x2=height/4;
        y2=height/4;
```

```
        rename("4x4 Cell 21 of 16");
        newtitle=getTitle;

        };


if (n==13) {

        x1=0;
        y1=(3*height)/4;
        x2=height/4;
        y2=height/4;

        rename("4x4 Cell 13 of 16");
        newtitle=getTitle;

        };


if (n==14) {

        x1=height/4;
        y1=(3*height)/4;
        x2=height/4;
        y2=height/4;

        rename("4x4 Cell 14 of 16");
        newtitle=getTitle;

        };

if (n==15) {

        x1=height/2;
        y1=(3*height)/4;
        x2=height/4;
        y2=height/4;

        rename("4x4 Cell 15 of 16");
        newtitle=getTitle;

        };

if (n==16) {

        x1=(3*height)/4;
        y1=(3*height)/4;
        x2=height/4;
        y2=height/4;

        rename("4x4 Cell 16 of 16");
        newtitle=getTitle;

        };
```

```
makeRectangle(x1, y1, x2, y2 );



run("Set Measurements...", "centroid redirect=None decimal=2");

run("Analyze Particles...", "minimum=1 maximum=999999999 bins=100 show=Nothing display clear
summarize");       // show results without image          // show results without image


//run("Analyze Particles...", "minimum=1 maximum=999999999 bins=100 show=Outlines display clear");
          // show results with image

//run("Analyze Particles...", "minimum=1 maximum=9999 bins=100 show=Outlines clear");          //don't
show results

q="Q"+n+" - ";
p=nResults;

directory="/Documents and Settings/Adam/Desktop/Split Images/Split Results/4x4/";

path=directory+q+title+" - "+p+" particles.xls";

selectWindow("Results");
saveAs("Measurements",path );

selectWindow(newtitle);
rename(title);
selectWindow(title);



restoreSettings();

                                    }


//**************************************
//        8x8 elctrode
//**************************************


for (n=1; n<65; n++)        {


if (n==1) {

          x1=(0*height)/8;
          y1=(0*height)/8;
          x2=height/8;
          y2=height/8;
```

```
        };

if (n==2) {

        x1=(1*height)/8;
        y1=(0*height)/8;
        x2=height/8;
        y2=height/8;

        };

if (n==3) {

        x1=(2*height)/8;
        y1=(0*height)/8;
        x2=height/8;
        y2=height/8;

        };

if (n==4) {

        x1=(3*height)/8;
        y1=(0*height)/8;
        x2=height/8;
        y2=height/8;

        };

if (n==5) {

        x1=(4*height)/8;
        y1=(0*height)/8;
        x2=height/8;
        y2=height/8;

        };

if (n==6) {

        x1=(5*height)/8;
        y1=(0*height)/8;
        x2=height/8;
        y2=height/8;

        };

if (n==7) {

        x1=(6*height)/8;
        y1=(0*height)/8;
        x2=height/8;
        y2=height/8;

        };
```

```
if (n==8) {

        x1=(7*height)/8;
        y1=(0*height)/8;
        x2=height/8;
        y2=height/8;

        };

if (n==9) {

        x1=(0*height)/8;
        y1=(1*height)/8;
        x2=height/8;
        y2=height/8;

        };

if (n==10) {

        x1=(1*height)/8;
        y1=(1*height)/8;
        x2=height/8;
        y2=height/8;

        };

if (n==11) {

        x1=(2*height)/8;
        y1=(1*height)/8;
        x2=height/8;
        y2=height/8;

        };

if (n==12) {

        x1=(3*height)/8;
        y1=(1*height)/8;
        x2=height/8;
        y2=height/8;

        };

if (n==13) {

        x1=(4*height)/8;
        y1=(1*height)/8;
        x2=height/8;
        y2=height/8;

        };

if (n==14) {
```

```
            x1=(5*height)/8;
            y1=(1*height)/8;
            x2=height/8;
            y2=height/8;

            };

if (n==15) {

            x1=(6*height)/8;
            y1=(1*height)/8;
            x2=height/8;
            y2=height/8;

            };

if (n==16) {

            x1=(7*height)/8;
            y1=(1*height)/8;
            x2=height/8;
            y2=height/8;

            };

if (n==17) {

            x1=(0*height)/8;
            y1=(2*height)/8;
            x2=height/8;
            y2=height/8;

            };

if (n==18) {

            x1=(1*height)/8;
            y1=(2*height)/8;
            x2=height/8;
            y2=height/8;

            };

if (n==19) {

            x1=(2*height)/8;
            y1=(2*height)/8;
            x2=height/8;
            y2=height/8;

            };

if (n==20) {

            x1=(3*height)/8;
            y1=(2*height)/8;
```

```
        x2=height/8;
        y2=height/8;

        };

if (n==21) {

        x1=(4*height)/8;
        y1=(2*height)/8;
        x2=height/8;
        y2=height/8;

        };

if (n==22) {

        x1=(5*height)/8;
        y1=(2*height)/8;
        x2=height/8;
        y2=height/8;

        };

if (n==23) {

        x1=(6*height)/8;
        y1=(2*height)/8;
        x2=height/8;
        y2=height/8;

        };

if (n==24) {

        x1=(7*height)/8;
        y1=(2*height)/8;
        x2=height/8;
        y2=height/8;

        };

if (n==25) {

        x1=(0*height)/8;
        y1=(3*height)/8;
        x2=height/8;
        y2=height/8;

        };

if (n==26) {

        x1=(1*height)/8;
        y1=(3*height)/8;
        x2=height/8;
        y2=height/8;
```

```
        };

if (n==27) {

        x1=(2*height)/8;
        y1=(3*height)/8;
        x2=height/8;
        y2=height/8;

        };

if (n==28) {

        x1=(3*height)/8;
        y1=(3*height)/8;
        x2=height/8;
        y2=height/8;

        };

if (n==29) {

        x1=(4*height)/8;
        y1=(3*height)/8;
        x2=height/8;
        y2=height/8;

        };

if (n==30) {

        x1=(5*height)/8;
        y1=(3*height)/8;
        x2=height/8;
        y2=height/8;

        };

if (n==31) {

        x1=(6*height)/8;
        y1=(3*height)/8;
        x2=height/8;
        y2=height/8;

        };

if (n==32) {

        x1=(7*height)/8;
        y1=(3*height)/8;
        x2=height/8;
        y2=height/8;

        };
```

```
if (n==33) {

        x1=(0*height)/8;
        y1=(4*height)/8;
        x2=height/8;
        y2=height/8;

        };

if (n==34) {

        x1=(1*height)/8;
        y1=(4*height)/8;
        x2=height/8;
        y2=height/8;

        };

if (n==35) {

        x1=(2*height)/8;
        y1=(4*height)/8;
        x2=height/8;
        y2=height/8;

        };

if (n==36) {

        x1=(3*height)/8;
        y1=(4*height)/8;
        x2=height/8;
        y2=height/8;

        };

if (n==37) {

        x1=(4*height)/8;
        y1=(4*height)/8;
        x2=height/8;
        y2=height/8;

        };

if (n==38) {

        x1=(5*height)/8;
        y1=(4*height)/8;
        x2=height/8;
        y2=height/8;

        };

if (n==39) {
```

```
            x1=(6*height)/8;
            y1=(4*height)/8;
            x2=height/8;
            y2=height/8;

            };

if (n==40) {

            x1=(7*height)/8;
            y1=(4*height)/8;
            x2=height/8;
            y2=height/8;

            };

if (n==41) {

            x1=(0*height)/8;
            y1=(5*height)/8;
            x2=height/8;
            y2=height/8;

            };

if (n==42) {

            x1=(1*height)/8;
            y1=(5*height)/8;
            x2=height/8;
            y2=height/8;

            };

if (n==43) {

            x1=(2*height)/8;
            y1=(5*height)/8;
            x2=height/8;
            y2=height/8;

            };

if (n==44) {

            x1=(3*height)/8;
            y1=(5*height)/8;
            x2=height/8;
            y2=height/8;

            };

if (n==45) {

            x1=(4*height)/8;
```

```
        y1=(5*height)/8;
        x2=height/8;
        y2=height/8;

        };

if (n==46) {

        x1=(5*height)/8;
        y1=(5*height)/8;
        x2=height/8;
        y2=height/8;

        };

if (n==47) {

        x1=(6*height)/8;
        y1=(5*height)/8;
        x2=height/8;
        y2=height/8;

        };

if (n==48) {

        x1=(7*height)/8;
        y1=(5*height)/8;
        x2=height/8;
        y2=height/8;

        };

if (n==49) {

        x1=(0*height)/8;
        y1=(6*height)/8;
        x2=height/8;
        y2=height/8;

        };

if (n==50) {

        x1=(1*height)/8;
        y1=(6*height)/8;
        x2=height/8;
        y2=height/8;

        };

if (n==51) {

        x1=(2*height)/8;
        y1=(6*height)/8;
        x2=height/8;
```

```
        y2=height/8;

        };

if (n==52) {

        x1=(3*height)/8;
        y1=(6*height)/8;
        x2=height/8;
        y2=height/8;

        };

if (n==53) {

        x1=(4*height)/8;
        y1=(6*height)/8;
        x2=height/8;
        y2=height/8;

        };

if (n==54) {

        x1=(5*height)/8;
        y1=(6*height)/8;
        x2=height/8;
        y2=height/8;

        };

if (n==55) {

        x1=(6*height)/8;
        y1=(6*height)/8;
        x2=height/8;
        y2=height/8;

        };

if (n==56) {

        x1=(7*height)/8;
        y1=(6*height)/8;
        x2=height/8;
        y2=height/8;

        };

if (n==57) {

        x1=(0*height)/8;
        y1=(7*height)/8;
        x2=height/8;
        y2=height/8;
```

```
        };

if (n==58) {

        x1=(1*height)/8;
        y1=(7*height)/8;
        x2=height/8;
        y2=height/8;

        };

if (n==59) {

        x1=(2*height)/8;
        y1=(7*height)/8;
        x2=height/8;
        y2=height/8;

        };

if (n==60) {

        x1=(3*height)/8;
        y1=(7*height)/8;
        x2=height/8;
        y2=height/8;

        };

if (n==61) {

        x1=(4*height)/8;
        y1=(7*height)/8;
        x2=height/8;
        y2=height/8;

        };

if (n==62) {

        x1=(5*height)/8;
        y1=(7*height)/8;
        x2=height/8;
        y2=height/8;

        };

if (n==63) {

        x1=(6*height)/8;
        y1=(7*height)/8;
        x2=height/8;
        y2=height/8;

        };
```

```
if (n==64) {

	x1=(7*height)/8;
	y1=(7*height)/8;
	x2=height/8;
	y2=height/8;

	};


	cell = "8x8 Cell "+n+" of 64";

	rename(cell);
	newtitle=getTitle;


makeRectangle(x1, y1, x2, y2 );




run("Set Measurements...", "centroid redirect=None decimal=2");

run("Analyze Particles...", "minimum=1 maximum=999999999 bins=100 show=Nothing display clear
summarize");	// show results without image		// show results without image


//run("Analyze Particles...", "minimum=1 maximum=999999999 bins=100 show=Outlines display clear");
		// show results with image

//run("Analyze Particles...", "minimum=1 maximum=9999 bins=100 show=Outlines clear");		//don't
show results

q="Q"+n+" - ";
p=nResults;

directory="/Documents and Settings/Adam/Desktop/Split Images/Split Results/8x8/";

path=directory+q+title+" - "+p+" particles.xls";

selectWindow("Results");
saveAs("Measurements",path );

selectWindow(newtitle);
rename(title);
selectWindow(title);


restoreSettings();

				}


//**************************************
```

```
//        16x16 elctrode
//****************************************


for (n=1; n<257; n++)       {


if (n==1) {

            x1=(0*height)/16;
            y1=(0*height)/16;
            x2=height/16;
            y2=height/16;

            };

if (n==2) {

            x1=(1*height)/16;
            y1=(0*height)/16;
            x2=height/16;
            y2=height/16;

            };

if (n==3) {

            x1=(2*height)/16;
            y1=(0*height)/16;
            x2=height/16;
            y2=height/16;

            };

if (n==4) {

            x1=(3*height)/16;
            y1=(0*height)/16;
            x2=height/16;
            y2=height/16;

            };

if (n==5) {

            x1=(4*height)/16;
            y1=(0*height)/16;
            x2=height/16;
            y2=height/16;

            };

if (n==6) {

            x1=(5*height)/16;
            y1=(0*height)/16;
```

```
            x2=height/16;
            y2=height/16;

            };

if (n==7) {

            x1=(6*height)/16;
            y1=(0*height)/16;
            x2=height/16;
            y2=height/16;

            };

if (n==8) {

            x1=(7*height)/16;
            y1=(0*height)/16;
            x2=height/16;
            y2=height/16;

            };

if (n==9) {

            x1=(8*height)/16;
            y1=(0*height)/16;
            x2=height/16;
            y2=height/16;

            };

if (n==10) {

            x1=(9*height)/16;
            y1=(0*height)/16;
            x2=height/16;
            y2=height/16;

            };

if (n==11) {

            x1=(10*height)/16;
            y1=(0*height)/16;
            x2=height/16;
            y2=height/16;

            };

if (n==12) {

            x1=(11*height)/16;
            y1=(0*height)/16;
            x2=height/16;
            y2=height/16;
```

```
        };

if (n==13) {

        x1=(12*height)/16;
        y1=(0*height)/16;
        x2=height/16;
        y2=height/16;

        };

if (n==14) {

        x1=(13*height)/16;
        y1=(0*height)/16;
        x2=height/16;
        y2=height/16;

        };

if (n==15) {

        x1=(14*height)/16;
        y1=(0*height)/16;
        x2=height/16;
        y2=height/16;

        };

if (n==16) {

        x1=(15*height)/16;
        y1=(0*height)/16;
        x2=height/16;
        y2=height/16;

        };

if (n==17) {

        x1=(0*height)/16;
        y1=(1*height)/16;
        x2=height/16;
        y2=height/16;

        };

if (n==18) {

        x1=(1*height)/16;
        y1=(1*height)/16;
        x2=height/16;
        y2=height/16;

        };
```

```
if (n==19) {

        x1=(2*height)/16;
        y1=(1*height)/16;
        x2=height/16;
        y2=height/16;

        };

if (n==20) {

        x1=(3*height)/16;
        y1=(1*height)/16;
        x2=height/16;
        y2=height/16;

        };

if (n==21) {

        x1=(4*height)/16;
        y1=(1*height)/16;
        x2=height/16;
        y2=height/16;

        };

if (n==22) {

        x1=(5*height)/16;
        y1=(1*height)/16;
        x2=height/16;
        y2=height/16;

        };

if (n==23) {

        x1=(6*height)/16;
        y1=(1*height)/16;
        x2=height/16;
        y2=height/16;

        };

if (n==24) {

        x1=(7*height)/16;
        y1=(1*height)/16;
        x2=height/16;
        y2=height/16;

        };

if (n==25) {
```

```
            x1=(8*height)/16;
            y1=(1*height)/16;
            x2=height/16;
            y2=height/16;

            };

if (n==26) {

            x1=(9*height)/16;
            y1=(1*height)/16;
            x2=height/16;
            y2=height/16;

            };

if (n==27) {

            x1=(10*height)/16;
            y1=(1*height)/16;
            x2=height/16;
            y2=height/16;

            };

if (n==28) {

            x1=(11*height)/16;
            y1=(1*height)/16;
            x2=height/16;
            y2=height/16;

            };

if (n==29) {

            x1=(12*height)/16;
            y1=(1*height)/16;
            x2=height/16;
            y2=height/16;

            };

if (n==30) {

            x1=(13*height)/16;
            y1=(1*height)/16;
            x2=height/16;
            y2=height/16;

            };

if (n==31) {

            x1=(14*height)/16;
```

```
        y1=(1*height)/16;
        x2=height/16;
        y2=height/16;

        };

if (n==32) {

        x1=(15*height)/16;
        y1=(1*height)/16;
        x2=height/16;
        y2=height/16;

        };

if (n==33) {

        x1=(0*height)/16;
        y1=(2*height)/16;
        x2=height/16;
        y2=height/16;

        };

if (n==34) {

        x1=(1*height)/16;
        y1=(2*height)/16;
        x2=height/16;
        y2=height/16;

        };

if (n==35) {

        x1=(2*height)/16;
        y1=(2*height)/16;
        x2=height/16;
        y2=height/16;

        };

if (n==36) {

        x1=(3*height)/16;
        y1=(2*height)/16;
        x2=height/16;
        y2=height/16;

        };

if (n==37) {

        x1=(4*height)/16;
        y1=(2*height)/16;
        x2=height/16;
```

```
        y2=height/16;

        };

if (n==38) {

        x1=(5*height)/16;
        y1=(2*height)/16;
        x2=height/16;
        y2=height/16;

        };

if (n==39) {

        x1=(6*height)/16;
        y1=(2*height)/16;
        x2=height/16;
        y2=height/16;

        };

if (n==40) {

        x1=(7*height)/16;
        y1=(2*height)/16;
        x2=height/16;
        y2=height/16;

        };

if (n==41) {

        x1=(8*height)/16;
        y1=(2*height)/16;
        x2=height/16;
        y2=height/16;

        };

if (n==42) {

        x1=(9*height)/16;
        y1=(2*height)/16;
        x2=height/16;
        y2=height/16;

        };

if (n==43) {

        x1=(10*height)/16;
        y1=(2*height)/16;
        x2=height/16;
        y2=height/16;
```

```
        };

if (n==44) {

        x1=(11*height)/16;
        y1=(2*height)/16;
        x2=height/16;
        y2=height/16;

        };

if (n==45) {

        x1=(12*height)/16;
        y1=(2*height)/16;
        x2=height/16;
        y2=height/16;

        };

if (n==46) {

        x1=(13*height)/16;
        y1=(2*height)/16;
        x2=height/16;
        y2=height/16;

        };

if (n==47) {

        x1=(14*height)/16;
        y1=(2*height)/16;
        x2=height/16;
        y2=height/16;

        };

if (n==48) {

        x1=(15*height)/16;
        y1=(2*height)/16;
        x2=height/16;
        y2=height/16;

        };

if (n==49) {

        x1=(0*height)/16;
        y1=(3*height)/16;
        x2=height/16;
        y2=height/16;

        };
```

```
if (n==50) {

        x1=(1*height)/16;
        y1=(3*height)/16;
        x2=height/16;
        y2=height/16;

        };

if (n==51) {

        x1=(2*height)/16;
        y1=(3*height)/16;
        x2=height/16;
        y2=height/16;

        };

if (n==52) {

        x1=(3*height)/16;
        y1=(3*height)/16;
        x2=height/16;
        y2=height/16;

        };

if (n==53) {

        x1=(4*height)/16;
        y1=(3*height)/16;
        x2=height/16;
        y2=height/16;

        };

if (n==54) {

        x1=(5*height)/16;
        y1=(3*height)/16;
        x2=height/16;
        y2=height/16;

        };

if (n==55) {

        x1=(6*height)/16;
        y1=(3*height)/16;
        x2=height/16;
        y2=height/16;

        };

if (n==56) {
```

```
            x1=(7*height)/16;
            y1=(3*height)/16;
            x2=height/16;
            y2=height/16;

            };

if (n==57) {

            x1=(8*height)/16;
            y1=(3*height)/16;
            x2=height/16;
            y2=height/16;

            };

if (n==58) {

            x1=(9*height)/16;
            y1=(3*height)/16;
            x2=height/16;
            y2=height/16;

            };

if (n==59) {

            x1=(10*height)/16;
            y1=(3*height)/16;
            x2=height/16;
            y2=height/16;

            };

if (n==60) {

            x1=(11*height)/16;
            y1=(3*height)/16;
            x2=height/16;
            y2=height/16;

            };

if (n==61) {

            x1=(12*height)/16;
            y1=(3*height)/16;
            x2=height/16;
            y2=height/16;

            };

if (n==62) {

            x1=(13*height)/16;
            y1=(3*height)/16;
```

```
        x2=height/16;
        y2=height/16;

        };

if (n==63) {

        x1=(14*height)/16;
        y1=(3*height)/16;
        x2=height/16;
        y2=height/16;

        };

if (n==64) {

        x1=(15*height)/16;
        y1=(3*height)/16;
        x2=height/16;
        y2=height/16;

        };

if (n==65) {

        x1=(0*height)/16;
        y1=(4*height)/16;
        x2=height/16;
        y2=height/16;

        };

if (n==66) {

        x1=(1*height)/16;
        y1=(4*height)/16;
        x2=height/16;
        y2=height/16;

        };

if (n==67) {

        x1=(2*height)/16;
        y1=(4*height)/16;
        x2=height/16;
        y2=height/16;

        };

if (n==68) {

        x1=(3*height)/16;
        y1=(4*height)/16;
        x2=height/16;
        y2=height/16;
```

```
        };

if (n==69) {

        x1=(4*height)/16;
        y1=(4*height)/16;
        x2=height/16;
        y2=height/16;

        };

if (n==70) {

        x1=(5*height)/16;
        y1=(4*height)/16;
        x2=height/16;
        y2=height/16;

        };

if (n==71) {

        x1=(6*height)/16;
        y1=(4*height)/16;
        x2=height/16;
        y2=height/16;

        };

if (n==72) {

        x1=(7*height)/16;
        y1=(4*height)/16;
        x2=height/16;
        y2=height/16;

        };

if (n==73) {

        x1=(8*height)/16;
        y1=(4*height)/16;
        x2=height/16;
        y2=height/16;

        };

if (n==74) {

        x1=(9*height)/16;
        y1=(4*height)/16;
        x2=height/16;
        y2=height/16;

        };
```

```
if (n==75) {

        x1=(10*height)/16;
        y1=(4*height)/16;
        x2=height/16;
        y2=height/16;

        };

if (n==76) {

        x1=(11*height)/16;
        y1=(4*height)/16;
        x2=height/16;
        y2=height/16;

        };

if (n==77) {

        x1=(12*height)/16;
        y1=(4*height)/16;
        x2=height/16;
        y2=height/16;

        };

if (n==78) {

        x1=(13*height)/16;
        y1=(4*height)/16;
        x2=height/16;
        y2=height/16;

        };

if (n==79) {

        x1=(14*height)/16;
        y1=(4*height)/16;
        x2=height/16;
        y2=height/16;

        };

if (n==80) {

        x1=(15*height)/16;
        y1=(4*height)/16;
        x2=height/16;
        y2=height/16;

        };

if (n==81) {
```

```
            x1=(0*height)/16;
            y1=(5*height)/16;
            x2=height/16;
            y2=height/16;

            };

if (n==82) {

            x1=(1*height)/16;
            y1=(5*height)/16;
            x2=height/16;
            y2=height/16;

            };

if (n==83) {

            x1=(2*height)/16;
            y1=(5*height)/16;
            x2=height/16;
            y2=height/16;

            };

if (n==84) {

            x1=(3*height)/16;
            y1=(5*height)/16;
            x2=height/16;
            y2=height/16;

            };

if (n==85) {

            x1=(4*height)/16;
            y1=(5*height)/16;
            x2=height/16;
            y2=height/16;

            };

if (n==86) {

            x1=(5*height)/16;
            y1=(5*height)/16;
            x2=height/16;
            y2=height/16;

            };

if (n==87) {

            x1=(6*height)/16;
```

```
        y1=(5*height)/16;
        x2=height/16;
        y2=height/16;

        };

if (n==88) {

        x1=(7*height)/16;
        y1=(5*height)/16;
        x2=height/16;
        y2=height/16;

        };

if (n==89) {

        x1=(8*height)/16;
        y1=(5*height)/16;
        x2=height/16;
        y2=height/16;

        };

if (n==90) {

        x1=(9*height)/16;
        y1=(5*height)/16;
        x2=height/16;
        y2=height/16;

        };

if (n==91) {

        x1=(10*height)/16;
        y1=(5*height)/16;
        x2=height/16;
        y2=height/16;

        };

if (n==92) {

        x1=(11*height)/16;
        y1=(5*height)/16;
        x2=height/16;
        y2=height/16;

        };

if (n==93) {

        x1=(12*height)/16;
        y1=(5*height)/16;
        x2=height/16;
```

```
        y2=height/16;

        };

if (n==94) {

        x1=(13*height)/16;
        y1=(5*height)/16;
        x2=height/16;
        y2=height/16;

        };

if (n==95) {

        x1=(14*height)/16;
        y1=(5*height)/16;
        x2=height/16;
        y2=height/16;

        };

if (n==96) {

        x1=(15*height)/16;
        y1=(5*height)/16;
        x2=height/16;
        y2=height/16;

        };

if (n==97) {

        x1=(0*height)/16;
        y1=(6*height)/16;
        x2=height/16;
        y2=height/16;

        };

if (n==98) {

        x1=(1*height)/16;
        y1=(6*height)/16;
        x2=height/16;
        y2=height/16;

        };

if (n==99) {

        x1=(2*height)/16;
        y1=(6*height)/16;
        x2=height/16;
        y2=height/16;
```

```
        };

if (n==100) {

        x1=(3*height)/16;
        y1=(6*height)/16;
        x2=height/16;
        y2=height/16;

        };

if (n==101) {

        x1=(4*height)/16;
        y1=(6*height)/16;
        x2=height/16;
        y2=height/16;

        };

if (n==102) {

        x1=(5*height)/16;
        y1=(6*height)/16;
        x2=height/16;
        y2=height/16;

        };

if (n==103) {

        x1=(6*height)/16;
        y1=(6*height)/16;
        x2=height/16;
        y2=height/16;

        };

if (n==104) {

        x1=(7*height)/16;
        y1=(6*height)/16;
        x2=height/16;
        y2=height/16;

        };

if (n==105) {

        x1=(8*height)/16;
        y1=(6*height)/16;
        x2=height/16;
        y2=height/16;

        };
```

```
if (n==106) {

        x1=(9*height)/16;
        y1=(6*height)/16;
        x2=height/16;
        y2=height/16;

        };

if (n==107) {

        x1=(10*height)/16;
        y1=(6*height)/16;
        x2=height/16;
        y2=height/16;

        };

if (n==108) {

        x1=(11*height)/16;
        y1=(6*height)/16;
        x2=height/16;
        y2=height/16;

        };

if (n==109) {

        x1=(12*height)/16;
        y1=(6*height)/16;
        x2=height/16;
        y2=height/16;

        };

if (n==110) {

        x1=(13*height)/16;
        y1=(6*height)/16;
        x2=height/16;
        y2=height/16;

        };

if (n==111) {

        x1=(14*height)/16;
        y1=(6*height)/16;
        x2=height/16;
        y2=height/16;

        };

if (n==112) {
```

```
            x1=(15*height)/16;
            y1=(6*height)/16;
            x2=height/16;
            y2=height/16;

            };

if (n==113) {

            x1=(0*height)/16;
            y1=(7*height)/16;
            x2=height/16;
            y2=height/16;

            };

if (n==114) {

            x1=(1*height)/16;
            y1=(7*height)/16;
            x2=height/16;
            y2=height/16;

            };

if (n==115) {

            x1=(2*height)/16;
            y1=(7*height)/16;
            x2=height/16;
            y2=height/16;

            };

if (n==116) {

            x1=(3*height)/16;
            y1=(7*height)/16;
            x2=height/16;
            y2=height/16;

            };

if (n==117) {

            x1=(4*height)/16;
            y1=(7*height)/16;
            x2=height/16;
            y2=height/16;

            };

if (n==118) {

            x1=(5*height)/16;
            y1=(7*height)/16;
```

```
        x2=height/16;
        y2=height/16;

        };

if (n==119) {

        x1=(6*height)/16;
        y1=(7*height)/16;
        x2=height/16;
        y2=height/16;

        };

if (n==120) {

        x1=(7*height)/16;
        y1=(7*height)/16;
        x2=height/16;
        y2=height/16;

        };

if (n==121) {

        x1=(8*height)/16;
        y1=(7*height)/16;
        x2=height/16;
        y2=height/16;

        };

if (n==122) {

        x1=(9*height)/16;
        y1=(7*height)/16;
        x2=height/16;
        y2=height/16;

        };

if (n==123) {

        x1=(10*height)/16;
        y1=(7*height)/16;
        x2=height/16;
        y2=height/16;

        };

if (n==124) {

        x1=(11*height)/16;
        y1=(7*height)/16;
        x2=height/16;
        y2=height/16;
```

```
        };

if (n==125) {

        x1=(12*height)/16;
        y1=(7*height)/16;
        x2=height/16;
        y2=height/16;

        };

if (n==126) {

        x1=(13*height)/16;
        y1=(7*height)/16;
        x2=height/16;
        y2=height/16;

        };

if (n==127) {

        x1=(14*height)/16;
        y1=(7*height)/16;
        x2=height/16;
        y2=height/16;

        };

if (n==128) {

        x1=(15*height)/16;
        y1=(7*height)/16;
        x2=height/16;
        y2=height/16;

        };

if (n==129) {

        x1=(0*height)/16;
        y1=(8*height)/16;
        x2=height/16;
        y2=height/16;

        };

if (n==130) {

        x1=(1*height)/16;
        y1=(8*height)/16;
        x2=height/16;
        y2=height/16;

        };
```

```
if (n==131) {

        x1=(2*height)/16;
        y1=(8*height)/16;
        x2=height/16;
        y2=height/16;

        };

if (n==132) {

        x1=(3*height)/16;
        y1=(8*height)/16;
        x2=height/16;
        y2=height/16;

        };

if (n==133) {

        x1=(4*height)/16;
        y1=(8*height)/16;
        x2=height/16;
        y2=height/16;

        };

if (n==134) {

        x1=(5*height)/16;
        y1=(8*height)/16;
        x2=height/16;
        y2=height/16;

        };

if (n==135) {

        x1=(6*height)/16;
        y1=(8*height)/16;
        x2=height/16;
        y2=height/16;

        };

if (n==136) {

        x1=(7*height)/16;
        y1=(8*height)/16;
        x2=height/16;
        y2=height/16;

        };

if (n==137) {
```

```
            x1=(8*height)/16;
            y1=(8*height)/16;
            x2=height/16;
            y2=height/16;

            };

if (n==138) {

            x1=(9*height)/16;
            y1=(8*height)/16;
            x2=height/16;
            y2=height/16;

            };

if (n==139) {

            x1=(10*height)/16;
            y1=(8*height)/16;
            x2=height/16;
            y2=height/16;

            };

if (n==140) {

            x1=(11*height)/16;
            y1=(8*height)/16;
            x2=height/16;
            y2=height/16;

            };

if (n==141) {

            x1=(12*height)/16;
            y1=(8*height)/16;
            x2=height/16;
            y2=height/16;

            };

if (n==142) {

            x1=(13*height)/16;
            y1=(8*height)/16;
            x2=height/16;
            y2=height/16;

            };

if (n==143) {

            x1=(14*height)/16;
```

```
            y1=(8*height)/16;
            x2=height/16;
            y2=height/16;

            };

if (n==144) {

            x1=(15*height)/16;
            y1=(8*height)/16;
            x2=height/16;
            y2=height/16;

            };

if (n==145) {

            x1=(0*height)/16;
            y1=(9*height)/16;
            x2=height/16;
            y2=height/16;

            };

if (n==146) {

            x1=(1*height)/16;
            y1=(9*height)/16;
            x2=height/16;
            y2=height/16;

            };

if (n==147) {

            x1=(2*height)/16;
            y1=(9*height)/16;
            x2=height/16;
            y2=height/16;

            };

if (n==148) {

            x1=(3*height)/16;
            y1=(9*height)/16;
            x2=height/16;
            y2=height/16;

            };

if (n==149) {

            x1=(4*height)/16;
            y1=(9*height)/16;
            x2=height/16;
```

```
        y2=height/16;

        };

if (n==150) {

        x1=(5*height)/16;
        y1=(9*height)/16;
        x2=height/16;
        y2=height/16;

        };

if (n==151) {

        x1=(6*height)/16;
        y1=(9*height)/16;
        x2=height/16;
        y2=height/16;

        };

if (n==152) {

        x1=(7*height)/16;
        y1=(9*height)/16;
        x2=height/16;
        y2=height/16;

        };

if (n==153) {

        x1=(8*height)/16;
        y1=(9*height)/16;
        x2=height/16;
        y2=height/16;

        };

if (n==154) {

        x1=(9*height)/16;
        y1=(9*height)/16;
        x2=height/16;
        y2=height/16;

        };

if (n==155) {

        x1=(10*height)/16;
        y1=(9*height)/16;
        x2=height/16;
        y2=height/16;
```

```
        };

if (n==156) {

        x1=(11*height)/16;
        y1=(9*height)/16;
        x2=height/16;
        y2=height/16;

        };

if (n==157) {

        x1=(12*height)/16;
        y1=(9*height)/16;
        x2=height/16;
        y2=height/16;

        };

if (n==158) {

        x1=(13*height)/16;
        y1=(9*height)/16;
        x2=height/16;
        y2=height/16;

        };

if (n==159) {

        x1=(14*height)/16;
        y1=(9*height)/16;
        x2=height/16;
        y2=height/16;

        };

if (n==160) {

        x1=(15*height)/16;
        y1=(9*height)/16;
        x2=height/16;
        y2=height/16;

        };

if (n==161) {

        x1=(0*height)/16;
        y1=(10*height)/16;
        x2=height/16;
        y2=height/16;

        };
```

```
if (n==162) {

        x1=(1*height)/16;
        y1=(10*height)/16;
        x2=height/16;
        y2=height/16;

        };

if (n==163) {

        x1=(2*height)/16;
        y1=(10*height)/16;
        x2=height/16;
        y2=height/16;

        };

if (n==164) {

        x1=(3*height)/16;
        y1=(10*height)/16;
        x2=height/16;
        y2=height/16;

        };

if (n==165) {

        x1=(4*height)/16;
        y1=(10*height)/16;
        x2=height/16;
        y2=height/16;

        };

if (n==166) {

        x1=(5*height)/16;
        y1=(10*height)/16;
        x2=height/16;
        y2=height/16;

        };

if (n==167) {

        x1=(6*height)/16;
        y1=(10*height)/16;
        x2=height/16;
        y2=height/16;

        };

if (n==168) {
```

```
            x1=(7*height)/16;
            y1=(10*height)/16;
            x2=height/16;
            y2=height/16;

            };

if (n==169) {

            x1=(8*height)/16;
            y1=(10*height)/16;
            x2=height/16;
            y2=height/16;

            };

if (n==170) {

            x1=(9*height)/16;
            y1=(10*height)/16;
            x2=height/16;
            y2=height/16;

            };

if (n==171) {

            x1=(10*height)/16;
            y1=(10*height)/16;
            x2=height/16;
            y2=height/16;

            };

if (n==172) {

            x1=(11*height)/16;
            y1=(10*height)/16;
            x2=height/16;
            y2=height/16;

            };

if (n==173) {

            x1=(12*height)/16;
            y1=(10*height)/16;
            x2=height/16;
            y2=height/16;

            };

if (n==174) {

            x1=(13*height)/16;
            y1=(10*height)/16;
```

```
        x2=height/16;
        y2=height/16;

        };

if (n==175) {

        x1=(14*height)/16;
        y1=(10*height)/16;
        x2=height/16;
        y2=height/16;

        };

if (n==176) {

        x1=(15*height)/16;
        y1=(10*height)/16;
        x2=height/16;
        y2=height/16;

        };

if (n==177) {

        x1=(0*height)/16;
        y1=(11*height)/16;
        x2=height/16;
        y2=height/16;

        };

if (n==178) {

        x1=(1*height)/16;
        y1=(11*height)/16;
        x2=height/16;
        y2=height/16;

        };

if (n==179) {

        x1=(2*height)/16;
        y1=(11*height)/16;
        x2=height/16;
        y2=height/16;

        };

if (n==180) {

        x1=(3*height)/16;
        y1=(11*height)/16;
        x2=height/16;
        y2=height/16;
```

```
        };

if (n==181) {

        x1=(4*height)/16;
        y1=(11*height)/16;
        x2=height/16;
        y2=height/16;

        };

if (n==182) {

        x1=(5*height)/16;
        y1=(11*height)/16;
        x2=height/16;
        y2=height/16;

        };

if (n==183) {

        x1=(6*height)/16;
        y1=(11*height)/16;
        x2=height/16;
        y2=height/16;

        };

if (n==184) {

        x1=(7*height)/16;
        y1=(11*height)/16;
        x2=height/16;
        y2=height/16;

        };

if (n==185) {

        x1=(8*height)/16;
        y1=(11*height)/16;
        x2=height/16;
        y2=height/16;

        };

if (n==186) {

        x1=(9*height)/16;
        y1=(11*height)/16;
        x2=height/16;
        y2=height/16;

        };
```

```
if (n==187) {

        x1=(10*height)/16;
        y1=(11*height)/16;
        x2=height/16;
        y2=height/16;

        };

if (n==188) {

        x1=(11*height)/16;
        y1=(11*height)/16;
        x2=height/16;
        y2=height/16;

        };

if (n==189) {

        x1=(12*height)/16;
        y1=(11*height)/16;
        x2=height/16;
        y2=height/16;

        };

if (n==190) {

        x1=(13*height)/16;
        y1=(11*height)/16;
        x2=height/16;
        y2=height/16;

        };

if (n==191) {

        x1=(14*height)/16;
        y1=(11*height)/16;
        x2=height/16;
        y2=height/16;

        };

if (n==192) {

        x1=(15*height)/16;
        y1=(11*height)/16;
        x2=height/16;
        y2=height/16;

        };

if (n==193) {
```

```
            x1=(0*height)/16;
            y1=(12*height)/16;
            x2=height/16;
            y2=height/16;

            };

if (n==194) {

            x1=(1*height)/16;
            y1=(12*height)/16;
            x2=height/16;
            y2=height/16;

            };

if (n==195) {

            x1=(2*height)/16;
            y1=(12*height)/16;
            x2=height/16;
            y2=height/16;

            };

if (n==196) {

            x1=(3*height)/16;
            y1=(12*height)/16;
            x2=height/16;
            y2=height/16;

            };

if (n==197) {

            x1=(4*height)/16;
            y1=(12*height)/16;
            x2=height/16;
            y2=height/16;

            };

if (n==198) {

            x1=(5*height)/16;
            y1=(12*height)/16;
            x2=height/16;
            y2=height/16;

            };

if (n==199) {

            x1=(6*height)/16;
```

```
        y1=(12*height)/16;
        x2=height/16;
        y2=height/16;

        };

if (n==200) {

        x1=(7*height)/16;
        y1=(12*height)/16;
        x2=height/16;
        y2=height/16;

        };

if (n==201) {

        x1=(8*height)/16;
        y1=(12*height)/16;
        x2=height/16;
        y2=height/16;

        };

if (n==202) {

        x1=(9*height)/16;
        y1=(12*height)/16;
        x2=height/16;
        y2=height/16;

        };

if (n==203) {

        x1=(10*height)/16;
        y1=(12*height)/16;
        x2=height/16;
        y2=height/16;

        };

if (n==204) {

        x1=(11*height)/16;
        y1=(12*height)/16;
        x2=height/16;
        y2=height/16;

        };

if (n==205) {

        x1=(12*height)/16;
        y1=(12*height)/16;
        x2=height/16;
```

```
        y2=height/16;

        };

if (n==206) {

        x1=(13*height)/16;
        y1=(12*height)/16;
        x2=height/16;
        y2=height/16;

        };

if (n==207) {

        x1=(14*height)/16;
        y1=(12*height)/16;
        x2=height/16;
        y2=height/16;

        };

if (n==208) {

        x1=(15*height)/16;
        y1=(12*height)/16;
        x2=height/16;
        y2=height/16;

        };

if (n==209) {

        x1=(0*height)/16;
        y1=(13*height)/16;
        x2=height/16;
        y2=height/16;

        };

if (n==210) {

        x1=(1*height)/16;
        y1=(13*height)/16;
        x2=height/16;
        y2=height/16;

        };

if (n==211) {

        x1=(2*height)/16;
        y1=(13*height)/16;
        x2=height/16;
        y2=height/16;
```

```
        };

if (n==212) {

        x1=(3*height)/16;
        y1=(13*height)/16;
        x2=height/16;
        y2=height/16;

        };

if (n==213) {

        x1=(4*height)/16;
        y1=(13*height)/16;
        x2=height/16;
        y2=height/16;

        };

if (n==214) {

        x1=(5*height)/16;
        y1=(13*height)/16;
        x2=height/16;
        y2=height/16;

        };

if (n==215) {

        x1=(6*height)/16;
        y1=(13*height)/16;
        x2=height/16;
        y2=height/16;

        };

if (n==216) {

        x1=(7*height)/16;
        y1=(13*height)/16;
        x2=height/16;
        y2=height/16;

        };

if (n==217) {

        x1=(8*height)/16;
        y1=(13*height)/16;
        x2=height/16;
        y2=height/16;

        };
```

```
if (n==218) {

        x1=(9*height)/16;
        y1=(13*height)/16;
        x2=height/16;
        y2=height/16;

        };

if (n==219) {

        x1=(10*height)/16;
        y1=(13*height)/16;
        x2=height/16;
        y2=height/16;

        };

if (n==220) {

        x1=(11*height)/16;
        y1=(13*height)/16;
        x2=height/16;
        y2=height/16;

        };

if (n==221) {

        x1=(12*height)/16;
        y1=(13*height)/16;
        x2=height/16;
        y2=height/16;

        };

if (n==222) {

        x1=(13*height)/16;
        y1=(13*height)/16;
        x2=height/16;
        y2=height/16;

        };

if (n==223) {

        x1=(14*height)/16;
        y1=(13*height)/16;
        x2=height/16;
        y2=height/16;

        };

if (n==224) {
```

```
            x1=(15*height)/16;
            y1=(13*height)/16;
            x2=height/16;
            y2=height/16;

            };

if (n==225) {

            x1=(0*height)/16;
            y1=(14*height)/16;
            x2=height/16;
            y2=height/16;

            };

if (n==226) {

            x1=(1*height)/16;
            y1=(14*height)/16;
            x2=height/16;
            y2=height/16;

            };

if (n==227) {

            x1=(2*height)/16;
            y1=(14*height)/16;
            x2=height/16;
            y2=height/16;

            };

if (n==228) {

            x1=(3*height)/16;
            y1=(14*height)/16;
            x2=height/16;
            y2=height/16;

            };

if (n==229) {

            x1=(4*height)/16;
            y1=(14*height)/16;
            x2=height/16;
            y2=height/16;

            };

if (n==230) {

            x1=(5*height)/16;
            y1=(14*height)/16;
```

```
            x2=height/16;
            y2=height/16;

            };

if (n==231) {

            x1=(6*height)/16;
            y1=(14*height)/16;
            x2=height/16;
            y2=height/16;

            };

if (n==232) {

            x1=(7*height)/16;
            y1=(14*height)/16;
            x2=height/16;
            y2=height/16;

            };

if (n==233) {

            x1=(8*height)/16;
            y1=(14*height)/16;
            x2=height/16;
            y2=height/16;

            };

if (n==234) {

            x1=(9*height)/16;
            y1=(14*height)/16;
            x2=height/16;
            y2=height/16;

            };

if (n==235) {

            x1=(10*height)/16;
            y1=(14*height)/16;
            x2=height/16;
            y2=height/16;

            };

if (n==236) {

            x1=(11*height)/16;
            y1=(14*height)/16;
            x2=height/16;
            y2=height/16;
```

```
        };

if (n==237) {

        x1=(12*height)/16;
        y1=(14*height)/16;
        x2=height/16;
        y2=height/16;

        };

if (n==238) {

        x1=(13*height)/16;
        y1=(14*height)/16;
        x2=height/16;
        y2=height/16;

        };

if (n==239) {

        x1=(14*height)/16;
        y1=(14*height)/16;
        x2=height/16;
        y2=height/16;

        };

if (n==240) {

        x1=(15*height)/16;
        y1=(14*height)/16;
        x2=height/16;
        y2=height/16;

        };

if (n==241) {

        x1=(0*height)/16;
        y1=(15*height)/16;
        x2=height/16;
        y2=height/16;

        };

if (n==242) {

        x1=(1*height)/16;
        y1=(15*height)/16;
        x2=height/16;
        y2=height/16;

        };
```

```
if (n==243) {

        x1=(2*height)/16;
        y1=(15*height)/16;
        x2=height/16;
        y2=height/16;

        };

if (n==244) {

        x1=(3*height)/16;
        y1=(15*height)/16;
        x2=height/16;
        y2=height/16;

        };

if (n==245) {

        x1=(4*height)/16;
        y1=(15*height)/16;
        x2=height/16;
        y2=height/16;

        };

if (n==246) {

        x1=(5*height)/16;
        y1=(15*height)/16;
        x2=height/16;
        y2=height/16;

        };

if (n==247) {

        x1=(6*height)/16;
        y1=(15*height)/16;
        x2=height/16;
        y2=height/16;

        };

if (n==248) {

        x1=(7*height)/16;
        y1=(15*height)/16;
        x2=height/16;
        y2=height/16;

        };

if (n==249) {
```

```
            x1=(8*height)/16;
            y1=(15*height)/16;
            x2=height/16;
            y2=height/16;

            };

if (n==250) {

            x1=(9*height)/16;
            y1=(15*height)/16;
            x2=height/16;
            y2=height/16;

            };

if (n==251) {

            x1=(10*height)/16;
            y1=(15*height)/16;
            x2=height/16;
            y2=height/16;

            };

if (n==252) {

            x1=(11*height)/16;
            y1=(15*height)/16;
            x2=height/16;
            y2=height/16;

            };

if (n==253) {

            x1=(12*height)/16;
            y1=(15*height)/16;
            x2=height/16;
            y2=height/16;

            };

if (n==254) {

            x1=(13*height)/16;
            y1=(15*height)/16;
            x2=height/16;
            y2=height/16;

            };

if (n==255) {

            x1=(14*height)/16;
```

```
        y1=(15*height)/16;
        x2=height/16;
        y2=height/16;

        };

if (n==256) {

        x1=(15*height)/16;
        y1=(15*height)/16;
        x2=height/16;
        y2=height/16;


        };


        cell = "16x16 Cell "+n+" of 256";

        rename(cell);
        newtitle=getTitle;

makeRectangle(x1, y1, x2, y2 );




run("Set Measurements...", "centroid redirect=None decimal=2");

run("Analyze Particles...", "minimum=1 maximum=999999999 bins=100 show=Nothing display clear
summarize");       // show results without image          // show results without image


//run("Analyze Particles...", "minimum=1 maximum=999999999 bins=100 show=Outlines display clear");
        // show results with image

//run("Analyze Particles...", "minimum=1 maximum=9999 bins=100 show=Outlines clear");          //don't
show results

q="Q"+n+" - ";
p=nResults;

directory="/Documents and Settings/Adam/Desktop/Split Images/Split Results/16x16/";

path=directory+q+title+" - "+p+" particles.xls";

selectWindow("Results");
saveAs("Measurements",path );

selectWindow(newtitle);
rename(title);
selectWindow(title);

directory2="/Documents and Settings/Adam/Desktop/Split Images/Split Results/";
```

```
path2=directory2+title+" - results.xls";

selectWindow("Summary");
saveAs("text",path2 );

selectWindow(title);

restoreSettings();

                                }
```

9.1 Appendix A: Pair Correlation g(r) Code

```
// Define Variables
//-------------------------------------

var x=1;
var y=1;
var p=1;
var r=1;
var q=0;
var height=0;
var width=0;
var bmin=0.0;
var bmax=0.0;

var bwidth=1;  //bin width

var dx=0.0;
var dy=0.0;
var bnum=0;
var distij=0.0;
var rnddistij=0;
var maxvalue=0;
var grmaxvalue=0;
var density=0;
var roh=0;
var r=0;
var Jr=0;
var gr=0;
var Gr=0;
var val=0.0;
var scaler=1000000;                    // to convert from um to m
var rndbmax=0;
var grmin=0;
var grmax=0;
var title=0;


rijlist = newArray(10000);
rijxval = newArray(10000);
grlist = newArray(10000);
Grlist = newArray(10000);
DensityArray = newArray(10000);
line1 = newArray(10000);
line2 = newArray(10000);

//setLocation(0, 25);



//-------------------------------------

// "ParticleClusterAnalysis"
// Displays the percentage of particles that have a
```

```
// neighbor within 13nm (center-to-center). Such particles

// are assumed to be part of a cluster. The scale

// is assumed to be 3.997 pixels/nm.



title = getTitle;


//maxDistance = 500;        //um      //for PIXE work
maxDistance = 5300;        //um       //for microprobe work


height = getHeight;



//scale = 1;

//scale = 0.788;  //pixels/um


//scale = height/500;     //for PIXE work
scale = height/5300;   //for microprobe work



run("Set Scale...", "distance="+scale+" known=1 unit=um pixel=1");

title = getTitle();
//setAutoThreshold();
saveSettings();
run("Set Measurements...", "centroid redirect=None decimal=2");

 run("Analyze Particles...", "minimum=1 maximum=999999999 bins=100 show=Outlines display clear");
            // show results

//run("Analyze Particles...", "minimum=1 maximum=9999 bins=100 show=Outlines clear");          //don't
show results

restoreSettings();

n = nResults;
xloc = newArray(n);
yloc = newArray(n);

for (i=0; i<n; i++) {
            xloc[i] = getResult("X", i);
            yloc[i] = getResult("Y", i);    }

count = 0;
   for (i=0; i<n; i++) {
```

```
      if (i%10==0) showProgress(i, n);
      found = false;
      j = 0;
      while (j<n && !found) {
         dx = xloc[j]-xloc[i];
         dy = yloc[j]-yloc[i];
         distance = sqrt(dx*dx+dy*dy);
         if (distance>0 && distance<maxDistance) {
            count++;
            found = true;
         }
         j++;
      }
   }
   //print(title+": "+count+" out of "+n+" ("+d2s(count/n*100,2)+"%) particles are in clusters");


//setLocation(0, 475);


//-------------------------------------


            height = getHeight()/scale;              //image height (pixels)
            width = getWidth()/scale;  //image width (pixels)


            bmax = width/2;
            rndbmax = round(bmax);




            p = nResults;    //no of particles



/*
//-------------------------------------

 for (i=0; i<p; i++) {                           //loop to output centroid positions to summary


            x = getResult("X",i);
            y = getResult("Y",i);
            print(x);
            print(y);

            }

//-------------------------------------
*/
```

```
x1 = newArray(nResults);                    //array of centroid 'x' values
for (i=0; i<x1.length; i++)
   x1[i] = getResult("X",i);


y1 = newArray(nResults);                    //array of centroid 'y' values
for (i=0; i<y1.length; i++)
   y1[i] = getResult("Y",i);




        bnum = ((bmax-bmin)/bwidth)  // Number of bins

        denisty = p/((height)/scaler*(width)/scaler);          // Density


for (i=0; i<=bnum; i++){
   rijlist[i] = 0;
   grlist[i] = 0.0;
   Grlist[i] = 0.0;
   rijxval[i] = bmin+bwidth*i;
   line1[i] = 1;

   //DensityArray[i] = denisty;


                        }

        line1[bnum] = 0;


        f = File.open("/Documents and Settings/Adam/Desktop/rijlist.txt");          // Print rijlist to
file

lines=0;


 for (i=0; i<p; i++){




        for (j=i+1; j<p; j++)       {


                dx = abs(x1[i]-x1[j]);
```

```
                dy = abs(y1[i]-y1[j]);


if (i==4) {

                //drawLine(x1[i]*scale, y1[i]*scale, x1[j]*scale, y1[j]*scale);          // draw
connecting lines between particles

        };


if(2<distij){
        if(distij<4){

                        //drawLine(x1[i]*scale, y1[i]*scale, x1[j]*scale, y1[j]*scale);          // draw
connecting lines between particles of particular distance
                        lines=lines+1;
                        //print(distij);
                }
        }



                //drawLine(x1[i]*scale, y1[i]*scale, x1[j]*scale, y1[j]*scale);          // draw
connecting lines between particles

                //print("i = "+i+" j = "+j+"dx = "+dx+" dy = "+dy);


                if (dx>bmax) dx = width-dx;
                if (dy>bmax) dy = width-dy;

                distij = sqrt(dx*dx+dy*dy);
                rnddistij = round((distij-bmin)/bwidth);







                // print("rnddistij: "+rnddistij+"("+distij+")");



                if (distij<bmax) {

                                rijlist[rnddistij]=rijlist[rnddistij]+1;
```

```
                    if (maxvalue<rijlist[rnddistij]) maxvalue=rijlist[rnddistij];

                                        //print("rijxval: "+rijxval[i]+"   "+"rijist: "+rijlist[i]);









                                }



                                }

                        }

                rijlist[bmax] = 0;


                Plot.create(title+" - Rij", "r (µm)", "rij", rijxval, rijlist);          //plot r(ij)

                Plot.setLimits(0, rndbmax-1, 0, maxvalue+1);
                Plot.show();


print(lines);


/*
//-----------------------------------
                                                        // image of centroids


newImage("Centroids", "8-bit", width*scale, height*scale, 1)


for (i=0; i<p; i++)          {

drawOval((x1[i]*scale)-2.5, (y1[i]*scale)-2.5, 5, 5);


                        }


//-----------------------------------
*/
```

```
//  g(r):


        for (i=0; i<=bnum; i++)     {


                r = (bmin+(i+0.5)*bwidth)/scaler;

                Jr = rijlist[i] / p;                //Dougals:  Jr = 2*rijlist[i] / p;

                rho = Jr / (2*PI*r*(bwidth/scaler));



                val = rho / (p/((height)/scaler*(width)/scaler));                       //  val = rho/density

                grlist[i] = val;


         // if (maxvalue<rijlist[rnddistij]) maxvalue=rijlist[rnddistij];


                //print(f, r +"\t"+ Jr +"\t "+ rho +"\t"+ density +"\t"+ val +"\t"+grlist[i]);   //print results to
file


                //grlist[i] = (rijlist[i]/(2*PI*r))/DensityArray[i];


                //print("i = "+i+"   grlist "+grlist[i]+"   Density: "+DensityArray[i]);

                //print("i = "+i+"   "+"line1 = "+line1[i]);


                grmin = minOf(grlist[i],grmin);
                grmax = maxOf(grlist[i],grmax);
```

```
//print("grmin = "+grmin+"  "+"grmax = "+grmax);


}


grmin = round(grmin-0.5);
grmax = round(grmax+0.5);

//print("grmin = "+grmin+"  "+"grmax = "+grmax);


Plot.create(title+" - g(r) full", "r (µm)", "g(r)", rijxval, grlist);   //plot g(r)

Plot.setLimits(0, rndbmax-1, grmin, grmax);
drawLine(0, 1, bmax, 1);
setLineWidth(1)


Plot.add("line", rijxval, line1);

Plot.show();



Plot.create(title+" - g(r) limited x", "r (µm)", "g(r)", rijxval, grlist);        //plot g(r)

Plot.setLimits(0, 50, grmin, grmax);
drawLine(0, 1, 50, 1);
setLineWidth(1)

Plot.add("line", rijxval, line1);

//Plot.setLimits(0, bmax, 0, maxvalue+1);

Plot.show();
drawLine(0, 1, 50, 1);


// G(r)
//
//
//          for (i=0; i<=bnum; i++)     {
//
//
//                    r = bmin+(i-0.5)*bwidth;
//
//                    Grlist[i] = 2*PI*DensityArray[i]*r*(grlist[i]-1);
//
//
```

```
//
//
                    //print(f, rijxval[i] +"\t"+ rijlist[i] +"\t "+ grlist[i] +"\t"+ Grlist[i]);   //print results to file
                            }



                    //Plot.create("G(r)", "r", "G(r)", rijxval, Grlist);          //plot g(r)
                    //Plot.setLimits(0, bmax, 0, maxvalue+1);
                    //Plot.show()




/*
//Print summary


print("--------------------SUMMARY------------------------------")

print("particles: "+p);
print("width: "+width);
print("height: "+height);
print("bmax: "+bmax);
print("bnum: "+bnum);
print("density: "+denisty);
print("maxvalue: "+maxvalue);

print("---------------------------------------------------------------")

*/
```

9.2 Appendix C: Pair Correlation g(r) Plots for PIXE Data

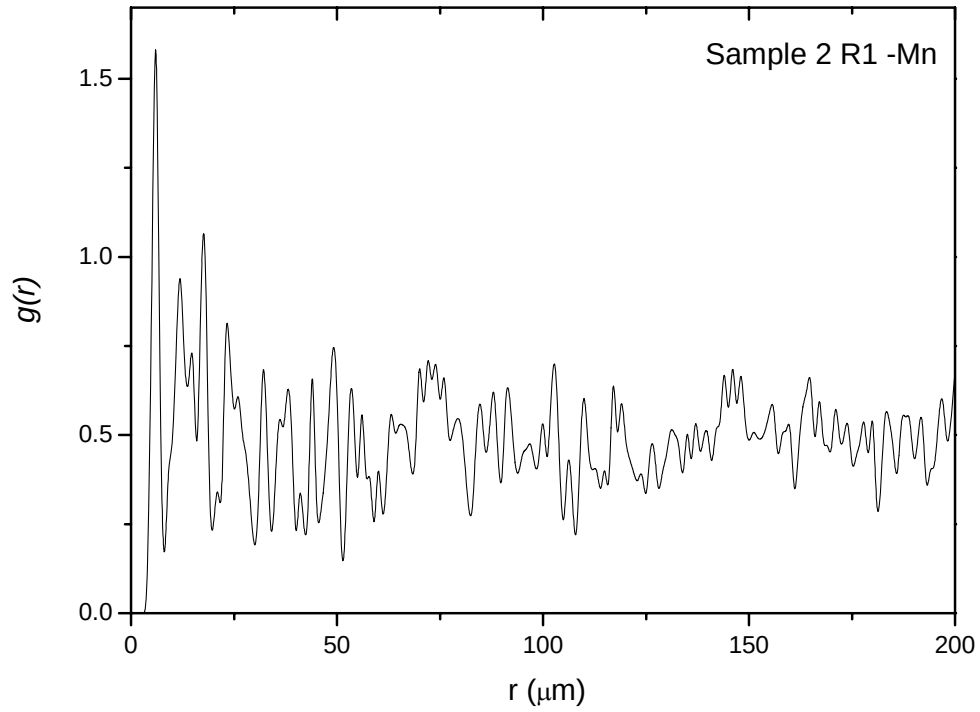

Figure 9-1: Pair correlation g(r) plot for PIXE sample 2 R1 Mn

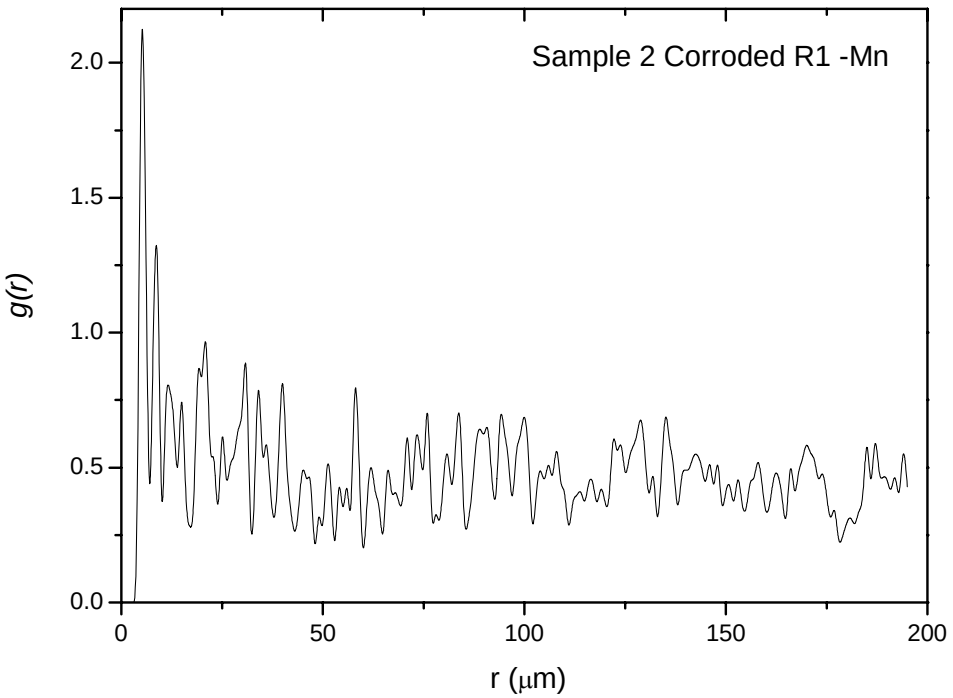

Figure 9-2: Pair correlation g(r) plot for PIXE sample 2 corroded R1 Mn

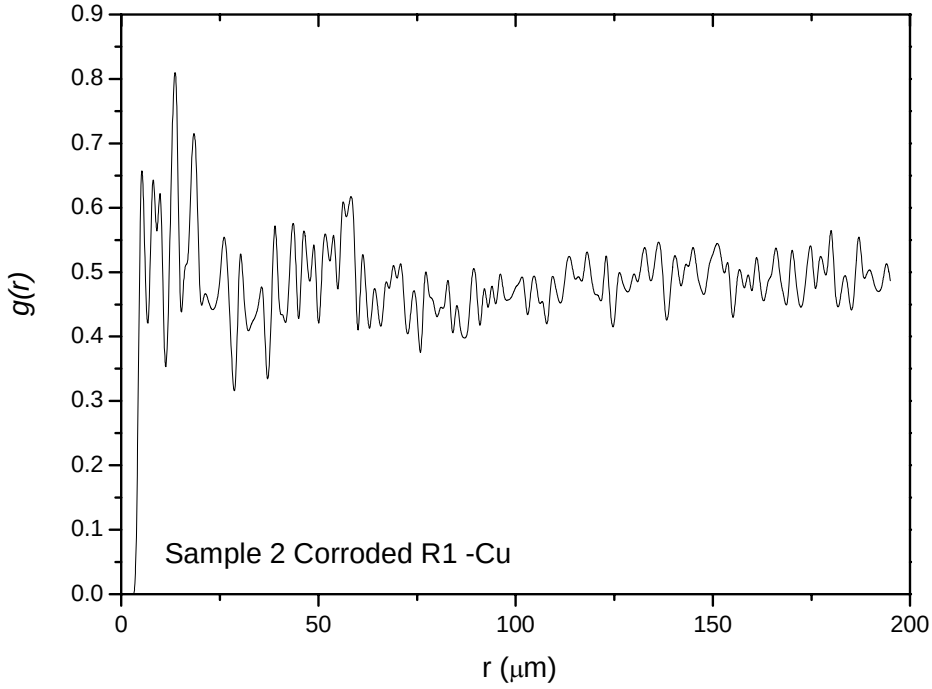

Figure 9-3: Pair correlation g(r) plot for PIXE sample 2 corroded R1 Cu

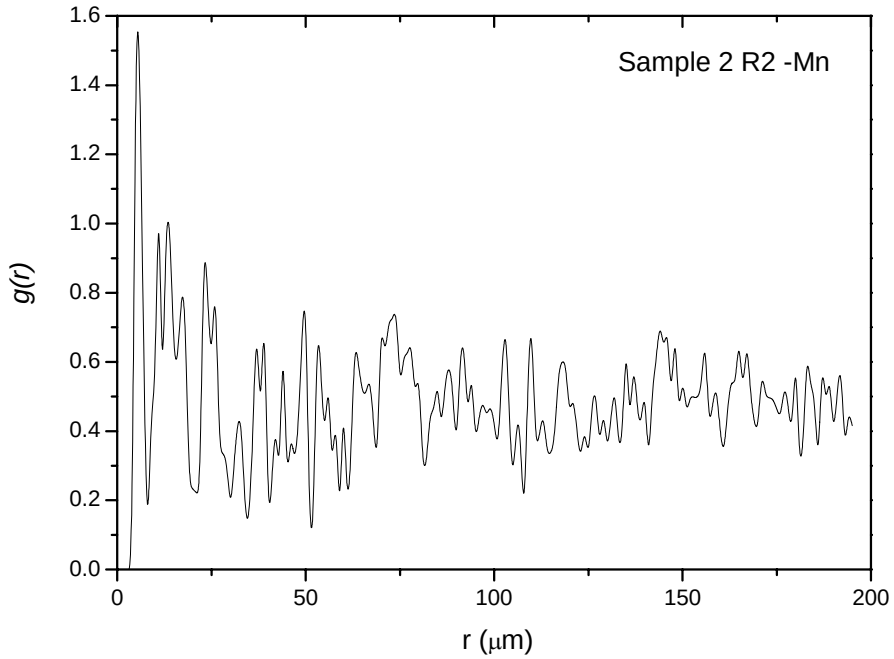

Figure 9-4: Pair correlation g(r) plot for PIXE sample 2 R2 Mn

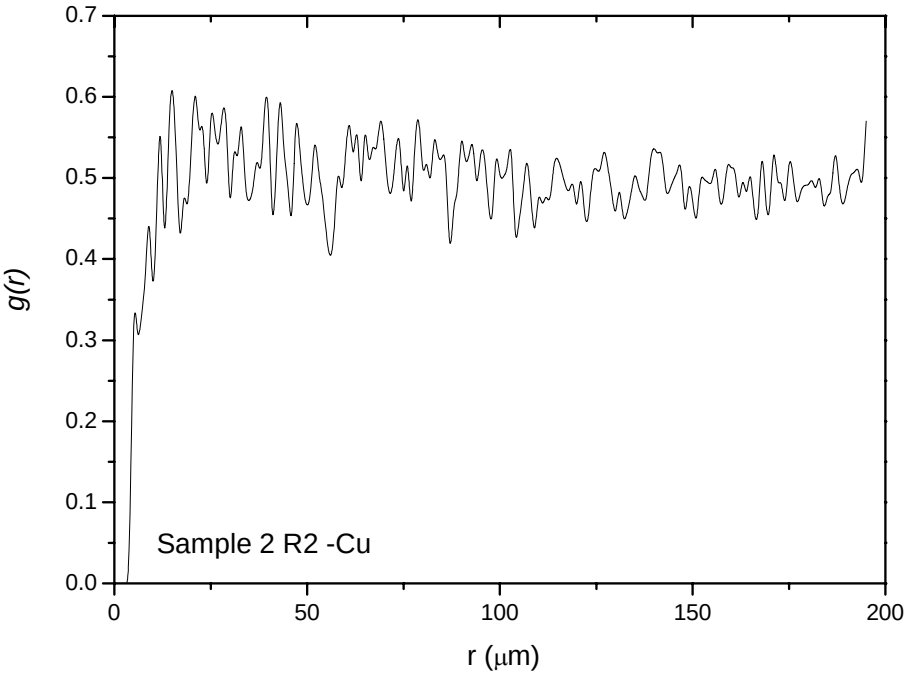

Figure 9-5: Pair correlation g(r) plot for PIXE sample 2 R2 Cu

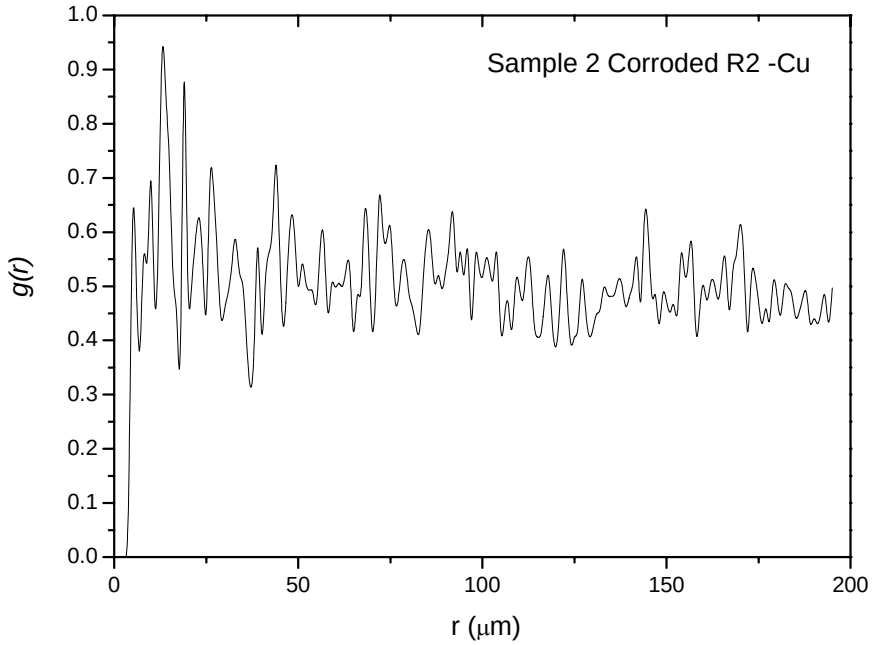

Figure 9-6: Pair correlation g(r) plot for PIXE sample 2 corroded R2 Cu

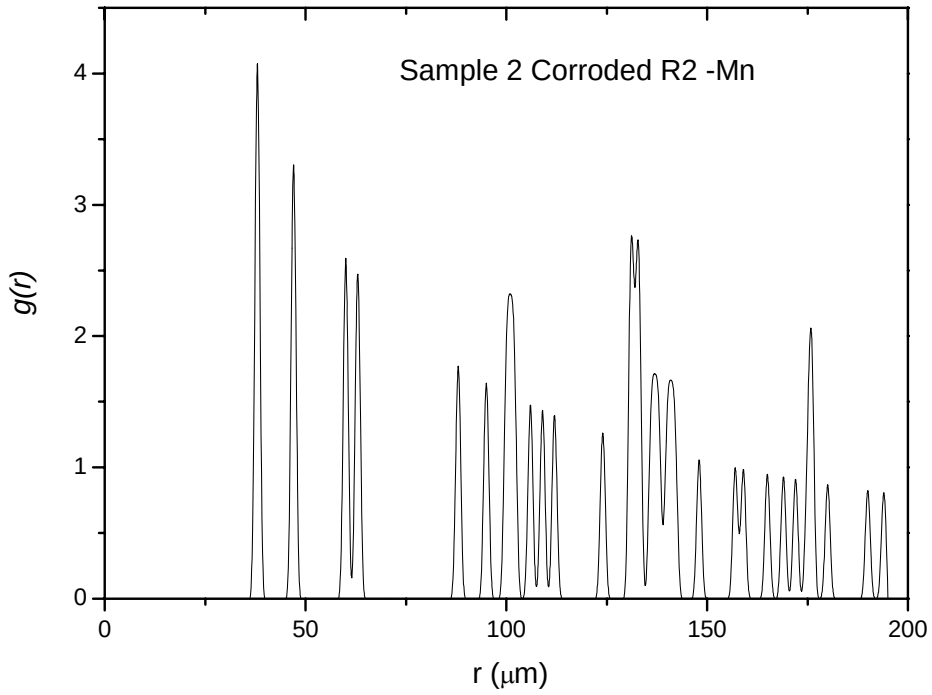

Figure 9-7: Pair correlation g(r) plot for PIXE sample 2 corroded R2 Mn

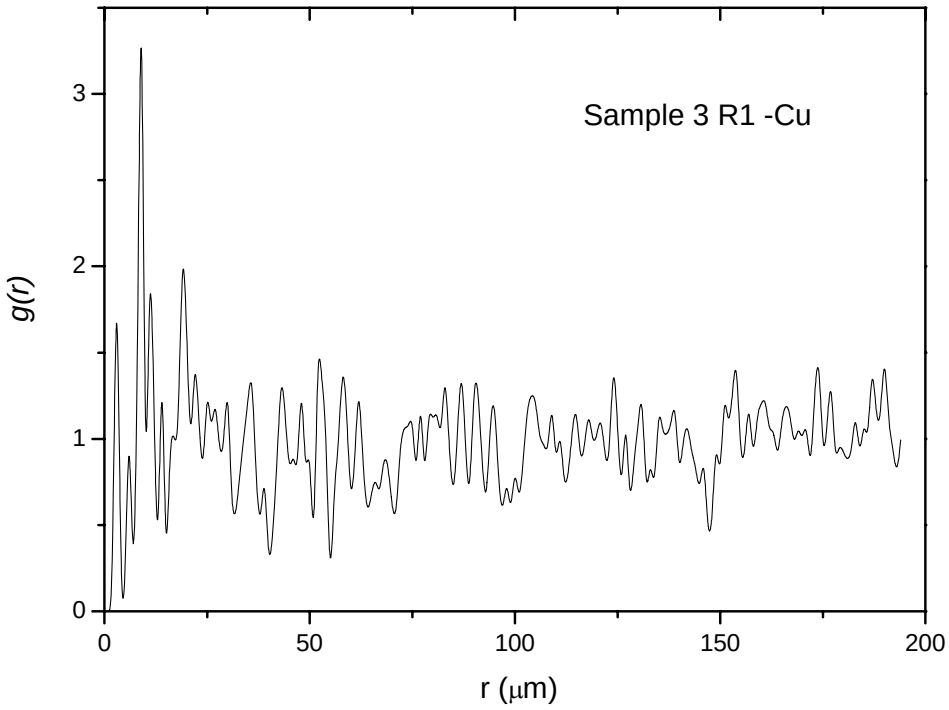

Figure 9-8: Pair correlation g(r) plot for PIXE sample 3 R1 Cu

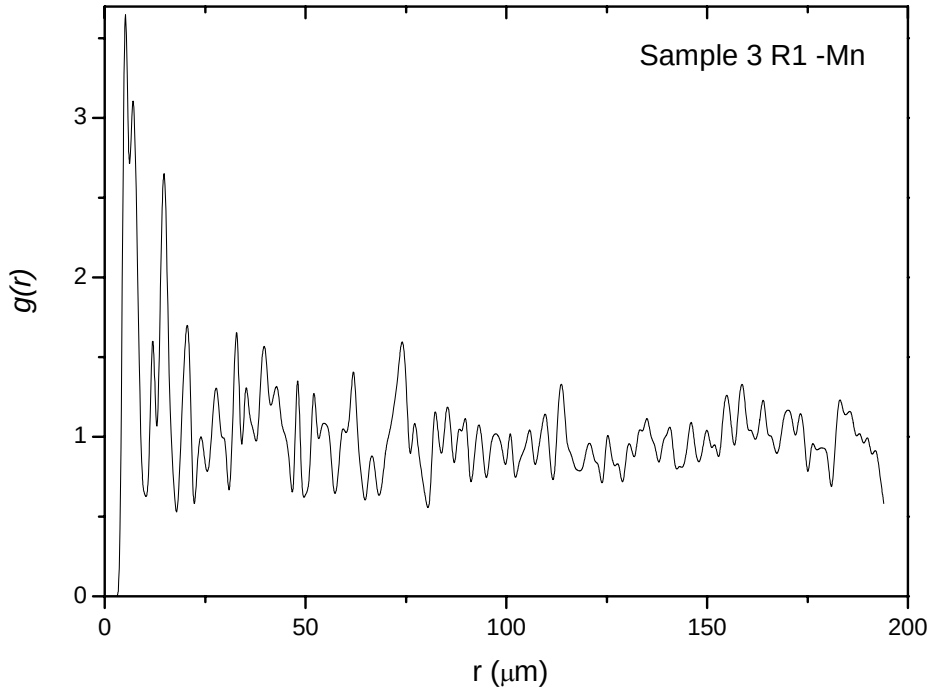

Figure 9-9: Pair correlation g(r) plot for PIXE sample 3 R1 Mn

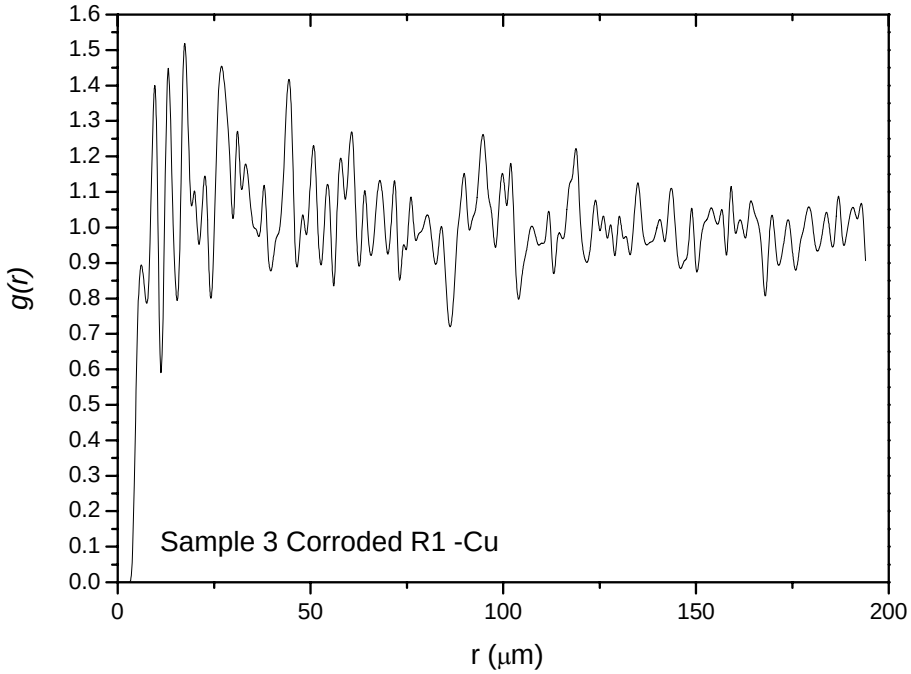

Figure 9-10: Pair correlation g(r) plot for PIXE sample 3 corroded R1 Cu

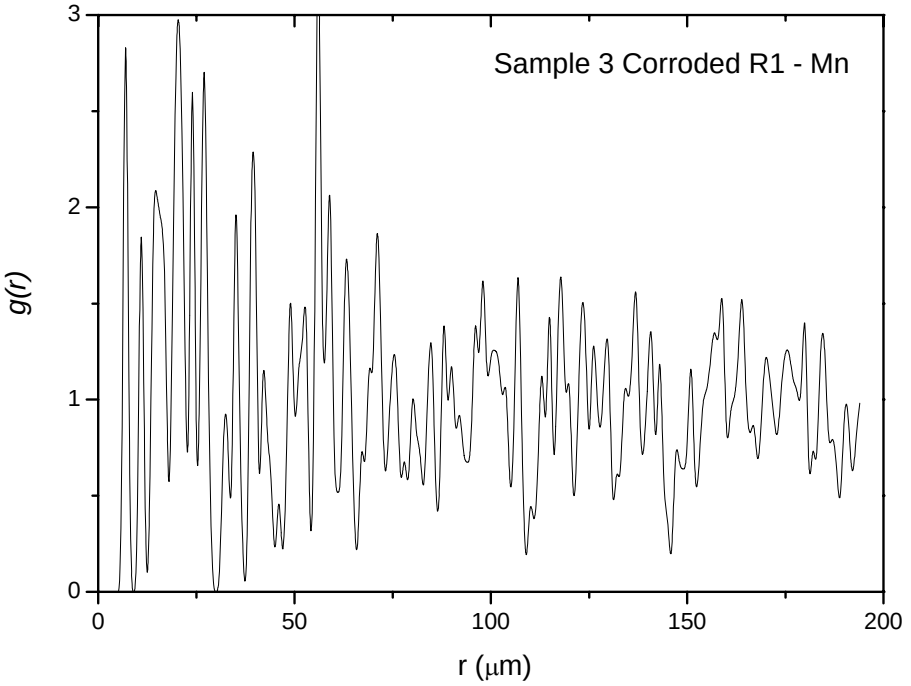

Figure 9-11: Pair correlation g(r) plot for PIXE sample 3 corroded R1 Mn

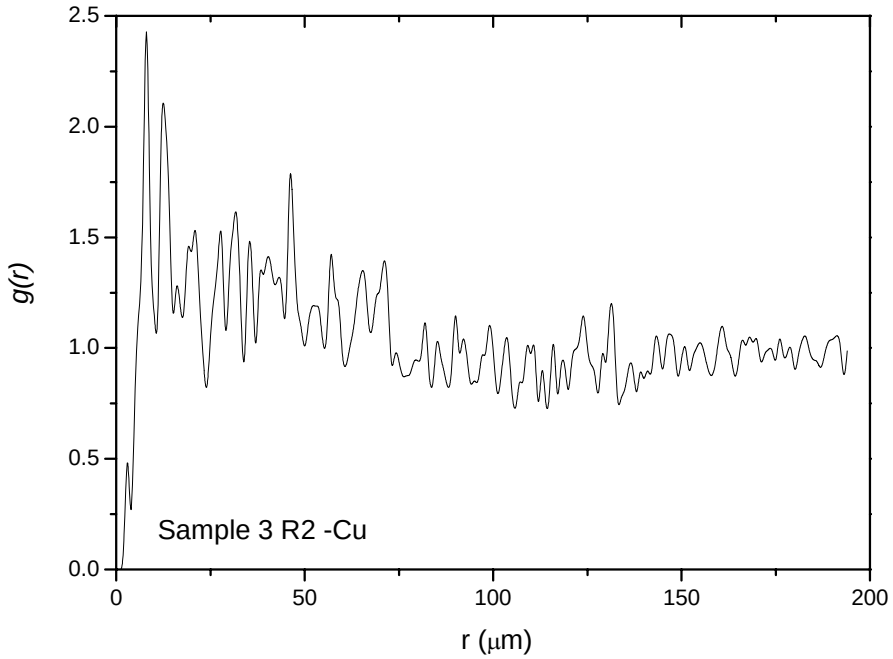

Figure 9-12: Pair correlation g(r) plot for PIXE sample 3 R2 Cu

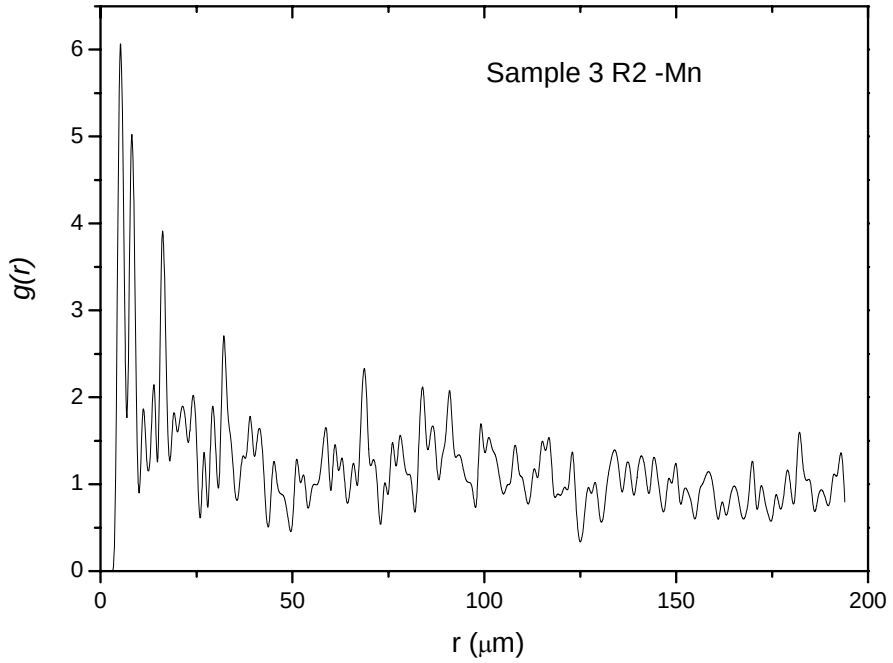

Figure 9-13: Pair correlation g(r) plot for PIXE sample 3 R2 Mn

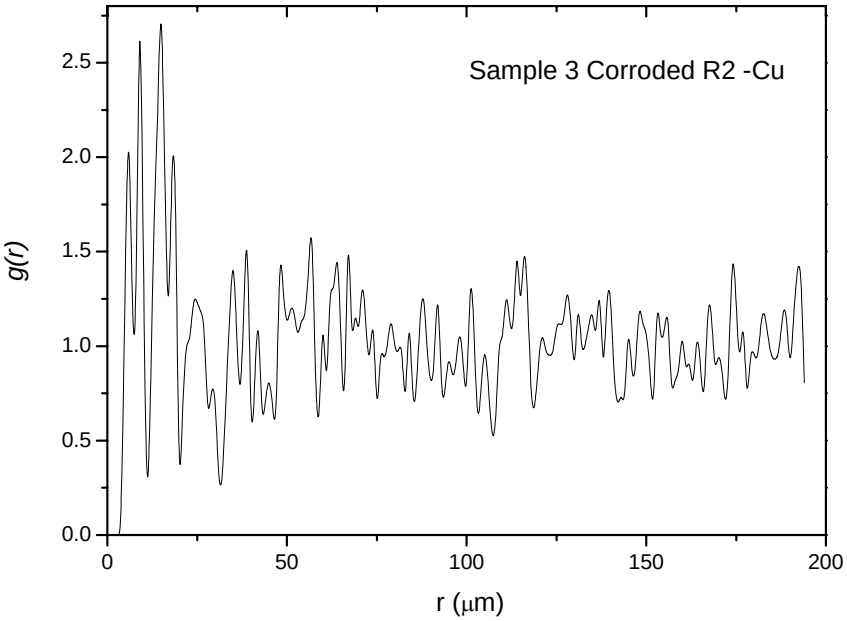

Figure 9-14: Pair correlation g(r) plot for PIXE sample 3 corroded R2 Cu

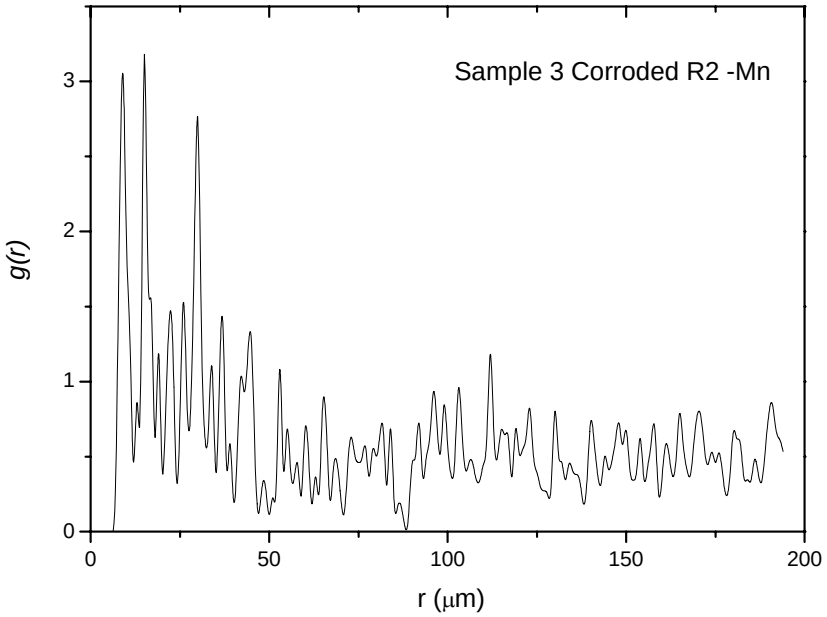

Figure 9-15: Pair correlation g(r) plot for PIXE sample 3 corroded R2 Mn

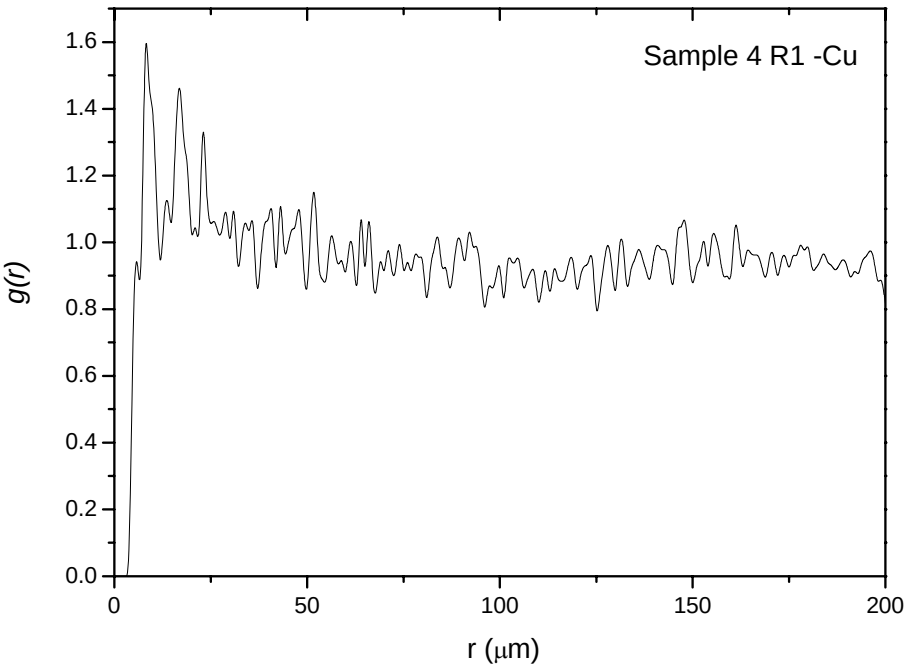

Figure 9-16: Pair correlation g(r) plot for PIXE sample 4 R1 Cu

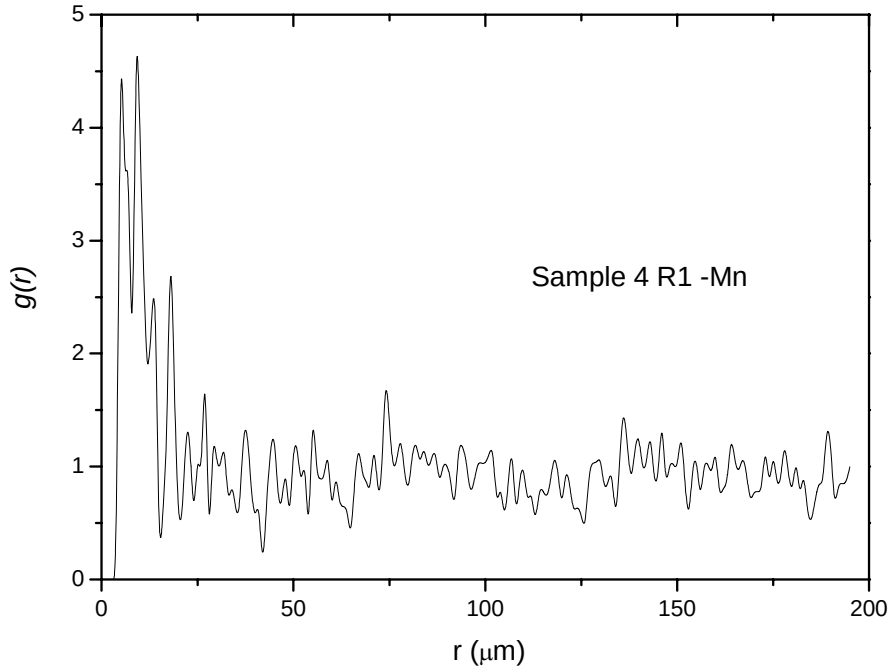

Figure 9-17: Pair correlation g(r) plot for PIXE sample 4 R1 Mn

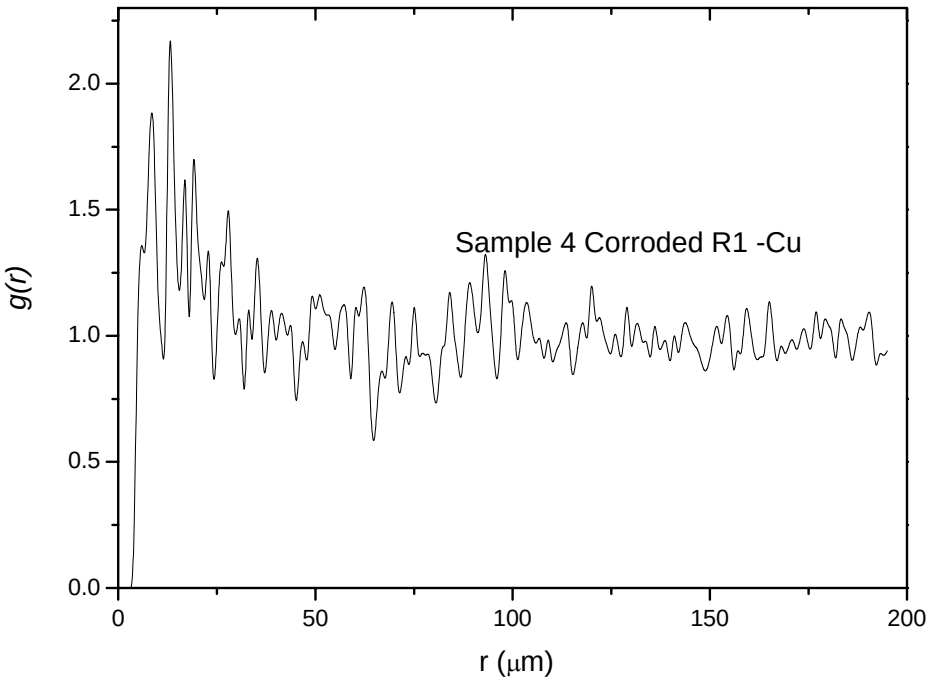

Figure 9-18: Pair correlation g(r) plot for PIXE sample 4 corroded R1 Cu

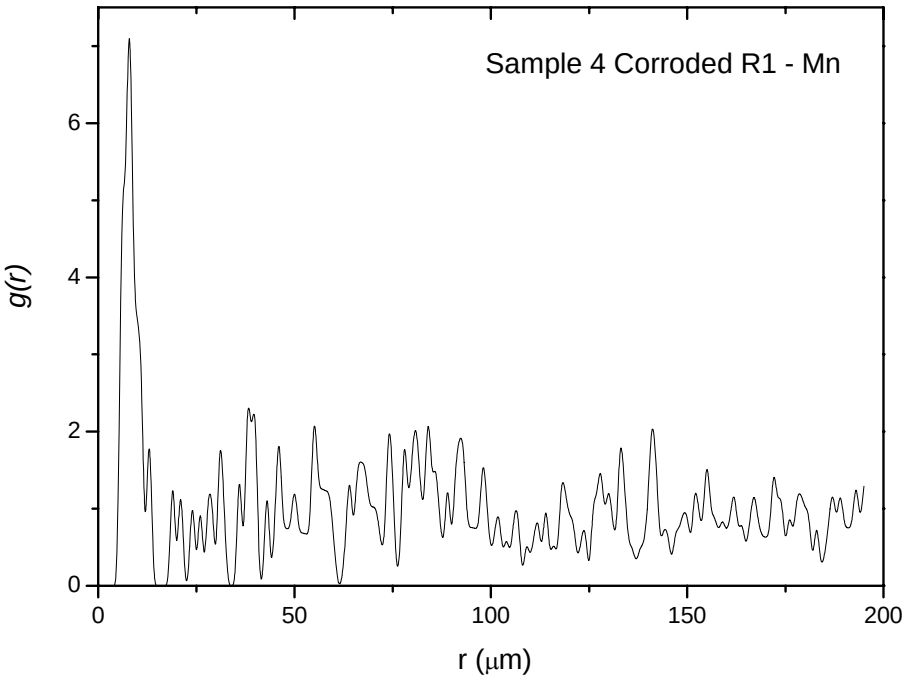

Figure 9-19: Pair correlation g(r) plot for PIXE sample 4 corroded R1 Mn

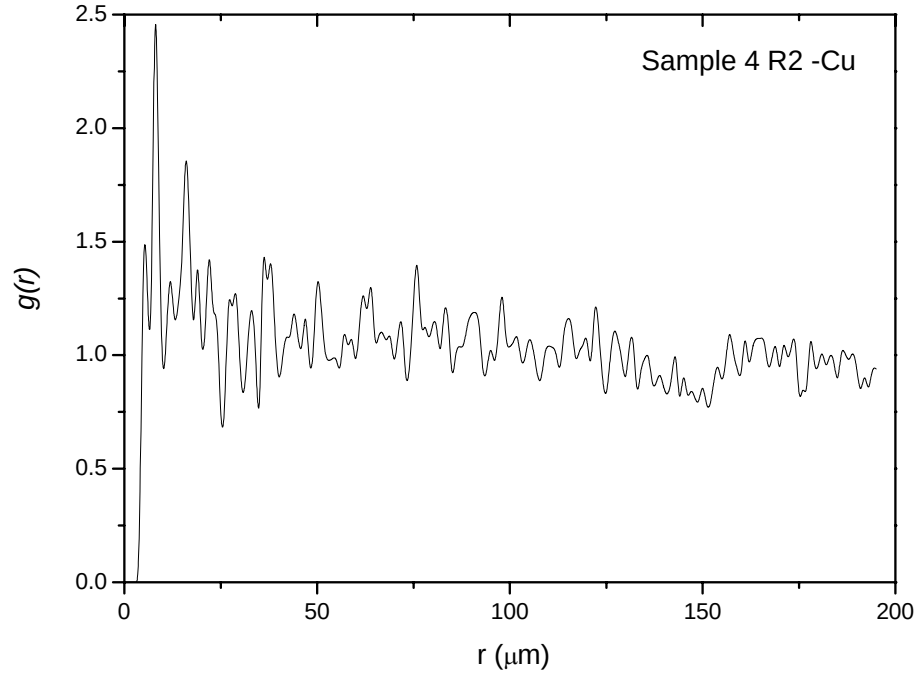

Figure 9-20: Pair correlation g(r) plot for PIXE sample 4 R2 Cu

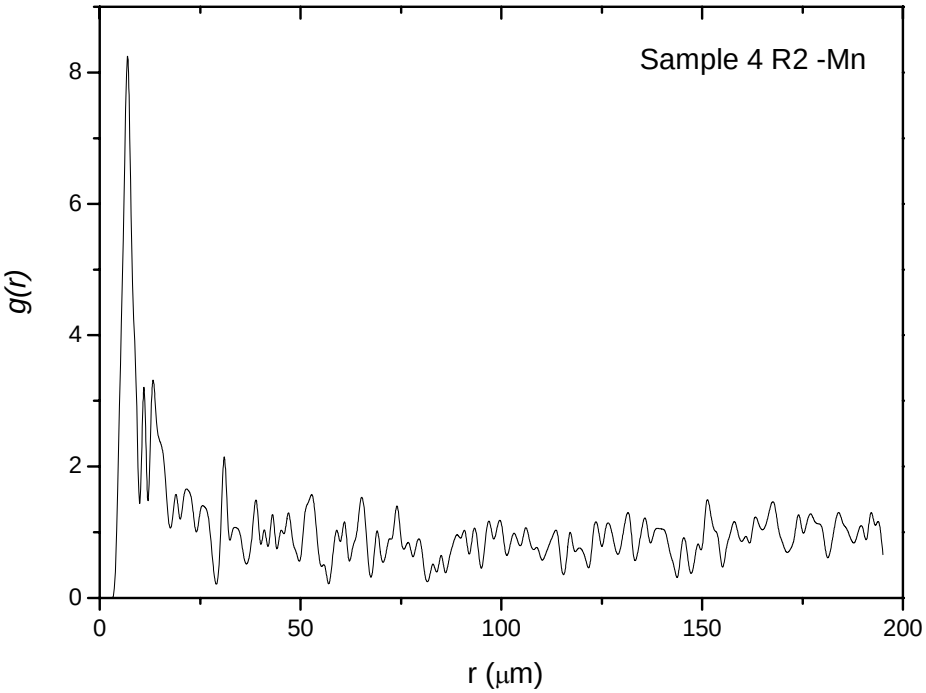

Figure 9-21: Pair correlation g(r) plot for PIXE sample 4 R2 Mn

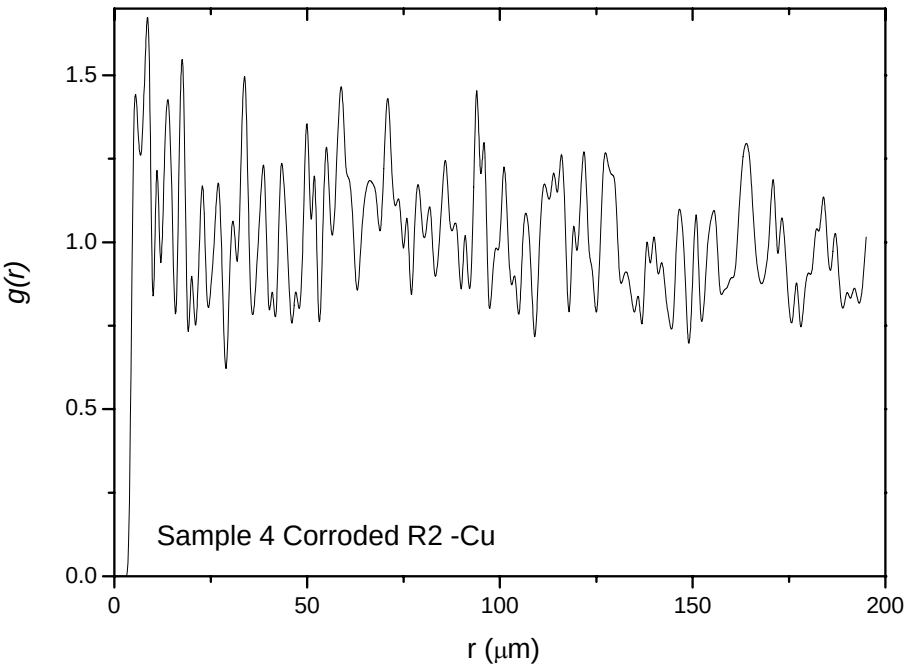

Figure 9-22: Pair correlation g(r) plot for PIXE sample 4 corroded R2 Cu

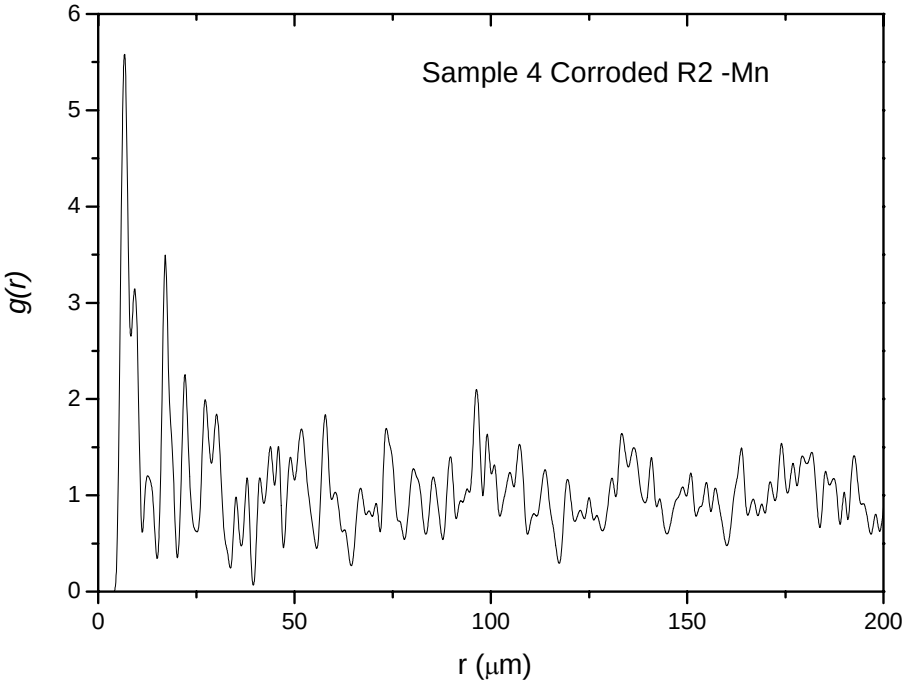

Figure 9-23: Pair correlation g(r) plot for PIXE sample 4 corroded R2 Mn

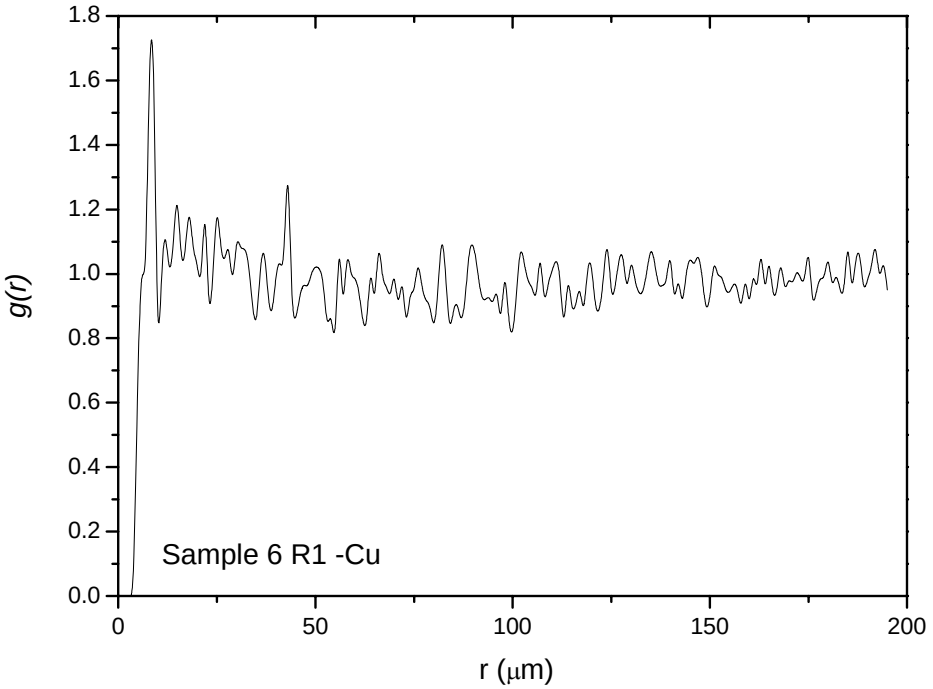

Figure 9-24: Pair correlation g(r) plot for PIXE sample 6 R1 Cu

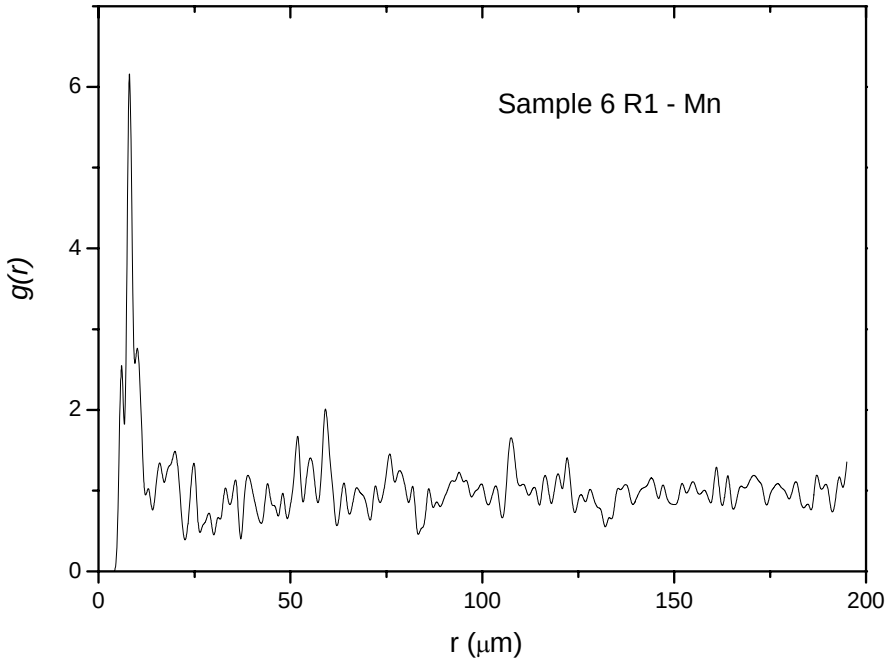

Figure 9-25: Pair correlation g(r) plot for PIXE sample 6 R1 Mn

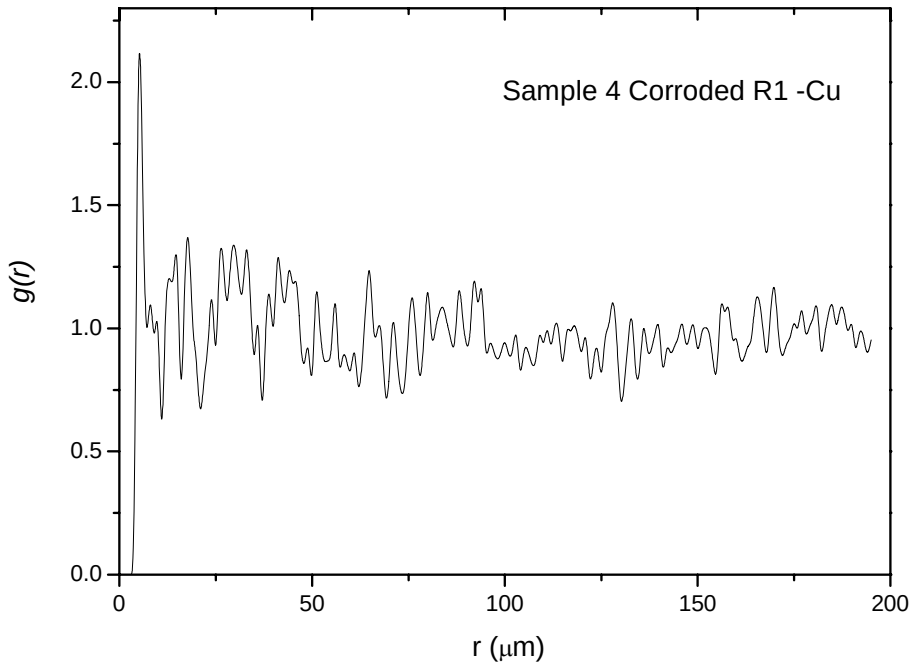

Figure 9-26: Pair correlation g(r) plot for PIXE sample 6 corroded R1 Cu

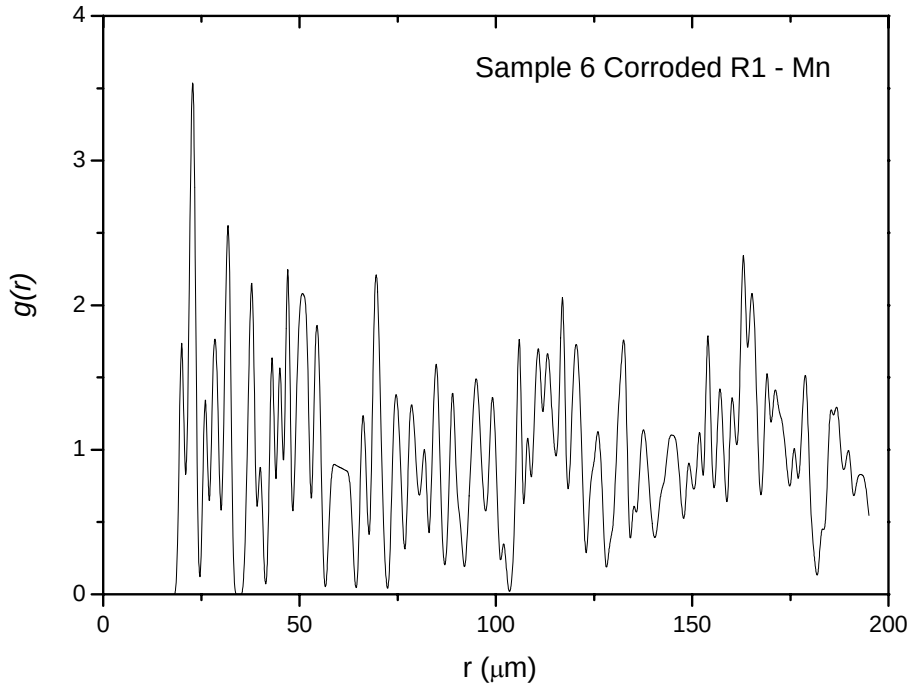

Figure 9-27: Pair correlation g(r) plot for PIXE sample 6 corroded R1 Mn

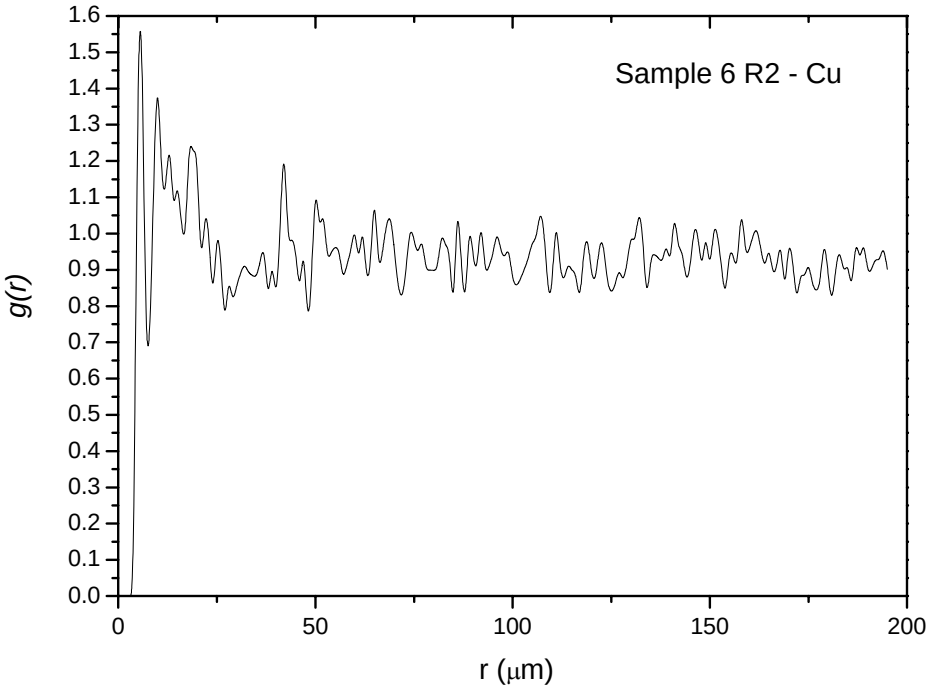

Figure 9-28: Pair correlation g(r) plot for PIXE sample 6 R2 Cu

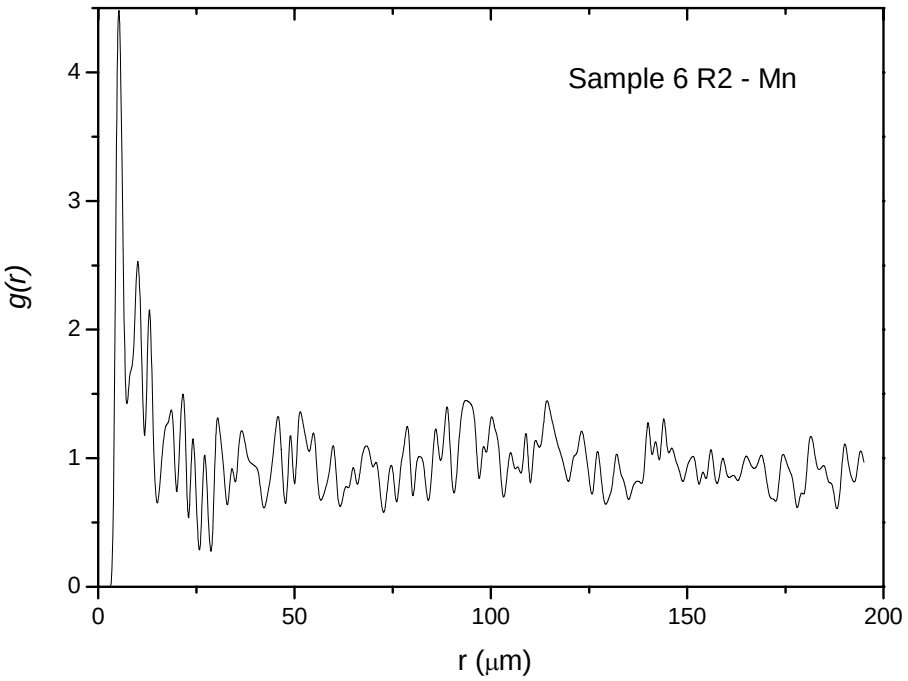

Figure 9-29: Pair correlation g(r) plot for PIXE sample 6 R2 Mn

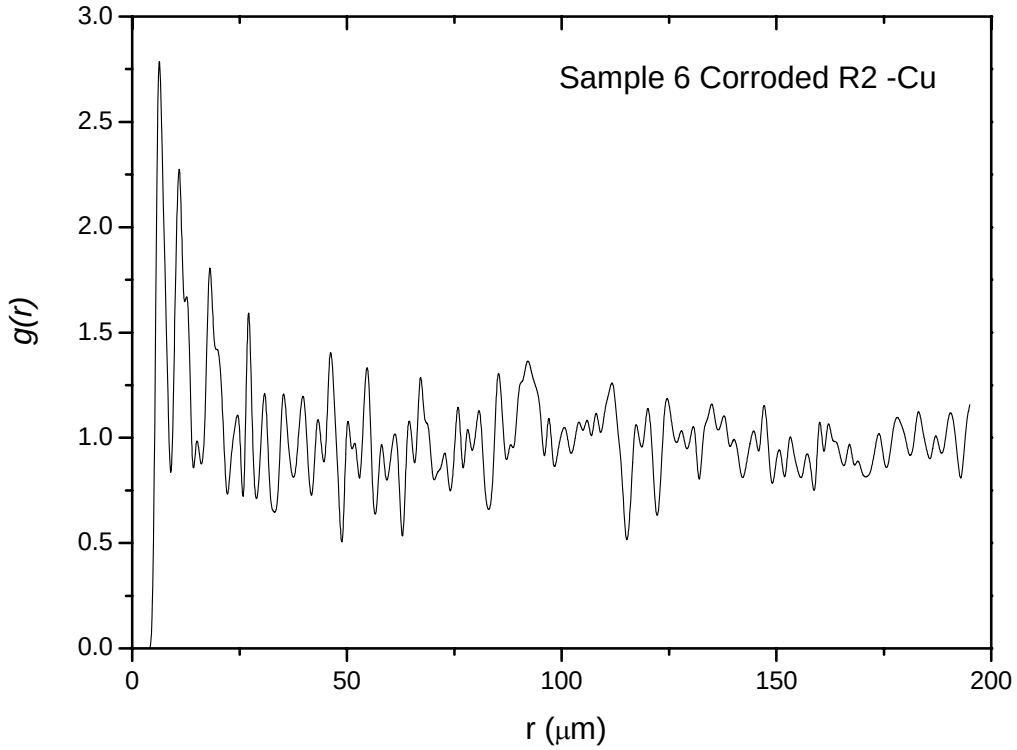

Figure 9-30: Pair correlation g(r) plot for PIXE sample 6 corroded R2 Cu

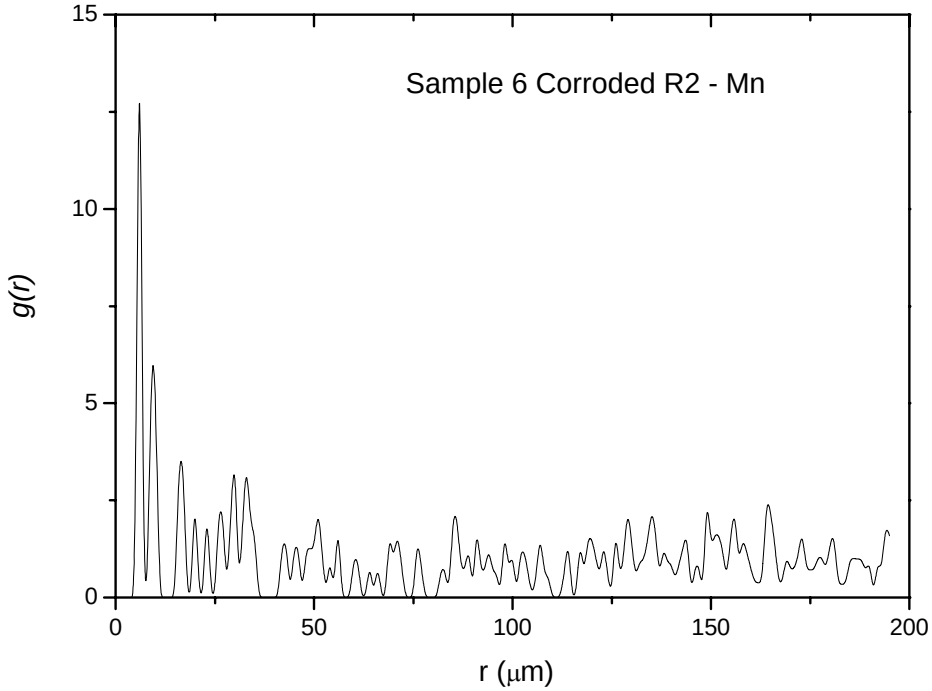

Figure 9-31: Pair correlation g(r) plot for PIXE sample 6 corroded R2 Mn

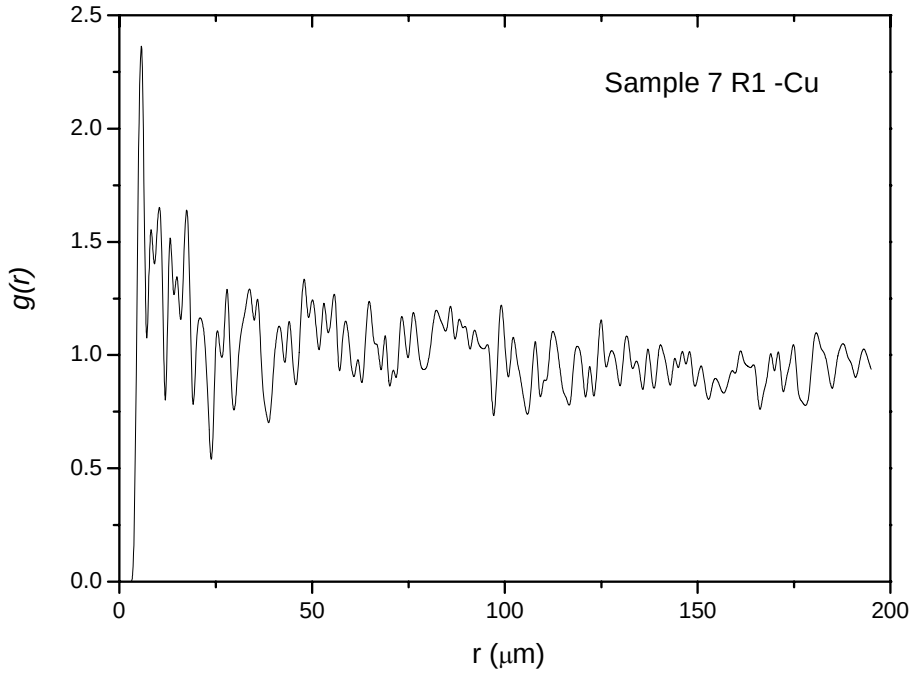

Figure 9-32: Pair correlation g(r) plot for PIXE sample 7 R1 Cu

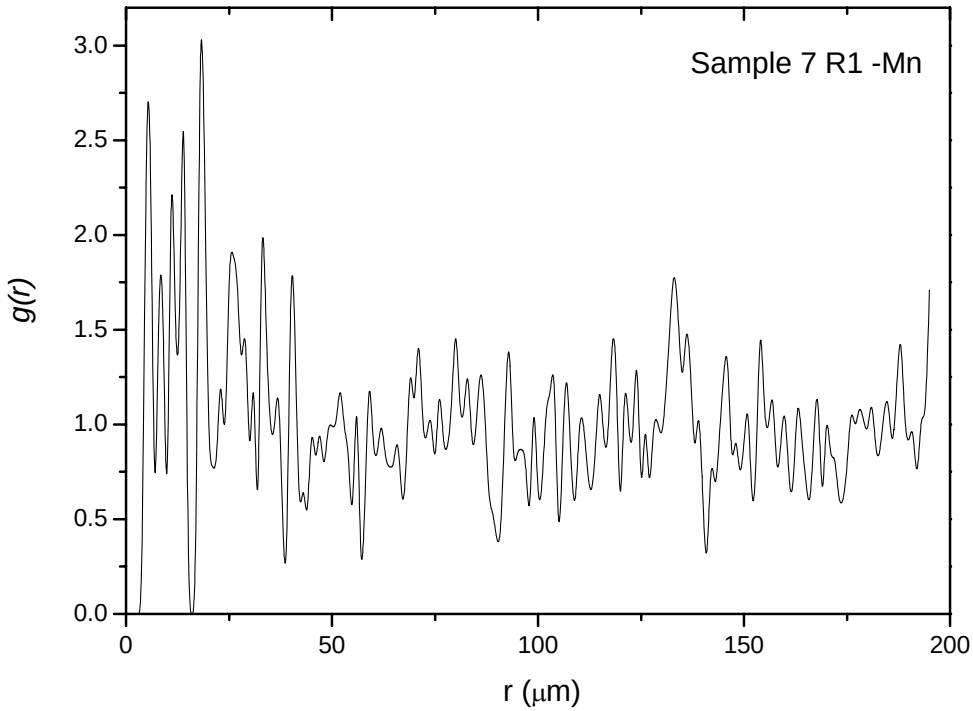

Figure 9-33: Pair correlation g(r) plot for PIXE sample 7 R1 Mn

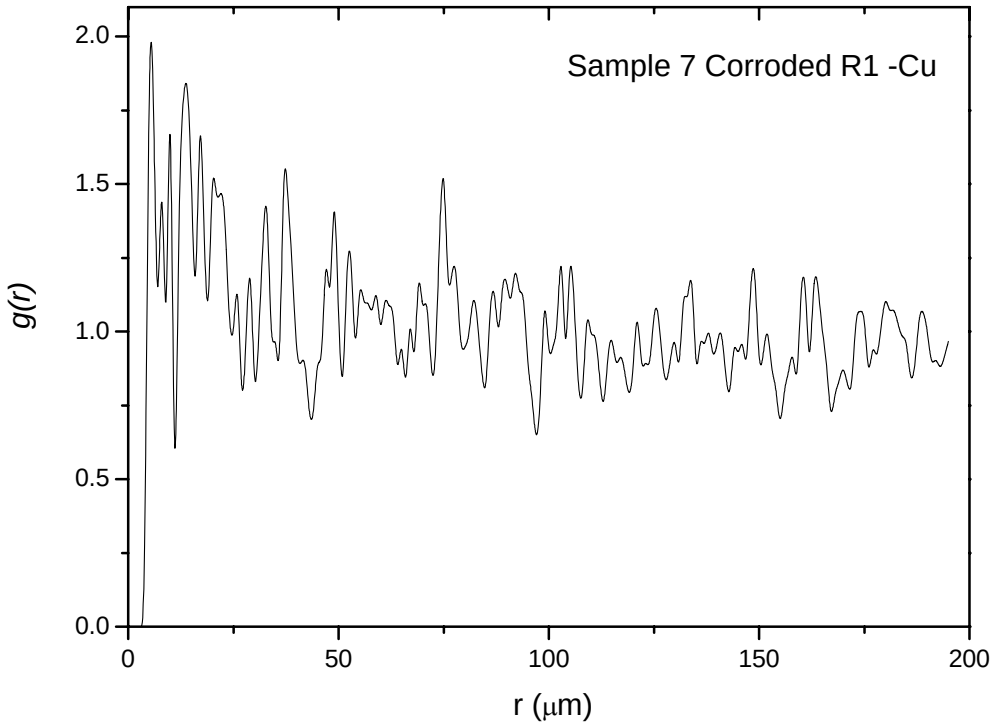

Figure 9-34: Pair correlation g(r) plot for PIXE sample 7 corroded R1 Cu

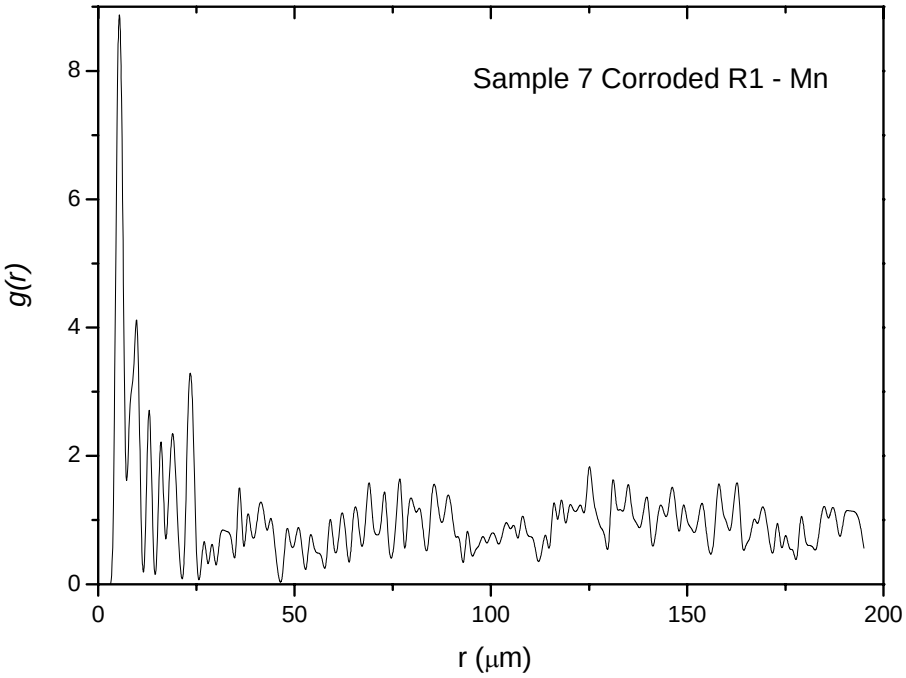

Figure 9-35: Pair correlation g(r) plot for PIXE sample 7 corroded R1 Mn

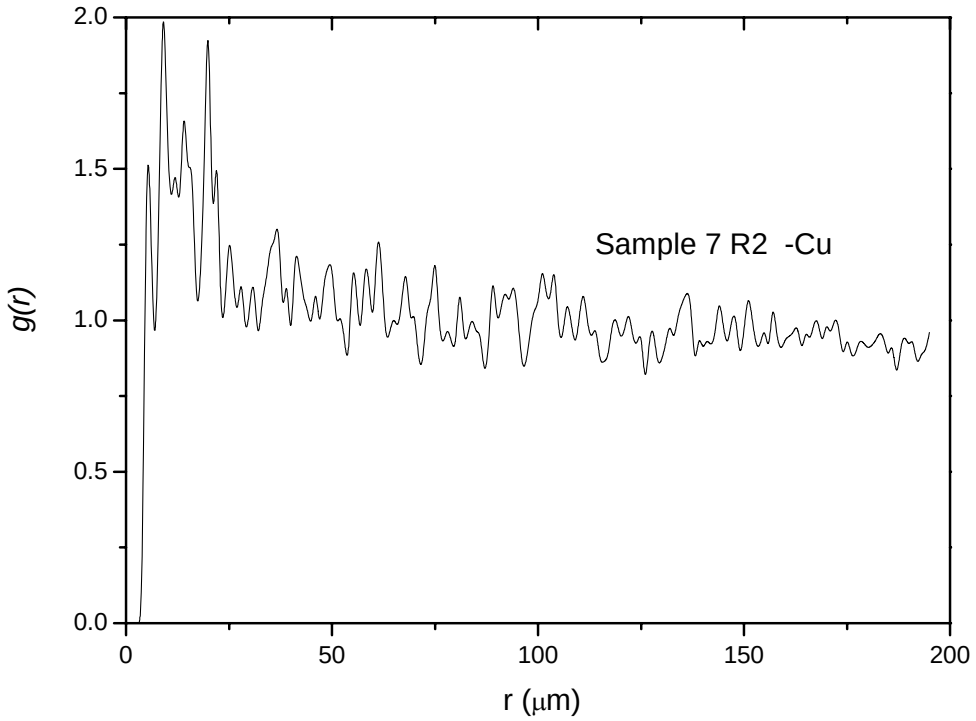

Figure 9-36: Pair correlation g(r) plot for PIXE sample 7 R2 Cu

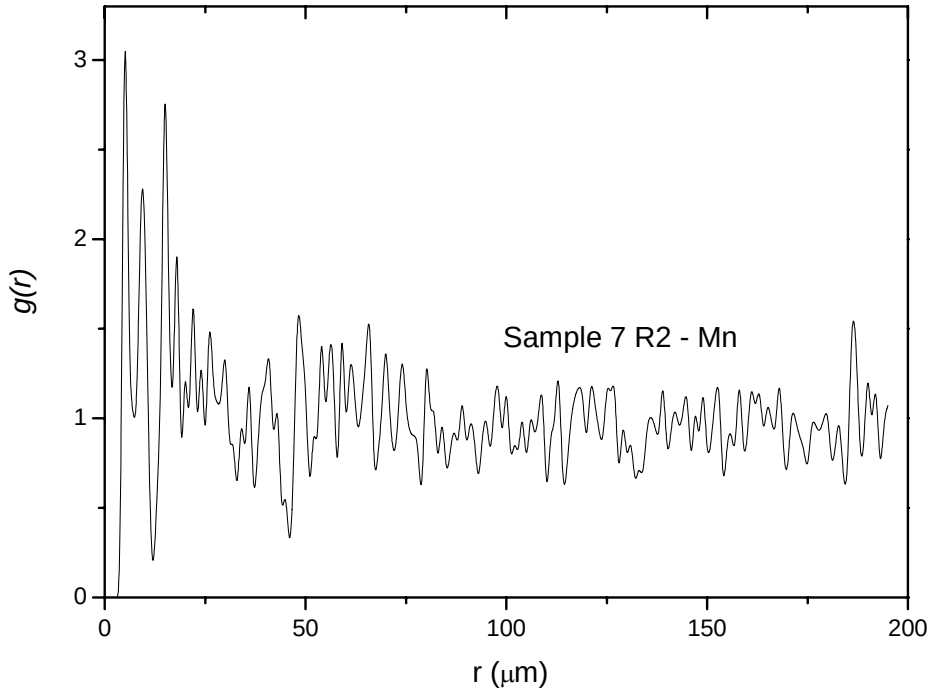

Figure 9-37: Pair correlation g(r) plot for PIXE sample 7 R2 Mn

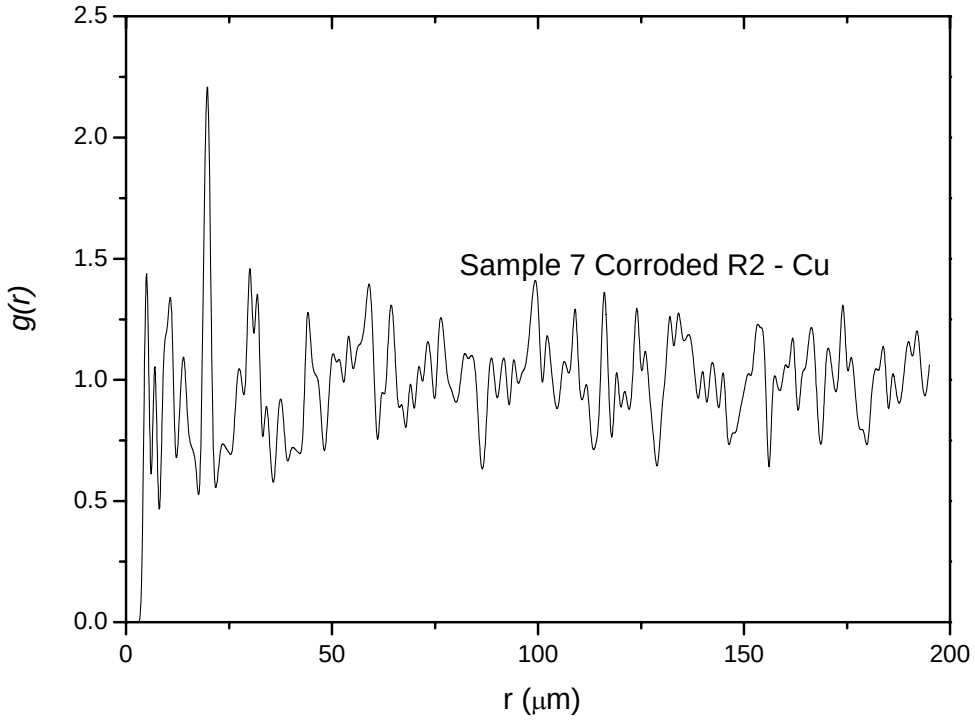

Figure 9-38: Pair correlation g(r) plot for PIXE sample 7 corroded R2 Cu

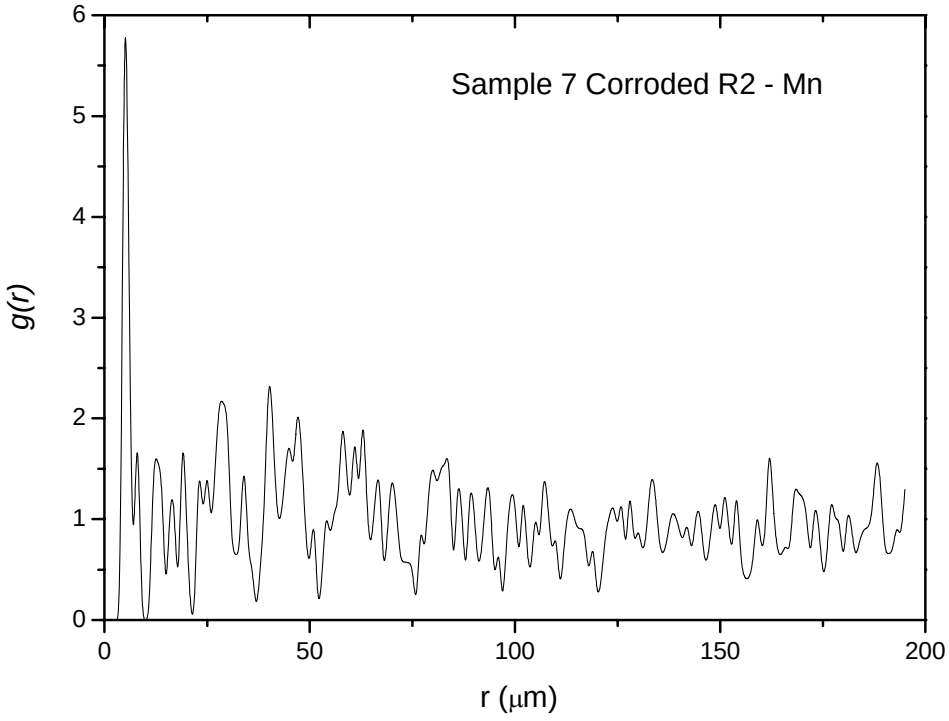

Figure 9-39: Pair correlation g(r) plot for PIXE sample 7 corroded R2 Mn

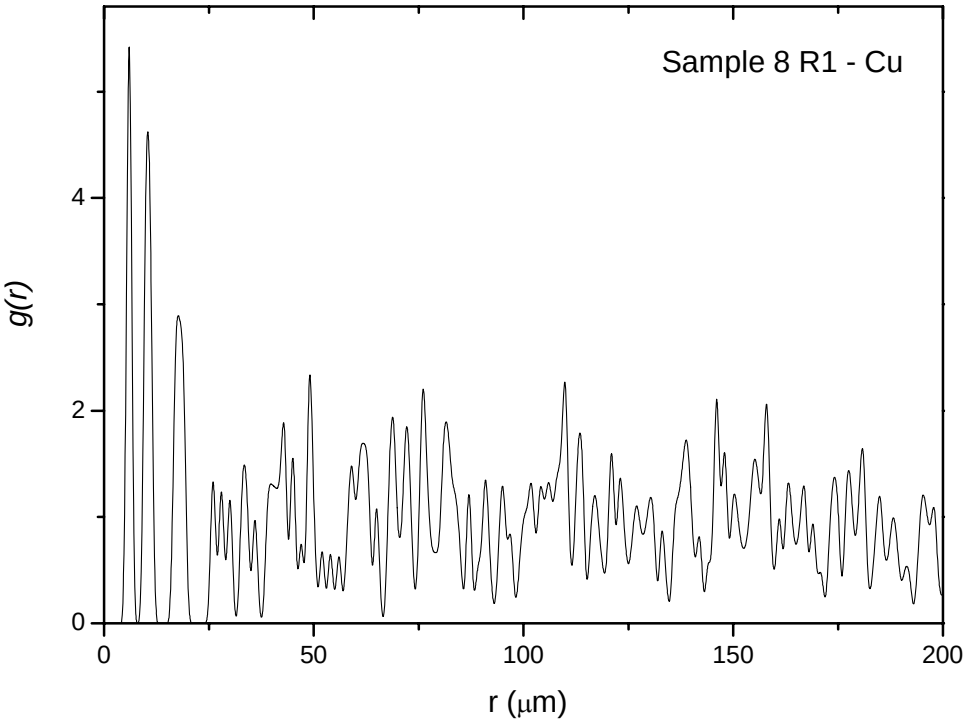

Figure 9-40: Pair correlation g(r) plot for PIXE sample 8 R1 Cu

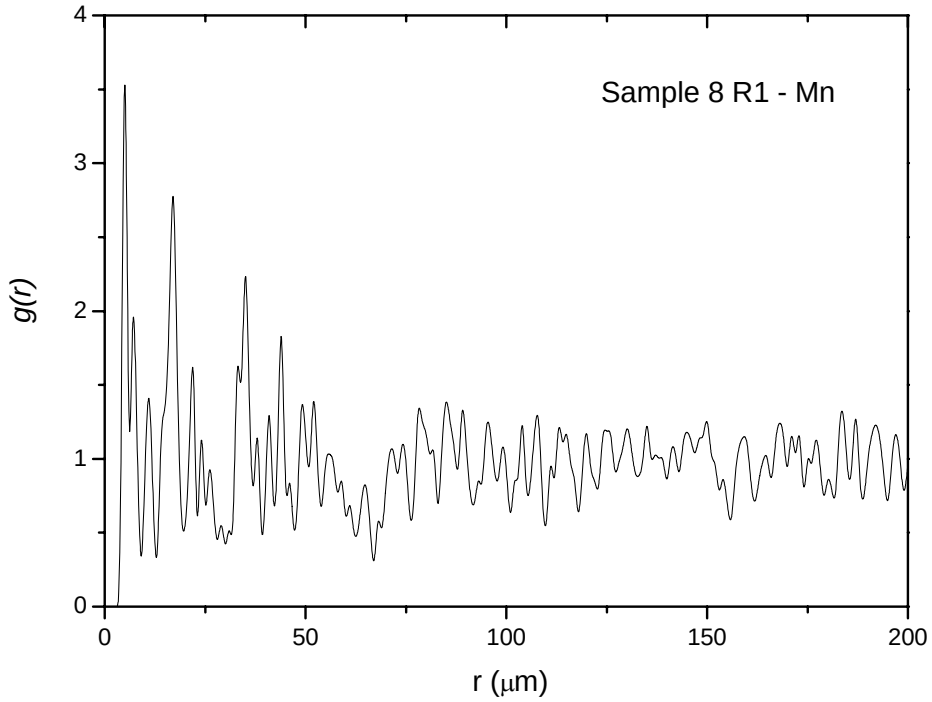

Figure 9-41: Pair correlation g(r) plot for PIXE sample 8 R1 Mn

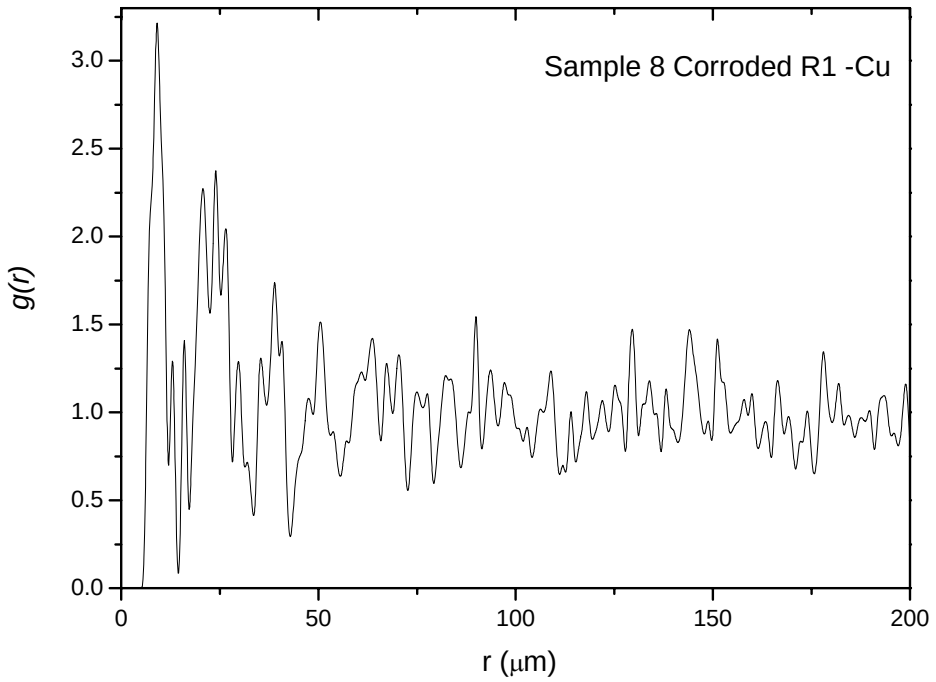

Figure 9-42: Pair correlation g(r) plot for PIXE sample 8 corroded R1 Cu

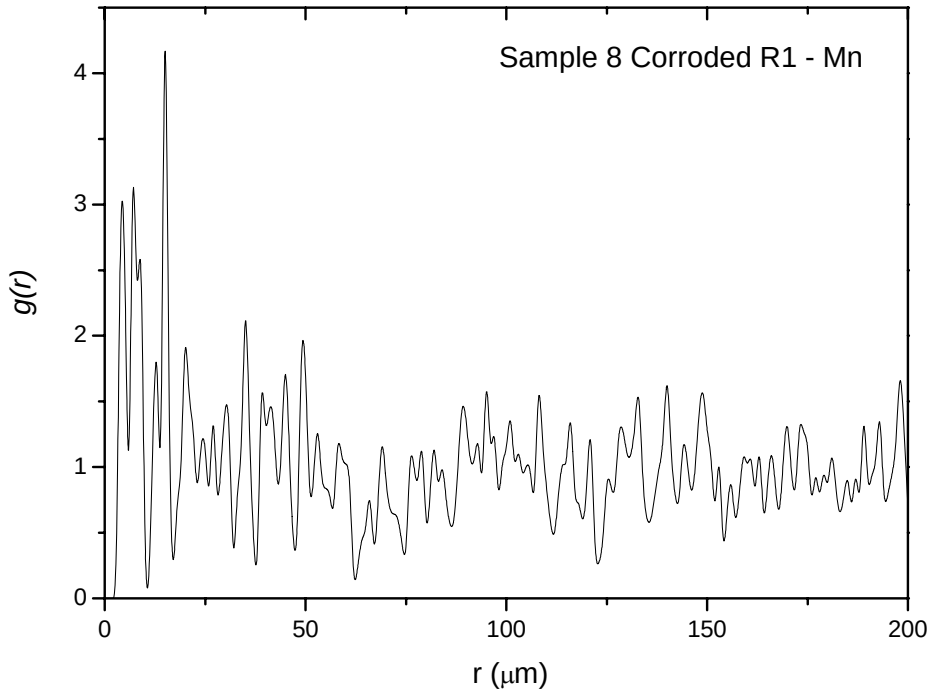

Figure 9-43: Pair correlation g(r) plot for PIXE sample 8 corroded R1 Mn

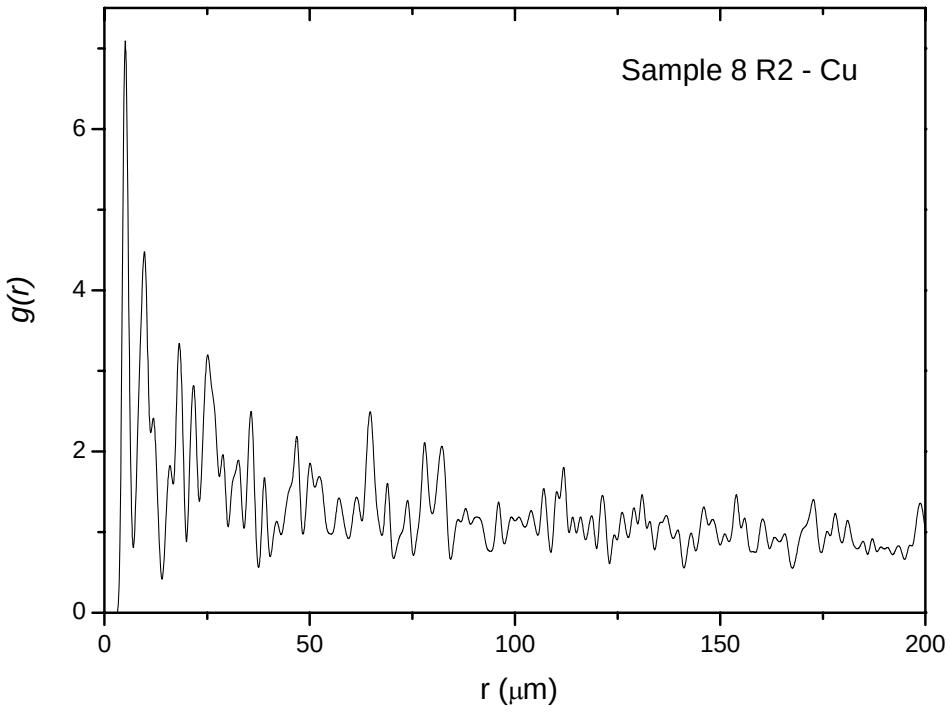

Figure 9-44: Pair correlation g(r) plot for PIXE sample 8 R2 Cu

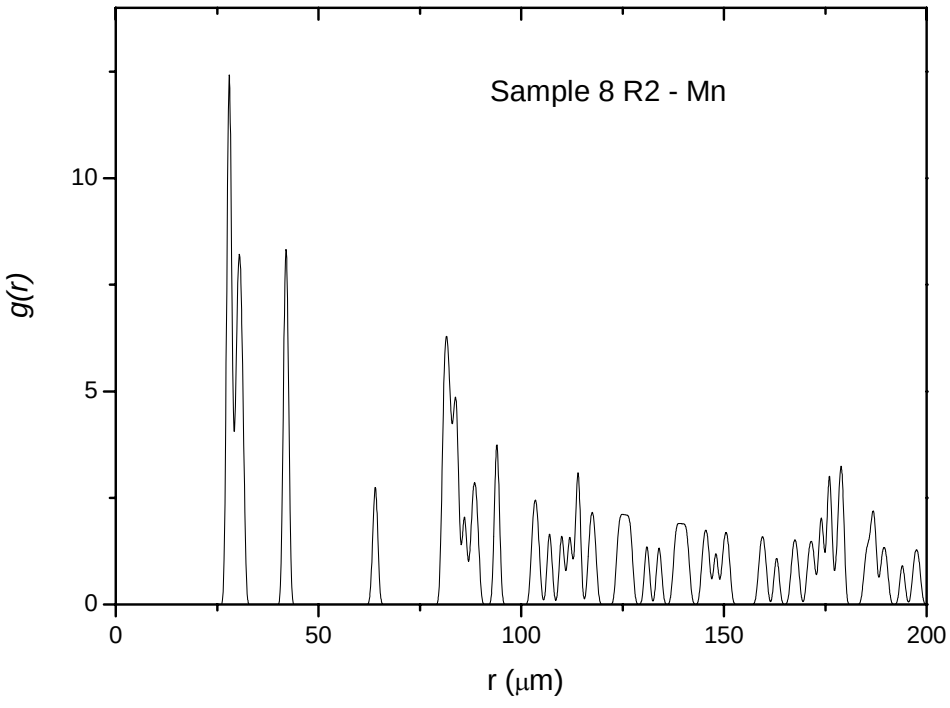

Figure 9-45: Pair correlation g(r) plot for PIXE sample 8 R2 Mn

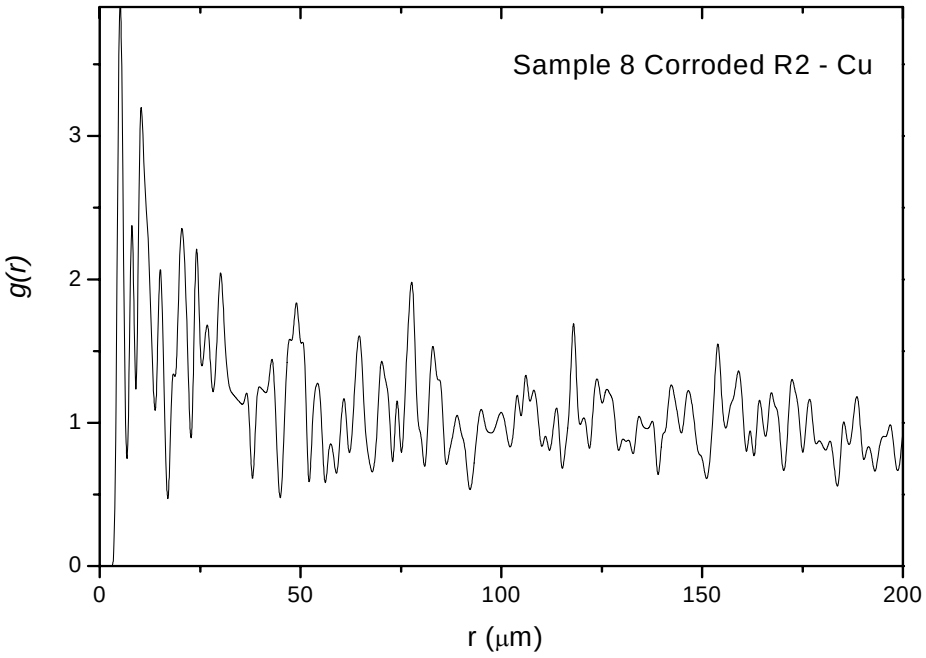

Figure 9-46: Pair correlation g(r) plot for PIXE sample 8 corroded R2 Cu

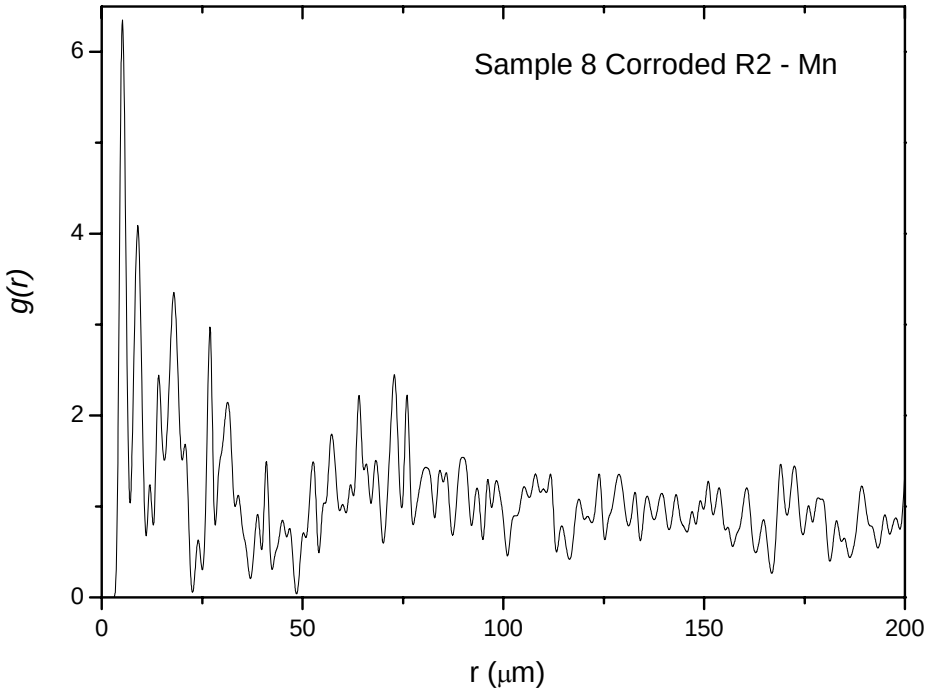

Figure 9-47: Pair correlation g(r) plot for PIXE sample 8 corroded R2 Mn